Analysis of the Hydrodynamics and Morphological Changes of the Gold Coast Seaway Ebb-Tidal Delta

ANALYSIS OF THE HYDRODYNAMICS AND MORPHOLOGICAL CHANGES OF THE GOLD COAST SEAWAY EBB-TIDAL DELTA

Mahnaz Sedigh, B. Eng, M. Eng. (Adv.)

Division of Civil Engineering
Griffith School of Engineering, Science group
Griffith Centre for Coastal Management (GCCM)

Submitted in fulfilment of the requirements of the degree of Doctor of Philosophy in Coastal Engineering

Principal Supervisor:	Prof. Rodger Tomlinson
Associate-Supervisor:	Dr. Nick Cartwright
Associate-Supervisor:	Dr. Amir Etemad-Shahidi
External-Associate-Supervisor:	Dr. Ali Golshani

Jan. 2017

Abstract

The Gold Coast Seaway (GCS), known as the Nerang River Entrance (NRE) prior to stabilisation, is located at one of Australia's premier tourist centres, and consequently, the provision of a safe navigation channel is significantly important for recreational boating and commercial craft activities between the ocean and the estuary. The tidal regime in the area is semi-diurnal with neap and spring tidal ranges of 0.3*m* to 2*m* respectively, and the entrance has a minor ebb dominant current regime. The dominant offshore wave climate is south to south east, and the beaches have a wave dominated, double bar morphology. The entrance location had undergone drastic changes due to natural processes prior to its stabilisation in 1986. These changes were significantly influenced by the dominant northward wave condition which, in combination with the resultant longshore sediment transport (LST), resulted in the entrance's net northward migration prior to the stabilisation. The entrance has experienced an alteration in the inlet tidal prism since stabilisation and the implementation of the artificial bypassing system. As a result, the extent of the ebb-tidal delta offshore and its equilibrium volume have changed.

The new ebb-tidal delta was formed at the river mouth, and continuous accretion in recent years has led to navigation safety concerns. Many studies, including analytical and numerical models, have been applied to the GCS to understand the hydrodynamics and sediment transport patterns in the area. The current literature, however, does not adequately explain the sediment transport pathways and physical mechanisms behind the continuous morphological changes in the ebb tidal delta. The research reported in this thesis aims to: extend the current understanding of the processes controlling the continuous changes in the ebb-tidal delta; provide an updated conceptual model of the sediment transport rate and pathways in the area based on measured field data; and provide a numerical model which can simulate the hydrodynamics of the inlet area and morphodynamics of the ebb-tidal delta properly.

In this study, the survey data during the past decade are first analysed. The results are then linked to the analysis from 1986 to 1999. The results show a continuous net growth of the ebb-tidal delta, at an average rate of 151,000 m^3/yr since stabilization. The results also show the continuous erosion of the inlet channel at an average rate of 31,000 m^3/yr, which, due to an ebb-dominant current in the inlet channel, can account for about 20% of the ebb-tidal delta growth. To find the governing source of sand to the ebb-tidal delta, the bathymetry changes of the ebb-

tidal delta are investigated along with measured wave data, flood history, and dredging and nourishments in the area. It is found that the ebb-tidal delta dynamics can be explained in terms of the natural hydrodynamic forces, such as wave and river discharge. Accretion occurred in the ebb-tidal delta during the intervals with major SE storms, or very significant flood events. It is suggested that during the former, the LST is leaking offshore from the sand-bypassing system; and during the latter, sediment is coming from within the estuary. Based on this analysis, it is also suggested that the ebb-tidal delta shows erosion during major NE storm events. An updated conceptual model of sediment transport pathways for the past decade is also proposed.

To provide more support for the suggested interpretations of the ebb-tidal delta dynamics and processes, as well as an understanding of the underlying physical processes and their interaction with sediments in the area, a process-based depth averaged numerical simulation using a MIKE 21/3 coupled depth-averaged model is applied. The hydrodynamics module is calibrated and validated against field measurements. The model is then used to simulate the LST rate, and the morphological changes of the ebb-tidal delta. The annual simulated LST for the simulation period, August 2008 to August 2009, is close to the suggested rate in previous studies and the artificial sand bypassing rate in that period. However, analysis of the time-series of the simulated LST versus the artificial bypassing rate illustrates that the model underestimated the LST during calmer weather conditions. In addition, it is shown that a significant portion of the simulated LST occurred during major storm events, such as East Coast Low (ECL) in May 2009. The cross-shore distribution of the LST during this event shows that most of the sediment transport during these events occurred more offshore than the sand bypassing jetty and the southern training wall. Therefore, this portion of LST during the major storm events leaks to the ebb-tidal delta. Hence, the LST for the simulated period, considering the simulated rate and the leakage volume during major storm events as well as the artificial sand bypassing rate, is close to that suggested by using the developed conceptual model.

Model capability of the morphological simulation of the ebb-tidal delta is then examined by simulation of the period between two survey data. The results show that the majority of the changes in the ebb-tidal delta during that period occur during major SE storm events, especially ECL in May 2009. Therefore, the skill of the model in predicting the morphological changes is calculated using the 12 day simulation of the ECL in May 2009. The resultant skill of the model prediction is found to be “good” based on the suggested categorization. Therefore, the developed model can be used for simulation of the morphological changes of the ebb-tidal delta

during major storm events, which are found to be the governing forces of the bathymetry changes of the ebb-tidal delta.

The developed numerical model is then used for a number of storm event scenarios, with various strength and directions. The results demonstrate that the major NE storm events, unlike SE storm events, have an erosional influence on the ebb-tidal delta, which confirm the results of analyses of the survey data. The resultant conceptualized models and graphs based on the storms accumulative wave powers and directions can be used for prediction of the LST and ebb-tidal delta volumetric change due to major storm events.

Statement of Originality

This work has not previously been submitted for a degree or diploma in any university. To the best of my knowledge and belief, the thesis contains no material previously published or written by another person except where due reference is made in the thesis itself.

_____

Mahnaz Sedigh

Table of Contents

List of Figures

List of Tables

List of Symbols

Roman symbols and abbreviations

A	Maximum H_s (m)
ABSS	Adjusted Brier Skill Score
A_c	Minimum flow cross section of the entrance channel (throat) measured below mean sea level (MSL) (m^2)
A_e	Horizontal eddy viscosity
AHD	Australian Height Datum (m)
ARMAE	Adjusted Relative Mean Absolute Error
BCSI	Bias-Corrected Scatter Index
Bias	Average error
BSS	Brier Skill Score
C	computed/predicted
C_w	Speed of wave propagation (m/s)
C'	Computed minus reference values (c - r)
c_f	Drag coefficient
CFL	Model Courant-Fridrich-Levy number
C_g	Group wave velocity (m/s)
$\vec{c}_g$	Magnitude of the group velocity of the wave energy relative to the current
Ch	Ch'ezy number
d	Water depth (m)
d_{16}	Diameter for which 16% of the particles in the sample are larger than d_{16}
d_{25}	Diameter for which 25% of the particles in the sample are larger than d_{25}
d_{50}	Sediment median grain size
$d_{50,s}$	Median sediment size in surfzone (m)
d_{75}	Diameter for which 75% of the particles in the sample are larger than d_{75}
d_{84}	Diameter for which 84% of the particles in the sample are larger than d_{84}
d_g	Grain diameter
D_{pm}	Mean peak wave direction of the storm event (˚)
D_s	Storm duration in seconds

DSD	Directional standard deviations
d_{sw}	Still water depth
D_w	Local water depth
E	Wave energy per unit horizontal area (J/m^2)
$\hat{E}$	Evaporation rate
ETA	There are 80 fixed hydrographic survey lines, along Gold Coast beaches
f	Coriolis parameter
f_r	Ordinary frequency
g	Gravity acceleration (9.8 m/s^2)
h	Total water depth
H_m	Average wave height in metres
H_s	Significant wave height (m)
$H_{s,br}$	Significant wave height at breaking (m)
K	Empirical coefficient in CERC longshore sediment transport volume formula
k	Magnitude of wave number vector $\vec{k}$ (wave number)
kn	Nikuradse roughness
k_s	Suspended load calibration factor
L	Wave length at intermediate depths (m)
M	measured/observed
M_n	Manning number ($1/n$)
M'	Measured minus reference values (M - r)
m_a	Coordinate axis perpendicular to the wave direction
MAE	Mean Absolute Error
m_b	Beach slope defined as the ratio of the water depth at the breaker line and the distance from the still water beach line to the breaker line
MSE	Mean Square Error
MSL	Mean Sea Level
M_{tot}	average annual LST brought to the inlet
MWD	Mean wave direction, $^\circ$
$MWPD$	Mean wave power direction
n	Manning number
n_s	Directional spreading index
$N(\vec{x},\sigma,\theta,t)$	Wave action density
P	Tidal prism corresponding to the spring range of tide (m^3)

$\hat{P}$	Precipitation rate
p	Probability that all the particles of a layer are moving
p_a	Atmospheric pressure
p_s	Sediment porosity factor
P_w	Wave power (W/m)
P_{wm}	Mean wave power for each storm event (W/m)
q_b	Bed load
q_{b1}	Bed load in the mean current direction
q_{b2}	Bed load normal to mean current direction
q_s	Suspended load
q_t	Total sediment transport load
$Q_{t,vol}$	Longshore sediment transport volume (m^3/s)
r	Reference values
R	Correlation coefficient
$RMAE$	Relative Mean Absolute Error
RMS	Root Mean Squared Error
S	Magnitude of the discharge due to point sources
s	Space coordinate axis in the wave direction
S_{bot}	Dissipation due to bottom friction
S_{ds}	Dissipation of wave energy due to whitecapping
SI	Scatter Index
S_{in}	Energy generation by wind
$Skill$	Ratio of the mean square error and the potential error
S_{nl}	Wave energy transfer due to non-linear wave-wave interaction
S_s	Sediment specific gravity
s_s	Relative sediment density of the bed material
S_{surf}	Dissipation of wave energy due to depth-induced breaking
S_T	Source term for energy balance equation (energy source term)
s_{xx}, s_{xy}, s_{yx} and s_{yy}	Components of radiation stress tensor
T	Tidal period
t	Time
T_{ch}	A characteristic time scale of the storm duration (hr)
T_{ij}	Lateral stresses which include include viscous friction, turbulent friction and

	differential advection
T_m	Time when the maximum H_s occurs
T_{mean}	Mean wave period
T_p	Peak wave period (s)
T_w	Wave period
u	Velocity component in the x direction
$\vec{u}_b = (u_b, v_b)$	Depth-averaged flow velocity
U	Inlet channel parallel velocity component
$\vec{U}$	Current velocity vector
u_i	Instantaneous flow velocity
u_s,v_s	Velocity by which the water is discharged into the ambient water
V	volume of sand stored in its ebb-tidal delta
v	Velocity component in the y direction
$\vec{v}$	Propagation velocity of a wave group= ($c_x, c_y, c_\sigma, c_\theta$)
W	Equilibrium channel width (m)
w	Settling velocity of the suspended sediment
W_{PT}	Total storm wave power ($W.s/m$)
x and y	Cartesian horizontal coordinates
$\overline{X}$	The average of selected modelled or measured variables
X_C	Set of N computed/predicted by model values
X_M	Set of N observed/measured values
z_0	Initial bed levels (reference) (m)
z_C	A set of N computed (predicted) by model bed level values (m)
z_M	A set of N observed (measured) bed levels (m)

Greek symbols

α	Coefficient of determination
α'	Phase association between c' and m' , denotes the skill in the absence of biases
β	Conditional bias
β'	Bias or amplitude error

γ	Wave breaking parameter (ratio of wave height over water depth)
δ	Sediment grading
ΔV	Simulated ebb-tidal delta volume change
ΔX_M	Errors in measurement
Δz_M	Measurement error
ε	Eddy viscosity
ε_s	Turbulant diffusion coeficient for the sediment
η	Surface elevation
θ	Direction of wave propagation
θ'	Shield's parameter
θ_{br}	Wave angle at breaking point (between wave crest line and coastline)
θ_c	Critical Shield's parameter
$\theta_{i,s}$	Angle between the inlet channel (outflow jet) and the shoreline
κ	Von Kárman's constant
λ	Normalized map-mean error
λ'	Represents the reduction of skill due to map mean errors
ρ_0	Reference density of water
ρ_{CM}	Weighted Pearson product-moment correlation between the predictions and the measurements
ρ_s	Sediment density (kg/m^3)
ρ_w	Water density (1025 kg/m^3)
σ	Relative angular frequency
σ_C	Predicted standard deviation
σ_{CM}	Weighted covariance of measured/observed and computed/predicted values
σ_{Cw}	Weighted standard deviations of computed/predicted values
σ_M	Measured standard deviation
σ_{Mw}	Weighted standard deviations of measured/observed values
τ_{bx}, τ_{by}	*x* and *y* components of the bottom stress/friction
τ_{sx}, τ_{sy}	*x* and *y* components of the surface wind stress
ϕ	Geographic latitude
$\phi_f(t)$	Direction of instantaneous flow
$\Phi_b(t)$	Dimensional bed load
Ω	Angular rate of revolution
∇	Four dimensional differential operator in the $\vec{x}$, σ and θ space

$\nabla_{\bar{x}}$	Two-dimensional differential operator in the (x,y) space

Acknowledgements

First of all, I wish to express my sincere thanks to my principal supervisor, Prof. Rodger Tomlinson, who initiated this research and gave me the opportunity to work on it and continuously guided and supported me. My deep gratitude also goes to my associate supervisors, Dr. Nick Cartwright, Dr Amir Etemad-Shahidi, and my external supervisor, Dr Ali Golshani, for all their support and insightful comments on my work.

My appreciation also extends to Dr. Darrell Strauss, Lawrence Hughes, Sally Kirkpatrick and other GCCM group members for all the assistance they provided me throughout this research project.

In addition, I thank my fellow PhD candidates, in particular Mimo Ghalami Sfahani, Nima Talebian, and Nick Dahl who were happy to assist me whenever I needed help throughout my research.

Most importantly I want to thank all my family, especially my mother, for their continuous encouragement, love and support, without which completion of this thesis would have been far more difficult.

Last, but not the least, I would like to thank my husband, Alireza, whose continuous support, patience and understanding made completing this thesis possible.

Funding for the present work and financial support for the author has been provided by Griffith University and Griffith Centre of Coastal Management (GCCM) Postgraduate Research Scholarship (Scholarships titles: GCCECMPRS, GUPRS), and Top Up Postgraduate Research Scholarship. GCCECMPRS Scholarship was partially funded by the City of Gold Coast. Without doubt, fewer students would be able to pursue research programs without such financial support.

The survey data used in this research was provided by Gold Coast Waterways Authority and the City of Gold Coast (CoGC). Measured buoys wave parameters, and wind were provided by Queensland Government and Australian Government Bureau of Meteorology, respectively. ADCPs data was provided by CoGC. Such data was fundamental to this research.

Publications

The following publications have so far been produced as a result of this research.

Journal Papers

Sedigh, M., Tomlinson, R., Cartwright, N. and Etemad-Shahidi, A., (2016). Numerical modelling of the Gold Coast Seaway area hydrodynamics and littoral drift. Ocean Engineering, 121: 47-61

Sedigh, M., Tomlinson, R., Cartright, N. and Etemad-Shahidi, A., (2016). Morphological evolution of the Nerang River Entrance ebb-tidal delta. Journal of Coastal Research: 238-242.

Conference Proceedings

Sedigh, M., Tomlinson, R., Golshani, A., Cartwright, N., (2011) "Analysis of Morphological changes in the Gold Coast Seaway", Coastal Engineering Practice. ASCE, San Diego, California, pp 495-508.

Sedigh, M., Tomlinson, R., Golshani, A. and Cartwright, N., (2012). Long term morphological evolution of the Gold Coast Seaway: Historical and numerical analysis, Coastal Engineering Proceedings, poster 28, Santander, Spain.

Sedigh, M., Tomlinson, R., Etemad-Shahidi, A. and Cartwright, N., (2014). Modelling the morphological response of an ebb-tidal delta to storm wave forcing. Coastal Engineering Proceedings, 1(34): 63.

Sedigh, M., Tomlinson, R., Cartwright, N., and Etemad Shahidi, A., (2015). Numerical simulation of the morphodynamics of the Gold Coast Seaway. Presented at the MODSIM 2015, Gold Coast, Australia.

1 – Introduction

1.1 Statement of the problem

One of the main concerns for both natural and trained river entrances is the sediment accumulation at the entrance and therefore the resultant navigation safety issues. The Gold Coast Seaway (GCS), located on the east coast of Australia (known as the Nerang River Entrance (NRE) prior to stabilisation), was stabilised with two training walls in 1986. The main reasons for stabilising the entrance was its continuous northward migration and highly dynamic (shallow water) bathymetry due to sand bar formation which resulted in navigation safety issues. At the same time, a sand bypassing system was also implemented to the south of the entrance to bypass the dominant northward longshore sediment transport (LST) downstream to minimise sediment accretion upstream and at the entrance mouth, as well as erosion downstream. Although the bypassing system has transported a volume of sand similar to previously suggested values of the LST, there has been a continuous sediment transport to the ebb-tidal delta just offshore from the entrance since the installation of the bypass system. This has resulted in relatively shallow (approx. 5m) water depths in the vicinity of the river entrance generating some navigation safety concerns which have resulted in dredging of the ebb-tidal delta in 2012. Although there have been several studies on the morphological changes of this area, the dynamics of the GCS and the reason for the ongoing growth of the ebb-tidal delta are not completely understood. Hence, this study was initiated to investigate the hydrodynamics, sediment transport and morphological changes in the vicinity of the GCS to better understand the factors leading to the continuous bathymetry changes of the ebb-tidal delta.

1.2 Objectives of the study

The overriding aim of this study is to develop a better understanding of the hydrodynamics and resultant morphological behaviour of the GCS ebb-tidal delta. For this context, the following research questions were formulated:

- Has the ebb-tidal delta sand volume reached an equilibrium condition with the more recent sediment transport patterns being only a temporary movement of sediment within the ebb-tidal delta due to significant wave or river discharge condition?

- If the ebb-tidal delta has not yet reached equilibrium, what is the main source of sediment and what governing forces that contribute to its changes?

Subsequently, the research questions are developed into the following objectives:

1. Analyse the historical behaviour of the ebb-tidal delta and surrounds, along with the governing forces in the area including tide, wave and inlet channel discharge.

2. Determine a conceptual pattern of the morphological evolution of the ebb-tidal delta and sediment transport pathways due to driving forces based on both historical survey data, along with the sand bypassing rate, nourishments, flood events, and recorded wave data in the area, during the past decade.

3. Develop a calibrated and verified process-based numerical model of the inlet area to investigate the dominant morphological processes and driving forces on the inlet ebb-tidal delta

4. Comparison and analysis of the model simulated LST rate, the LST rate predicted by empirical formulas and the sand bypassing rate.

5. Application of the numerical model to simulate the morphological changes of the ebb-tidal delta between two subsequent survey data, during which time the ebb-tidal delta had a significant rate of growth.

6. Use the validated numerical model to develop scenarios to be used for prediction of the ebb-tidal delta morphological evolution under different forcing conditions.

1.3 Methodologies

In order to reach the objectives of the study the following methods were used:

1. The ebb-tidal delta and inlet channel morphological evolution was analysed based on measured survey data from 2004 to 2015 and the results were linked to previous studies of the morphological evolution from the entrance stabilization, in 1986, to 1997. This was done to investigate the trend of morphological change in the more recent years and also to compare it to previous years.

2. The trend of morphological evolution of the ebb-tidal delta was analysed along with the driving forces and factors including major flood events, wave data measurement, dredging and nourishment records in the area, as well as artificial sand bypassing rates. A hypothesis was

derived from this analysis for the governing forces/factors influencing the ebb-tidal delta morphological changes. In addition, an updated conceptual model of sediment transport was suggested.

3. To better understand the hydrodynamics, sediment transport pathways and the resultant morphological changes in the area, as well as to investigate and validate the hypothesis presented in the previous step, a process-based numerical simulation of the study area was developed. The hydrodynamics of the numerical model was calibrated and verified against field measurements. The quality of the resultant morphological simulation of the ebb-tidal delta was assessed relative to survey data using Brier Skill Score (BSS) and Adjusted Brier Skill Score (ABSS) accuracy metrics.

4. The calibrated and verified numerical model was used to develop a parametytric study of the morphological response of the ebb-tidal delta to range of forcing scenarios. The result of these scenarios can be used to predict the likely consequences of future events.

1.4 Thesis outline

Chapter 2 provides an introduction to tidal inlets sediment transport and morphodynamics via an overview of the literature. The current gaps in, and limitations of, previous studies on ebb-tidal deltas in tidal inlets are pointed out in this chapter.

Chapter 3 provides a background literature review for the entrance before and after stabilisation. This chapter also provides a summary of different approaches that have been used to study the sediment transport and morphological changes in the area and identifies their limitations and gaps.

Chapter 4 provides an updated historical analysis of the morphological changes of the GCS after empirical relationships of the inlets in equilibrium are examined for the GCS. Based on the historical evolution of the inlet, an updated conceptual model for the sediment transport patterns in the vicinity of the inlet in the past decade is proposed. In this chapter, a prevailing source for the ebb-tidal delta morphological changes is suggested, which was examined using the numerical model in Chapter 5 and 6.

Chapter 5 presents the coupled process based numerical model using MIKE 21/3 coupled depth-averaged model developed by DHI Water and Environments. It includes the process of model input deployments such as bathymetry, bed resistance and boundary conditions. Current and wave measurements were used to calibrate and verify the model hydrodynamics. A series of

sensitivity analyses of the model results to various model settings and parameters were also presented.

Chapter 6 presents the application of the developed model in Chapter 5 for simulation of the LST in the area, as well as the morphological changes of the ebb-tidal delta between two survey intervals. The LST rate simulated by the model was compared with the rate of artificial bypassing, as well as with some results determined by existing empirical LST formulas, and the results were discussed. The limitation of the model in simulating long term morphological evolution was discussed and the skill of the model in prediction of the morphological changes was assessed. The dominant process that governs the ebb-tidal delta morphological changes, which was suggested in Chapter 4, was confirmed using numerical simulation.

Chapter 7 presents fifty model scenario results, where the inlet was forced by a number of defined storm events with various intensities and directions. The resultant graphs, for the LST and ebb-tidal delta morphological changes based on the storm power, were suggested to be useful for future prediction of the trend of morphological changes in the ebb-tidal delta.

Chapter 8 includes the key results of this study and possible directions for future research.

2 – Background

2.1 Introduction

Analysis of sediment transport near the tidal inlets is complex, and has made this coastal environment one of the most difficult systems to quantify (FitzGerald et al., 2000). The morphodynamics of inlets are related to combined action of various driving forces that create the hydrodynamic condition of each area. The presence of complex flow patterns in tidal inlet regions, which include tides, waves and freshwater discharge, and the interaction between them, cause complex morphological changes. There have been several research studies on different aspects related to sediment transport and morphodynamics of tidal inlets. In this chapter, a short review of work that has been completed is presented and the current gaps and limitations are pointed out.

2.2 Tidal inlets classification criteria

Evaluating quantities of sediment transport related to the various forces involved in the inlets has the highest level of difficulty and complexity (Komar, 1996). There have been several attempts to characterize different inlets, in order to use it as a guide to predict the morphological evolution of other inlets, which fall into the same groups with others. Some of the criteria that are used are explained below.

2.2.1 Dominant physical processes

The long-term morphodynamic evolution of a tidal inlet, on timescales of decades, depends on the competing effects of tides and waves. In an untrained tidal inlet, waves attempt to close and tides attempt to widen the tidal inlet after it is formed (De Swart and Zimmerman, 2009). The dominant process in various inlets, and even in various parts of one inlet, could be different, and there are several interpretations of how to define the dominant forces on morphological evolution in a tidal inlet environment and classify the inlets to be wave-dominated, tide-dominated, or mixed wave-tide influenced.

Based on the definition of Heward (1981), wave dominated inlets are the ones in which wave forcing causes significant amounts of sediment transport and therefore morphological changes; and the same definition goes for tide dominated inlets. This general definition is used for

different classifications. Many of the previous researchers consider inlets with poorly developed ebb delta as wave dominated. The tidal range at the locations of these inlets are within microtidal ranges, i.e. range < 2*m* (Davies and Clayton, 1980). On the other hand, they considered well-developed ebb deltas, which are developed in meso-tidal domains, i.e. 2 – 4*m*, to be tide-dominated. However, there are many exceptions for these types of generalizations.

Hayes (1979) presented the relationship between tidal processes and wave generated processes in a diagram based on many geographic areas (Figure 2.1). This graph shows that the relative effects of wave energy and tidal range can categorize a coastal zone as wave or tide dominated, or mixed energy. According to this graph a wide range of tidal inlets will fall under the mixed energy category; like the East Frisian Islands, in west German, inlets which were investigated by Fitzgerald et al. (1984).

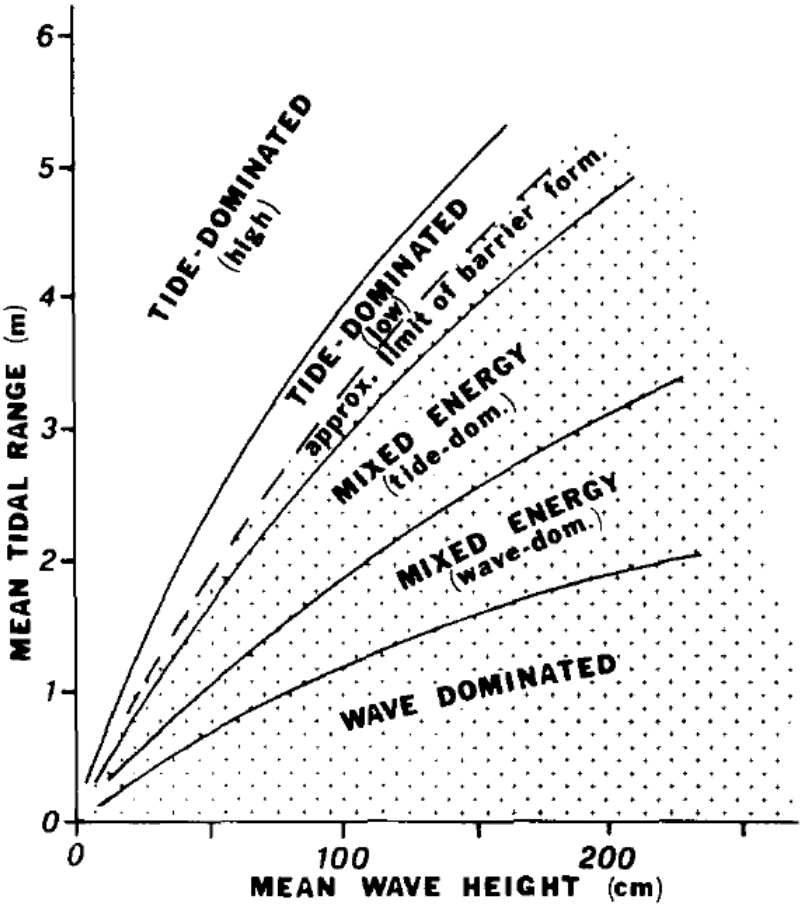

Figure 2.1. General relationships between tidal range and wave height as it relates to coastal morphology. A specific coastal region may span several fields (Davis and Hayes, 1984)

However, there are some other researchers like Nahon et al. (2012) who used numerical modelling to illustrate the limitations of empirical classifications such as those of Hayes.

Moreover, there are some inlets like the Ancao inlet (Morris et al., 2001) and western Florida inlets which do not follow the same morphological pattern predictions based on the Hayes Graph. For instance, the Ancao inlet, as noted by Morris et al. (2001), displays both tide and wave dominated characteristics. This might be due to the exposure of various parts of tidal inlets to diverse wave and current forces. Therefore, their morphological changes may be at various time scales (Nahon et al., 2012). Nahon et al. (2012) also noted that the magnitude of the seasonal behaviour of the inlets has an inverse relation with its size; in other words, smaller inlets can adapt to variation of forces more rapidly. Other studies by Oliveira et al. (2006) and Bertin et al. (2009a) also referred to seasonal behaviour of small tidal inlets, and noted that the tidal amplitude had a strong seasonal effect in a small coastal lagoon.

There are further studies which noted that apart from the relative effects of wave energy and tidal range, other variables should be considered for establishment of a general classification. According to Davis Jr and Hayes (1984), these variables in descending order of importance are coastal physiography, tidal prism, availability of sediment and the influence of riverine input. For example, the size of a tidal prism can be a critical factor in the morphological evolution of barrier island types of coastlines, and the presence of large tidal prisms in a low wave energy area can be the reason for the formation of well-developed ebb tidal deltas and the development of drumstick barriers (Davis and Richard, 1994).

Further, other studies have not limit the whole system of an inlet to be wave or tide dominated; Siegle et al. (2004) analyse the sediment transport and morphological evolution in the Teign inlet (Teignmouth, UK), and concluded that the relative importance of each physical process in the sediment transportation varies across the region. Therefore, they characterised the morphological evolution of different parts of the inlet to be dominated by wave or tide or both. According to Kana et al. (1999), wave-generated sand transport predominates in shallow water where wave breaking is the dominant process, like over shoals, along the beach, and along recurved spits at the edge of inlets for natural tidal inlets. On the other hand, sediment transport generated by tidal currents mostly occurs in depths more than the wave-breaking zone. It predominates in the channels, and is directed seaward only in the main ebb channel, and sometimes in smaller ones if there are any.

Other points of view about the effective drivers and dominant processes in morphodynamics of tidal inlets include, those of De Swart and Zimmerman (2009) where the morphodynamics of a tidal inlet, its formation, maintenance, and decay, are mostly dependent on the influence of two major components, namely: The hydrodynamics of tidal currents; and wind wave. The direction and magnitude of sediment transport, and the resultant morphological changes is extremely

dependent on these two factors, although in some cases, the storm surge might be a factor contributing to the breaching of the barrier and tidal inlet formation. De Swart and Zimmerman (2009) also mentioned a third component which is the morphology proper, which is a consequence from the deviation of the sediment transport between multiple inlet systems. There are several studies, such as those of Van de Kreeke (1990) and Tambroni and Seminara (2006), that investigate the stability of multiple inlets which are draining one backbarrier basin, and also a study by Van de Kreeke et al. (2008), in which stability analysis of the multiple inlet systems has shown that these systems can have various stable equilibrium states if the interaction between them is weak.

2.2.2 Geological Geometric effects

Studies such as that of Harris et al. (2005) indicates that the morphological evolution of any coastal zone area should not be assumed to be only the response of that coastal zone to hydrodynamic forces, but that the limiting forces of the inherited geological condition of each area and its interaction with these hydrodynamic forces should be considered as well.

Harris et al. (2005) investigated the relationship between the evolution of a classic mixed-energy coastal zone in central South Carolina and the complex varying geological geometries in the area, where five distinct, near surface geologic geometries could be identified. These included three near-surface units which directly influence the local scale evolution of the area and two types of paleoincisions which respond to the underlying framework. It was concluded that general coastal morphology is dominated by the mixed- energy effect of wave and tides. However, understanding the underlying stratigraphic effects on the coast is also essential since it can cause long term influences on the coastal evolution of each area, and it is unique for each individual site. It was suggested to include the distribution and geometry of the inherent geologic features as a variable in conceptual and mathematical models of coastal evolution in order to reach better predictions of morphological changes.

2.3 Modelling Approaches

According to the literature, there are several modelling approaches available for understanding tidal inlets' morphological behaviour in various time and spatial scales, from micro-scale to meso-scale to macro-scale. In this section, a number of such modelling approaches are presented.

2.3.1 Descriptive geomorphic and conceptual models

There are several studies on the morphological behaviour of tidal inlets in macro- time scales. Most of these studies are descriptive geomorphic inlet models, like that of Kana (1989), which are mostly based on the historical morphological behaviour of the inlet and empirical studies. In order to use these descriptive geomorphic models for the purpose of prediction in meso and micro time scales, a more simplified model for morphological changes of the inlet is essential.

One of the approaches in previous studies was the use of simplified conceptual modelling. For instance, Kana et al. (1999) applied conceptual modelling in order to understand the sediment transport trend in the region around the inlets, which seems to be the major reason for shoreline morphological changes in the adjacent areas. Their main focus was on mixed energy tidal inlets in the southeast US coast. In their research, the inlet region was divided into four primary domains, which included the main ebb channel (A), the ebb tidal-delta (B), shoal bypassing zones at the margins of the ebb-tidal delta (C) and spits adjacent to the inlet (D) (Figure 2.2).

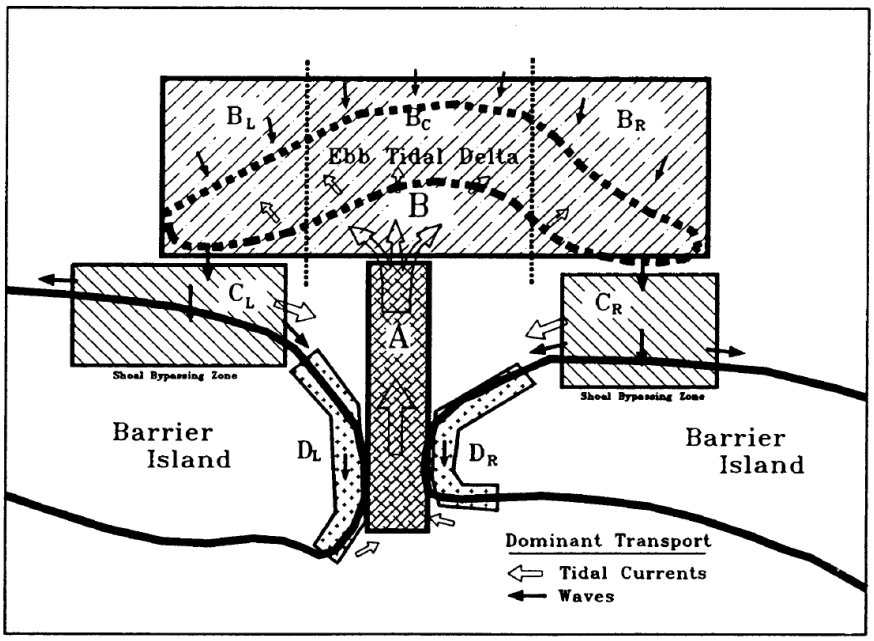

Figure 2.2. Principal model domains in the simplified conceptual tidal inlet model of Kana et al. (1999) for mixed energy tidal inlets

The flood tidal deltas were not included in the model since the focus of their study was on the sediment circulation offshore the inlet and its effect on the shoreline morphological changes in inlet adjacent beaches, and it seems that flood-tidal deltas have less influence on ocean shoreline morphodynamics than do ebb-tidal deltas.

The Kana et al. (1999) model explained the circulation trend of sediment between the four above mentioned domains using the potential sediment transport rate due to tidal current and wave action. Different algorithms were tested to use the model to simulate the tidal inlet sediment transport patterns at meso-time scales, although it was noted that the simplified conceptual model that was used involved several uncertainties that should be resolved before formulating a deterministic model at those scales.

Descriptive and conceptual models were used for various aspects of tidal inlet morphodynamics. Sha (1989) used conceptual models to explain the updrift or downdrift asymmetry of ebb deltas in the West and East Frisian Islands, which are located along the northern Dutch and German coasts. It was concluded that the variations in their asymmetry are due to the relative dominance of the tidal prism size and wave generated longshore sediment transport, with the tidal prism being the more important parameter. Like other conceptual models, it was suggested the models can be applied for other inlets around the world.

FitzGerald et al. (2000) explained the variety of sediment bypassing mechanisms for trained and untrained inlets in stable or unstable conditions, with nine conceptual models, six of which are for natural inlets and three for jettied inlets. It was noted that the processes of sediment bypassing in jettied inlets were not investigated enough, and further studies are required in this area.

More recently, Wheeler et al. (2010) used a conceptual model based on historical survey, aerial imagery, and digital hydro-data analysis from 1889 to 2009, to investigate the source of sediments of ebb and flood deltas (Figure 2.3).

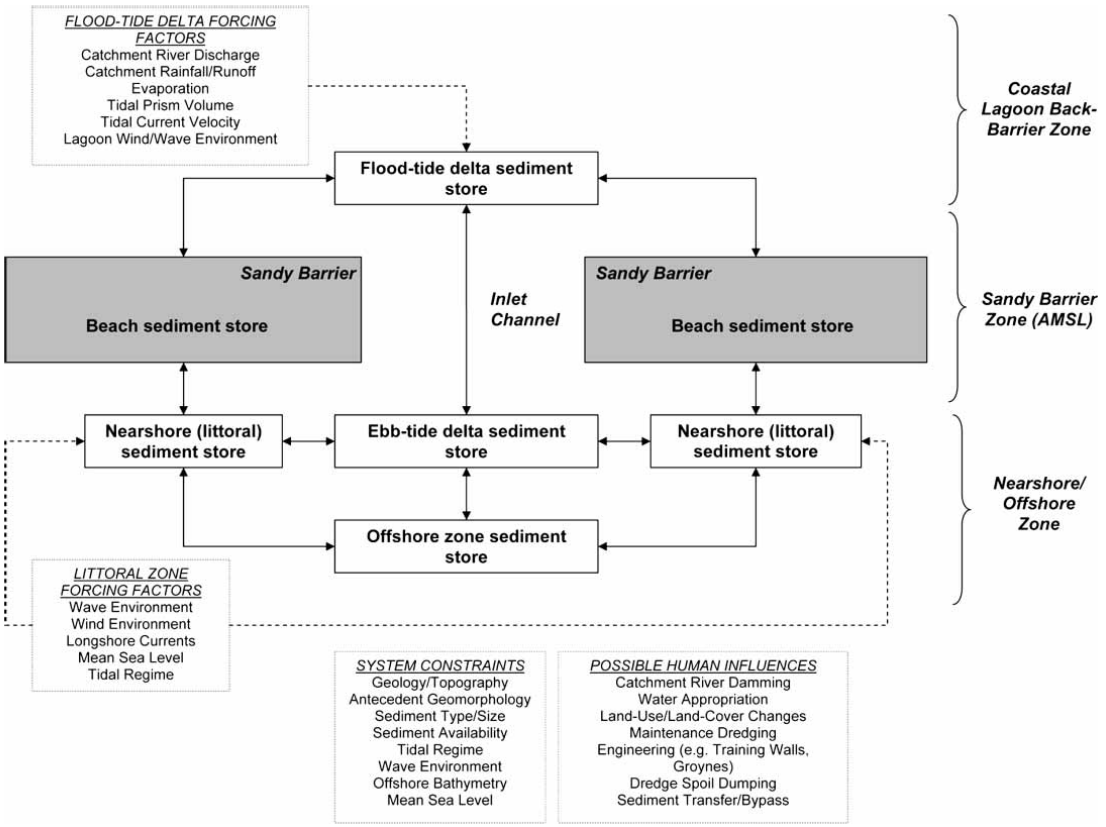

Figure 2.3. Conceptual diagram of links between sediment sources at coastal lagoon entrance (Wheeler et al., 2010)

In more recent studies which are based on numerical analysis, either the conceptual models that were already proposed by previous researchers were applied and discussed by numerical analysis (Van der Vegt et al., 2006; Dissanayake et al., 2009), or a new and more specific conceptual model was proposed based on the research area historical analysis (Andrews and Nielsen, 2001). Nienhuis and Ashton (2016) presented a mass balance numerical experiment in Delf3D-Swan, which incorporates multiple sediment pathways, to investigate the rate of inlet migration based on sediment sinks and sources around the inlet.

2.3.2 Numerical modelling analysis

The first step in understanding the morphodynamic behaviour of a system is to investigate the sediment transport processes and mechanisms. In this regard, several numerical models for various time and space scales have been developed to reduce the difficulties in understanding the relationship between the various hydrodynamic forces and sediment transport patterns and resultant morphological changes in complex coastal environments, including tidal inlets (e.g. De Vriend et al., 1993; Wang et al., 1995; Ranasinghe et al., 1999; Cayocca, 2001; Work et al.,

2001; Van Leeuwen and De Swart, 2002; Williams et al., 2003; Siegle et al., 2004; Bertin et al., 2009b; Nahon et al., 2012).

Some of the numerical process-based models, like those of van Leeuwen et al. (2003), Roelvink (2006), Van der Vegt et al. (2006), Dissanayake et al. (2009), Fortunato et al. (2009) and Van der Wegen et al. (2010), only applied tidal regime forcing in the model to verify or further develop the empirical theories such as, $P - A_c$ relationship (Chapter 4, section 4.3.1.1). The above mentioned process-based models show a good agreement between ebb channel and ebb-tidal delta orientation and the conceptual morphological change models of Sha (1989) and Sha and Van den Berg (1993). They also provide good agreement with $P - A_c$ relationships; However, the results of Dissanayake et al. (2009) demonstrated that, since no waves were included in the model, this resulted in the littoral drift being neglected, and the inlet channel cross-sections not reaching equilibrium. This means that in these models relatively constant conditions are described by the $P - A_c$ relationship. A variety of reasons for not including waves in these models were explained by the authors, a significant reason being that the tidal force is the dominant forcing in the specific research area. Some, like Fortunato et al. (2009), also mentioned the increasing computational costs when including waves as one of the reasons for ignoring them in his model.

Dissanayake et al. (2009) applied only tidal forcing in a 2DH process based model (Delft3D) to investigate the governing physical processes in Dutch Wadden's tidal inlets, which are defined as mixed energy tide dominated. In this study, a schematized model domain with an initial flat bed was used with similar dimensions to the one of those inlets - Ameland inlet - which experiences strong alongshore tidal currents and inlet channel currents. This model was used to describe the sensitivity to initial inlet width, direction and asymmetry of tidal forcing, sediment transport formulas, and relative position of the tidal basin to the inlet.

Van der Vegt et al. (2006) explained the equilibrium of a tide dominated tidal inlet by the balance of sediment transport between wave and tide forces in the inlet, only by adding the frontal waves to the hydrodynamic forces of the model. They also noted some differences between the model result and the observed ebb-tidal delta. Specifically, the depth of the inlet channel in the model result was more than the observation, and the model also underestimated the bending of the ebb-tidal delta around the ebb channel which is probably because of the non inclusion of oblique waves.

Eventually, some process-based morphodynamic models were developed and applied for tidal inlets under combined forces of tide and waves. There are many types of approaches in these

models as well. Some of them applied the model for idealized inlets, like Tung et al. (2008), Tung et al. (2009) and Tung (2011) who investigated the location and cross-sectional stability of an idealized tidal inlet by applying process-based morphodynamic modelling under different wave and tide conditions. Nahon et al. (2012) applied the latest version of MORSYS2D (Fortunato and Oliveira, 2004) (Figure 2.4), to investigate the morphological evolution of an idealized tidal inlet under the combined action of waves and tides.

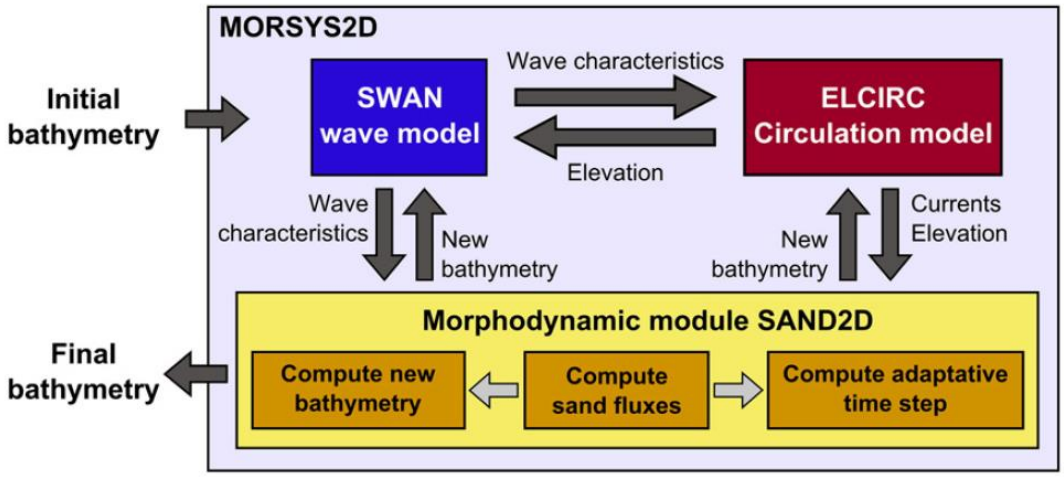

Figure 2.4. MORSYS2D scheme (Nahon et al., 2012)

MORSYS2D is a two dimensional depth averaged process based morphological model that couples various models for circulation, waves and sand transport. According to Nahon et al. (2012), the circulation model ELCIRC (Zhang et al., 2004), the spectral wave model SWAN (Booij et al., 1999), and the sand transport and bathymetry update model, SAND2D, (Fortunato and Oliveira, 2004; 2007; Bertin et al., 2009b), were coupled in MORSYS2D.

Ridderinkhof (2016) investigated the effect of the geometry of a back-barrier basin on the morphology of tide-dominated ebb-tidal delta using numerical simulation in an idealized set-up that consists of a tidal inlet, a back-barrier basin, and an open sea with no-delta coastline. He also used an idealized set-up to identify the different physical processes that are responsible for the formation and migration of shoals on ebb-tidal deltas.

Some of the models which included the effects of both tide and wave only investigated the sensitivity of the morphological changes to: different model parameters; specification of the domain; or sediment transport formulas. Also, some of them attempt to use the sensitivity analysis to improve empirical relations and classifications. For instance, Bertin et al. (2009b) used the morphodynamic modelling system, MORSYS2D, with an adaptive morphodynamic time step and applied it for a wave dominated beach located on the French coast to assess

various sediment transport formulas, which illustrated the high sensitivity of the morphological changes to the change of sediment transport formulas.

Nahon et al. (2012) compared their simulation results using MORSYS2D, both qualitatively and quantitatively, with empirical relations and classifications, like Hayes (1979) classification of tidal inlets, and empirical models of O'Brien (1931) and Bruun et al. (1978), and discussed the limitations of these empirical theories. The model results were partly validated by the $P - A_c$ relationship scaling parameters computed by Jarrett (1976). They concluded that other than tidal range and wave height, which were the only factors in Hayes classification, there are other factors which influence the morphological changes in the tidal inlets and were not included. For example, according to the O'Brien's formula, the channel cross section is directly dependent on the tidal prism, and since the lagoon area is the key factor in calculating tidal prism, the lagoon area can affect the characteristics of morphological changes in an inlet qualitatively. In other words, change in the lagoon size can change the dominant forcing regime of an inlet, and the resultant type of morphological changes. Also, sediment grain size is used in calculating the empirical constants of the O'Brien formula (Hughes, 2002), therefore it can indirectly influence the morphodynamics of the inlet. Finally, various sediment transport formulas can calculate seriously different sediment transport fluxes (Pinto et al., 2006), and as a result various bathymetry changes can be obtained. However, changes in sediment grain size as well as changes in sediment transport formula were shown to have a quantitative effect on the morphological changes of the inlet, and increase or decrease the amount and speed of it, but do not change it qualitatively. It was also suggested that the use of the Hayes and the Bruun classifications were limited to the tidal inlets which are in equilibrium. However, in practice tidal inlets might lose their equilibrium due to human interference, or seasonal variations of wave forces, such as variations of small inlets from wave dominated to tide dominated in different seasons (Nahon et al., 2012).

Lesser (2009) did a sensitivity analysis of the model results to various calibration parameters and one of the parameters that the model results seemed to be quite sensitive to it, was the bed roughness coefficient. This indicates that further research to find a reliable bed roughness under the combined action of wave and current is required.

In some other simulations, model results were compared qualitatively with what is expected to happen based on previous conceptual models and hypotheses. van Leeuwen et al. (2003) used a process based model on a schematized inlet to investigate the conceptual model proposed by Sha (1989). Nahon et al. (2012) partly validated his model results with the conceptual models of sediment bypassing of FitzGerald et al. (2000).

Vu (2013) introduced a 24.5 *hr* moving window method to infer hydraulic and morphodynamic changes from tidal records, since he suggested that the process based numerical models are still unreliable. However, it was noted that the morphological changes at inlets with training works in time scale of individual storms are usually not significant enough to be measurable via the tidal records. Moreover, his numerical morphological model of Pensacola Pass during and after Hurricane Katrina simulated insignificant erosion of the ebb-tidal delta compared to observation partially due to underestimation of the role of waves in sediment transport.

Some other numerical models which were applied for tidal inlets included the effects of both waves and tides and calculated the sediment fluxes, but did not allow morphological updates of the model. For instance, Elias and Hansen (2013) used a coupled wave, flow and sediment transport model (Delft3D flow and SWAN wave numerical model), in order to understand the sediment transport pattern and quantities exchanging between San Francisco Bay, the Golden Gate, and the adjacent Pacific Ocean coastline. They coupled a calibrated flow model to a sediment transport formula to estimate the sediment transport potential and they did not allow morphological updating in the model to prevent feedback between the flow and variation of bathymetry. In order to reduce the running time of the model, input reduction techniques of Lesser (2009) have been used in their model. In this method, input forces of the model, tide and waves, are schematized and representative estimates of yearly average forces are used in the model instead.

Siegle et al. (2004) set up a numerical model using MIKE21 for the Teign inlet (UK) to identify and estimate the relative importance of controlling forces in this complex inlet. Separate HD, NSW and ST modules were used for this purpose, and since the modules were not coupled and each one run independently, wave and current interactions were not included. Moreover, the ST module only estimates the sediment transport fluxes, and there is no morphological updating available in both HD and NSW modules, and the bed was updated only at the end of the run. The bed level prediction of the model for 14 days was assessed using probabilistic methods for different parts of the model, and varies from reasonable (but near poor quality) to bad quality, but it also mentioned that the model predicts the evolution of sandbar systems well for a particular stage. The researchers concluded that assessment of the validity of their model for other stages, and longer-terms, requires further work.

There are other studies which finally applied the actual bathymetry of a tidal inlet, and applied both wave and tide forcing and morphological updates to investigate the pattern of morphological changes in their research area, but the morphodynamic results were validated only qualitatively. Key features of the results of the models versus measurements were

discussed and compared in these research studies. Based on the authors' judgements, there were normally some features which were predicted well by the models, and some which were not (Bertin et al., 2009b; Bruneau et al., 2011; Jiang et al., 2013).

Bertin et al. (2009b) used MORSYS2D with an adaptive morphodynamic time step on a very dynamic tidal inlet in Portugal. The model application over a five week simulation predicted realistic morphological changes, which was expected based on previous observations of the production of the ebb tidal delta, but was not calibrated qualitatively or quantitatively against any subsequent surveys.

Jiang et al. (2013) investigated the morphological changes of a micro-tidal estuary in Port Stephens, New South Wales, which is a wave dominated coast under the combined action of waves and currents. Their model result suggested that due to infilling of the estuary, it is switching from flood dominant to ebb dominant which is consistent with the previous research, although no calibration and validation was conducted against measurements.

According to the time consumption of process- based morphological models and the necessity of long term simulations in these models, different methods were applied in order to reach a more practical computational cost in terms of time. The adaptive time step method that keeps the maximum Courant number, was one of these methods (Bertin et al., 2009a; Bertin et al., 2009b; Fortunato et al., 2009). Another method is the use of reduction techniques and methods of selection of representative conditions which were described by De Vriend et al. (1993) and Latteux (1995). Lesser et al. (2004) and Roelvink (2006) described long term morphodynamics by updating the bed level at each hydrodynamic time step, while accelerating the amount of variations by a constant factor which was called the Morphological factor or Morfac. According to the time scale that normally is needed for morphological changes, application of a morphological acceleration factor is very common in morphodynamic simulations. In this method, reduction techniques as well as feedback mechanism were used. This method was used by several other researchers in different study areas. Marciano et al. (2005) applied it to check the pattern of channel branching in the Wadden Sea tidal inlets. Dissanayake and Roelvink (2007) used it to perform long-term process based modelling for tidal inlets and to evaluate the effects of initial conditions on the results. Van der Wegen et al. (2006), Van der Wegen and Roelvink (2008) and Van der Wegen et al. (2008) applied this method to describe long-term morphological changes of a tidal embayment. Dissanayake et al. (2008) used this technique in evaluating the impact of the sea level rise on a schematized inlet. Dissanayake et al. (2009) applied this method to investigate the governing physical processes in Dutch Wadden's tidal inlets in a schematized model domain with initial flat bed with similar dimensions to one of

those inlets, i.e. Ameland inlet. Van der Wegen et al. (2010) applied this method in a 2D process based schematized inlet model to compare modelling results with empirical PA formula. Nahon et al. (2012) modelled three years of morphological evolution under various defined wave and tide conditions, nine combinations of tidal range and significant wave height, in an idealized tidal inlet using morphological factors. There are several other researchers who used the Morfac method for their morphodynamic modelling (Tung et al., 2008; Bertin et al., 2009b; Lesser, 2009; Tung et al., 2009; Tung, 2011). However, as Lesser (2009) mentioned, there are limitations for using this factor and it depends on the characteristics of the case study. Moreover, selection of a suitable morphological acceleration factor is dependent on the judgement and sensitivity testing of the modeller. Moreover Lesser's method seems to neglect the fact that the arrangement of severe storms, and the time interval between them, could affect the amount of resulting morphological changes.

Most of the morphodynamic simulations mentioned above, which utilised various models including Morsys2D, Delft3D or MIKE21, were applied in 2D depth averaging mode. The main constraint in 3D modelling of morphological changes is that they are extremely time consuming. There have been some research which compared the result of these two approaches, and concluded that when only bathymetry changes are important, 2D and 3D modelling results do not vary significantly and that 3D modelling is not significantly superior to 2D modelling. Lesser (2009) compared the results of modelling in 2DH and 3D mode, and suggested that the degree of overestimation of the morphological changes in 2DH mode is higher comparing to 3D mode. However, both methods qualitatively seem to have a reasonable agreement with measurement, although both of them overestimated the morphological changes in the considered area.

There have been some attempts to validate the result of morphological models quantitatively as well as qualitatively. Lesser (2009) used Morfac in running a simulation over a period of years for some case studies, such as the entrance to Willapa Bay in the state of Washington, USA. He explained that the model only can capture some of the pattern of morphological changes, and the quantities of erosion and deposition are overestimated or underestimated in various spots. It was concluded that the morphological results are far from perfect, however considerable calibration effort was required to reach even those results.

The quality of the results of morphological changes in the model can be assessed quantitatively with probabilistic assessments using so-called "Skill Scores". These are used as an estimation of accuracy of prediction relative to the accuracy of a baseline prediction. It ranges from less than zero, which represents bad results, to 1 which represents excellent results, as shown in Table 6.1

(Van Rijn et al., 2003). For instance, Siegle et al. (2004) calculated skill scores for validation of their sediment transport module, which only updates the morphology at the last time step, for a 14 day period run between two bathymetric surveys in November 1999. The skill scores of the result of their sediment transport of the model vary in different areas from 0.36 (reasonable but near poor quality) to less than zero (bad quality). However, it was also mentioned that the model predicted the evolution of the sandbar system well for a particular stage. Assessment of the validity of their model for other stages, and for longer-terms, is in need of further work.

In addition, it should be considered that each of these numerical models included some assumptions and limitations, and did not include some particular features in their modelling. For example, in Nahon et al. (2012) study, wind, river flow and baroclinic pressure were not considered in the models, and only a single tidal frequency, semi-diurnal lunar M2, was applied.

Availability of detailed bathymetric data more frequently, can help to improve the accuracy of morphological model simulations (Fortunato et al., 2014). Fortunato et al. (2014) suggested that according to several sources of uncertainty in morphological models of tidal inlets, especially in sediment transport formulas, the performance of these, when simulating periods of months or longer, are mostly poor, with very low and even negative values of Skill factor. He suggested using nudging technique to incorporate the available frequent bathymetric data in the results and improve model performance. This method can help to characterize the evolution of ephemeral tidal inlets when frequent survey data is available, although it is unsuitable for predictive modelling.

In conclusion, despite the extensive developments in numerical models, the results were still not accurate enough to be able to utilize these models for practical engineering applications. The main reasons of their inapplicability in engineering works was their high computational cost, numerical instabilities, and occurrence of large errors in their sediment fluxes and, as a result, in their morphological changes predictions. Some researchers have investigated the reasons for this inaccuracy in the models, and concluded that these errors can have two main sources (Fortunato et al., 2009).

The first source is related to the limitation of models, for example, sediment flux calculations in the models are often based on empirical sediment transport formulas which are rarely accurate by more than a factor of two, even in controlled laboratory tests (Van Rijn, 1990). Even the estimations of models that use multiplication of velocity by concentration to calculate sediment fluxes are no better than those using empirical formulas (Davies and Villaret, 2002). The second source of mistake in calculation of the amount of sediment transport is due to errors in model

inputs for sediment transport calculations. These inputs could be sediment properties, current velocity and bed resistance, among others, which can affect the sediment fluxes calculations. This is due to the fact that, as mentioned before, sediment fluxes are highly sensitive to some of these parameters (Van Rijn, 2007). Moreover, since velocity is very sensitive to bathymetry calculation errors (Blumberg and Georgas, 2008), in the models that have bathymetry updating and feedback included in calculations of hydrodynamics, it can cause rapid growth of inaccuracy in morphological predictions. There are some studies which address both sources of error, such as that of Fortunato et al. (2009). The focus of Fortunato et al. (2009) was on the second source of uncertainty in morphological models and in particular on d_{50} and velocity. According to their sensitivity analysis, model results were mostly sensitive to these two parameters specifically when only tidal forcing was considered in the model. It should be noted that, when waves are included in the model, other sources of uncertainty will be added, such as bottom friction, wave breaking parameters, and wave characteristics. It was concluded that the main source of uncertainty is the choice of sediment transport formulas in the model (Pinto et al., 2006; Fortunato et al., 2009), which is the reason for considerable research aiming to develop a more accurate sediment transport formula e.g. (Bhattacharya et al., 2007; Van Rijn, 2007; Camenen and Larson, 2008).

2.4 Stabilized tidal inlets

A number of studies have investigated the morphological evolution of trained tidal inlets. Tanaka et al. (2014) investigated the morphological changes of the Nanakita River mouth in Japan which is trained by a single jetty to prevent the river migration to the north due to the northward LST which results from the predominant ESE and SE wave direction. They concluded that the shoreline dynamics were affected by the seasonal changes, while the south of the river mouth is more stable. Their analysis showed that the dominant northward LST gradually resulted in the development of a spit from the south bank to the river mouth. This Spit, which developed in shallow water and blocked most of the river entrance before it was eroded away by an extreme event, might not have developed if there was another jetty and a sand bypassing system downstream of the inlet, similar to the GCS. Analysis of the aerial photos of the area which were presented in their study, and also Google Earth, did not show development of an extensive ebb-tidal delta in deeper water. However, a shallow ebb-tidal delta, similar to the GCS before stabilisation and the implementation of the sand bypassing system, is noticeable. Moreover, it was noted that the downstream (north) shoreline of the entrance was eroded due to the interference of the jetty with LST in the absence of enough natural or some sort of artificial sand bypassing.

Gelfenbaum and Kaminsky (2010) investigated the morphological evolution of the Columbia River inlet. It was shown that construction of jetties at this inlet has forced local changes in inlet depth and large scale changes in the position and depth of the nearby ebb-tidal delta. Their investigation shows that the loss of the local sand supply from the old ebb-tidal delta caused sand deficits along the shoreline, resulting in local shoreline retreat adjacent to the inlet. It was suggested that the dredging of the channel and the disposing of the sand into deeper water removed a source of sand supply to nearshore beaches. However, analysis of the GCS, which is presented in Chapter 4, shows that the GCS inlet is scouring naturally, even more than expected, due to the tidal prism size and the deficit of LST passing the entrance mouth. Gelfenbaum and Kaminsky (2010) model results suggested that the shoreline north of the entrance is susceptible to serious future retreat due to declining sediment supply. Similar issues, including deficiency of sediment budget downdrift the inlet during fair weather condition, entrance infilling and navigation issues during high wave energy conditions, were noted at Currumbin Creek Double jettied tidal inlet (Castelle et al., 2007).

Analysis of historical surveys and aerial imaginary at Gippsland Lakes Artificial Entrance confirm that emplacement of jetties at an entrance without some sort of sediment bypassing application will result in downdrift erosion and littoral drift ending up at the flood tide delta and interfering with the navigational channel (in this case) (Wheeler et al., 2010).

Analyses of other trained tidal inlets show that the application of artificial sand bypassing can be significantly beneficial for reducing the navigability issues created by gradual LST in calm hydrodynamic conditions. However, as will be described in further detail in Chapter 4, extreme event sediment transport is still causing some navigability issues at GCS. Information gained in this research from analyses of the unique sand bypassing system operated at GCS can facilitate using the same approach in managing the sediment transport in other trained entrances.

2.5 Summary

The morphological changes of tidal inlets have been studied using different methods. The presence of various driving forces including wave, tide, freshwater discharge has made them a complicated field of study. Therefore, many of the studies that have been done eliminated one, or several number of variables or forcings when analysing morphological evolution of tidal inlets. This has been done by analysing an idealized tidal inlet (simplified bathymetry) (Nahon et al., 2012) or removing the least prevailing force, for example wave or tide forcing (Dissanayake et al., 2009; Fortunato et al., 2009; Tung et al., 2009; Van der Wegen et al., 2010; Tung, 2011). Some of them did not simulate the hydrodynamics and morphological changes

simultaneously (Siegle et al., 2004). A few studies that included all of the forces and actual bathymetry of their case study did not calibrate their morphological changes simulation quantitatively (Bertin et al., 2009b; Bruneau et al., 2011; Jiang et al., 2013) or the quality of their results within the acceptable range (Siegle et al., 2004). Some studies only focused on historical analysis of the morphological changes and did not develop a numerical model (Kana, 1989; Sha, 1989). Therefore, the morphological evolution of tidal inlets was rarely investigated comprehensively: i.e. including historical analysis, developing a conceptual model, developing a calibrated numerical model, which can predict the morphological changes of tidal inlets with an acceptable skill.

3 – Review of the studies conducted on the Nerang River Entrance/Gold Coast Seaway

3.1 Introduction

In the case of the Gold Coast Seaway (GCS), and many other river entrances that have infilling problems and navigation issues, it is crucial to understand the waterway dynamics and the different variables that affect their morphology. Since the late 1800s, there have been considerable variations in the location of the Nerang River Entrance (NRE) due to the formation of sandbars around, and within, the entrance and its northward migration (Polglase, 1987). After construction of the Seaway in 1986 and despite the existence of a mechanical bypassing system, the growth of the ebb-tidal delta is still one of the main navigational safety concerns. There have been a number of studies examining the hydrodynamics in the vicinity of the GCS, such as that of Mirfenderesk and Tomlinson (2008). Moreover, a number of studies have also been carried out on the different factors that influence the morphological changes in the Seaway area and the growth of the delta (DHL, 1970; 1976; Chapman, 1981; Polglase, 1987; Munday, 1995; WRL and GCCM, 1998; D'Agata and Tomlinson, 2004; Voisey, 2004; McCauley and Tomlinson, 2006; Patterson, 2007; Sennes et al., 2007). Nevertheless, the dynamics of the GCS and the development of the ebb-tidal delta are not completely understood. In this chapter, literature which has focused on the history, hydrodynamics and morphological changes of the GCS area are presented and discussed to reach a better understanding of the problems of this inlet.

3.2 Study Area

The GCS is located on the Australian East coast at a latitude of 27°56’10S and a longitude of 153°25’60E and links an intra-coastal waterway known as The Broadwater with the Pacific Ocean (Figure 3.1). The coastline in this area, which extends from the Tweed River entrance in the south to the Nerang River in the north, has developed over the past 6,000 years with a Holocene barrier dune system and barrier island separating the Nerang River and the Broadwater from the ocean. The whole Holocene unit is composed of mature marine sand, mainly supplied from strong onshore sand transport during the last post-glacial transgression, and also from the northward longshore sediment transport from northern New South Wales and the southern Gold coast to Moreton Bay in the north (Patterson, 2007).

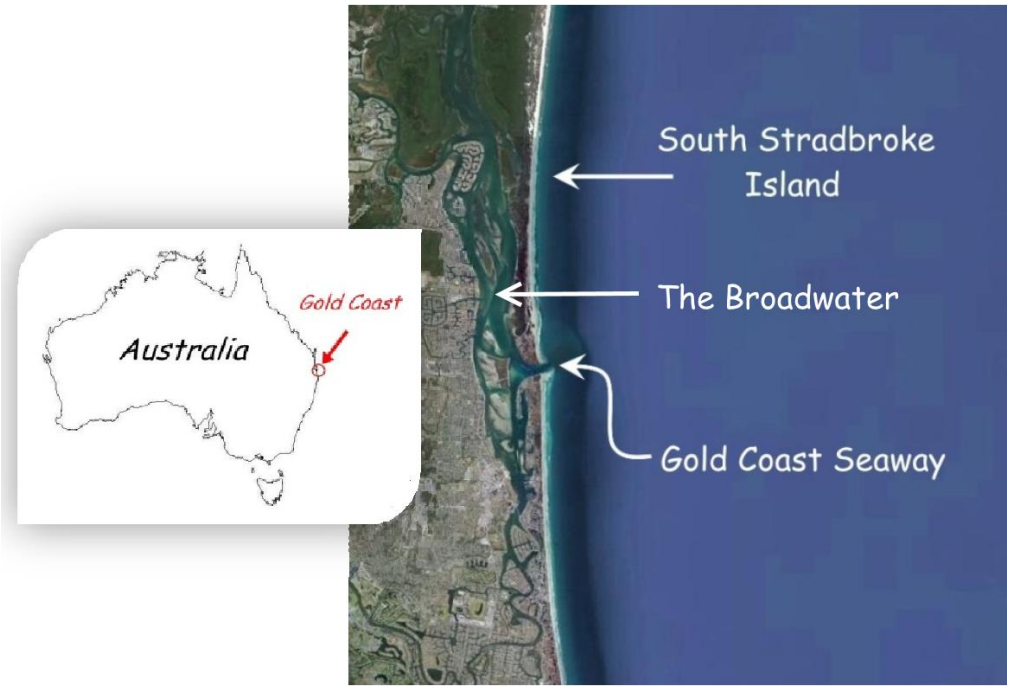

Figure 3.1. Gold Coast Seaway location (Google-Earth, 2015)

The tidal regime in the area is semi-diurnal with neap and spring tidal ranges of 0.3*m* to 2*m* respectively, and a mean of 1*m*, and is therefore characterised as a microtidal coastal environment (Davies and Moses (1964) as cited in Munday (1995)). Based on the phase difference criteria suggested by Speer and Aubrey (1985), the GCS has a minor ebb dominant current regime (Mirfenderesk and Tomlinson, 2008). According to the measured data, Mirfenderesk and Tomlinson (2008) found that the mean velocity and the resultant net discharge through the GCS is zero, despite the minor tidal asymmetry. This indicated that the longer duration of the flood tide in the GCS is in balance with the higher peak velocity during the ebb tide. In addition, freshwater inflow into the estuary of the Nerang River is insignificant for most of the year, except for some of the significant episodic inflows due to extreme weather systems (including ECLs, Cyclones). Hinze Dam, which is located 37 *km* upstream the Nerang river mouth, usually retains a lot of the runoff resulting from the heavy storms during the summer (Mirfenderesk and Tomlinson, 2009). The discharge rate at the GCS can reach a minimum of about 1600 m^3/s during the neap tide and a maximum of about 4100 m^3/s during the spring tide. Seventy percent (70%) of this rate has been found to be from the Northern channel, while 30% of it is from the southern channel (Mirfenderesk and Tomlinson, 2007).

Wave conditions in the entrance region can be categorized into five main groups: ground swell (GS), medium-period swell (MS), local wind Seas (WS), and two storm categories which are East Coast Lows (ECL), and tropical cyclones (TC). GS is the dominant GCS offshore wave

climate with periods of more than ten seconds, which is typically generated in the southern Ocean and mid-latitudes. These waves, which have long periods and low wave heights coming from the south to south east, occur all year round. MS ($8s < T_p < 10s$), which occurs year round, is the dominant inshore wave climate along the East Coast of Australia and is generated in the Tasman Sea. WS ($T_p < 8s$), which are locally generated during the Australian summer, are short period waves and their height and direction depend on the strength, duration and direction of wind. These waves are often superimposed on top of longer period swells. In terms of the storm wave categories, ($H_s > 3m$), ECLs are frequently generated in the Tasman Sea in the southeast of Australia. These are intense low pressure systems which typically occur in the Australian autumn and winter (April – August) and mostly in June. The duration of these storms varies from several days to a week and they bring large waves, high winds, rains and storm surges. TC, which are normally generated in the Coral Sea in Northern Queensland, occur in the late Australian summer to autumn (January – March), and rarely reach as far south as the Gold Coast. The ones that do bring waves from east to northeast and sometimes east to southeast (Splinter et al., 2011; Splinter et al., 2012). While average deep-water significant wave heights for GCS generally vary from 0.8 to 1.4*m* with mean periods of 7 – 9 seconds, extreme events such as cyclones can generate wave heights up to 14*m* and wave periods up to 18 seconds (Allen and Callaghan, 1999). The Gold Coast region can be classified as a wave dominated mixed energy coast (Davis and Hayes, 1984) or a transitional coast (Hubbard et al., 1979) based on the waves and tide conditions in the area.

The nearshore morphology of the Gold Coast can be described as a double-barred system (Van Enckevort et al., 2004), with sediment consisting of well-sorted fine sand, $200\ \mu m < d_{50} < 300\ \mu m$ (d_{50} is the sediment median grain size), with size sorting values of 1.2 to 1.5 across samples calculated from equation (3.1), increasing in the offshore direction. In equation (3.1), 25% of the particles in the sample are larger than d_{25}, and 75% of the particles are larger than d_{75}.

$$Sorting = \sqrt{\frac{d_{25}}{d_{75}}} \tag{3.1}$$

The prevailing longshore drift along the Gold Coast is estimated to be about 500,000 m^3/yr toward the north, which is the balance between 650,000 m^3/yr toward the north and 150,000 m^3/yr toward the south (DHL, 1970). Munday (1995) suggested that cyclones, which occur once a year on average, are capable of transporting up to 25% of the annual LST in each event. Seismic profiling undertaken along a shore parallel line about 500*m* offshore indicates that bed rock is approximately 2 to 10*m* below the seafloor with a lateral extent of over 1 *km* (Munday, 1995).

3.3 History of the entrance

The first step in understanding the trend of sedimentation and sediment movement within the GCS region is to gain more knowledge about the behaviour of the NRE prior to the construction of the Seaway in 1985, as well as the period since then.

3.3.1 Prior to the GCS construction

According to Helman (2010), in the early 1820's, which is the approximate time of the earliest available historical records; there was no permanent opening location between the ocean and the Broadwater, which was probably due to recurring drought from 1790 to 1820 and the absence of any major floods. In 1823, two natural openings occurred between the Broadwater and the ocean located at Narrowneck and the Basin (Figure 3.2, 3.3), both located at the intersections of the landward moving coastline and the most seaward meander bends of the Nerang River.

Figure 3.2. Oblique aerial photograph (1966) looking north over the Nerang River, southern Broadwater and Southport Bar, Gold Coast. (Photo: Gold Coast Weekender, December 13-14, 2003) (Helman, 2010)

Due to northern LST, the Narrowneck entrance gradually closed and the spit elongated to the north until the 1860's. The NRE then widened due to severe storms in the 1870's and the offshore bar moved to the south. Therefore, in 1878, the entrance was about 500*m* south of its previous location in 1840 (Longhurst, 1996). By the 1880's, the NRE had moved further south, about 800*m*, and did not change its location until 1901 (Connah, 1946) (Figure 3.3). There has been conjecture about the southward relocation of the entrance, such as that of WRL and

GCCM (1998), in which it was suggested that this might have indeed been a southern breaching of the coastal barrier. Moreover, Patterson (2007) mentioned that for the period of 1860 to 1920, the NRE remained just north of main beach (Figure 3.4), where an ebb-tidal delta formed offshore from the entrance.

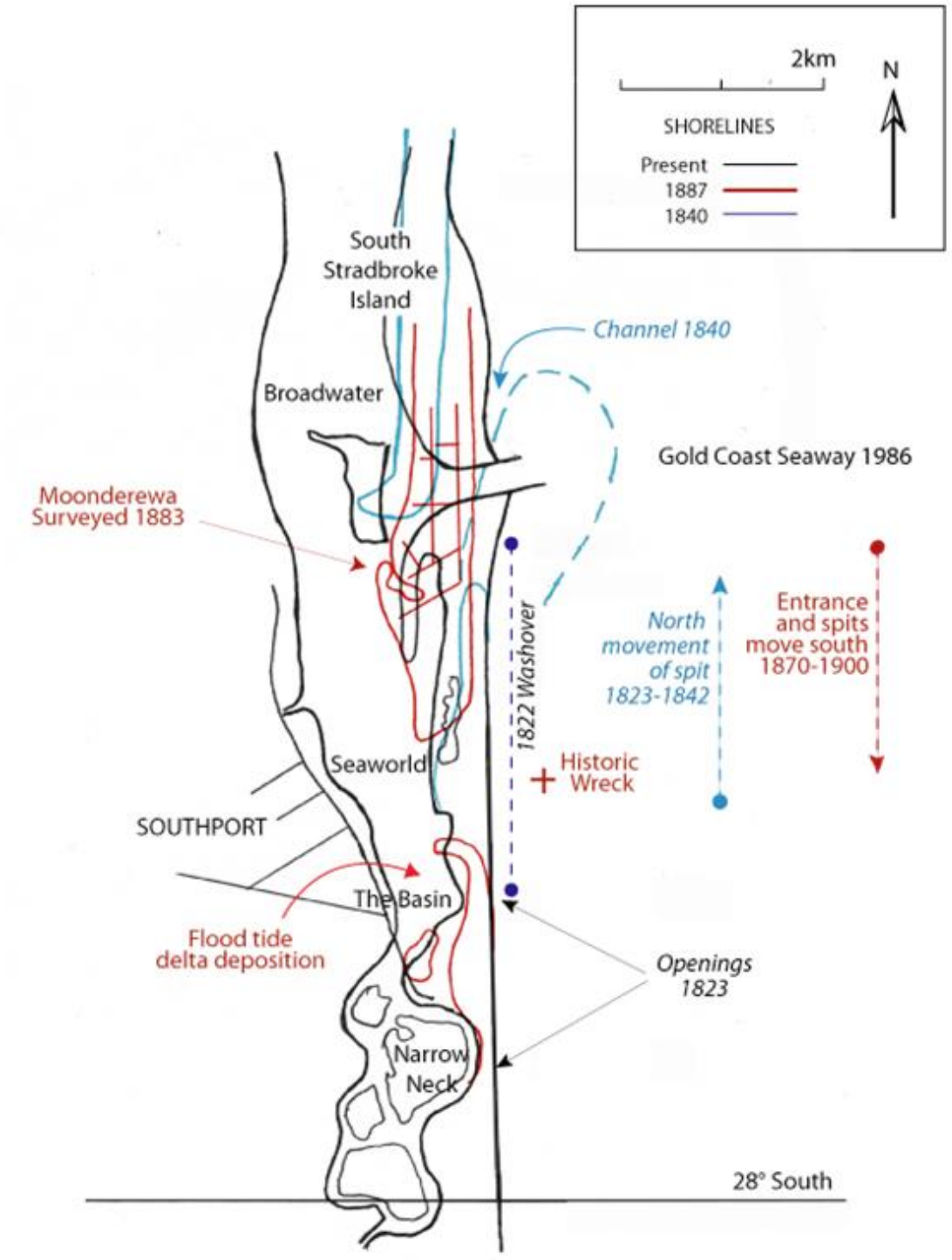

Figure 3.3. Opening of NRE at the Basin and formation of Stradbroke Island in 1823. The position of the bar in 1840 (Blue) and 1887 (Red) is compared to the current position of the GCS (Black) (Helman, 2010)

The other feature that affected the NRE location was the opening of the Jumpinpin inlet, initially as a breach of barrier dunes in 1895 and 1896, and finally by the breach of the channel in 1898. This entrance, which has remained open since 1898, led to the formation of two

separate barrier Islands: North and South Stradbroke Island (Salter, 2002; McCauley and Tomlinson, 2006). The opening of the Jumpinpin inlet has captured some of the river and tidal flow which previously flowed south and out flowed at the NRE. Consequently, the ebb tide flow in the NRE decreased, and the tidal prism of the inlet was significantly reduced (Brooks, 1953; Munday, 1995). As a result of the re-distribution of tidal flow, the entrance migrated to the north again after 1901 with an increased rate. This was attributed to the reduction in the capacity of tidal flow that used to remove the sand, and consequently, the sand was accreted on the spit from longshore sediment transport (WRL and GCCM, 1998). The rate of northward migration during this time has been variable, ranging from an average of about 60 *m/yr* during 1901-1968 to 26 *m/yr* 1944-1968 (DHL, 1970).

There is an uncertainty about the rate of the Broadwater infilling, mainly in the vicinity of the entrance, from the longshore sediment transport during these years. According to Helman (2010), the NRE migrated about 4.6 *km* to the north from 1901 to 1977 while depositing 180,000 m^3/yr in the Broadwater. Alternatively, according to DHL (1970), for the period between 1901 to 1968, sand accumulated in the Broadwater at an average rate of 143,000 m^3/yr, while it diminished after 1944 with a lower average rate of 61,000 m^3/yr from 1944 to 1968. In contrast to the sedimentation of the Broadwater created by longshore drift, the sediment contribution to the ocean from the Nerang River was about 9,200 m^3/yr (DHL, 1970). Therefore, the average diversion of sand to the Broadwater from LST and possible erosion of the South Stradbroke Island was suggested to be approximately 134,000 m^3/yr from 1901 to 1968.

The Jumpinpin entrance tended to have a similar behaviour to that of the NRE; there were some northward movement and south breaching from 1904 to 1934. However, the northward movement of the Jumpinpin entrance was limited by hard strata around the Swan Bay channel (McCauley and Tomlinson, 2006). In 1936, continued erosion, which had started in 1934, caused further breaching at a location about 1 *km* to the south of the main Jumpinpin channel as well as a breach on the Southport spit between the Southport Surf Life Saving Club and the current Sheraton Mirage. In order to protect the coastline from further erosion and the occurrence of breaching, protective timber or rock walls were constructed in the early 1950's at Narrowneck and Main Beach following cyclone erosion (Kindler and O'Connor, 1951; GCCM, 2014). It should be noted that during all these years, the South Stradbroke Island beach alignment was stable (WRL and GCCM, 1998). This means that the sand that was supplied from the natural bypassing of the entrance was in equilibrium with the LST potential at South Stradbroke Island.

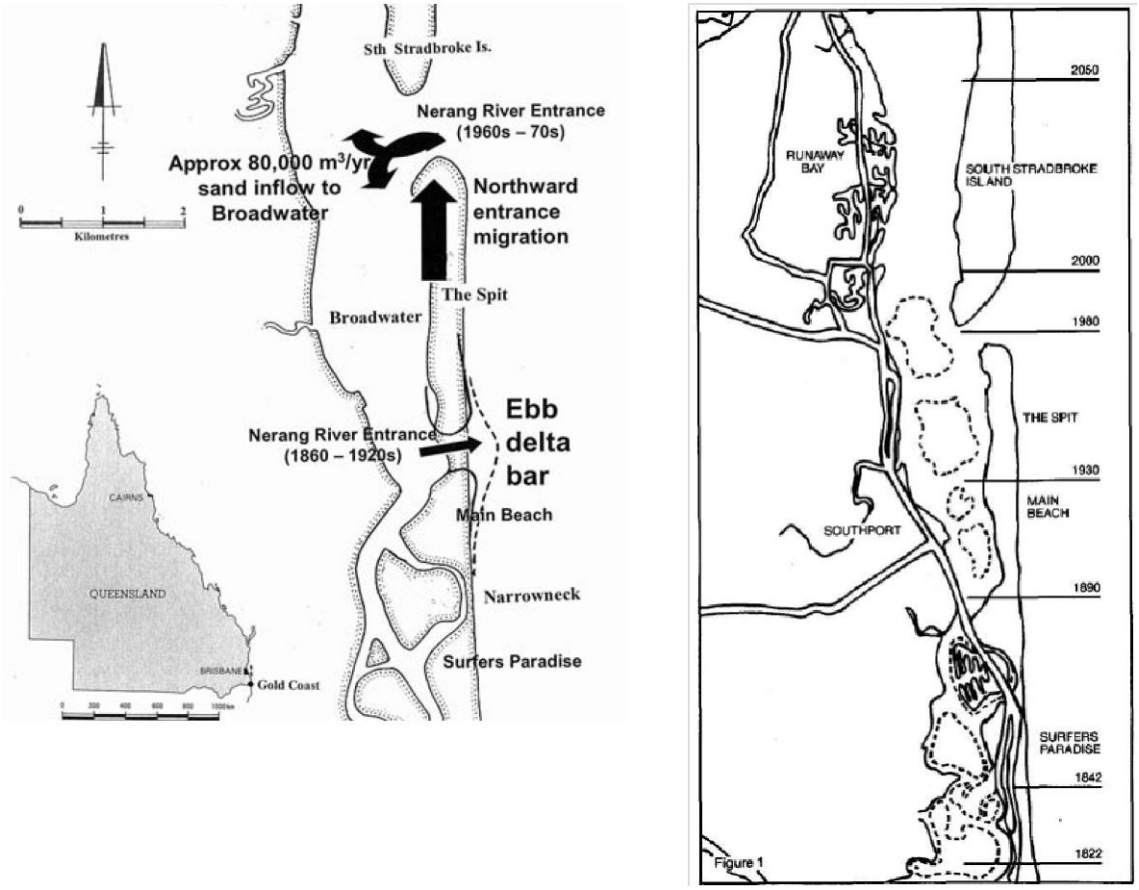

Figure 3.4. Plan of actual and predicted locations of NRE (WRL and GCCM, 1998; Patterson, 2007)

By the early 1980's, boating activity increased vastly due to the rapid growth of the Gold Coast into the nation's premier tourist resort area. The developed and dynamic ebb-tidal delta and shallow NRE were dangerous obstacles which resulted in a number of boating accidents, and it was then decided to train the NRE to provide a safe navigation channel (Sennes et al., 2007). It was predicted that in the absence of the GCS construction, the NRE would have continued to migrate northward, till either a major event caused a new breach to the south or a geomorphological control, like that of Jumpinpin, stopped its migration (WRL and GCCM, 1998).

3.3.2 Post GCS construction

3.3.2.1 Setting

The NRE was mechanically relocated 500 metres updrift (south) its natural location in 1985 and was stabilised with two rock walls, a 400 metre offshore length wall to the north and a 600 metre length wall to the south (Witt and Hill, 1987). The crest width of the training walls is about 12*m* with +4.0*m* AHD crest elevation, and the walls are extended to the -5.5*m* AHD

depth. The parallel breakwaters are 320*m* apart and are oriented 15 degrees to the north of east. The new stabilised dredged channel was 170*m* wide with a design depth of 5.5*m* below AHD at the time of construction (Munday, 1995). The dredging of the stabilised channel was followed by dredging of the navigation channel in the Broadwater, from the GCS to the Sundale Bridge in the south (Figure 3.5). The average depth in the GCS channel increased over the following 20 years as a result of erosion (Mirfenderesk et al., 2007; Mirfenderesk and Tomlinson, 2009). To reduce the wave penetration and protect the western shore of the Broadwater, a new artificial island, known as Wave Break Island, was created at the same time.

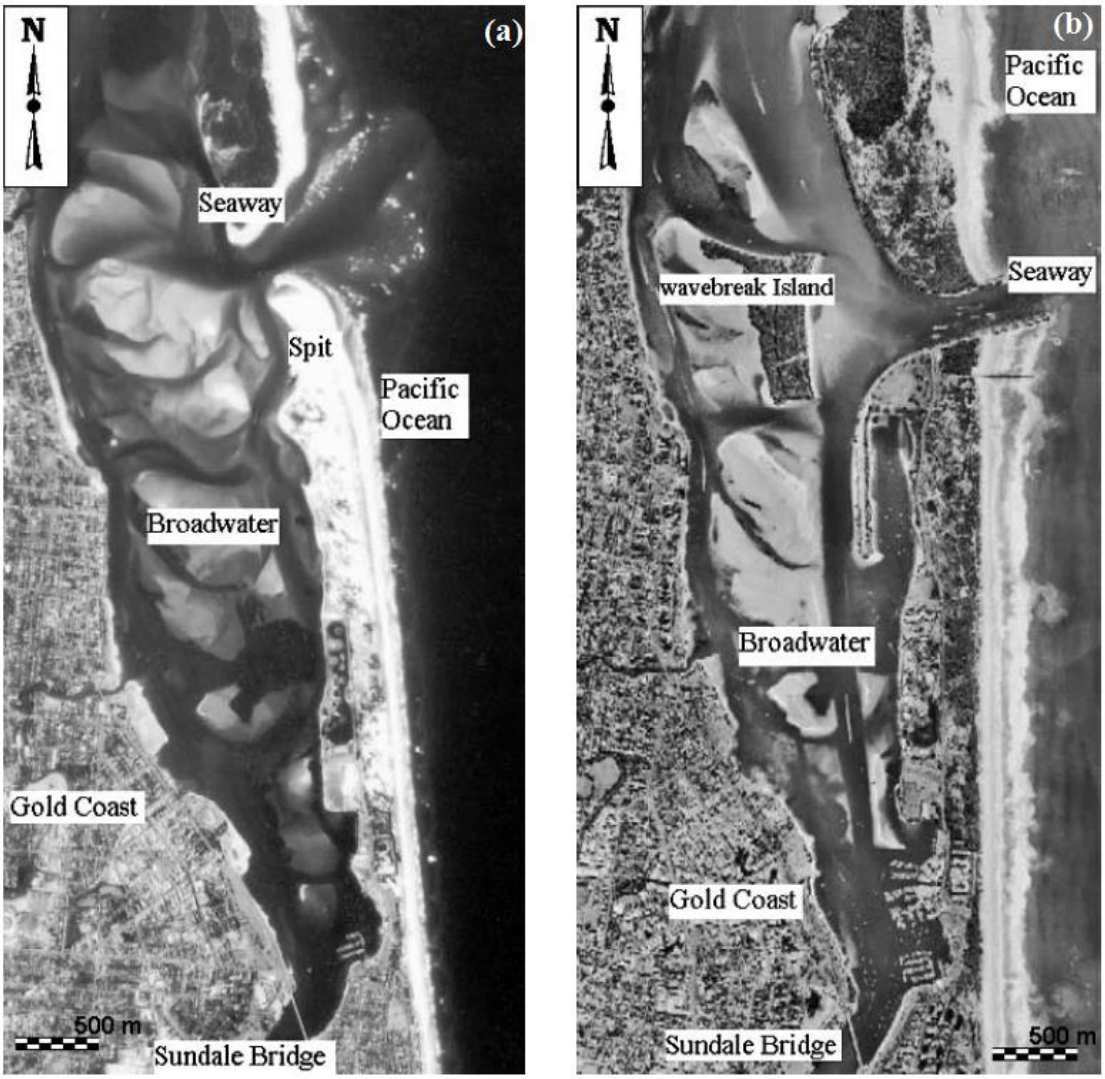

Figure 3.5. (a) GCS region in 1980 (b) GCS region in 2005 (Mirfenderesk and Tomlinson, 2009)

According to DHL (1970), due to the high magnitude of the northerly longshore drift on the Gold Coast, any scheme to stabilise the entrance would necessitate the implementation of an artificial sand bypassing system across the entrance. Therefore, a bypassing plant was

implemented and completed in 1986 (Sennes et al., 2007), the design criteria and final implemented sand bypassing system is explained in more detail in the section 3.3.2.2. The sand bypassing system was designed to interrupt the northward LST, and move the sand from the southern side of the entrance to the beach north of the entrance to prevent the formation of a bar across the entrance and infilling of the entrance.

Due to the increased capability of the jetted ebb flow to move sediment seaward, the new ebb-tidal delta crest moved much further offshore as compared to the old one (Munday, 1995). Prior to stabilisation, the ebb-tidal delta crest depth was about -2.5 to -3.5*m*, which was equal to the limiting depth for wave breaking similar to what was suggested by Tomlinson (1991). The new ebb-tidal delta crest depth, after stabilisation, is about -7*m*, which is below the depth controlled by the wave breaking of the waves with the average significant wave height. Munday (1995) suggested that the limited supply of sand into the inlet after stabilisation, because of the artificial sand bypassing system, has allowed the tidal current and wave induce LST to maintain the crest depth. Therefore, the crest depth has been maintained at a depth equal to the base of wave induced longshore sediment transport, which is approximately about -6*m* and -7.3*m* during fair-weather conditions in the study area (Hallermeier, 1981; Chapman and Smith, 1983). Only the wave induced current under high energy wave conditions can displace this ebb-tidal delta crest onshore (Munday, 1995), since only under such circumstances the ruling depth on the ebb delta shoal is related to the cross-shore wave dominated processes rather than the tidal currents (Marino and Mehta, 1987a).

3.3.2.2 The GCS sand Bypassing system

As a result of a decision made by the Queensland Government to provide a safe navigable channel, the Department of Harbours and Marine, together with Delf Hydraulics Laboratory developed a physical and mathematical model and conducted site investigate studies. Late in 1983 tenders were called for design and construction of a sand bypassing system which can transport:

1) Net annual transport of 500,000 m^3 with allowance for 50% variation
2) Maximum monthly transport for return period 2-5 years of 200,000 m^3
3) Maximum 5 day transport for return period 2 to 5 years of 100,000 m^3

So the system design was expected to cope with a normal or low volume of LST, as well as with a peak volume of LST that occurs once or twice per year (Polglase, 1987).

The basic principal of the sand trap was to create and maintain an excavated trench at right angles to the beach, and the sand would flow into this trench and be removed from it. Rationally, the deeper end of the trap which is in the broken wave zone will receive a greater rate of sand inflow. Therefore, the volume of sand that will be transported is dependent on the littoral drift volumes together with a wave-generated easing of the sand trap side slopes and general levelling of the local seabed and beach (Polglase, 1987).

It was decided to use a series of 10 "Genflo Sandbug" fixed condition jet pumps for bypassing the sand. These were located every 30*m* and supported by an access jetty, which is 500*m* long and is located approximately 250*m* south of the southern training wall. Therefore, the total available sand trap length was 270*m* to a depth of 11*m* below mean sea level (MSL). The general arrangement of the designed sand bypassing system is shown in Figure 3.6. Jet pumps were selected since they have no moving parts and therefore less maintenance cost, and also because they can start up while buried in the sand and therefore they can be fixed in elevation and horizontal location. The jet pumping system of the sand bypass can operate 24 *hrs* a day, even during violent storms (Coughlan and Robinson, 1990), and has a maximum pumping capacity of 595 m^3/hr (Polglase, 1987).

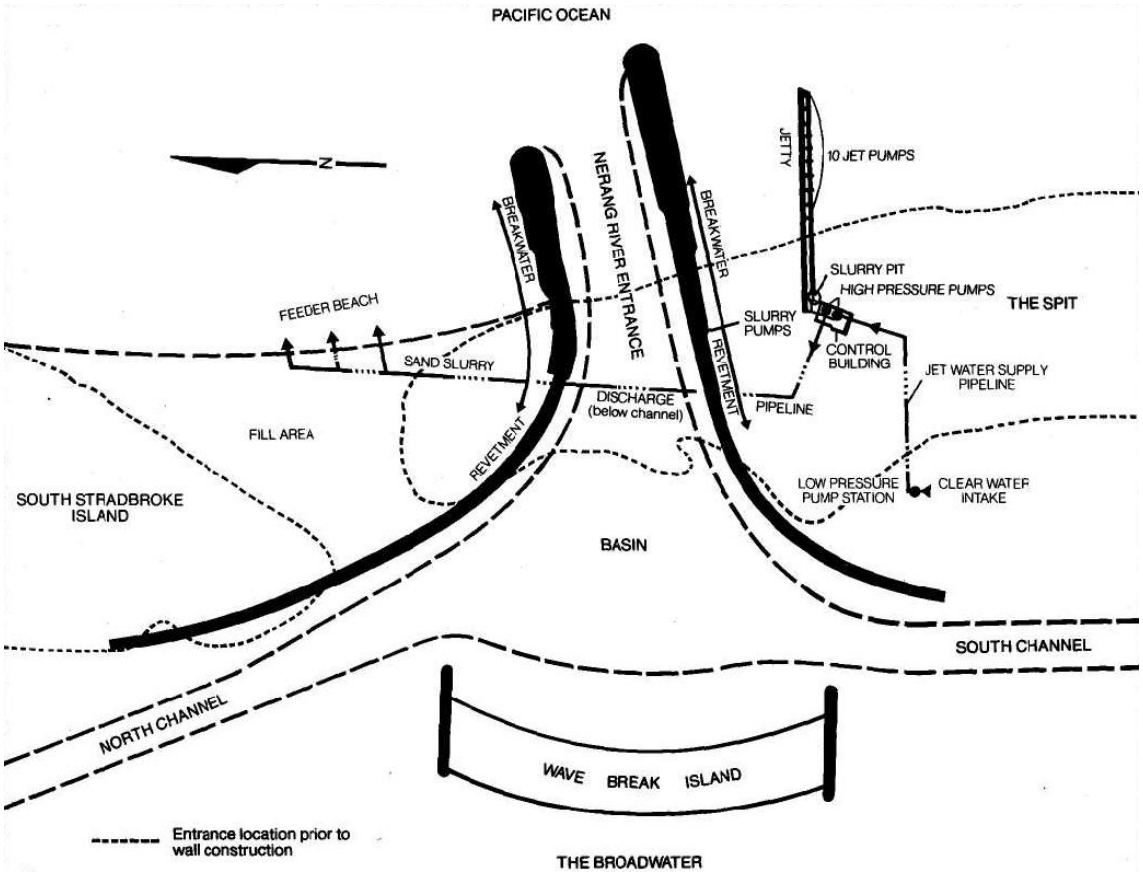

Figure 3.6. NRE stabilisation and sand bypassing scheme (Polglase, 1987)

The motive water, which is sourced from the inner harbour, pumps at low pressure (200 *kPa*) to the control building where its pressure is boosted to 1200 *kPa* and delivered to the jet pumps. Then the sand slurry from the jet pumps is transported along the jetty to a conical hopper adjacent to the control building using an elevated flume pipe. The excess water is emptied back to the beach there and the concentrated sand slurry pumped and transported through a 406 *mm* diameter pipeline across to the northern side of the entrance (Figure 3.7).

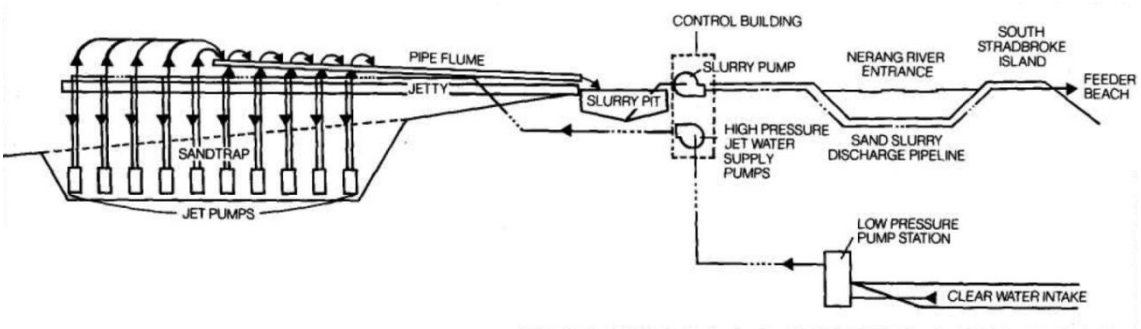

Figure 3.7. The sand bypassing system schematic process (Polglase, 1987)

Based on the criteria of the design, the maximum sand transport requirement is 100,000 m^3 during 5 days. The volume of this LST that can fill the empty sand traps is about 30,000 m^3, which means that the nett transported sand during this 5-day period should be 70,000 m^3. This is equal to 14,000 m^3/day (Polglase, 1987).

3.3.2.3 Inlet channel

The initial design plan for the inlet channel was a cross sectional area of 1700 m^2 below +1.3*m* AHD (DHL, 1976), but since stabilisation of the NRE the channel scouring has resulted in a much larger minimum cross sectional area, e.g. 2800 m^2 below +1.3*m* AHD (2400 m^2 below AHD) in 1992 (Munday, 1995). The initial scouring of the inlet channel was both desired and typical and the increase in the GCS tidal prism after stabilisation was the main reason for this scouring. Several relationships between the inlet cross sectional area and its tidal prism have been suggested, for example Munday (1995) applied the $P - A_c$ relationship developed by O'Brien (1931; 1969), which is for inlets with two training walls:

$$A_c = 4.35\times10^{-5}(35.3P)^{0.85} \tag{3.2}$$

where A_c is the minimum cross sectional area (below MSL) in m^2, and P is the tidal prism in m^3. A tidal prism can be calculated by multiplying the basin surface area by the tidal range near the inlet entrance. The $P - A_c$ relationship shows that any change in the inlet cross sectional area will cause a corresponding change in the inlet tidal prism and vice versa.

Calculation of the tidal prism for the GCS is a complicated task due to the connection of the Broadwater with Southern Morton Bay, and also the vicinity of the Jumpinpin inlet which also drains the Broadwater. Munday (1995) applied equation (3.2) to estimate the tidal prism of the GCS in 1992; it should be noted this should be done based on the assumption that the inlet has reached a dynamic equilibrium. According to WBM (1992), the cross sectional area of the inlet was 2400 m^2 below AHD. Therefore, the calculated tidal prism using this formula was 36×10^6 m^3. This showed at least a 24% increase as compared to the upper limit of the tidal prism for the inlet before stabilisation, when the cross sectional area was 1900 m^2 below +1.3*m* AHD according to the study by Witt and Hill (1987). Based on later studies, the inlet erosion has continued since then. Therefore, the entrance was not at a dynamic equilibrium condition and the tidal prism was even bigger than 36×10^6 m^3, which was calculated by Munday (1995). Mirfenderesk and Tomlinson (2008) suggested that the tidal prism of the GCS in 2005 was 66×10^6 m^3 with an approximate cross section area of 3500 m^2, both more than those of 1992. Substituting the tidal prism in equation (3.2), the required cross sectional area would be about 4000 m^2, which suggests a continuous scouring of the inlet in the following years. Mirfenderesk and Tomlinson (2008) also suggested that the GCS has been eroded since stabilisation, but the rate of erosion has decreased gradually and it has approached a more stable condition in recent years. According to Mirfenderesk and Tomlinson (2009), the average depth of the inlet channel was about 11*m* in 2005, with a maximum depth of about 20*m* at some points.

Munday (1995) explained that the increase in the tidal range in the Broadwater since pre-stabilisation is the main reason for the increase in the tidal prism. Before stabilisation, the natural ebb and flood shoals in shallow depths near the NRE (ebb delta crest height of -2.5 to -3.5*m* depth (Munday, 1995)) attenuated the ocean tidal range within the Broadwater by up to 60% (WBM, 1992). Therefore, dredging and construction of the new entrance increased the tidal range in the Broadwater to the same range as the ocean coast, which resulted in the growth of the tidal prism and finally more channel scouring right after stabilisation. The development of more tidal canal estates in the Nerang River estuary over the years has also resulted in an increase in the tidal prism of the GCS (Mirfenderesk and Tomlinson, 2009). However, the continuous scouring in the channel well below the design depth, which was not predicted, was found to be more dominant due to the presence of artificial sand bypassing and reduced sand supply to the inlet channel (Munday, 1995). Therefore, it has been suggested that the sediment supply will ultimately control the inlet cross sectional area, and the resulting tidal prism size as well as a more offshore and deeper location for the ebb tidal delta. Without any artificial sand bypassing and dredging, the inlet channel morphology would have returned to a morphology

similar to what it was prior to stabilisation; with an ebb-tidal delta at a much shallower depth (Munday, 1995).

It should also be noted that two major scour holes have developed in the inlet channel since 1986. One is located against the southern breakwater, and the other is just inside the northern wall's seaward edge (Figure 3.8). Both scour holes have maintained a relatively consistent position since they were first developed. The scour hole against the southern wall has developed mainly due to the greater ebb flow from the northern channel of the Broadwater. The dominant cause of the deep scour hole next to the northern wall tip has been suggested to be the result of wave action (WBM, 1992).

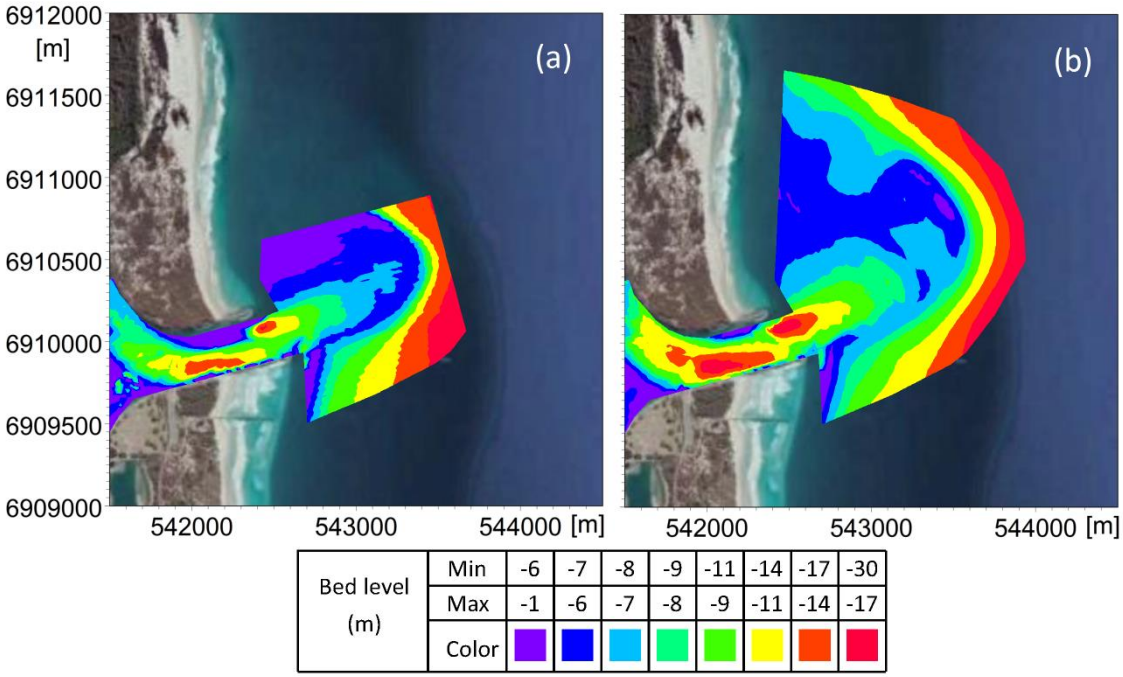

Figure 3.8. Location of two major holes in the inlet channel (a) November 1990 (b) April 2015

3.3.2.4 Ebb-tidal delta

Even after the implementation of the sand-bypassing system, analyses of historical survey data have shown continuous growth of the ebb-tidal delta. Since 1986 there have been various estimations of the rate of the ebb tidal growth. WRL and GCCM (1998) analyses have suggested that between 1986 and 1992 the average rate of deposition on the ebb delta was around 185,000 m^3/yr, which is considerably less than 470,000 m^3/yr estimated by Munday (1995). According to Munday (1995), the total volume of ebb-tidal delta in 1992 was 12×10^6 m^3, while it was approximately 8.6×10^6 m^3 when the entrance was stabilised. WRL and GCCM (1998) estimated a much lower growth rate of about 75,000 m^3/yr for the ebb-tidal delta from

1992 to 1998. Andrews and Nielsen (2001) and WBM (2001) also used historical survey data from 1986 to 1999 and 2D numerical modelling for the period 1990 to 1995. They estimated that the ebb-tidal delta has grown continuously, initially at a rate of around 450,000 m^3/yr from 1986 to 1990, then decreasing to: about 220,000 m^3/yr from 1990 to 1994; 200,000 m^3/yr from 1994 to 1996; and 180,000 m^3/yr from 1996 to 1994. These rates were higher than other estimates, such as those of WRL and GCCM (1998). This difference can be explained by the different definitions of calculated deposition areas in various studies. For example, WRL and GCCM (1998) suggested that the ebb tidal delta calculation by Munday (1995) only included the areas of the ebb delta which were actively accreting, while the WRL and GCCM (1998) report included the whole defined ebb delta survey area (Figure 3.12) which might include some scouring as well. Generally the growth of ebb delta was to the northeast, probably due to the combination of dominant waves (from the Southeast) and the mean ebb tide discharge path to the delta (to the northeast). Some wave induced swash bars have also formed on the southern part of the ebb delta. The net estimated sand transport at the jetty for the 1986-1998 period was about 550,000 m^3/yr to the north, and the sand bypassing system bypassed 440,000 m^3/yr on average (Andrews and Nielsen, 2001).

The cross-shore distribution of sediment transport was found to be sensitive to both wave conditions and the depth of water at the offshore bar; and a significant amount occurs at the offshore bar most of the time (Andrews and Nielsen, 2001). The offshore bar location also depends on both wave conditions and the location of the seaward end of the southern breakwater; and it has occasionally been observed seaward of the bypassing jetty. It was suggested by Andrews and Nielsen (2001) that the main source of sand for the continuous growth of the ebb tidal delta has been this leakage of sand offshore from the sand bypassing system (around 115,000 m^3/yr, which has been about 20% of the annual net longshore sediment transport), and also through the bypassing jetty (around 80,000 m^3/yr). This is illustrated in Figure 3.9. Mirfenderesk and Tomlinson (2008) also suggested that the crescent like offshore lobe of the ebb-tidal delta after stabilisation, which has connected upstream to downstream, indicates that the LST has been partially transported naturally along with the artificial sand bypassing system. It has also been suggested that another probable source of sediment for the ebb-tidal delta was the redistribution of sand from the discharge location of the bypassed sand downstream. Scouring of the channel between 1990 and 1995 was initially at a rate of 100,000 m^3/yr, and this gradually diminished to about 10,000 m^3/yr. The scoured sediment was the other source of sand trapped in the ebb-tidal delta (Andrews and Nielsen, 2001). On the other hand, WRL and GCCM (1998) suggested that there has been about 50,000 m^3/yr of natural bypassing on the ebb tidal delta, while the major supply of sand to the ebb-tidal growth has been from the

Broadwater input in 1998 (0-240,000 m^3/yr). Andrews and Nielsen (2001) suggested that the beach between the southern breakwater and the bypassing jetty seemed to act as a sand source or sink, depending on the imbalance between the longshore sediment transport and the artificial sand bypassing rate.

Due to the leakage of sand offshore from the sand bypassing jetty to the ebb tidal delta, and the related possible trapping in the ebb tidal delta, shoreline recession downdrift the inlet was expected. It was suggested by Andrews and Nielsen (2001) that other sources of sand were the main reasons that prevented the downstream recession. These sources included: the old natural entrance delta which was further to the north of the GCS; sand from inlet channel scouring; and also suspension of sand entry through the entrance.

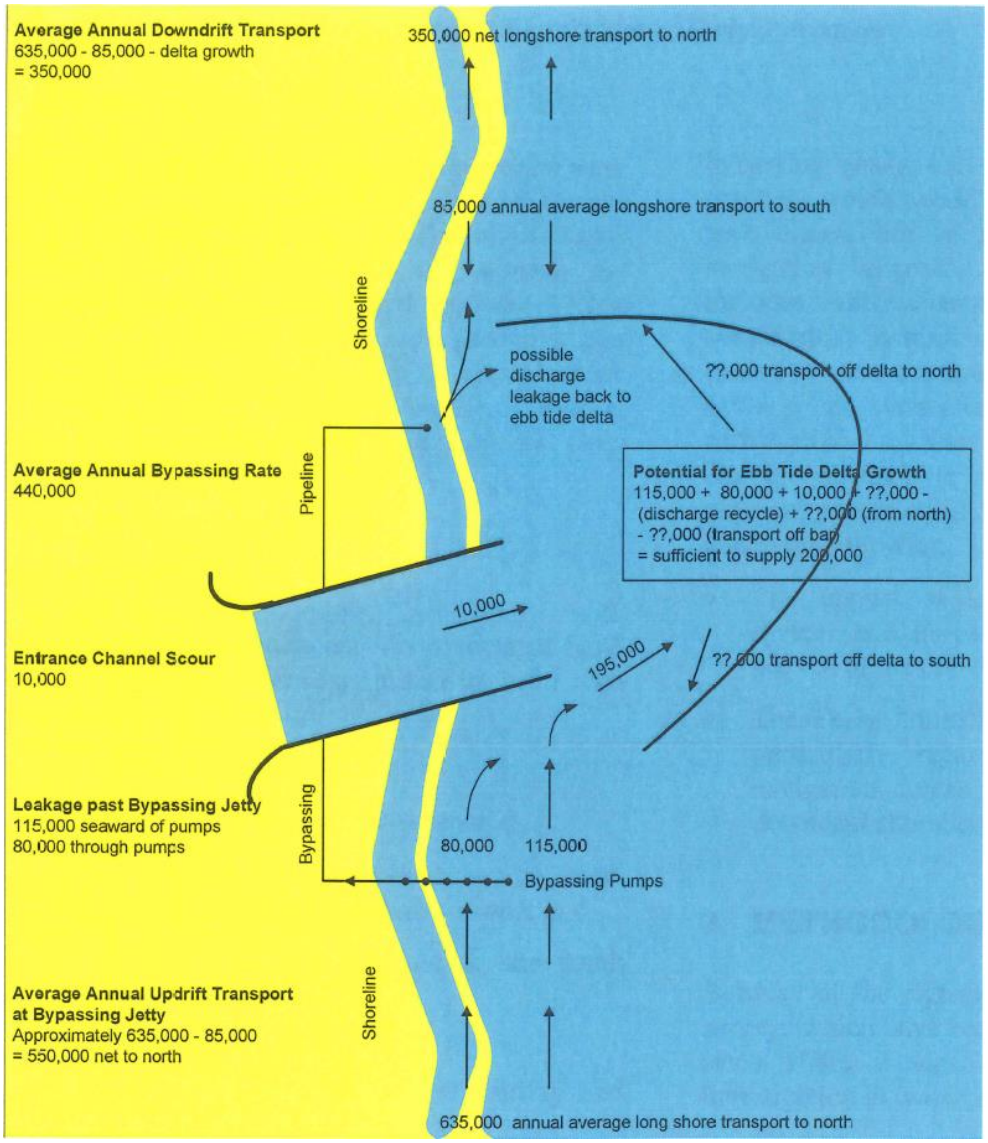

Figure 3.9. Suggested longshore sediment transport distribution around the GCS and potential ebb delta Growth from 1986 to 1998 (Andrews and Nielsen, 2001)

3.4 Previous Approaches

3.4.1 Longshore sediment transport

The longshore sediment transport in the vicinity of the GCS was first estimated by DHL (1970). Its estimation was about 500,000 m^3/yr comprising of 610,000 m^3/yr northward and 110,000 m^3/yr southward. This net rate, which was estimated based on ship-based observed data, has subsequently been confirmed by a number of other studies. Pattearson and Patterson (1983) investigated the LST based on the recorded wave data from 1973 to 1981. The estimated LST along Letitia Spit (Figure 3.10), based on the rate of accretion updrift the Tweed River training walls during their construction, was used to calibrate the CERC formula for calculation of longshore sediment transport in the region. Then, the calibrated formula was applied to various points along the Gold Coast shoreline, including the Spit. The resultant estimate of longshore sediment transport for various points along the entire Gold Coast was approximately 500,000 m^3/yr using both CERC and Bijker (1968) equations (Pattearson and Patterson, 1983). Therefore, Pattearson and Patterson (1983) has also concluded that no long term gradual erosion of Gold Coast beaches is expected, and the only factors affecting the coastline are storm erosions (short term). Erosion or accretion is also expected in the downdrift and updrift beaches of any constructed groyne/training wall respectively, which is due to the interruption to sediment supply.

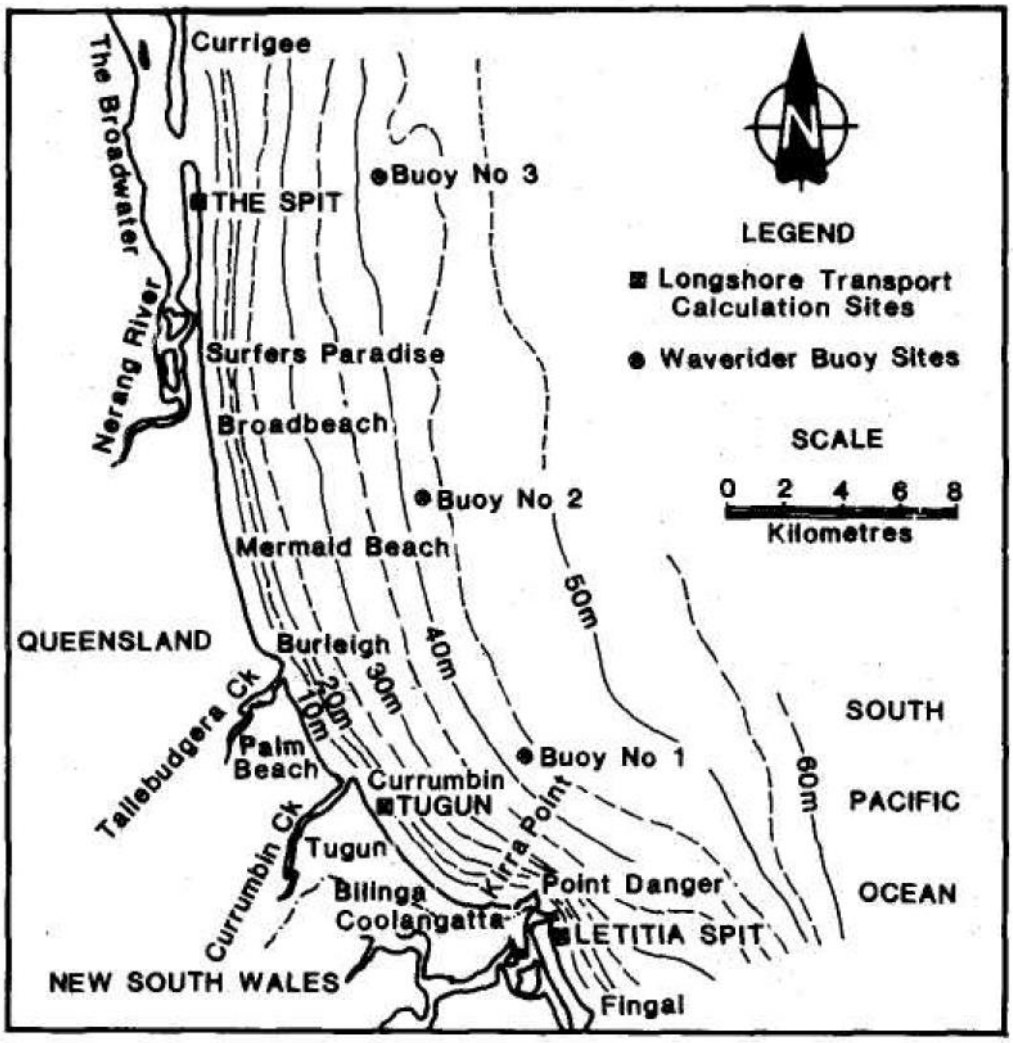

Figure 3.10. Gold Coast region (Pattearson and Patterson, 1983)

An analysis of the sediment budget in the GCS vicinity by WRL and GCCM (1998) has shown that net alongshore sediment supply reaching the Spit is around 500,000 m^3/yr. Along the Gold Coast Coastline there are a few sediment sinks, such as those at Currumbin, Tallebudgera Creek and the Broadwater. These were estimated to have trapped about 80,000 m^3/yr of sediment before 1998. Patterson (2007) investigated the pattern of sand transport on a 10 *km* length of the northern Gold Coast between Surfers Paradise (ETA 57) and the Gold Coast Seaway (ETA 80) over the period of 1966 to 2002. The net general estimated rate using the "Queens" method (Kamphuis, 1991) was 540,000 to 560,000 m^3/yr, while a higher rate of 635,000 m^3/yr, similar to that given by Andrews and Nielsen (2001), was estimated at the northern end of the spit. This higher rate was explained as being due to a slightly further seaward shoreline alignment at the end of the spit, which Patterson justified to be from the onshore sand supply from the residual old ebb tidal delta further in the south (2007). This residual of the old ebb-tidal delta was also

noted in the survey profile analysis by Munday (1995). The location of this old ebb-tidal delta was at about 1.5 *km* south of the old inlet, or 1 *km* south of the stabilized inlet (Munday, 1995).

Splinter et al. (2012) estimated longshore sediment transport on six ETA lines along a 35 *km* length of Gold Coast coastline using the Kamphuis (1991) formula for a 50 year (1958 to 2009) hindcast of the offshore directional wave conditions. A data clustering method was applied to condense the annual ERA (the European Centre for Medium-Range Weather Forecasts (ECMWF) wave Re-Analysis data sets) wave data into a representative number of data points. In their research they assumed d_{50} = 220μm, porosity of 0.4, ρ_s = 2650 kg/m^3, ρ_w = 1025 kg/m^3 for the area. The time averaged estimated net transport rate from 1958 to 2009 for ETA67 (Narrowneck), and ETA 79 (The Spit) were 546,000 m^3/yr and 715,000 m^3/yr, respectively. These estimates were relatively close to those of Patterson (2007), who used the Brisbane Buoy time series, and estimated 540,000 m^3/yr for Narrowneck and 635,500 m^3/yr for the Spit. The lower estimated longshore sediment transport for the Spit by Patterson (2007), compared to that of Splinter et al. (2012), was explained to be probably due to slight variations in the shoreline orientation, sediment diameter, source of wave data, and using time series versus wave clustering.

Splinter et al. (2011) applied two sediment transport formulas, one derived from Kamphuis (2002) and the other from Bayram et al. (2007), to estimate longshore sediment transport along eight different ETA lines. Classified wave groups for 25 years were applied in their estimations. Their results showed a considerable difference when using different formulas, and the estimation derived from Bayram et al. (2007) was closer to those of previous studies like that of Patterson (2007). The results from Splinter et al. (2011) have highlighted that longshore sediment transport varies temporally due to storm frequency, intensity and direction, and seabed morphology. It also varies spatially depending on the shoreline configuration and wave exposure.

3.4.2 Conceptual models

Based on historical survey data, aerial photos and some numerical models, a few conceptual models have been suggested to determine the pattern of sediment transport in the GCS vicinity. Some of these conceptual models are related to the NRE morphological evolution prior to stabilisation. For example, Sennes et al. (2007) analysed the period from 1955 to 1985 and adapted a conceptual model for the NRE. It was suggested that the entrance has followed a cyclic downdrift movement, in agreement with the model by FitzGerald et al. (2000). Sennes et

al. (2007) suggested a three stage conceptual model for the NRE with a ten year cycle. These stages are illustrated in Figure 3.11.

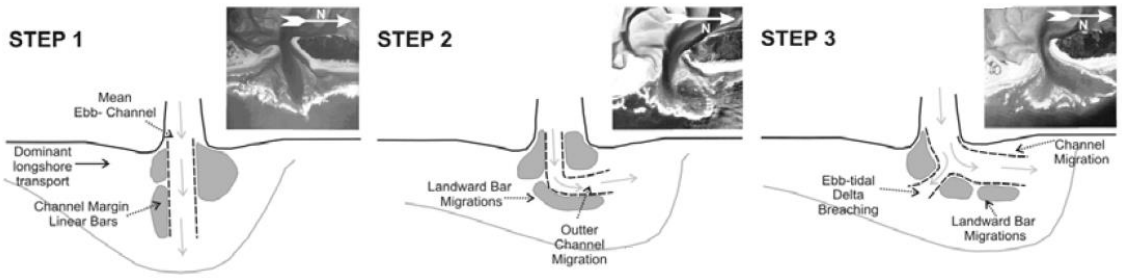

Figure 3.11. Conceptual model of the GCS evolution prior to stabilisation (Sennes et al., 2007)

WRL and GCCM (1998) provided a more refined conceptual model of the GCS vicinity sediment budget analysis after the stabilisation. Their model was based on the conceptual model presented in the ICM (1997) report. Six regions within, and around, the Seaway were defined, following Hayes (1980) and Boothroyd (1985): the ebb delta (E); the updrift fillet (D); the downdrift fillet (U); the channel (C); the flood shoal (F) and South Stradbroke Island (see Figure 3.12). Volumetric analysis was done for the first five areas, and South Stradbroke Island changes were analysed using aerial photographs to assess shoreline alignment trends. Areas D and U were parts of the ebb tidal delta beyond the training walls where sediment could be trapped and were not under the full effect of ebb tidal currents. Area C's western limit extended to the sand bypassing pipeline crossing the Seaway. The included area of South Stradbroke Island was defined from the northern edge of area E to the limit of the survey data (ETA 89), which was approximately 3.5 *km* northward.

The resultant conceptual model from their analysis is shown in Figure 3.13. They concluded that the net LST rate at the time of the study was about 500,000 m^3/yr along the Gold Coast area (South of the GCS). This rate decreased at South Stradbroke Island due to its more easterly alignment. It was suggested that the coastline adjacent to GCS seemed to be in an equilibrium condition, which meant that most of the ebb tidal growth in its initial years was dominated by deposition of sediment transported offshore from the Seaway by ebb-tidal flow. It was also suggested that there was about 50,000 m^3/yr of natural bypassing on the ebb tidal delta, which in addition to 450,000 m^3/yr of artificial sand bypassing by the jetty, were in balance with the area's longshore sediment transport requirement. It was also noted that sand transport driven by tidal currents was independent of longshore littoral processes, and was ebb-tide dominated (WRL and GCCM, 1998). Andrews and Nielsen (2001) or WBM (2001) developed another conceptual model for the GCS which was explained in section 3.3.2 (Figure 3.9).

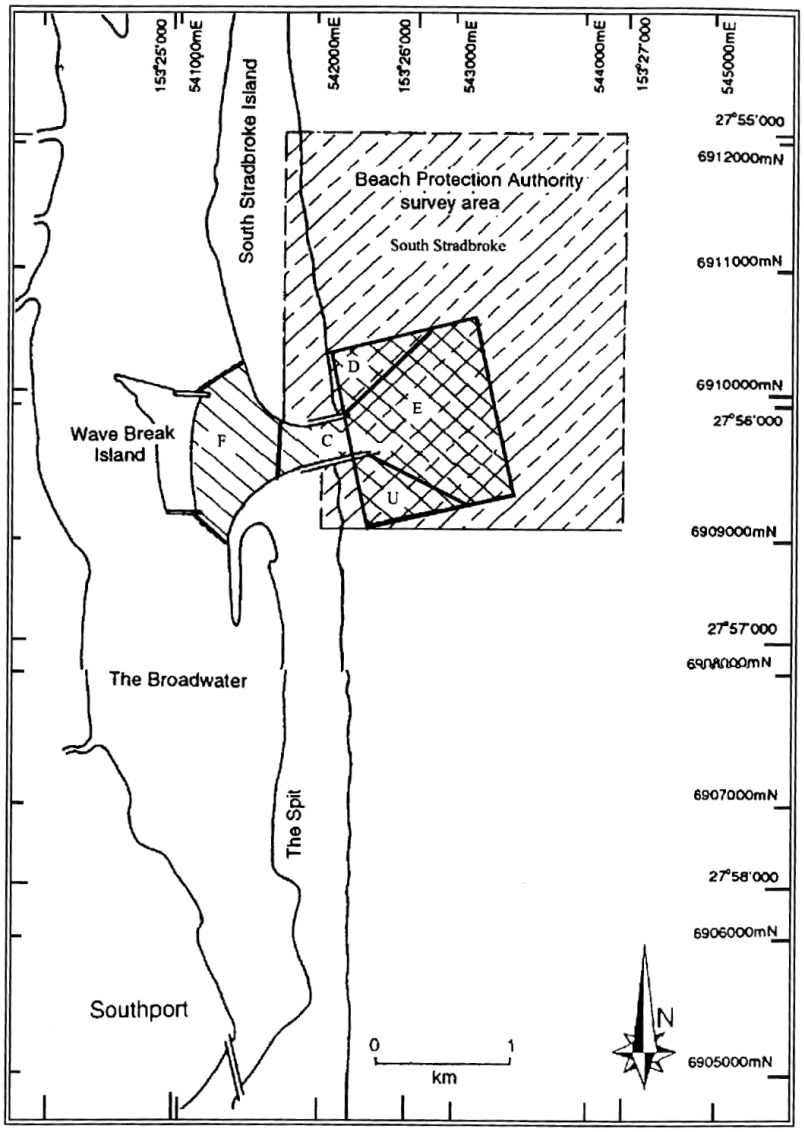

Figure 3.12. Definition of the GCS regions (E: Ebb delta, D: Downdrift fillet, U: Updrift fillet, C: Channel, F: Flood shoal) (WRL and GCCM, 1998)

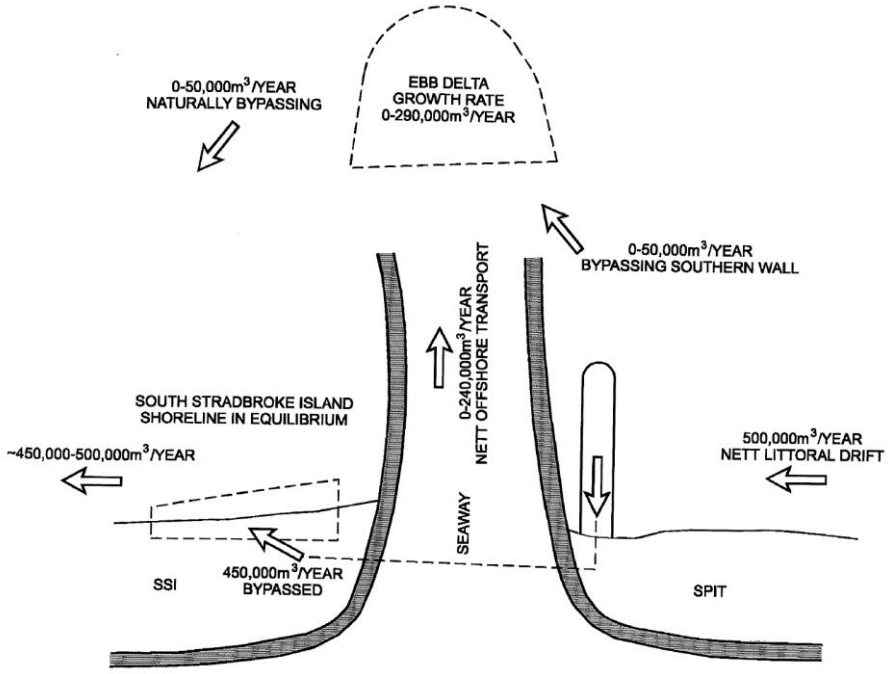

Figure 3.13. Suggested conceptual model of sediment transport in the GCS area in 1998 (WRL and GCCM, 1998)

GHD (2007) reviewed and updated the conceptual model suggested in WBM (2001) report. They suggested a conceptual model for sediment transport pathways and average yearly quantities in the vicinity of the GCS for 2002 to 2006 (Figure 3.14). Assuming that 20% of the longshore sediment transport occurs seaward of the end of the bypassing jetty, as was suggested by WBM (2001), GHD (2007) analysis of the bypassing rates indicates that the total northerly sediment transport could be as high as 846,000 m^3/yr. This was about 33% higher than the rate suggested by WBM (2001). As shown in Figure 3.14, the major portion of the ebb-tidal delta growth was suggested to be sourced from the leakage of longshore sediment transport offshore the sand bypassing jetty.

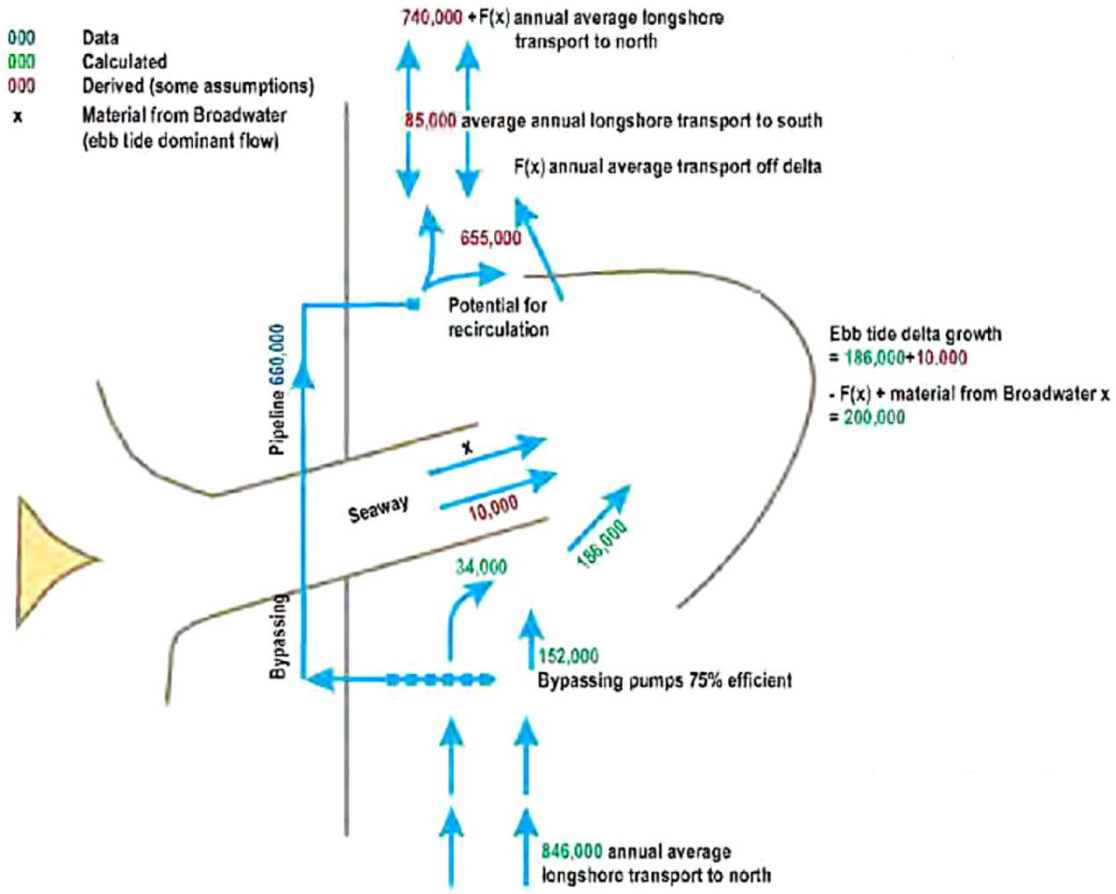

Figure 3.14. Sediment transport pathways and average annual rates from 2002 to 2006 (GHD, 2007)

WBM (2013) has also suggested a conceptual sand budget model for the GCS system (Figure 3.15). This was based on the analysis of the estimated longshore sediment transport, using numerical modelling, and the bypassing rate from 1997 to 2012. They suggested that there is a substantial movement of sand, both from the longshore sediment transport to/from the bar, and within the ebb-tidal delta, without any substantial net transport across the system. Based on their conceptual model, the net source of sand for the ebb-tidal growth was from the sediment export from the Broadwater (~80,000 m^3/yr).

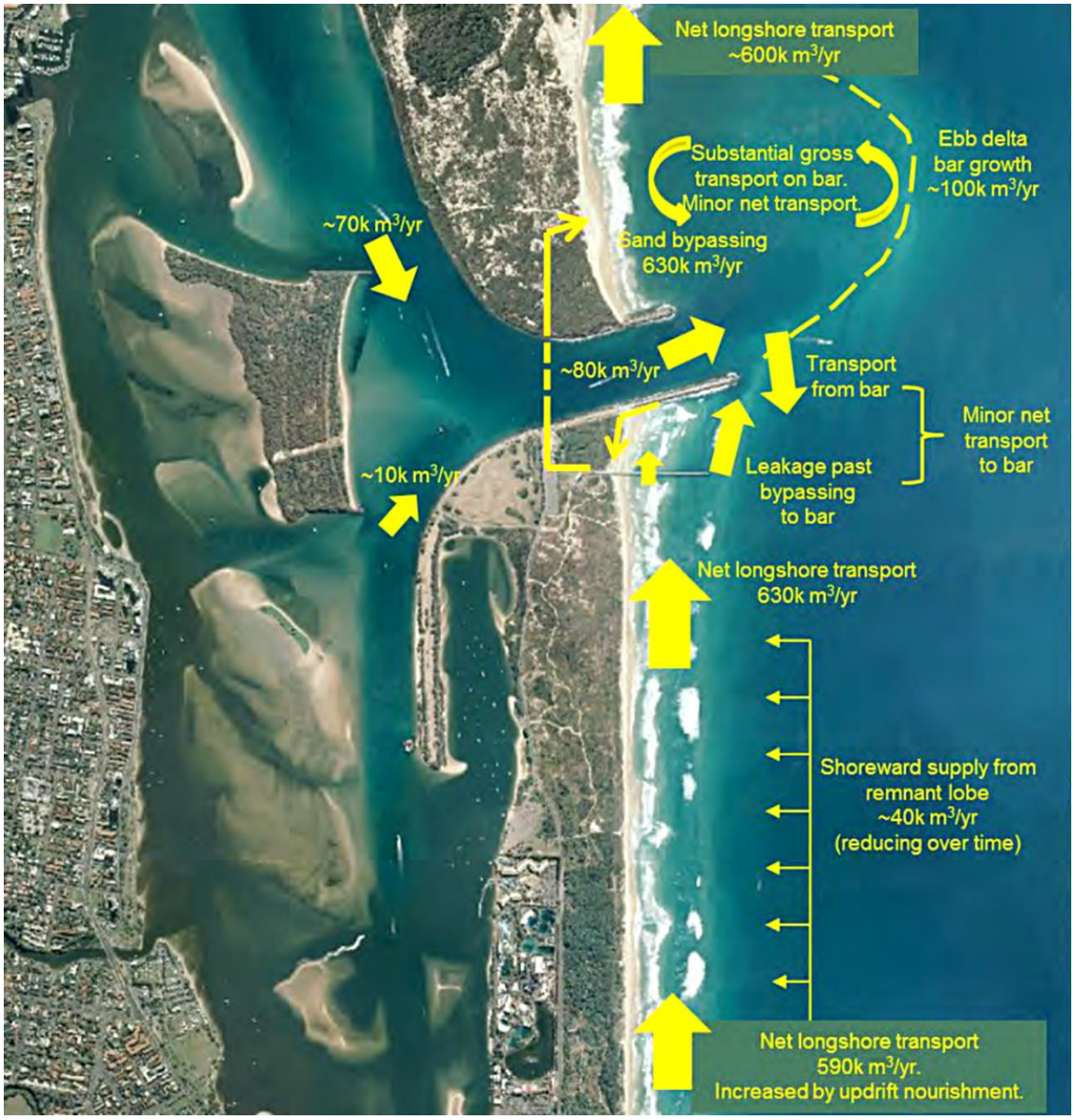

Figure 3.15. Sand budget conceptual model suggested by WBM (2013)

A summary of the suggested sand budget components in the GCS region, as suggested by conceptual models in previous studies, is shown in Table 3.1.

Table 3.1. Summary of the suggestions from previous studies on the sand budget components in the GCS area

Reference	**Net LST (m^3/yr)**	**Sand volume from within the inlet channel and the estuary to the ebb-tidal delta (m^3/yr)**	**Net leakage volume move past bypassing to the ebb-tidal delta (m^3/yr)**	**Ebb-tidal delta growth (m^3/yr)**
WRL and GCCM (1998)	500,000	0 – 240,000	0 – 50,000	0 – 290,000
Andrews and Nielsen (2001)	635 to the north 550,000 net	10,000	195,000	200,000 (1986 to 1998)
GHD (2007)	Up to 846,000 to the north	10,000	186,000	200,000 (2002 to 2006)
WBM (2013)	630,000	80,000	Negligible net value	100,000 (1997 to 2012)

3.4.3 Numerical modelling

There are only a few studies investigating the GCS which have incorporated sediment transport and morphological evolution modelling, as well as the hydrodynamics of the GCS (WRL and GCCM, 1998; Andrews and Nielsen, 2001; Sennes et al., 2007). Other studies, such as those of McInnes et al. (2002) and Mirfenderesk and Tomlinson (2007) only focused on the simulation of the hydrodynamics in the Broadwater and GCS. A short description of these studies, their limitations and findings are given below.

WRL and GCCM (1998) developed a shoreline evolution model using a GENSIS shoreline model to examine a number of coastal management options on the shoreline evolution in the GCS vicinity. The model was calibrated by adjusting the calibration parameters so that it reproduced a mean annual longshore sediment transport rate of around 500,000 m^3/yr, as suggested by previous research investigating the study area (DHL, 1970; Pattearson and Patterson, 1983; DHL, 1992). Then, the model was used to investigate the effects of the rate of the annual longshore sediment transport and mechanical bypassing on the long term trend of the shoreline evolution. Although the model had several limitations, such as an inability to incorporate the impact of extreme storm events, these events were indirectly included by considering their contribution to the annual longshore transport.

It was concluded that only about 50,000 m^3/yr of natural bypassing sand was occurring over the ebb tidal delta, which was assumed to be originally from the bypassing system leakage. Next, the cross shore distribution of longshore sediment was simulated using the UNIBEST model to

check the GCS training wall effectiveness in blocking the longshore sediment transport. It was found that under average wave climates, a negligible amount of transport (< 5%) was occurring offshore of the seaward tip of the southern breakwater at the GCS (located approximately 400*m* offshore). This was noted to be probably a lower estimate of the actual rate of natural bypassing due to local two dimensional surf zone circulations in the GCS vicinity and the diurnal tidal exchange through the entrance (WRL and GCCM, 1998).

The offshore distribution of longshore sediment transport under average wave climates was also found to be insensitive to wave direction. However, the results of their simulations showed that under extreme storm conditions ($H_s \geq 4m$), which have a probability of occurrence of less than 1% based on 22 years of data, a much higher rate of longshore sediment transport occured in deeper waters than the tip of the southern breakwater. This rate for the maximum observed significant wave height during the same 22 years, $H_s = 7m$, was simulated to be up to 80% offshore from the GCS breakwater. It was anticipated that on these rare occasions, a significant amount of natural bypassing would occur (WRL and GCCM, 1998).

Andrews and Nielsen (2001) developed a coupled model for sediment transport which was a combination of the Delft wave model SWAN, the RMS two dimensional hydrodynamic model (King, 1997) and the two dimensional water quality model, RMA11 (King, 1998). The model simulated the net sediment transport at the bypassing jetty to be in the order of 550,000 m^3/yr to the north. The crossshore distribution of the LST was also investigated, which was explained in more detail in section 3.3.2 Figure 3.9. It should be noted that flow and waves were not calibrated in this study.

McInnes et al. (2002) applied the coastal ocean model GCOM2D, the atmospheric model RAMs, and the spectral wave model WAM, for the east coast of Australia, including the GCS. The GCOM2D model, which was capable of modelling overland flow of flood due to tides and storm surge, has been further developed by McInnes et al. (2002) to incorporate additional physical processes such as wave set up, and riverine runoff. The model has been implemented for the entire Broadwater region and applied for two severe events. First, a tropical low storm (East Coast Low, ECL) event in April 1989, during which severe erosion of the beaches along the Sunshine coast occurred and heavy rainfall produced widespread flooding. Second, tropical cyclone Wanda in January 1974, which resulted in major flooding in Brisbane and the Gold Coast and severe beach erosion along the south Queensland coast. The purpose of their study was to develop an integrated model which included various physical processes that would have contributed to high sea levels and flooding in the Broadwater.

The results concluded that the current speed and direction, as well as the storm surge, wave set up and tides contributed to the sea level heights of the Broadwater and GCS area during these two severe events. The ECL in April 1989 was simulated with a high degree of accuracy (for water levels), and the results showed that wave setup had a greater contribution to the water levels than the storm surge. The January 1974 flood event caused by cyclone Wanda, which occurred prior to the entrance stabilisation, was reasonably well simulated. The results indicated that rainfall can considerably worsen the impact of extreme storm tide events. Therefore, freshwater runoff should be considered in combination with wave setup and storm surge when modelling severe flood event risks in the Broadwater. The results from McInnes et al. (2002) have also shown that deepening the entrance channel after stabilization can minimise flooding when severe runoff is the major contributor. No current velocity calibration was presented in this study (McInnes et al., 2002).

Sennes et al. (2007) developed a 2DH numerical model of the GCS using the Delft 3D to simulate tide and wave induced currents in the GCS under typical wave conditions. The sediment transport pathways and morphological evolution, with and without the sand bypassing system, were compared and investigated qualitatively in a 12 day simulation without any sediment transport calibration. While the results showed a channel infilling problem, they also revealed the effectiveness of the artificial sand bypassing system in reducing erosion in the downdrift beaches. The research also suggested that the entrance stabilisation and the construction of Wavebreak Island decreased the intertidal areas and tidal flats and caused more tidal asymmetry; and as a result the ebb-dominance of the entrance decreased. This resulted in persistent entrance channel infilling problems. In the study by Mirfenderesk and Tomlinson (2007), a depth averaged numerical model using MIKE 21 was developed to understand the tidal characteristic in the Broadwater. The water level in the study area was simulated under the action of tidal forces, with and without wind, and it was confirmed that the current in the Broadwater is semidiurnal, and the effect of wind force is insignificant. However, as explained above, there has been no coupled model comparing the results of the real time morphological simulation of the GCS ebb-tidal delta with the survey data, neither qualitatively nor quantitatively. This thesis aims to address this knowledge gap.

3.5 Summary and Conclusion

There have been several studies investigating the GCS before and after stabilisation. Although the developed training walls and the artificial bypassing system have provided a stabilised and safer navigation channel, the continuous growth of the ebb tidal delta at the river mouth is inducing a growing concern. To retain a safe navigable channel, some dredging at the river

mouth is essential, which is a costly procedure. There have been some conceptual models which have investigated the morphological evolution of the entrance, which have suggested different sources of sediment for the ebb-tidal delta growth. Moreover, some numerical analyses have been developed to study the flow, wave, sediment transport and some schematic morphological evolution in the GCS area. However, there has been no numerical modelling which has simulated and calibrated the morphological evolution of the case study area, either qualitatively or quantitatively under real current and wave conditions. In this study, first, the morphological evolution of the GCS ebb-tidal delta in the past decade is investigated in detail and an updated conceptual model is presented (Chapter 4). Then, in order to gain a better understanding of the governing processes of the ebb-tidal delta morphological evolution, a coupled flow-wave-morphological model has been developed and is presented in Chapters 5 and 6.

4 – Morphological Analysis of the Gold Coast Seaway

4.1 Introduction

In this chapter the morphological evolution of the GCS area is investigated and compared to previous studies. Initially, the GCS equilibrium condition is investigated based on the suggested empirical relationships proposed in previous studies. Then, the morphological evolution of the GCS ebb-tidal delta and channel are investigated, mainly for the past decade. Several sources of data, including bathymetry, dredging, nourishment, flood and wave data, are used for this investigation. A part of the analysis includes a comparison of the results from this research with those of previous studies. Finally, a conceptual model of the sediment transport pattern in the GCS area is suggested.

4.2 Data sources

Hydrographic survey data of the study area was used to investigate the trend of morphological changes of the GCS ebb tidal delta and the adjacent areas. The survey data consisted firstly, of widely-spaced shore normal survey lines (ETA lines) from 1966 to 2014 which covered the area from the GCS to Burleigh Heads, about 18.5 kilometres south of the entrance (Figure A.1, Appendix A). This data was provided by the City of Gold Coast (CGC). These profiles, which have variable temporal and spatial offshore extensions, extend from behind the frontal dune up to two kilometres offshore. The second survey data sets were provided by the Gold Coast Waterways Authority (GCWA) and were detailed survey data of the entrance with variable extensions to the north and south from 1989 to 2015. The GCWA data sets mainly covered the ebb-tidal delta area and the GCS channel.

CGC survey data was used to analyse the evolution of the shoreline, mainly south and only partially north of the GCS, to an extent of about two kilometres offshore in Appendix A. This was because there was limited data available for the few survey lines north of the entrance. The GCWA data was used to assess the morphological evolution of the GCS ebb-tidal delta as well as its channel. The GCWA data's horizontal and vertical datum were not the same for all data sets; therefore, they were converted to a consistent format first. Gday software was used to convert the data with the AGD84 horizontal datum to GDA94, and tidal tables for various years were applied to convert the vertical datum to Australian Height Datum (AHD).

In addition to the bathymetry data, the artificial sand bypassing, nourishments and dredging volumes provided by GCWA, and major flooding events dates provided by CGC; were used in the analysis of the morphological evolution. Although the development of the ebb-tidal delta was the major focus of this study, a brief examination of the adjacent beach processes was also required. Therefore, a brief analysis of the morphological evolution of the shoreline based on available survey data is presented in Appendix A.

4.3 Analysis of the morphological evolution of the GCS ebb-tidal delta

Analysis of the morphological evolution of the GCS was carried out in four stages. First, the suggested empirical relationships for tidal inlets in equilibrium were examined for the GCS. Second, using detailed survey data of the area, the whole ebb-tidal delta area and inlet channel were defined and their volumetric changes were investigated and compared to the results obtained from previous studies. In addition, the possible sources of sand for the ebb-tidal growth were discussed, considering the wave condition, sand bypassing volumes, dredging and current in the inlet channel. Third, the validity of the resultant hypothesis for the possible sources of sand was tested utilising estimation of wave energy during storm events. Fourth, in order to better understand the pattern of the morphological evolution in the ebb-tidal delta, it was divided into nine sub-areas and the morphological evolution of each sub-area was analysed. Following these four stages, a new conceptual model for the trend of morphological evolution of the ebb-tidal delta was presented. All of these steps are explained in detail in the following sections (4.3.1, 4.3.2, 4.3.3, 0 and 4.4).

4.3.1 Examining the GCS dynamic equilibrium

A tidal inlet reaches a dynamic equilibrium when there is a balance between the tidal prism, which tends to increase the channel cross-sectional area, and the volume of sediment transported to the inlet by waves and currents, which tends to reduce the inlet cross sectional area (Kieslich, 1981). A number of empirical relationships between an inlet tidal prism, cross sectional area, LST and volume of the ebb-tidal delta have been suggested (Heath, 1975; Bruun et al., 1978; O'Brien, 1969; Walton and Adams, 1976; Brunn, 1986) for stable inlets or the ones in a state of dynamic equilibrium. The term "stable" means relatively little change over long periods in the morphodynamic context (Bruun, 1986).

4.3.1.1 Tidal prism versus flow cross sectional-area (*P* – *A*) relationships

There are a number of empirical relationships suggested between the flow cross sectional area and the inlet tidal prism for tidal inlets in equilibrium. A number of these relationships, the regions of their studied inlets and their characteristics are shown in Table 4.1. There are some studies which suggested general relationships for all tidal inlets as well as more specific relationships for dual-jettied tidal inlets, such as those of Jarrett (1976) and O'Brien (1969) . The dual-jettied relationships of these studies are included in this table since GCS is a dual-jettied tidal inlet. In these relationships, A_c is the minimum flow cross section of the entrance channel (throat) measured below mean sea level (MSL) (m^2), and P is the tidal prism corresponding to the spring range of tide (m^3).

Table 4.1. Tidal inlet spring tidal prism and minimum cross-sectional area empirical relationships in metric units

Empirical Relationship	Reference	Inlet location	Characteristics	
$A_c = 9.015\times10^{-4}(P)^{0.85}$	O'Brien (1969)	Pacific coast in the USA	Dual-jettied inlets; tidal prism ranges from 3.1×10^5 to 1.1×10^9 m^3	(4.1)
$A_c = 1.584\times10^{-4}(P)^{0.95}$	Jarrett (1976)	Atlantic coast in the USA	19 Dual-jettied inlets; tidal prism ranges from 8.5×10^6 to 1.4×10^9 m^3	(4.2)
$A_c = 1.015\times10^{-3}(P)^{0.85}$	Jarrett (1976)	Pacific coast in the USA	15 Dual-jettied inlets; tidal prism ranges from 9×10^6 to 4.3×10^8 m^3	(4.3)
$A_c = 5.059\times10^{-5}(P)^{1.02}$	Heath (1975)	New Zealand	16 inlets; tidal prism at spring tides ranges from 1.5×10^7 to 2×10^9 m^3	(4.4)

There are other analytical-empirical relationship forms between A_c and P, such as that of Hughes (2002) (equation (4.5)), in which additional physical parameters of the inlet have been included:

$$A_c = 0.87\left[\frac{W^{1/9}}{[g(S_s-1)]^{4/9} d_{50}{}^{1/3} T^{8/9}}\right] P^{8/9} \tag{4.5}$$

where W is the equilibrium channel width, T is the tidal period, d_{50} is the median grain-size diameter, and S_s is sediment specific gravity. This equation is dimensional homogeneous, which means they can be applied using any consistent set of units. Hughes (2002) noted that this relationship closely resembles the equations of O'Brien (1969) and Jarrett (1976). The data from 102 tidal inlets from around the US showed good correspondence with this equation. However,

most of the equilibrium cross sectional areas were found to be larger than the minimum predicted by equation (4.5). This was suggested to be caused by different primary flow channels during ebb and flood tide in some of the inlets, which means a portion of the cross-section carries less than the maximum discharge (Hughes, 2002).

To examine the equilibrium of the GCS the values of A_c and P are required. Estimation of the GCS basin area for calculation of the inlet tidal prism is a complicated task due to the connection of the Broadwater to the southern Moreton Bay and in particular the close relative location of the Jumpinpin inlet. Thus, a calibrated hydrodynamic model of the study area, which will be explained in chapter 5, was used to calculate the inlet tidal prism during a spring tide. From the model results, the cumulative discharge entering the inlet during the spring tide in May 2009 was calculated. The resultant tidal prism was about $60.8\times10^6\ m^3$, which was close to the one calculated by Mirfenderesk and Tomlinson (2008) ($66\times10^6\ m^3$) for 2005. The minimum cross sectional area, based on the survey data provided by GCWA in June 2009, was 2807 m^2. The A_c values were calculated by substituting $60.8\times10^6\ m^3$ for P in the equations in Table 4.1. It was also calculated by substituting $W = 260m$, $T = 50400\ s$, $d_{50} = 2 \times 10^{-4}m$, $S_s = 2.65$, and P in equation (4.5). The results are shown and compared to the measured A_c in June 2009 (Figure 4.1). As illustrated, the June 2009 cross sectional area is smaller than the suggested values for a stable tidal inlet, which suggests that the inlet channel have a net erosional pattern until it reaches an equilibrium condition.

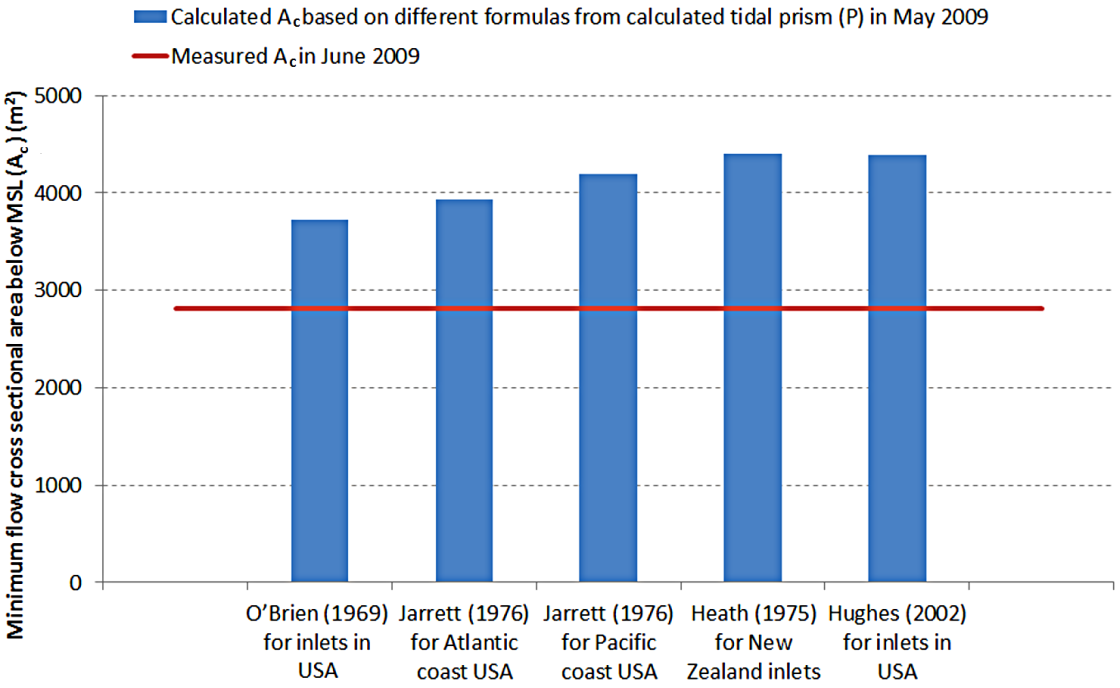

Figure 4.1. Calculated minimum inlet cross sectional area below MSL (A_c) using different empirical formulas based on the calculated tidal prism (P) in May 2009 and comparison with the measure A_c in June 2009

It should be noted that the LST reaching to the throat of the GCS inlet was reduced by the artificial sand bypassing system, and several studies, such as that of Kraus (1998) suggested that reduced LST results in a larger cross-sectional area for the same tidal prism. This is due to the fact that less material has to be removed from the inlet flood or ebb bars during each tidal cycle and relatively higher tidal energy remains for expanding the inlet area. On the other hand, Bruun et al. (1978) and Van der Wegen et al. (2010) suggested that dual-jettied inlets tend to require smaller cross-sectional areas than free inlets to convey the same tidal prism. This is because of their relatively deep cross-sectional areas which reduce the role of friction on the flow and therefore, lead to a more efficient flow.

4.3.1.2 Tidal prism versus volume of ebb-tidal delta (*P-V*) relationship

Marino and Mehta (1987b) suggests that the ebb-tidal delta volume of an inlet depends on the inlet spring tidal prism, inlet aspect ratio (width to depth), flow cross sectional area and tidal amplitude. Moreover, Walton and Adams (1976) suggested that the ebb-tidal delta volume for an inlet in a state of dynamic equilibrium can be correlated with the inlet spring tidal prism. Their study was based on 44 inlets in the USA, and they defined different constants for their proposed empirical formula based on an approximate quantitative description of the energy potential available at the inlet to modify the ebb-tidal delta. The value of $H_m^2 T_{mean}^2$ (where H_m is

the average wave height in metres and T_{mean} is the mean wave period in seconds) was used as a basic measurement of the wave energy to classify energy environments (Table 4.2). Using this classification, the GCS coast is classified as a 'moderately exposed coast', and the volume of sand stored in its ebb-tidal delta (V) in cubic metres, assuming that it has reached a dynamic equilibrium, can be calculated based on its tidal prism (P) using equation (*4.6*) (Walton and Adams, 1976) .

$$V = 8.03\times10^{-5}(35.3P)^{1.23} \tag{4.6}$$

Table 4.2. Clasification of coaslines by wave energy (Walton and Adams, 1976)

$H_m^2 T_{mean}^2$	**Energy category**
0 – 30	Mildly exposed coast
30 – 300	Moderately exposed coast
> 300	Highly exposed coast

Hicks and Hume (1996) studied 17 ebb-tidal deltas off natural inlets on the New Zealand North Island coast. They suggested that the main controls on the ebb-tidal delta volume are the tidal prism (P), the angle between the inlet channel (outflow jet) and the shoreline ($\theta_{i,s}$), and the wave climate. They suggested an empirical equation for the volume of sand trapped in the ebb-tidal delta as follows:

$$V = 1.37\times10^{-3}P^{1.32}(\sin\theta_{i,s})^{1.33} \tag{4.7}$$

To assess the total volume of the ebb-tidal delta above natural bathymetry in the defined ebb-tidal delta area at the GCS (Figure 4.2a), a natural (inlet free) bathymetry was produced (Figure 4.2b) based on the bathymetry of the nearshore area updrift and downdrift of the inlet. Then, survey data of June 2009 was compared to the no inlet bathymetry, and the resultant volume was calculated to be 11.64×10^6 m^3. The equilibrium volume of the ebb-tidal delta was also calculated by applying previously calculated P in May 2009 (60.8×10^6 m^3) and $\theta_{i,s} \approx 105^\circ$ in equations (*4.6*) and (4.7). The resultant volume (V) was 24.14×10^6 and 24.63×10^6 m^3 respectively. These are much higher than the actual volume of the ebb-tidal delta in June 2009. This suggests a dominant depositional trend in the GCS ebb-tidal delta for the coming years.

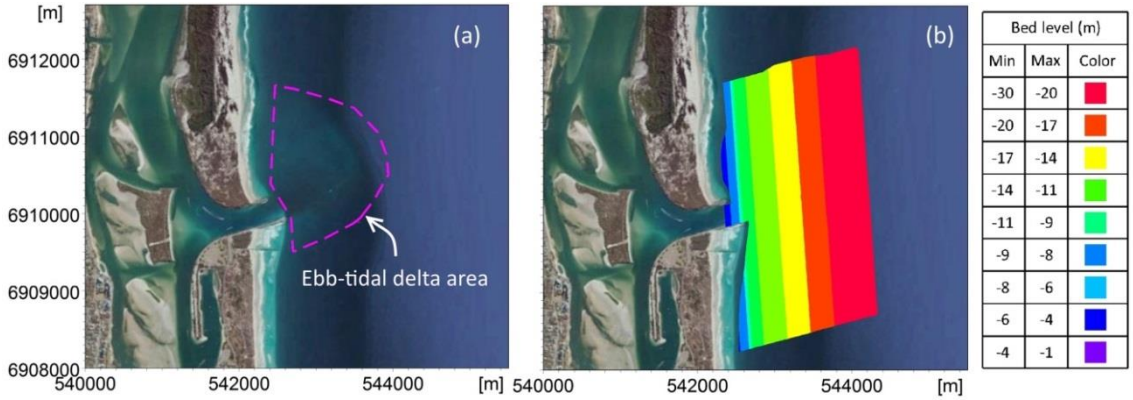

Figure 4.2. (a) Defined ebb-tidal delta area (b) Assumed "natural" (no inlet) bathymetry based on the morphology of adjacent beaches

4.3.2 Volumetric analysis of the ebb-tidal delta and the inlet channel

In order to understand the morphological evolution pattern of the GCS ebb-tidal delta during the past decade, hydrographic survey data from GCWA were used. Some of the available sets did not cover the whole ebb-tidal delta area. Therefore, 12 data sets which covered the desired area were selected. These 12 data sets for the analysis covered a period of 11 years from January 2004 to April 2015. The sets in a year/month format were as follows: 2004/01, 2004/07, 2005/07, 2007/04, 2008/08, 2009/06, 2010/07, 2011/03, 2012/03, 2012/09, 2013/07, 2015/04. In addition to these 12 data sets, survey data for December 1997, which encompassed the major portion of the defined ebb-tidal delta, was also used to provide a link between the analysis of the WRL and GCCM (1998) to the current study (Figure 4.3). The resultant bathymetries from the 12 data sets are presented in Figures 4.4 and 4.5.

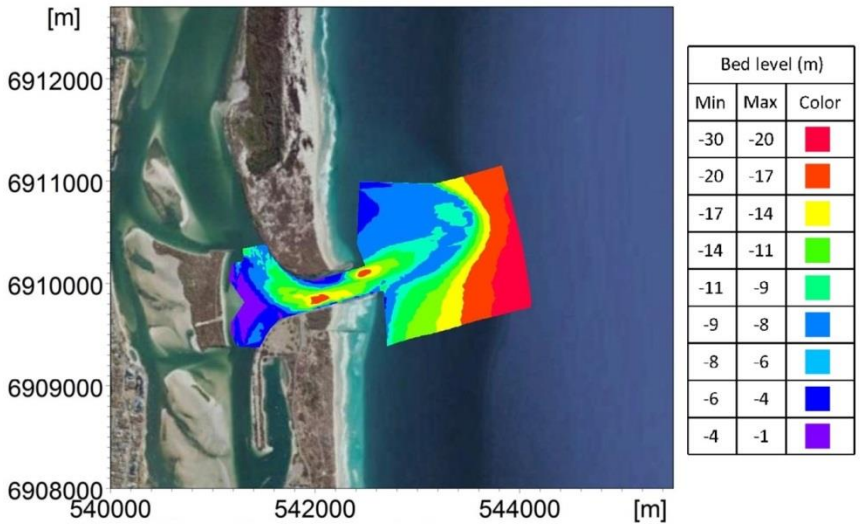

Figure 4.3. December 1997 bathymetry

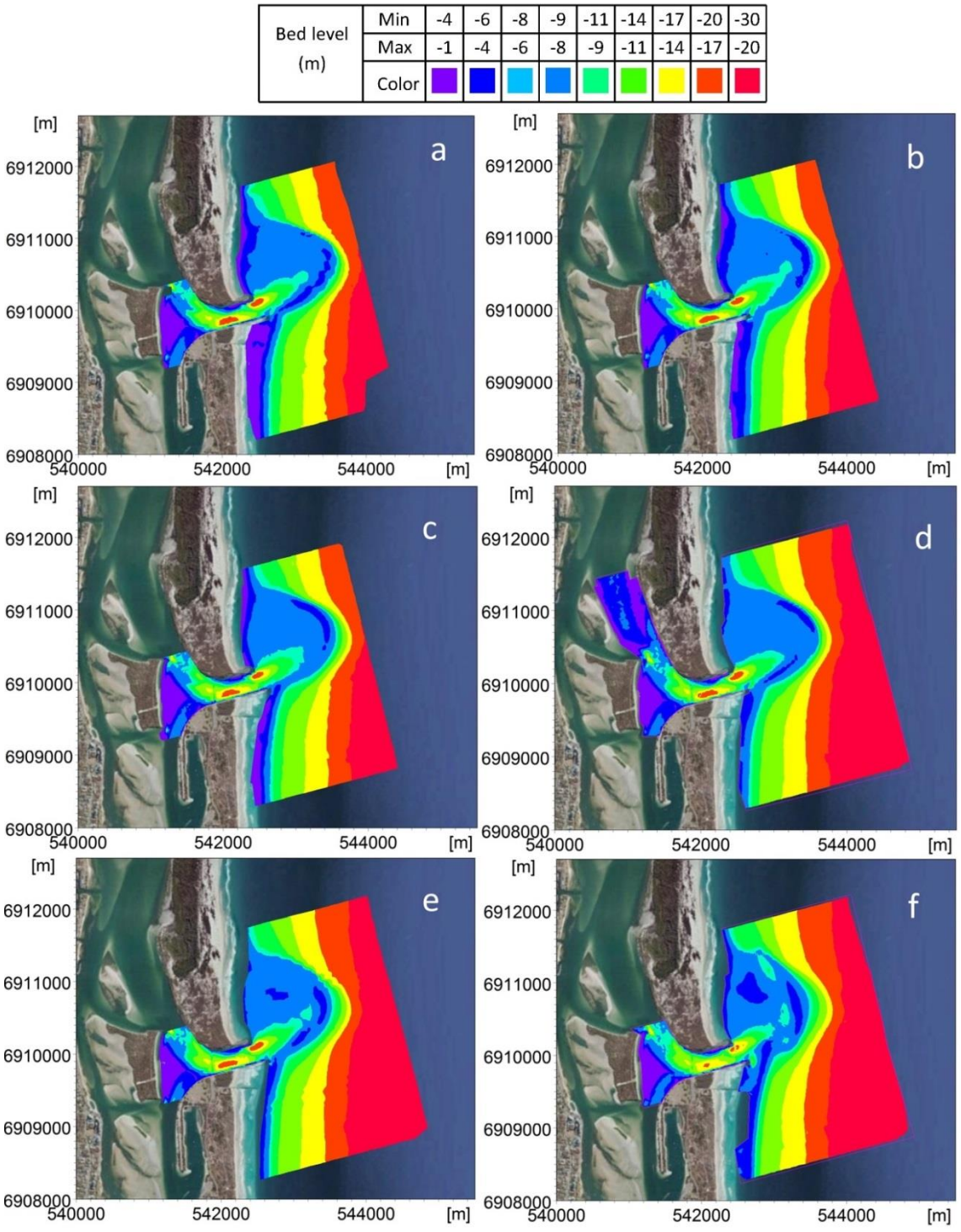

Figure 4.4 Generated bathymetries from GCWA survey data (a) January 2004 (b) July 2004 (c) July 2005 (d) April 2007 (e) August 2008 (f) June 2009

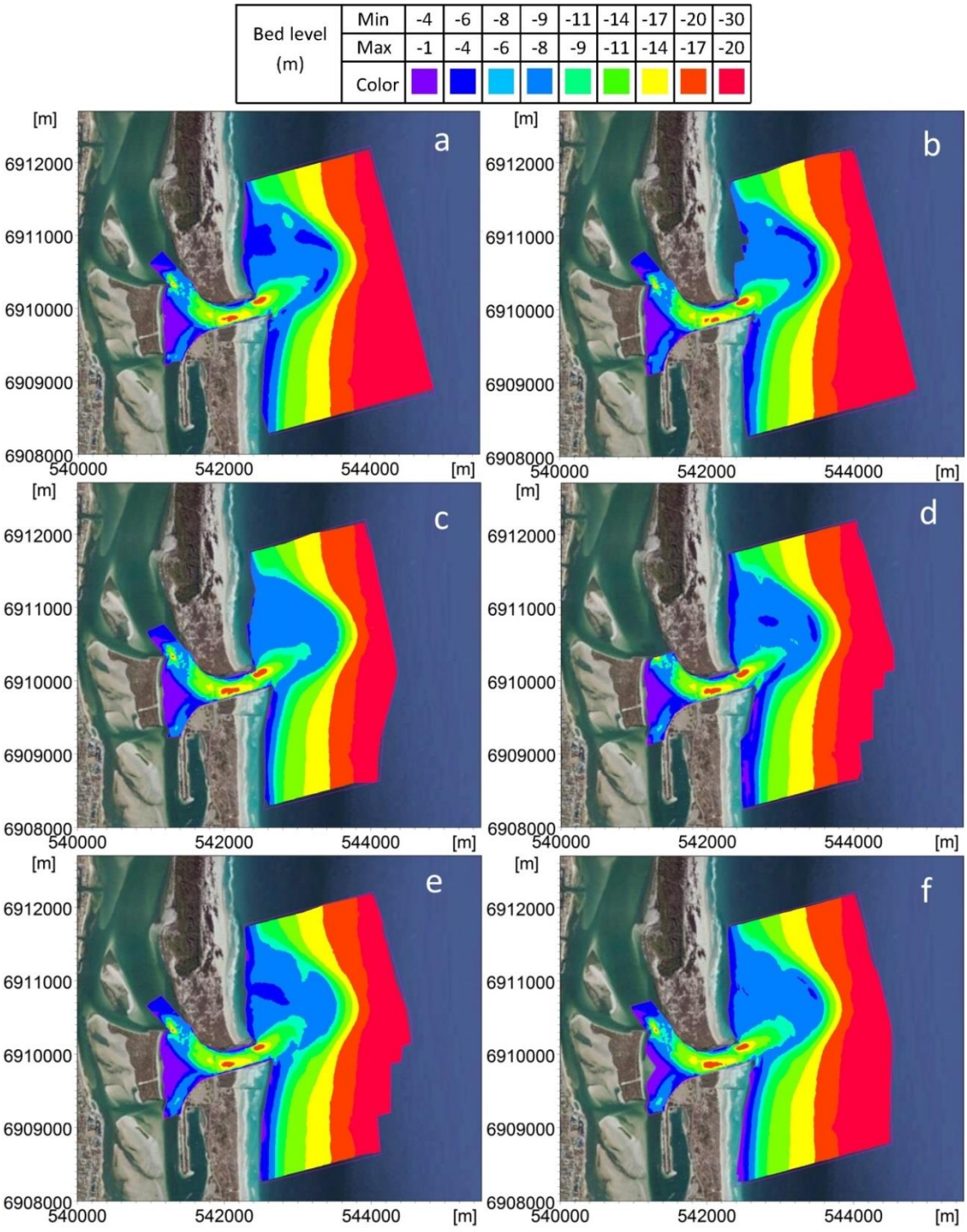

Figure 4.5. Generated bathymetries from GCWA survey data (a) July 2010 (b) March 2011 (c) March 2012 (d) September 2012 (e) July 2013 (f) April 2015

Volumetric analysis was undertaken based on the shared survey area of the selected data sets. First, the area of the ebb-tidal delta for volumetric analysis was defined based on the area with active morphological evolution from January 2004 to April 2015 (Figure 4.6, region A1). The shared inlet channel area was also defined to be used for analysis of the inlet channel volumetric

changes as a possible source or sink of sand (region A2 in Figure 4.6). To calculate the total volumetric change, each set was compared to the following set and the resultant bathymetry changes are shown in Figures 4.7 and 4.8.

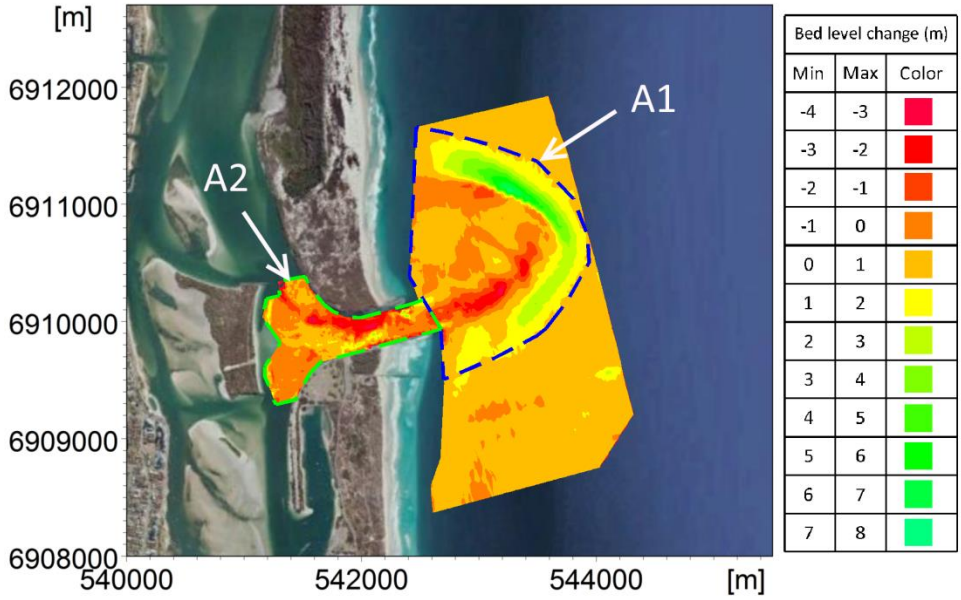

Figure 4.6. Morphological evolution of the GCS, on the offshore extension of the GCWA survey data, from January 2004 to April 2015. Region A1 is defined as the area of ebb tidal delta, and region A2 is the GCS channel

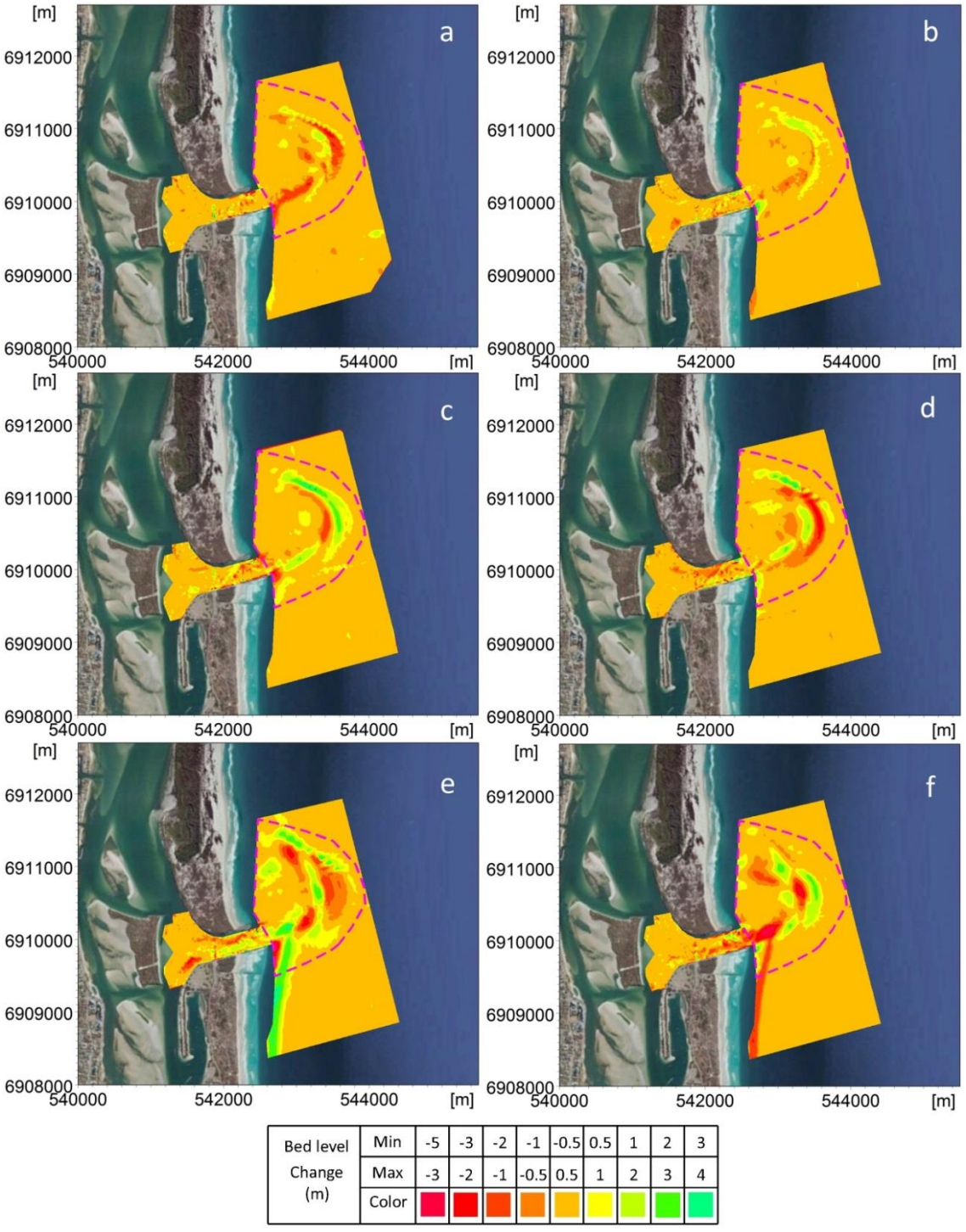

Figure 4.7. Bed level changes in the survey data intervals (a) January 2004 to July 2004 (b) July 2004 to July 2005 (c) July 2005 to April 2007 (d) April 2007 to August 2008 (e) August 2008 to June 2009 (f) June 2009 to July 2010 (Positive values mean deposition and negative values mean erosion)

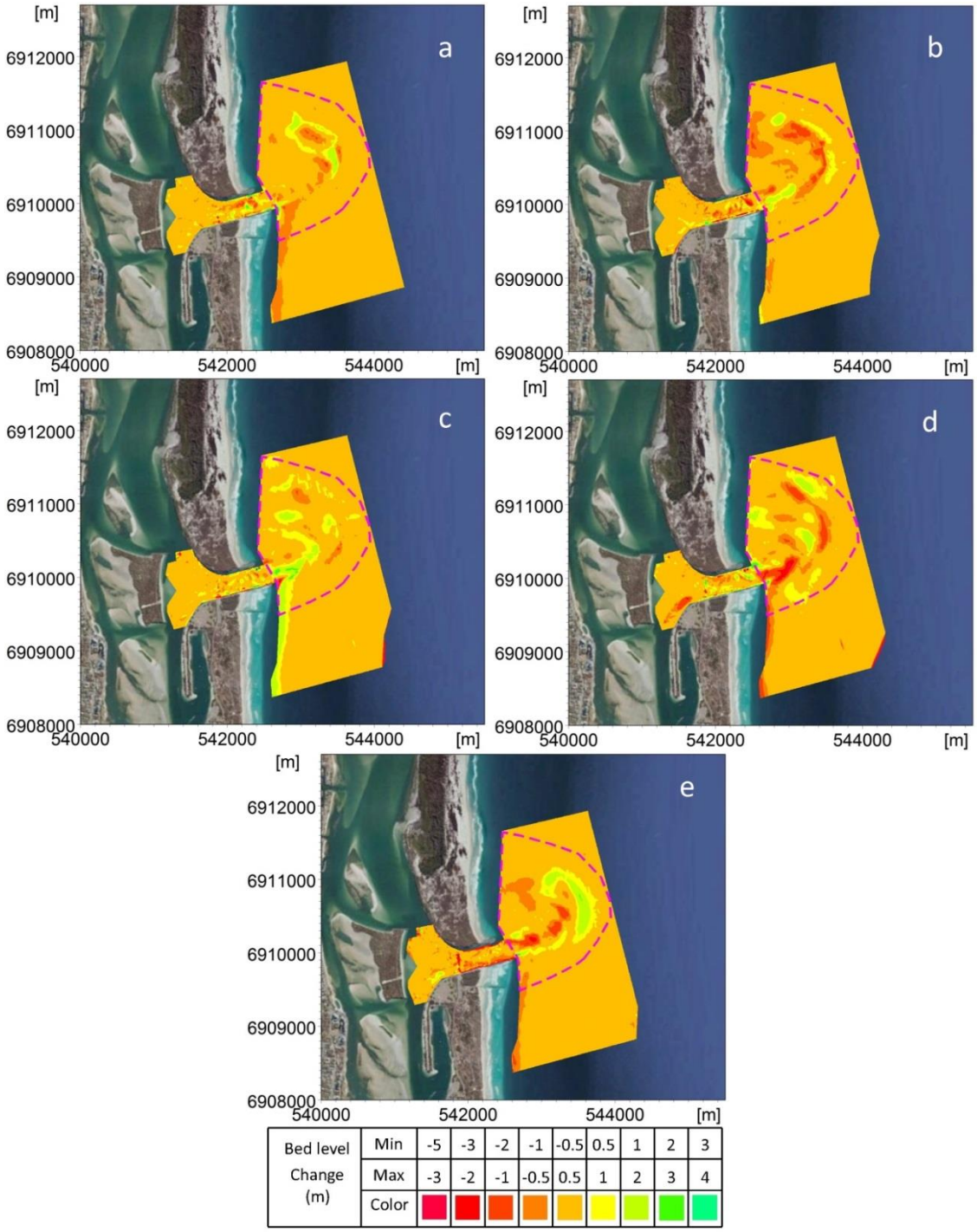

Figure 4.8. Bed level changes in the survey data intervals (a) July 2010 to March 2011 (b) March 2011 to March 2012 (c) March 2012 to September 2012 (d) September 2012 to July 2013 (e) July 2013 to April 2015 (Positive values mean deposition and negative values mean erosion)

Once the volumetric changes of the ebb-tidal delta from 2004 to 2015 were calculated; the results were used to supplement those of the WRL and GCCM (1998) study, which presented the volumetric analysis of the ebb-tidal delta from October 1984 to March 1997. The March 1997 data set, used in the WRL and GCCM (1998) study, was not available. Therefore, in order

to link the results from this study to the WRL and GCCM (1998) study, a relatively good quality survey data closest to the most recent WRL and GCCM (1998) study date was required. Thus, the survey data of December 1997 was used and the volumetric change of the ebb-tidal delta between December 1997 and January 2004 was estimated. Since the December 1997 survey data did not include the northern portion of the defined ebb-tidal delta area (A1 in Figure 4.6), this volume was enlarged relatively to maintain consistency. The cumulative volume of the ebb-tidal delta of December 1997 compared to March 1997 (last data set in the study of WRL and GCCM (1998)) was estimated based on the trend of volumetric changes of previous years. It should be noted that the defined area of the ebb-tidal delta in WRL and GCCM (1998) (region E in Figure 3-11, Chapter 3) was smaller than the one used in this study (region A1 in Figure 4.6). However, since it included the major portion of the active ebb-tidal delta during that time, the overall trend of the ebb-tidal delta volumetric change can be taken as being sufficiently reliable for the purpose of this study.

The trend of the ebb-tidal delta cumulative volume evolution since 1984 is shown in Figure 4.9. The first two parts of the graph were extracted from the WRL and GCCM (1998) report. The results show that the ebb-tidal delta grew at an average rate of 12,500 $m^3/month$ or 151,000 m^3/yr from October 1984 to April 2015, despite the continuous artificial sand bypassing at an average rate of 570×10^3 m^3/yr from January 1987 to December 2014 based on data provided by GCWA. This continuous growth confirms that the ebb-tidal delta had not reached an equilibrium volume, as mentioned in section (4.3.1.2). The only dredging from the ebb-tidal delta area (region A1 in Figure 4.6) since 1985 was a dredging program from May 2011 to Mar 2012 which removed 260,000 m^3 and then a further 66,000 m^3 from March 2012 to December 2012 (based on data provided by GCWA). This dredging is the main reason for the significant drop of about 365,000 m^3 in the volume of the ebb-tidal delta for the March 2011-March 2012 interval as illustrated in Figure 4.9.

As shown in Figure 4.6, the growth of the ebb tidal delta is concentrated on the offshore side of the delta. The more northward orientation of the growth is due to the dominant northward longshore current owing to the prevailing wave action. The ebb-tidal delta volumetric analysis from February 1993 to March 1997 (last data point of WRL report in Figure 4.9) in the WRL and GCCM (1998) report was dependent on the seaward extension of the survey data sets supplied by GCWA. The seaward extensions of these data sets were less than the ones used in this study, which explains the suggested decreased rate of ebb-tidal delta growth for 1992 to 1998 (75,000 m^3/yr) in the WRL and GCCM (1998) study.

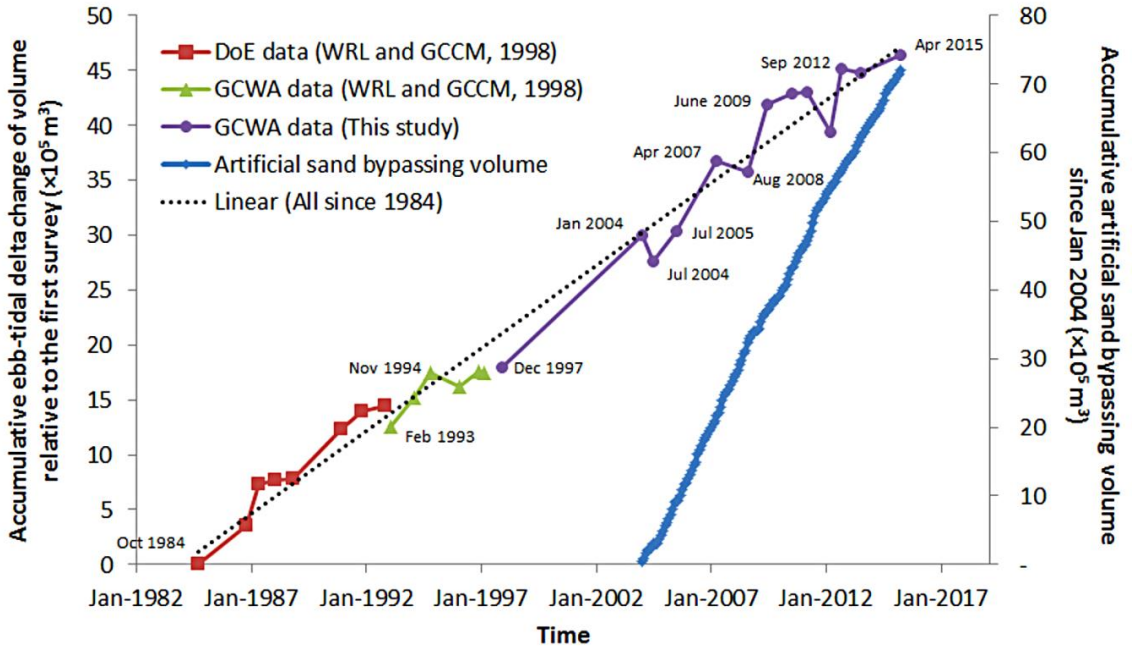

Figure 4.9. Cumulative volume of the ebb-tidal delta since 1984 based on Department of Environment (DoE) and Gold Coast Waterways Authority (GCWA) survey data (left graphs); cummulative artificial sand bypassing volume since January 2004 (right graph)

There are several sand sources that may have supplied the sand for the ebb-tidal delta growth. As mentioned in Chapter 3 (3.3.2), since the stabilization, the GCS channel (region A2 in Figure 4.6) has continued to scour well beyond its designed depth (5.5*m*) during past decades (Mirfenderesk and Tomlinson, 2009). Since the tidal current in the GCS channel was found to be ebb dominated (Mirfenderesk and Tomlinson, 2008; Sedigh et al., 2016), it can be concluded that the eroded sand was transported to the ebb-tidal delta by the ebb tidal flow jet, contributing to the growth of the delta. Figure 4.10 shows the trend of the cumulative morphological changes in the GCS channel since 1984. The defined area of the inlet channel was approximately the same for both the WRL and GCCM (1998) study (regions C and F in Figure 3.11, chapter 3) and the current study (region A2 in Figure 4.6). The continuous net scouring of the inlet channel confirms that it had not reached an equilibrium state, as suggested in section 4.3.1.1. It should be noted that there were some dredging activities in this area. The first one was a major dredging of the whole GCS and the northern and southern channels at the time of the GCS construction in 1985. There were two other recorded dredgings specifically within the inlet channel (region A2 in Figure 4.6). These included 15,000 m^3 in 2009 and about 65,000 m^3 in 2013. The second dredging has contributed to the major drop (erosion) from July 2013 to April 2015 shown in Figure 4.10. Including the dredging activities, the average rate of the inlet erosion from October 1984 to April 2015 was about 2,600 $m^3/month$ or 31,000 m^3/yr, which is about 20% of the average accretion rate in the ebb-tidal delta.

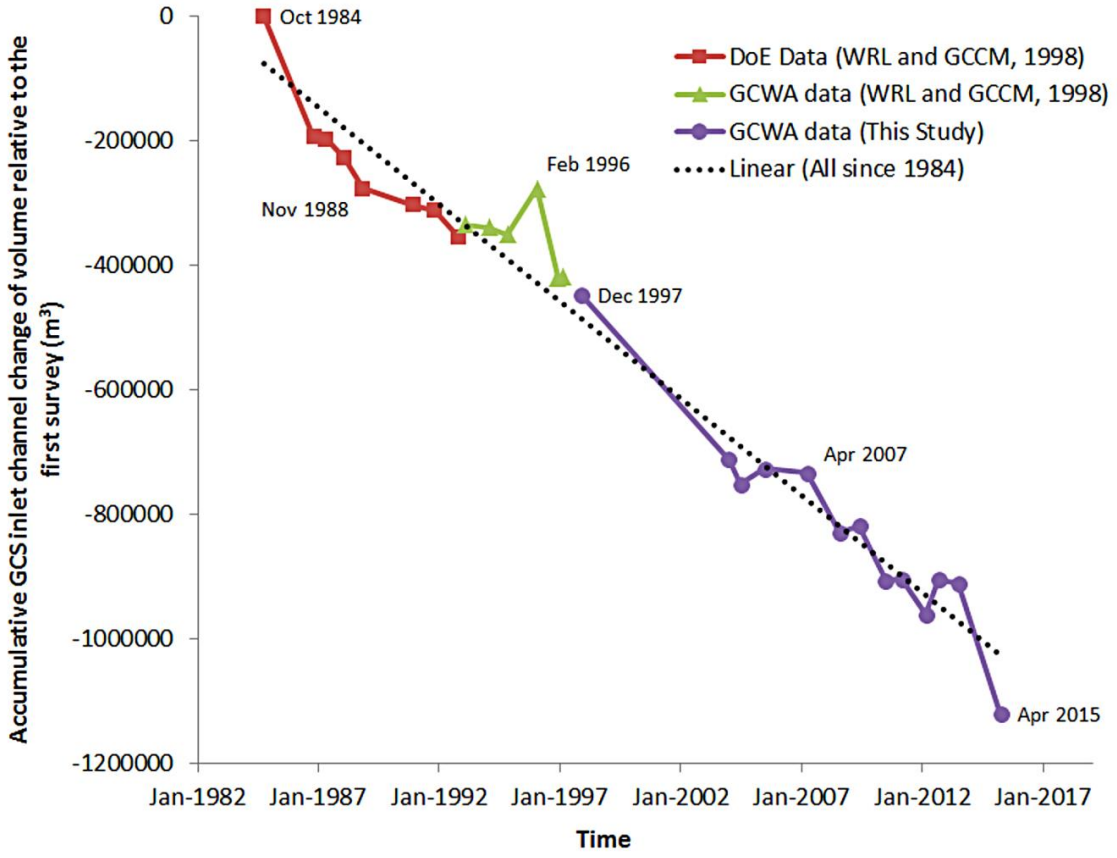

Figure 4.10. Cumulative volume of the GCS Channel (A2 in Figure 4.6) since 1984 based on Department of Environment (DoE) and Gold Coast Waterways Authority (GCWA) survey data.

The other source of sand to the ebb-tidal delta could be the sand transported from within the estuary offshore. An analysis by Mirfenderesk and Tomlinson (2009) has shown a flood-dominant tidal regime within the estuary of the Nerang River (Broadwater), and has suggested that any eroded sand in the Broadwater channels will remain in the estuary. However, their study has also shown that the estuary has become less flood-dominant in the past two decades. It was suggested that as a result, more sand might be transported out of the estuary compared to previous years. For a more detailed study of the morphological evolution of the Broadwater and its effects, subsequent survey data of the whole estuary is required, which is not available at this stage.

Another source of sediment for the ebb-tidal delta was suggested to be from the leakage of the dominant wave-induced northward LST offshore the sand-bypassing system and the southern training wall. To investigate the existence of any relationship between the wave conditions, which this leakage originated from, and the morphological changes of the ebb-tidal delta from January 2004 to April 2015, measured wave data for this period were considered. The measured wave data at the Gold Coast offshore wave buoy, located about one kilometre offshore with a water depth of about 17 metres and about 3.5 kilometres south of the entrance (Figure 4.11),

was used. The significant wave height, peak wave direction, and wave roses at the Gold Coast Buoy for the survey intervals are shown in figures 4.12 to 4.15. However, since wave directions were not recorded at the Gold Coast Buoy prior to July 2007, for the time intervals before then, the recorded wave directions at the Brisbane buoy (Figure 4.11) were applied in Figure 4.12.

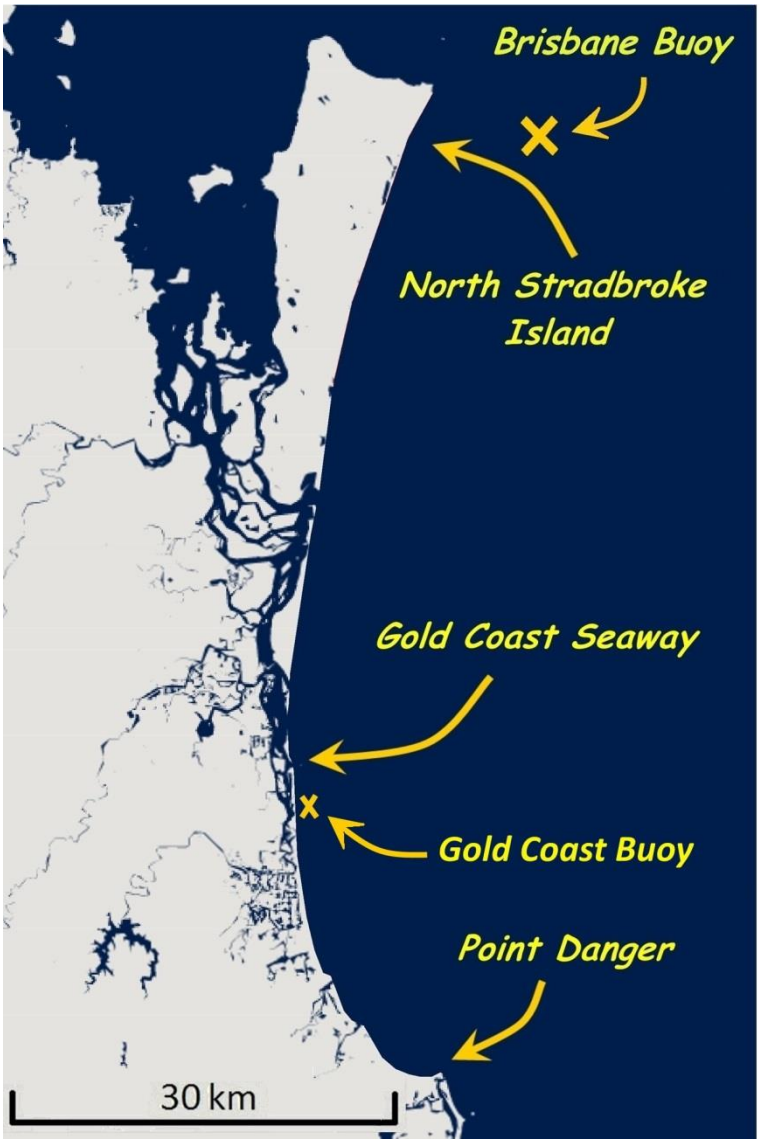

Figure 4.11. Gold Coast (Southport) and Brisbane buoy locations

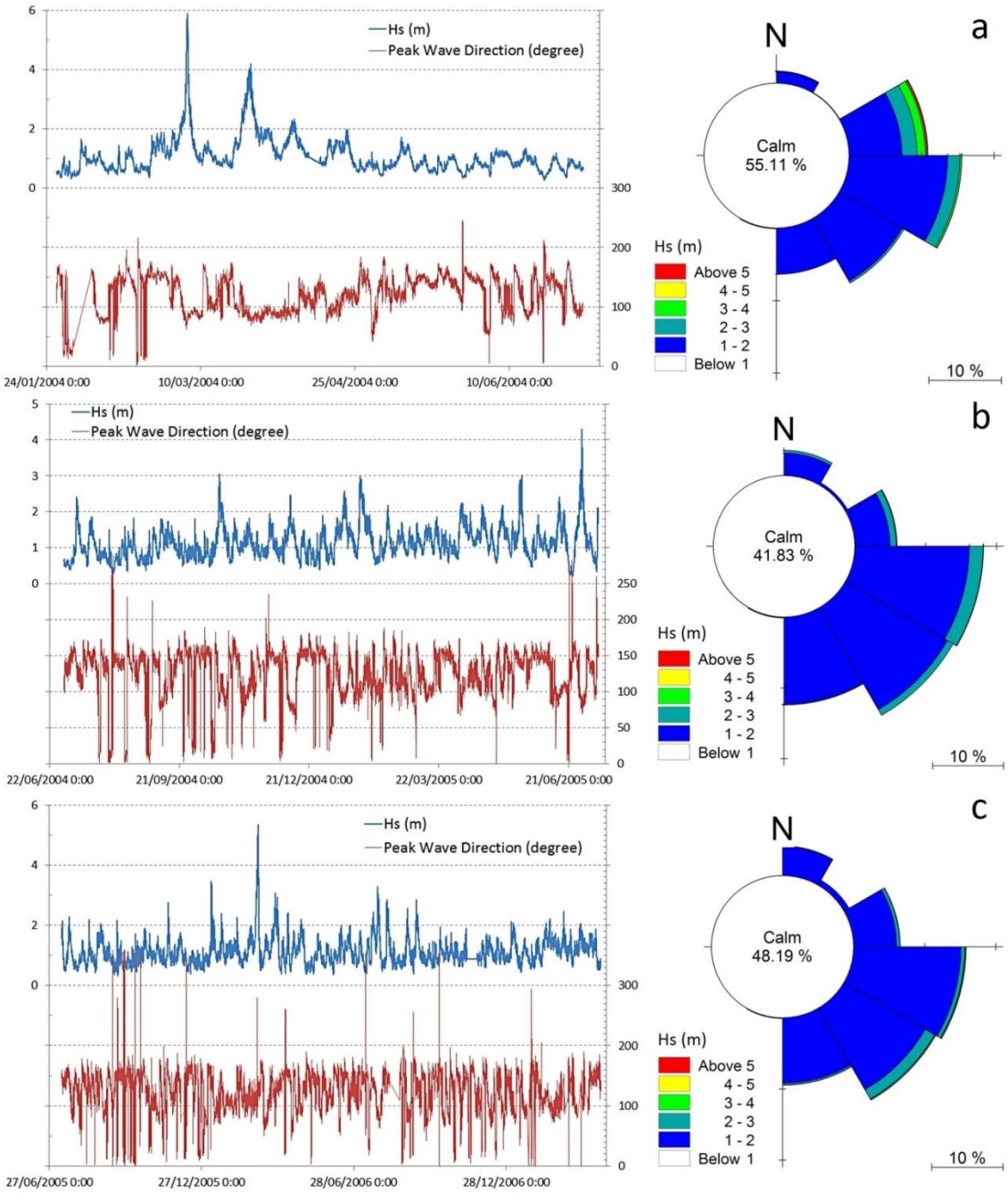

Figure 4.12. Significant wave height and peak wave direction time series and wave roses (a) January 2004 to July 2004 (b) July 2004 to July 2005 (c) July 2005 to April 2007 time intervals

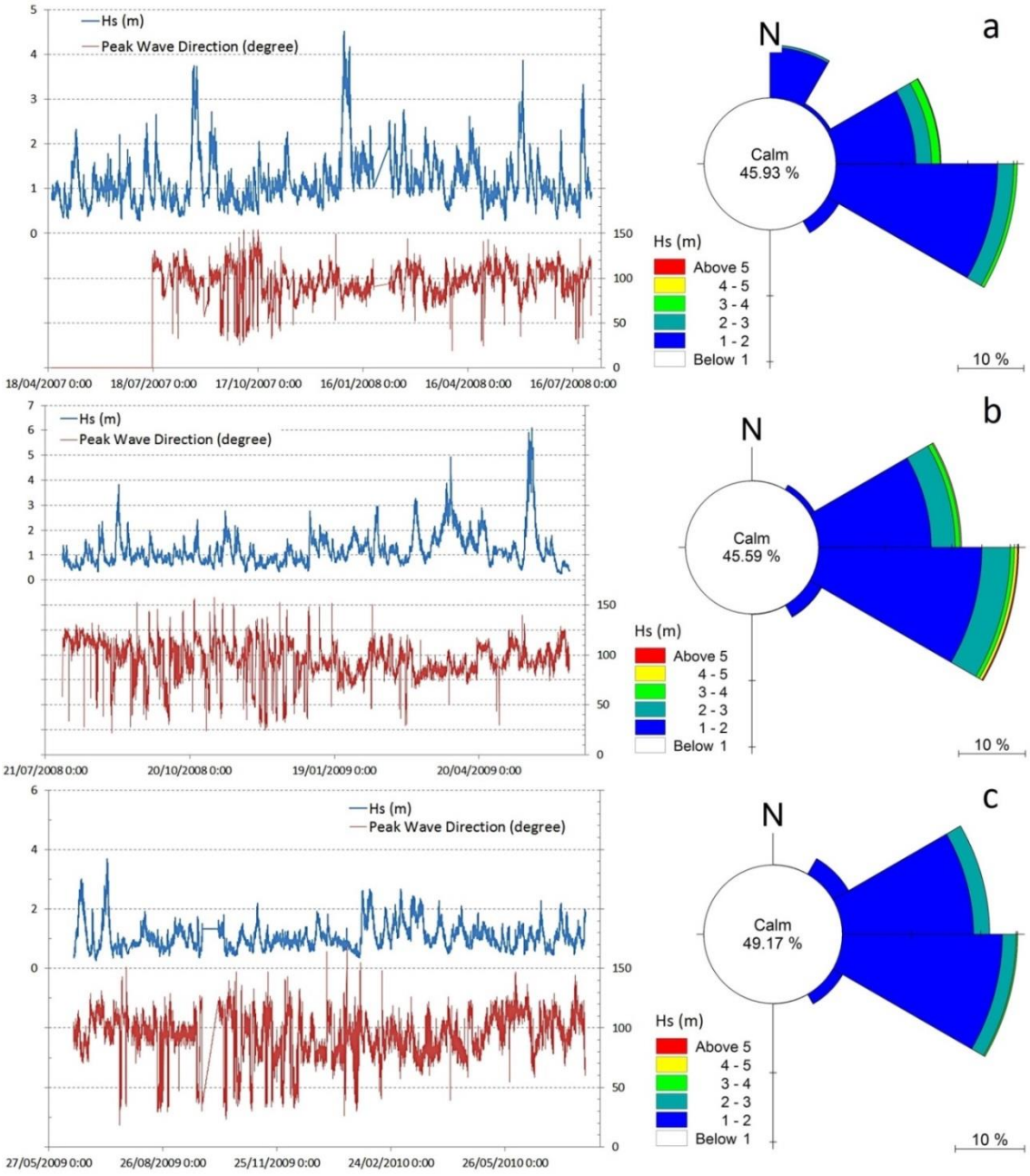

Figure 4.13. Significant wave height and peak wave direction time series and wave roses (a) April 2007 to August 2008 (b) August 2008 to June 2009 (c) June 2009 to July 2010 time intervals

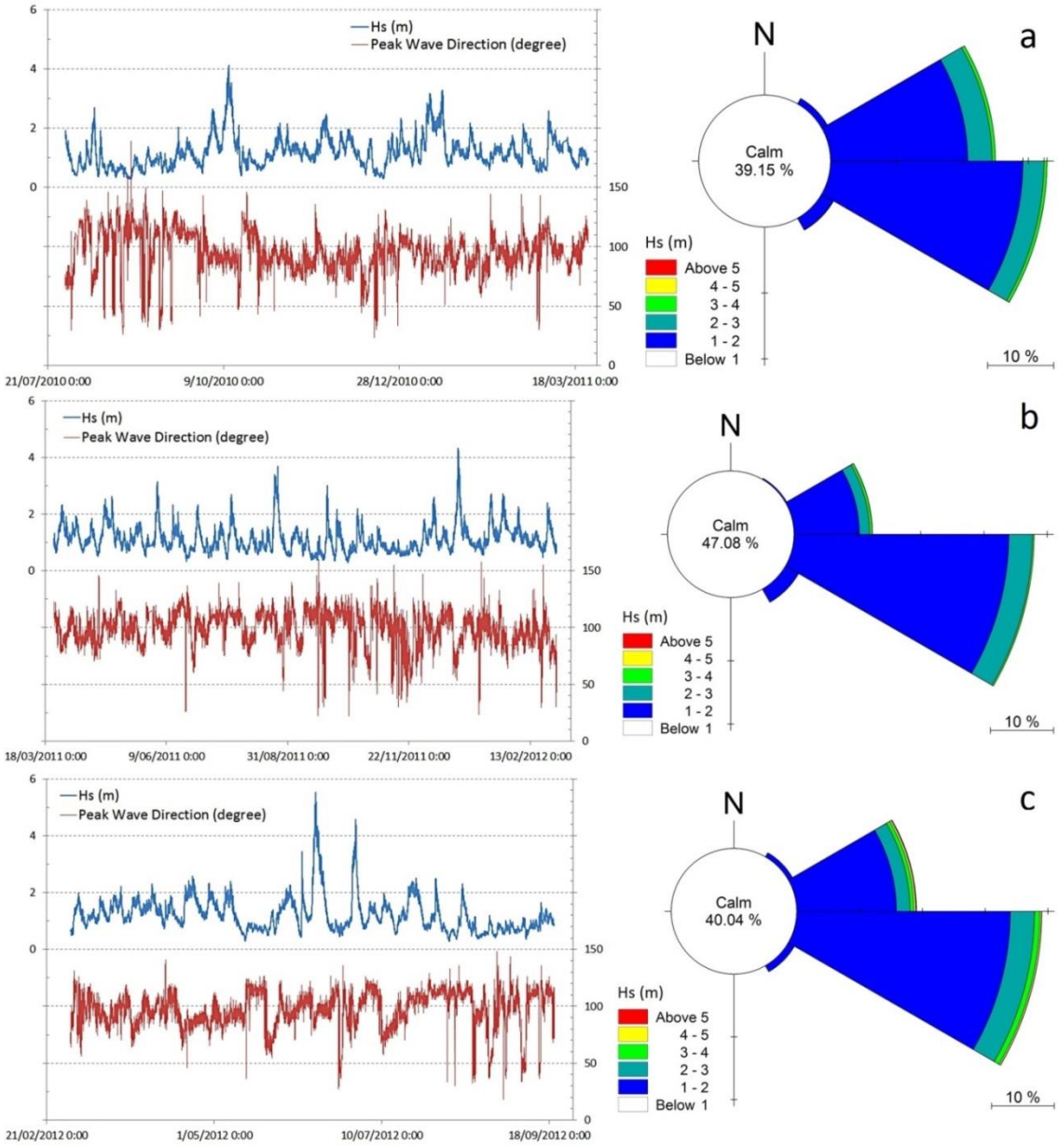

Figure 4.14. Significant wave height and peak wave direction time series and wave roses (a) July 2010 to March 2011 (b) March 2011 to March 2012 (c) March 2012 to September 2012 time intervals

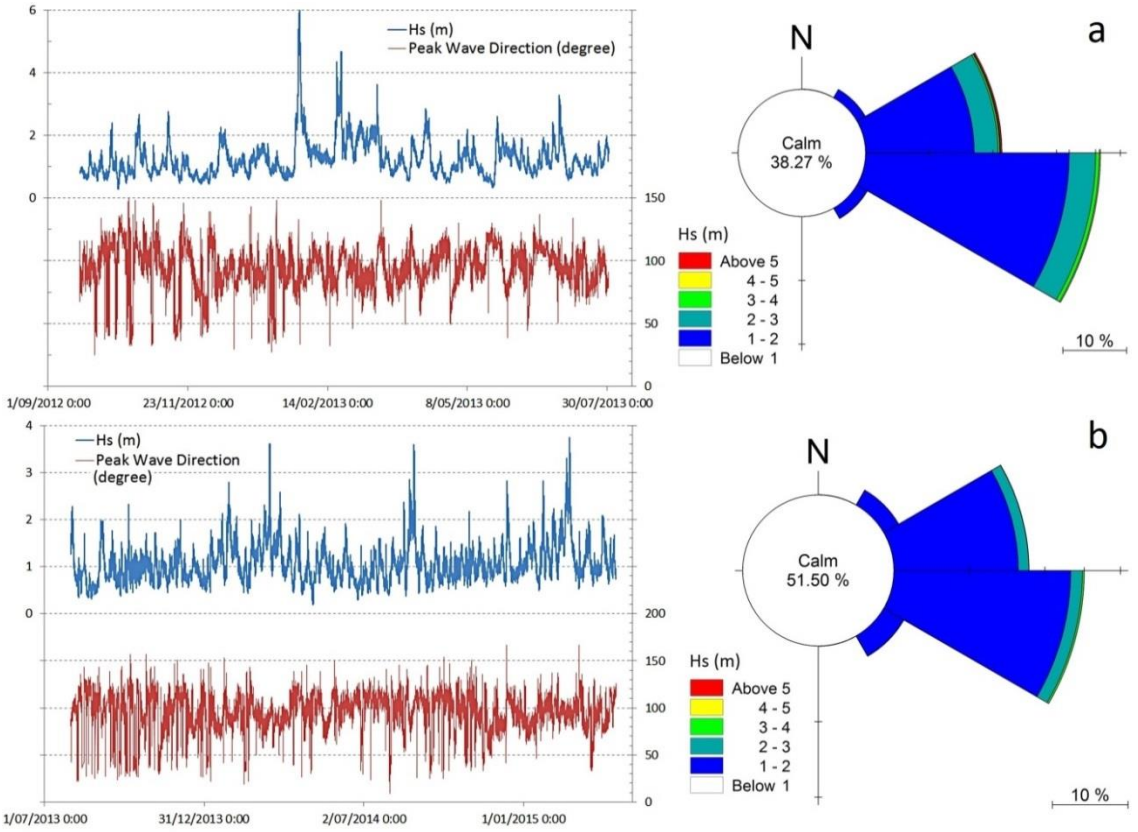

Figure 4.15. Significant wave height and peak wave direction time series and wave roses (a) September 2012 to July 2013 (b) July 2013 to April 2015

Analysis of the ebb-tidal delta morphological changes in the survey intervals from 2004 to 2015 (Figure 4.9), along with the recorded wave data at the Gold Coast buoy (Figures 4.12 to 4.15), suggests that this leakage rate should have been significant during the intervals with major SE storm events. This will be examined in more details in section 4.3.3. Three of the intervals with significant accretion in the ebb-tidal delta area are July 2005-April 2007, August 2008-June 2009 and March 2012-September 2012 periods, during which major SE storm events (East Coast Lows) occurred in March 2006, May 2009 and June 2012. The bed level evolutions of August 2008-June 2009 and March 2012-September 2012 are shown in Figure 4.7e and Figure 4.8c. Since the last survey in these two intervals was not long after the major storm events, movement of the bar further offshore than the seaward extension of the sand bypassing jetty and the southern training wall in both intervals is noticeable. As illustrated in Figure 4.7e and Figure 4.8c, it is suggested that a significant amount of LST was transported to the ebb tidal delta area during these intervals. Much of this sand initially accumulates at the seaward extension of the inlet channel (e.g. Figure 4.7e and Figure 4.8c) and is one of the main reasons of concern for navigation safety. This accreted sand is expected to be transported gradually offshore to the ebb-tidal delta offshore crest due to the dominant ebb tidal flow during lower energy wave conditions.

4.3.3 Analysis of wave power for storm events

As suggested in section 4.3.2, a significant portion of the ebb-tidal delta growth has occurred during storm events due to increased leakage past the sand bypassing jetty. In order to further investigate this hypothesis, the wave power (P_w) (*W/m*) of storm events between consecutive surveys was calculated. Linear wave theory was applied to calculate the incident storm wave power based on the wave energy per unit horizontal area (E) (J/m^2) and the group wave velocity (C_g) (*m/s*) (Equations (4.8) to (4.10) (Vila-Concejo et al., 2004; Nielsen, 2009)).

$$P_w = EC_g \tag{4.8}$$

$$E = \frac{1}{8}\rho_w g H_s^2 \tag{4.9}$$

$$C_g = \frac{1}{2}C_w\left(1+\frac{2kd}{\sinh(2kd)}\right) \tag{4.10}$$

where ρ_w is the water density (1025 kg/m^3), g is the gravity acceleration (9.8 m/s^2), H_s is the significant wave height (*m*), T_p is the peak wave period (*s*), d is the water depth (*m*), C_w is the speed of wave propagation (*m/s*) (equation (4.11)), and k is the wave number (equation (4.12)).

$$C_w = \frac{L}{T} \tag{4.11}$$

$$k = \frac{2\pi}{L} \tag{4.12}$$

In equations (4.11) and (4.12), L is the wave length at intermediate depths (*m*) which can be calculated with good approximation from equation (4.13) (Fenton and McKee, 1990).

$$L = \frac{gT_p^2}{2\pi}\left[\tanh\left(\frac{2\pi}{T_p}\sqrt{\frac{d}{g}}\right)^{3/2}\right]^{2/3} \tag{4.13}$$

Since the measured wave data at GC buoy was used, the water depth (d) of 17*m*, was used in these equations.

Then, the total storm wave power for each storm (W_{PT}) was calculated from equation *(4.14)*.

$$W_{PT} = P_{wm} \times D_s \tag{4.14}$$

where P_{wm} is the mean wave power for each storm event, and D_s is the storm duration in seconds.

The storm threshold used was defined as high energy events with $H_s > 3m$ and a minimum duration of two hours. The storm events were also categorized based on direction with storms from the northern quadrant (wave direction of less than 90 degrees from North clockwise), and from the southern quadrant (more than 90 degrees). Due to the approximate North-South orientation of the coastline, these two quadrants are assumed to generate southward and northward LST, respectively. The storm events with mean wave direction of less than 90 degrees were called north-east (NE) storm events, and the ones with mean direction of more than 90 degrees were called south-east (SE) storm events. Based on this categorization, the storm events which took place from January 2004 to April 2015 are shown in Table 4.3. In this table D_{pm} is the mean peak wave direction of the storm event.

Table 4.3. Storm wave power from January 2004 to April 2015

Time interval	**SE storm events**			**NE Storm events**		
	Time	D_{pm} (°)	$W_{PT}\times10^9$ **(W.s/m)**	**Time**	D_{pm} (°)	$W_{PT}\times10^9$ **(W.s/m)**
January 2004- July 2004				05/03/2004 11:30 AM to 06/03/2004 2:00 PM	79	24.62
				23/03/2004 3:30 AM to 25/03/2004 1:30 PM	84	32.70
July 2004 - July 2005				29/06/2005 5:30 AM to 30/06/2005 5:00 PM	82	19.41
July 2005 –April 2007	07/01/2006 9:00 PM to 08/01/2006 9:30 AM	144	5.24	26/07/2006 5:00 PM to 27/07/2006 2:00 AM	87	3.79
	03/03/2006 3:00 AM to 05/03/2006 5:30 PM	114	44.58			
April 2007 -August 2008	21/08/2007 12:30 PM to 23/08/2007 7:30 PM	100	25.43	23/08/2007 8:30 PM to 25/08/2007 10:30 AM	82	16.96
	04/01/2008 11:00 AM to 05/01/2008 12:00 AM	93	7.35	29/12/2007 9:30 AM to 04/01/2008 10:30 AM	84	83.30
	24/07/2008 6:30 PM to 25/07/2008 8:30 AM	95	5.09	02/06/2008 1:00 AM to 03/06/2008 4:00 AM	80	12.30
August 2008- June 2009	04/08/2008 3:30 PM to 05/09/2008 6:00 AM	102	5.92	10/03/2009 10:00 AM to 11/03/2009 6:00 PM	74	12.58
	30/03/2009 6:30 PM to	95	34.31	30/03/2009 5:00 AM to	85	6.97

	02/04/2009 5:00 AM			30/03/2009 6:00 PM		
	20/05/2009 1:00 AM to 25/05/2009 2:00 AM	91	105.81	02/04/2009 5:30 AM to 03/04/2009 12:00 AM	86	11.11
June 2009 - July 2010	11/07/2009 8:00 PM to 13/07/2009 6:30 AM	103	17.89			
July 2010 - March 2011	10/10/2010 11:30 AM to 11/10/2010 6:00 PM	93	13.94	11/10/2010 7:00 PM to 12/10/2010 7:00 PM	86	10.54
	10/01/2011 6:00 PM to 11/01/2011 12:30 AM	102	2.41	16/01/2011 11:00 AM to 16/01/2011 8:00 PM	82	4.42
March 2011- March 2012	21/08/2011 11:30 PM to 23/08/2011 1:30 AM	101	10.91	24/08/2011 12:00 AM to 24/08/2011 4:30 AM	85	2.25
				25/12/2011 4:30 AM to 26/12/2011 7:30 PM	79	21.21
March 2012- September 2012	11/06/2012 11:30 AM to 14/06/2012 6:00 PM	93	58.57	28/06/2012 8:30 AM to 29/06/2012 11:30 AM	83	15.93
	27/06/2012 11:00 PM to 28/06/2012 7:30 AM	96	3.42			
September 2012 - July 2013	28/01/2013 7:30 PM to 29/01/2013 8:30 AM	94	8.76	27/01/2013 9:00 AM to 28/01/2013 7:00 PM	80	36.11
	20/02/2013 9:00 AM to 22/02/2013 12:30 PM	101	29.59	19/02/2013 10:30 AM to 20/02/2013 2:00 AM	76	8.08
	15/03/2013 10:00 AM to 15/03/2013 4:30 PM	100	3.50			
	1/07/2013 4:30 PM to 2/07/2013 2:30 AM	105	3.97			
July 2013 -April 2015	15/03/2014 11:00 PM to 16/03/2014 6:00 AM	91	3.96			
	28/08/2014 5:30 AM to 29/08/2014 2:00 AM	102	9.84			
	19/02/2015 10:30 AM to 19/02/2015 4:30 PM	95	2.57			
	22/02/2015 10:30 AM to 23/02/2015 7:00 AM	94	9.44			

The cumulative north-east (NE) and south-east (SE) W_{PT} for each time interval were calculated and plotted against the volumetric change of the ebb-tidal delta as shown in Figure 4.16. A number of trends can be seen in this figure. First, in most of the time intervals that the cumulative W_{PT} from NE was more dominant, including January 2004-July 2004, April 2007-August 2008 and March 2011-March 2012 intervals, erosion occurred in the ebb-tidal delta.

However, it should be noted that the more significant erosion that occurred in March 2011-March 2012 was due to about 260,000 m^3 of sand being dredged from the ebb-tidal delta area between May 2011 and March 2012 (as mentioned in section 4.3.2).

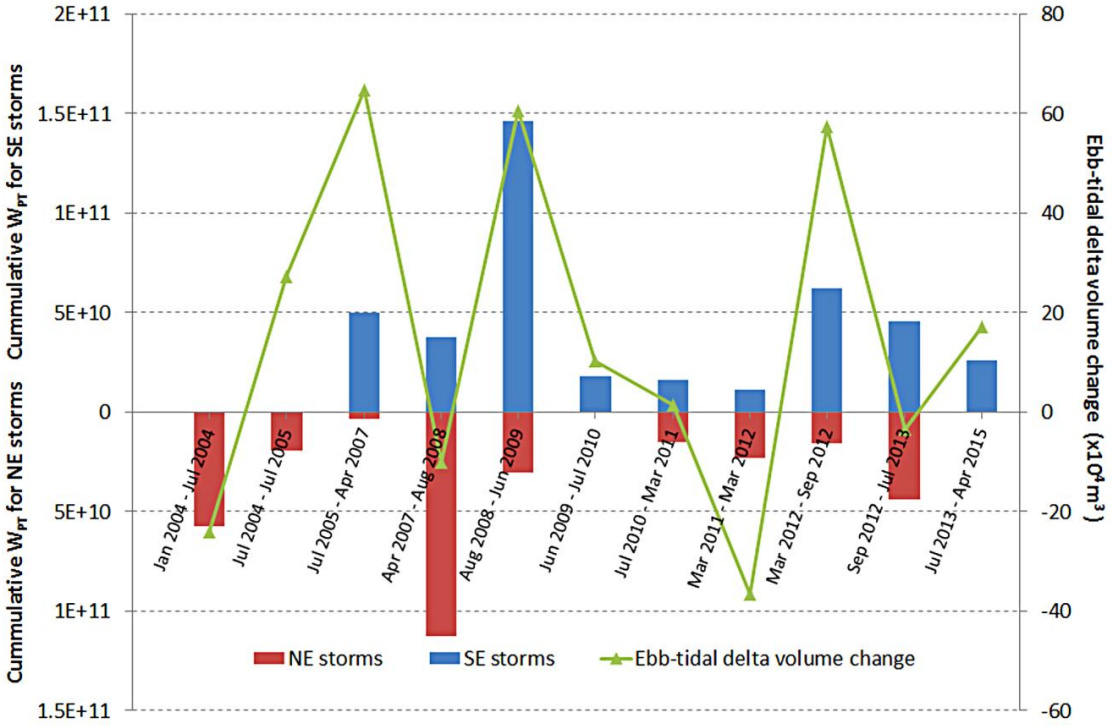

Figure 4.16. Cumulative W_{PT} ($W.s/m$) for storm events from NE and SE against the volumetric change of the ebb-tidal delta in each time interval

In addition, accretion occurred in July 2004-July 2005 although only one NE storm event occurred in this time interval. The reason for this accretion was investigated more and it was found that based on the data provided by City of Gold Coast (CGC), there was a major flood event (with a return period of about 1 in 20 years) at Loders, Biggera, Coomera and Nerang catchments at the end of June 2005. It is likely that this flood event, which was approximately four times the magnitude of other major flood events during the 11 years of study, transported a significant amount of sediment from within the estuary and flushed it out towards the ebb-tidal delta.

Second, in the time intervals that the cumulative W_{PT} from SE was more dominant, including July 2005- April 2007, August 2008-June 2009, June 2009-July 2010, March 2012-September 2012 and July 2013- April 2015, accretion occurred in the ebb-tidal delta. As illustrated in Figure 4.16, this accretion was more significant in July 2005-April 2007, August 2008-June 2009 and March 2012 to September 2012 intervals during which the accumulated SE storm event powers were larger. As shown in Table 4.3 during these three intervals, a significant SE

storm event with $W_{PT} \geq 30\times10^{9}$ *(W.s/m)* occurred, which is called a major storm event in this study. However, it should be noted that the rate of deposition was not proportional to the cumulative (SE) W_{PT} in these intervals. For instance, the rate of deposition in the July 2005-April 2007 time interval was as high as that of August 2008-June 2009, although the cumulative W_{PT} from SE in the former was less than the latter. As shown in Figure 4.12c, July 2005-April 2007 was the only survey interval with a notable percentage of less significant storm events ($2 < H_s < 3m$) with wave direction of more than 120˚. It is suggested that these less significant storm events with higher directions and the resultant northward wave induced current have contributed to the leakage of LST offshore from the sand bypassing jetty and training wall to the ebb-tidal delta (this will be examined in Chapter 7). This could be the main reason for the relatively higher deposition rate in this interval. In addition, the relatively higher deposition rate in March 2012-September 2012 compared to the cumulative W_{PT} from SE in this interval is due to the recovery process after the significant dredging from March 2011 to March 2012. The third trend that was noticed in Figure 4.16 was the negligible volumetric changes of the ebb-tidal delta in the time intervals that the cumulative W_{PT} from SE and NE were approximately the same, including July 2010- March 2011 and September 2012-July 2013.

4.3.4 Morphological evolution of Ebb-tidal delta subdivisions

To further investigate the pattern of the morphological evolution within the ebb-tidal delta area (region A1 in Figure 4.6) it was divided into nine sub areas, 1,600 metres north and 560 metres south of the entrance centreline. These sub areas which have been presented in Figure 4.17 were defined partly based on the net volumetric change from 2004 to 2015, and partly based on the active areas of accretion or erosion in various time intervals.

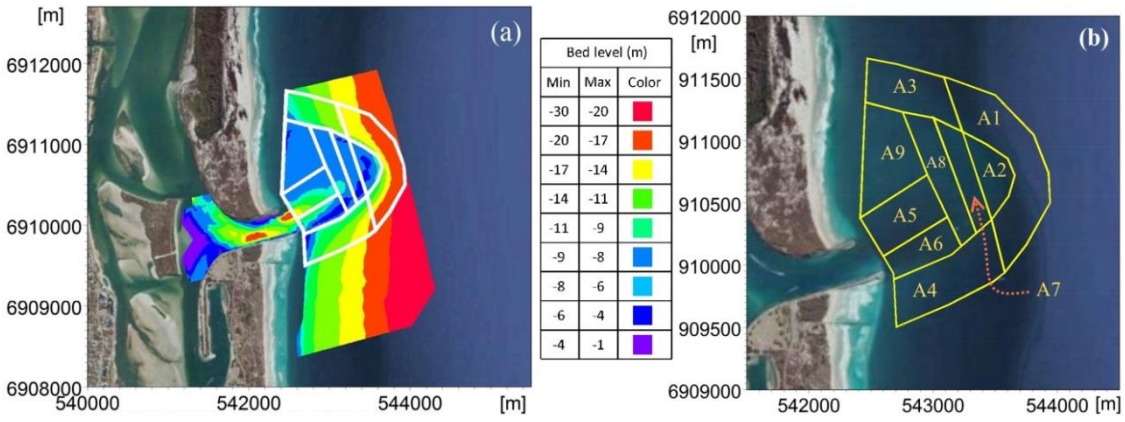

Figure 4.17. Ebb tidal delta subdevisions, (a) shows the sub areas on January 2004 Bathymetry (b) the number assigned to the sub areas.

To determine the response of each area individually, volumetric calculations were performed for each area, as well as to the whole ebb-tidal delta area and the results are shown in Table 4.4. The calculated volumes are totals, and the different periods between the survey data have not been considered in Table 4.4. Therefore, the average net monthly rates of change for each survey period were calculated and presented in Table 4.5 in order to facilitate the analysis in some cases.

Table 4.4. Net volume changes for sub areas 1 to 9 between successive surveys from 2004 to 2015. Volumes are in $m^3 \times 10^3$. Negetaive numbers mean erosion.

Time interval	**Areas**									
	A1	**A2**	**A3**	**A4**	**A5**	**A6**	**A7**	**A8**	**A9**	**Total**
Jan 2004- Jul 2004	-8.69	**-66.38**	+10.83	+10.06	+2.75	-112.28	-5.17	-46.13	-26.24	-241.4
Jul 2004 - Jul 2005	+142.52	+36.62	+54.79	+35.20	+8.35	-16.36	+16.73	+1.23	-7.77	+271.3
Jul 2005 -Apr 2007	+246.01	+58.83	**+139.56**	**+87.98**	+16.47	+52.34	-32.08	+49.11	+30.19	+648.2
Apr 2007 -Aug 2008	-37.44	**-89.42**	+79.54	-40.34	-29.59	+34.85	-6.06	-31.96	+18.24	-102.2
Aug 2008- Jun 2009	+121.38	**-134.05**	**+136.18**	**+227.91**	**+60.84**	**+59.66**	**+111.72**	**-104.81**	**+127.35**	+606.5
Jun 2009 - Jul 2010	+89.39	+134.69	+8.69	+23.74	-20.23	**-155.18**	-43.99	+109.91	-45.11	+101.9
Jul 2010 - Mar 2011	+56.06	+53.79	+18.14	-60.02	+1.36	-19.17	-25.68	+26.01	-35.68	+14.8
Mar 2011- Mar 2012	+45.89	**-40.46**	-20.96	-63.98	**-71.40**	+45.92	**-87.80**	**-44.75**	**-127.47**	-365.2
Mar 2012- Sep 2012	+92.49	**+18.88**	**+80.94**	**+103.12**	**+35.02**	**+117.00**	-1.01	+15.12	**+112.83**	+574.3
Sep 2012 - Jul 2013	+125.20	**-87.83**	-1.06	+29.63	-1.61	**-155.96**	+11.85	-18.34	+63.19	-34.8
Jul 2013 -Apr 2015	+206.18	+104.67	-12.88	+9.65	-8.91	-43.72	+7.72	-11.86	-79.99	+170.9
Total	+1079	-11	+494	+363	-7	-193	-54	-56	+30	+1644

Table 4.5. Average monthly rate of volume changes for sub areas 1 to 9 between successive surveys, 2004 to 2015. Volumes are in m^3. Negetaive numbers mean erosion.

Time interval	**Days**	**Areas**									
		A1	**A2**	**A3**	**A4**	**A5**	**A6**	**A7**	**A8**	**A9**	**Total**
Jan 2004- Jul 2004	157	-1661	-12684	2069	1922	525	-21455	-988	-8815	-5014	-46127
Jul 2004 - Jul 2005	375	**11402**	2930	4383	2816	668	-1309	1338	98	-622	21704
Jul 2005 - Apr 2007	648	**11389**	2724	**6461**	**4073**	763	2423	-1485	2274	1398	**30009**
Apr 2007 - Aug 2008	468	-2400	-5732	5099	-2586	-1897	2234	-388	-2049	1169	-6551
Aug 2008- Jun 2009	319	**11415**	-12607	**12807**	**21434**	**5722**	**5611**	**10507**	**-9857**	**11976**	**57038**
Jun 2009 - Jul 2010	408	6573	9904	639	1746	-1488	-11410	-3235	8082	-3317	7493
Jul 2010 - Mar 2011	238	7066	6780	2287	-7566	171	-2416	-3237	3279	-4497	1866
Mar 2011- Mar 2012	344	4002	-3528	-1828	-5580	-6227	4005	**-7657**	**-3903**	**-11117**	-31849
Mar 2012- Sep 2012	202	**13736**	2804	**12021**	**15315**	**5201**	**17376**	-150	2246	**16757**	**85292**
Sep 2012 - Jul 2013	314	**11962**	-8391	-101	2831	-154	-14901	1132	-1752	6037	-3325
Jul 2013 - Apr 2015	625	9897	5024	-618	463	-428	-2099	371	-569	-3840	8203
Total per month	4098	**7899**	-78	**3615**	**2657**	-51	-1412	-394	-413	216	12037

The characteristics of each sub area and their resultant trend of morphological evolution obtained from volumetric analysis are explained below.

A1) Ebb-tidal delta offshore crest area: an area of about 0.5km^2 which is the most seaward active area of the ebb-tidal delta.

The morphological evolution of this area is much more evident over long term periods (on a scale of 10 years) rather than shorter periods. As shown in Table 4.4, accretion occurred in most of the time intervals in this area. Most of the net growth of the ebb-tidal delta over the 11 year study period is due to the accumulative deposition in this area, as shown in Figure 4.6. Table 4.5 shows that the rate of growth in this area was more significant for five of the eleven time intervals, which include: July 2004-July 2005; July 2005- April 2007; August 2008-June 2009; March 2012-September 2012; and September 2012-July 2013. As mentioned in section 4.3.3 there was a major flood event at the end of June 2005 which most probably transported a significant amount of sediment from within the estuary and flushed it out to the ebb-tidal delta. It is suggested that this sediment deposited more significantly in sub areas 1, 2, 3 and 4 due to the expected significant flushing jet current from the inlet channel during this event.

The next three intervals with major deposition in sub area 1 are the ones which included one or two major SE storm events ($W_{PT} \geq 30\times10^9$ *W.s/m*), which were the March 2006, March and May 2009 and June 2012 storm events. To explain the reason for the significant growth in September 2012-July 2013, further investigation was required, which is explained below.

Analysis of the morphological evolution of the GCS so far illustrated the continuous growth of the ebb-tidal delta. The main hypothesis made so far in this study was that this growth during the study period mainly occurred due to the major SE storm events or major flood events if any. It is suggested that storm or flood events transport significant volumes of sediment to the ebb-tidal delta area. Part of this sediment is deposited in sub areas 1, 3 and 4, and the other part is trapped, initially in some of the ebb-tidal delta inner sub areas (especially sub area 6), and is gradually transported further from the inlet throat mostly to sub area 1 due to the combination of the dominant ebb-tidal and wave induced currents in calmer conditions. This process could take place gradually (more than a year) during calmer weather conditions by the dominant ebb-tidal and northward longshore current, similar to the time intervals after August 2008-June 2009 which did not include any relatively major ($W_{PT} \geq 20\times10^9$ *W.s/m*) storm events (see Table 4.5). On the other hand, this process might be accelerated due to the occurrence of a subsequent relatively major SE storm event not long ($\leq$ 12 months) after a major one in a previous time interval, which was the case for September 2012-July 2013. To illustrate, there was a SE storm event with W_{PT} of 29×10^9 in February 2013, which was about 6 months after the major storm event with W_{PT} of 59×10^9 (*W.s/m*) in June 2012 in previous time interval. This event probably accelerated the transportation of the trapped sand to sub area 1 in the September 2012-July 2013 time interval and resulted in the significant recorded rate of deposition in that area.

A2) Crest subarea: a sub area of 0.135 km^2 which is exactly in the middle of the offshore crest.

The morphological evolution of this sub area varied from erosional to depositional at various time intervals depending on the wave condition, dredging and recovery process. Major erosion of the crest sub area is noticeable in the intervals that had two characteristics. First, major SE or north-east (NE) storm event(s) ($W_{PT} \geq 30\times10^9$ *W.s/m*) took place during the interval. Second, this storm event occurred late (within six months) in the survey data time interval and therefore, there was insufficient recovery time. However, there are two exceptions to this trend. First, during the March 2011- March 2012 interval, when erosion occurred in sub area 2 although there were no major storm events in this interval. Second, during March 2012-September 2012 interval, this sub area had a slight deposition although there was a major SE storm event. To explain these, it should be noted that as mentioned in section 4.3.2, there was a huge dredging program from the ebb-tidal delta area from May 2011 to March 2012. According to this data,

the ebb-tidal delta last lobe (A2) was one of the sub areas that was specifically dredged. Therefore, the erosion of sub area 2 in March 2011- March 2012 interval is most likely due to this dredging activity. Meanwhile, the dredging program significantly contributed to the failure of the expected erosion in March 2012-September 2012 by providing insufficient sediment, on the crest of the ebb-tidal delta area, above the necessary height to cause storm waves to break. The resultant volumetric analysis also shows the erosion of this area was gradually recovered in the following months (< 6 months) with calmer wave conditions (e.g. see the related changes for August 2008-June 2009 and June 2009-July 2010 in Table *4.4*). As a result, the total morphological change in this area from 2004 to 2015 was negligible and it can be concluded that this area is in a state of dynamic equilibrium.

A3) Downdrift fillet: a sub area of 0.25 km^2 on the northward extension of the ebb-tidal delta.

This sub area encompassed the second biggest portion of net accumulation of sand from 2004 to 2015; which, similar to sub area 1, experienced accretion in most of the time intervals (see Table 4.4 and Table 4.5). It is noticeable that this sub area had major depositions in the time intervals with major SE storm events ($W_{PT} > 30\times10^9$ *W.s/m*), such as in March 2006, March and May 2009, and June 2012 occurred.

A4) Updrift fillet: a sub area of 0.35 km^2 on the southward extension of the ebb-tidal delta where the nearshore edge covers the distance between the southern training wall and the sand bypassing jetty.

This sub area covered the third biggest portion of the net accretion from January 2004 to April 2015, which has been mostly depositional but had more erosional time intervals compared to those of sub areas 1 and 3, as shown in Table *4.4*. Similar to A3, major accretion occurred in this sub area in the time intervals which featured major SE storm events ($W_{PT} > 30\times10^9$ *W.s/m*).

The inlet channel was subdivided into two sub areas, A5 and A6 (see Figure 4.17b), based on their pattern of sedimentation at various time intervals.

A5) Northern inlet channel: an area of 0.23 km^2 which encompasses the deepest part of the ebb-tidal delta except its offshore edge.

As shown in Table *4.4*, the net morphological change of this area from 2004 to 2015 is negligible, although there have been significant depositions during the intervals which included major SE storm events late (within six months) in the survey data time interval, and therefore there was insufficient recovery time, such as August 2008-June 2009 and March 2012-

September 2012. The negligible net morphological change of this area from 2004 to 2015 shows that the volumes of sand which were deposited in this area during storm events were eventually eroded in calmer weather conditions, most probably to the offshore extension of the ebb-tidal delta due to the dominant ebb tidal current. Therefore, it can be concluded that this sub area was in a state of dynamic equilibrium during this period. The significant erosion in this sub area in the March 2011-March 2012 interval was partly due to the previously mentioned major dredging from May 2011 to March 2012 from the ebb-tidal delta area.

A6) Southern inlet channel: a sub area of 0.15 km^2 which had a net erosional pattern from 2004 to 2015.

However, similar to A5, as shown in Table 4.4, relatively significant accretions occurred in this area during intervals with major storm events, such as March and May 2009 in August 2008-June 2009 interval and June 2012 in March 2012-September 2012 interval. These storm events occurred late (within six months) in the survey data time interval and therefore, there was insufficient recovery time. In the following intervals of both events, significant erosion occurred in this area, much higher than the previously deposited sand. The reason for this difference could not be explained.

The middle remaining part of the ebb-tidal delta was divided into two separate sub areas (A7 and A8) based on their characteristics, and are mostly spread northward to southward (see Figure 4.17b).

A7) Eastern middle delta area: a sub area of 0.15 km^2 which has been defined based on its depositional pattern during the major SE storm event in May 2009 (W_{PT} of 106×10^9 W.s/m).

The eroded sediment from the crest area (A2) during this event was suggested to be partially deposited in this area. However, it should be noted that this area does not show the same pattern during the intervals including other major SE storm events such as the ones in March 2006 and June 2012, which were fairly weaker than that of May 2009 (W_{PT} of $45\sim59\times10^9$ *W.s/m*). Significant erosion occurred in this sub area in the March 2011- March 2012 interval which was most probably due to the previously mentioned dredging activity. By considering this dredging in the volumetric analysis, it can be concluded that this sub area was in a state of dynamic equilibrium from 2004 to 2015.

A8) Western middle delta area: a sub area of 0.21km^2

Similar to area 7 shows insignificant total erosion from 2004 to 2015 which is most probably because this sub area was also dredged from May 2011 to December 2012 (see Table 4.4). Therefore, it can be concluded that, similar to A7, this sub area was in a state of dynamic equilibrium from 2004 to 2015. The trend of morphological evolution of this sub area, depositional or erosional, was very similar to that of A2 except for the July 2013-April 2015 interval. The resultant volumetric analysis also shows that this sub area had been significantly eroded in the August 2008-June 2009 interval and then recovered in the following interval (June 2009-July 2010), similar to area 2.

A9) Downdrift nearshore fillet: a sub area of 0.31 km^2 which is offshore to the downdrift discharge location of the bypassed sand.

As shown in Table 4.4, similar to sub areas 2, 5, 7 and 8, this sub area was in an approximate state of dynamic equilibrium from 2004 to 2015. The most significant depositions in this sub area occurred in the time intervals that included major SE storm events ($W_{PT} > 30\times10^9$ *W.s/m*) late (within six months) in the survey data time interval, and therefore there was insufficient recovery time, such as in March and May 2009 and June 2012. However, the deposited sand has been eroded during the successive time intervals with calmer wave conditions. In addition, there was a significant erosion in March 2011- March 2012 interval, which is considered to be mostly from the previously mentioned major dredging activity in that interval from the ebb-tidal delta area.

4.4 Conceptual model

The main purpose of this chapter was to provide an updated conceptual model of the sediment transport in the GCS area using the most recent data. This can be used for improving the bypassing rates or the inlet design to avoid unnecessary dredging or nourishment costs. As illustrated in Figures 4.9 and 4.10, the GCS area morphological evolution is still in a transitional phase, and has not reached equilibrium. Also, the trend of the ebb tidal delta evolution since 2004 does not show any decrease in the average rate of the ebb tidal growth compared to the WRL and GCCM's (1998) study.

The average artificial sand bypassing rate from January 2004 to April 2015 was about 650,000 *m^3/yr* (Figure 4.9), which ranged from a minimum of 480,000 *m^3/yr* in 2004 to a maximum of 810,000 *m^3/yr* in 2011. The maximum rate of delta growth during these years was

approximately 620,000 m^3/yr, which occurred in the August 2008 to June 2009 survey interval. Based on the analysis presented in section 4.3.3, this growth mainly occurred during the major SE storm events. Therefore, the maximum annual artificial bypassing rate period, which encompassed the SE storm events (from March to end of May 2009), was found. This was about 690,000 m^3/yr from June 2008 to the end of May 2009. Based on the analyses of the morphological evolution of the ebb-tidal delta since 2004, it is also suggested that during major SE storm events, other than the leakage seaward of the sand bypassing jetty and the southern training wall, the erosion of more offshore areas upstream is also contributing to the sediment accumulation in the ebb-tidal delta.

Therefore, assuming that: first, the GCS adjacent coastline alignment has remained approximately stable during these years (Appendix A); second, no leakage has occurred in 2004 (since no accretion occurred in the ebb-tidal delta); third, the bypassing rate was mainly sourced from the LST, while the cross-shore sediment transport had a negligible contribution; and forth, negligible amount of sand was supplied from inside the estuary except during major flood events; it can be concluded that the net northward LST updrift the entrance varied from 480×10^3 to $1{,}100\times10^3$ m^3/yr, and is strongly dependant on the frequency of the major SE storm events. The ebb-tidal delta had the maximum rate of decay in 2004 during which two storms from NE occurred. Thus, it has been suggested that a part of the sand on the ebb-tidal delta was transported to the downdrift, and the other part was transported to the updrift coastlines in response to these NE storm events. The suggested conceptual model of the sediment transport from January 2004 to April 2015 is shown in Figure 4.18.

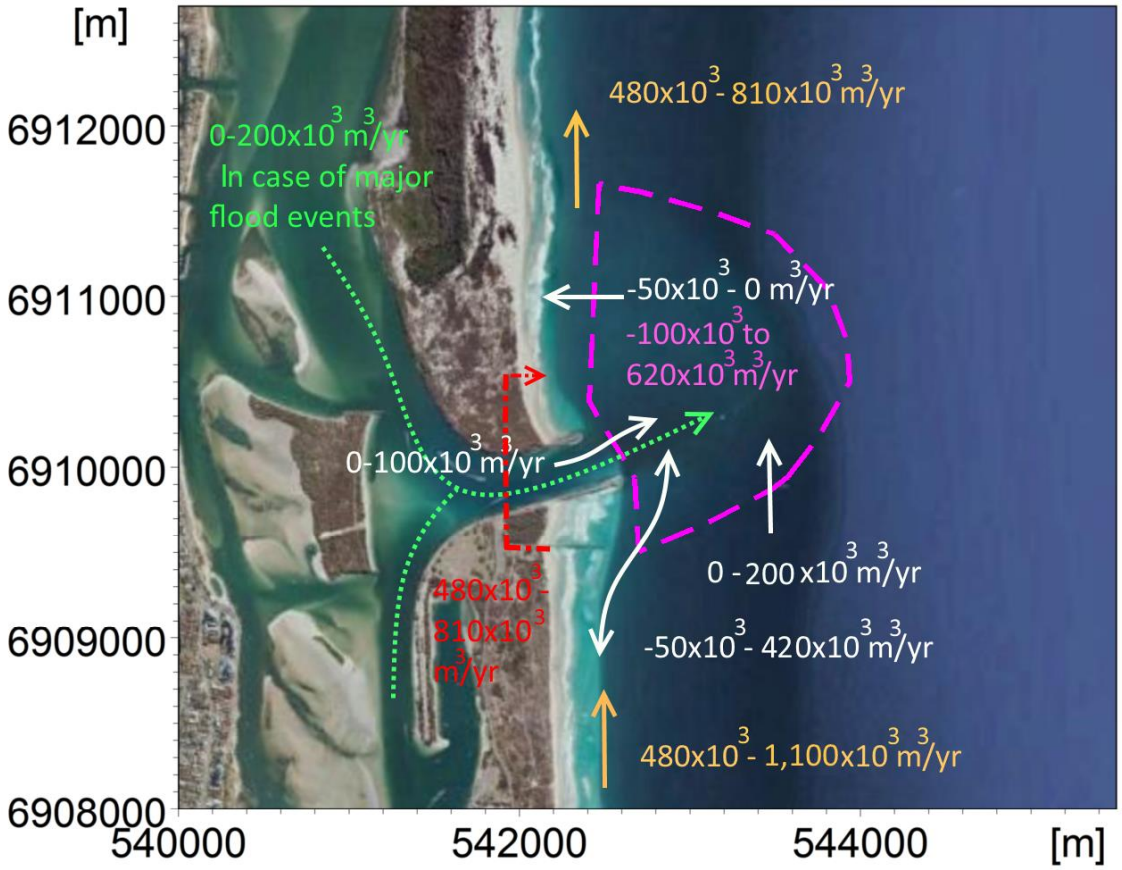

Figure 4.18. Conceptual model of sediment transport from January 2004 to April 2015 (Background image source: GoogleEarth©). Negative numbers mean 'erosion from' and positive numbers mean 'deposition in' the ebb-tidal delta. Red numbers are the bypassing rates, yellow numbers are suggested LST rates, pink numbers are the range of the ebb tidal delta volumetric changes, and green numbers are the suggested rate of sediment transport from erosion of the estuary to the ebb-tidal delta due to the major flood event.

There are a number of differences between the suggested conceptual model in this study and the ones from previous studies (Chapter 3, section 3.4.2). In previous conceptual models mostly an average LST and ebb-tidal delta growth were suggested, while in this study a range was suggested, the values of which strongly depend on the occurrence of major storm and flood events. It should be noted that the estimated average rate of ebb-tidal delta growth was about 150,000 m^3/yr (Figure 4.9) since 1984, while the average rate of the inlet channel erosion was 30,000 m^3/yr (Figure 4.10). The suggested range of sediment from within the estuary in this study (0-200,000 m^3/yr) is similar to that in the WRL and GCCM (1998) study (0-240,000 m^3/yr). However, they suggested this to be the main source of the ebb-tidal delta growth while, in this study, the upper value of this range is suggested to occur only in the case of a major flood event, such as the one in June 2005. None of the previous conceptual models suggested a source of sediment to the ebb-tidal delta from offshore. This suggested rate is mainly based on numerical simulation results of the study area (Chapter 6). The average rate of northward LST

upstream the GCS, suggested by GHD (2007) for 2002 to 2006, was similar to the one in this study. However, the suggested rate downdrift the inlet was higher, and they did not suggest any rate for the material coming from within the estuary. Unlike GHD (2007) and the current study, WBM (2013) suggested a negligible net transport to the ebb-tidal delta from the LST. Based on WBM (2013) conceptual model, the main source of ebb-tidal delta growth, which they suggested to be about 100,000 m^3/yr, was sourced from within the estuary.

4.5 Summary

Following the construction of the GCS and its associated bypassing system, there have been significant changes to the overall dynamics of sediment movement in the region. The volume of stored sand in the new ebb tidal delta, developed after construction of the GCS, is still increasing. This issue has caused problems for the navigation system and dredging seems essential to maintain the safe navigability of the channel.

Analyses of the morphological evolution of the GCS ebb-tidal delta for the past decade have shown that the changes in the dynamics of sediment transport in the region are still very much in a transitional state as a new dynamic equilibrium is yet to be established and dredging activities slow down the natural processes for reaching equilibrium. This was also confirmed by the empirical equations suggested in the previous studies.

Based on the analysis explained in section 4.3.3 and 0, the prevailing source of sediment for the continuous growth of the ebb-tidal delta is suggested to be from the leakage of dominant northward LST seaward the sand bypassing system and the southern training wall during storm events. This will be examined in Chapter 6 using numerical simulations. It is also suggested that the leakage of LST seaward of the southern training wall also occurs during less significant storm events ($2 < H_s < 3m$) with wave direction of more than 120° which will be examined in Chapter 7. In addition, this study also suggests that NE storm events, which are much less common in this region compared to SE ones, tend to erode the ebb-tidal delta. This will also be examined in Chapter 7.

In the following chapters, the morphodynamics of the ebb-tidal delta will be assessed through numerical modelling. This will help to better understand the relative importance and impacts of tidal currents, waves and river discharge across the region, and confirm the suggested conceptual model in this chapter.

5 – Numerical simulation of the Gold Coast Seaway hydrodynamics

5.1 Introduction

There have been several studies to understand the physical processes in the Gold Coast Seaway (GCS) area after it was stabilized (Andrews and Nielsen, 2001; Voisey, 2004; Mirfenderesk and Tomlinson, 2007; Patterson, 2007; Sennes et al., 2007; Mirfenderesk and Tomlinson, 2008). In these studies, hydrodynamic calibrations were mainly performed qualitatively, and were mostly focused on the calibrations of water level and discharge within the Broadwater (Mirfenderesk and Tomlinson, 2007; Sennes et al., 2007; Davies et al., 2009).

Implementing a numerical model which can predict the sediment transport and the resultant morphological changes of tidal inlets is a highly challenging task, and developing a well-calibrated and verified hydrodynamic model is the first vital step. In this study, a two dimensional depth averaged numerical model was developed to simulate physical processes including flow, wave and sediment transport in the GCS area. The model was calibrated and verified against available observed current and wave data. Various statistical errors suggested in the literature were used to quantify the performance of model predictions for all components of flow and wave. In the following chapter, the resultant longshore sediment transport (LST) will be calculated and compared with previous studies. In addition, the model will be applied for simulation of morphological changes of the case study.

5.2 Numerical Modelling

A numerical model, using MIKE 21/3 coupled depth-averaged model, was developed to simulate the flow, wave and sediment transport of the tidal inlet. In this study, all of the simulations were performed in 2DH (depth averaged) due to two main reasons. First, the computational time was a constraint, and using a 3D simulation would increase the simulation time significantly. Although a fully 3D approach presents the physics of hydrodynamics more comprehensively, its advantages may not outweigh its higher computational time. Second, it has been shown in several studies that 2DH models are capable of simulating and reproducing the physical processes in tidal inlets (Bertin et al., 2009a; Bruneau et al., 2011; Tung, 2011). In

addition, according to Grunnet et al. (2004), the use of a 2DH model is sufficient when the ultimate goal is the prediction of bathymetry changes.

In order to reach a better calibration and verification for hydrodynamics of the model whilst minimizing the computation time as much as possible, a total of three numerical models were developed which include a regional HD model, a regional SW model, and a local coupled HD-SW-ST model. In the coupled local model all three of the modules (HD, SW and ST) are coupled. HD, SW and ST stand for Hydrodynamics, Spectral Waves and Sediment Transport, respectively. The boundary conditions of the local model were mainly extracted from the first two regional models to improve the precision of model prediction.

The HD and SW modules are the basic computational components of the coupled model. The HD Module simulates water level variations and flows in response to a variety of forcing functions including wind shear stress, bottom shear stress and wave radiation stress (from SW module). The SW Module simulates the growth, decay and transformation of wind-generated waves and swell in offshore and coastal areas while incorporating the current and water level variations simultaneously from the HD module. The coupled model makes simulating the mutual interaction between waves, currents and sand transport possible by using a dynamic coupling between HD, SW and ST modules. Hence, comprehensive feedback of the bed level changes is included in the waves and flow calculations from the ST module at each time step.

5.2.1 Model formulation

In this section a brief description of the governing equations, which are the base of numerical simulations in MIKE 21/3 coupled depth-averaged model, is presented.

5.2.1.1 Hydrodynamics Module

MIKE 21 HD is a flexible mesh-based model, with an unstructured grid providing an optimal degree of flexibility in simulating complex geometries and smooth boundaries. The spatial domain is discretised by subdivision of the continuum into non-overlapping element/cells (DHI, 2014c). The hydrodynamic module consists of continuity, momentum, temperature, salinity and density equations, and it is closed by a turbulent closure scheme. The spatial discretization of the governing equations is performed using a cell-centred finite volume method. The model simulation is developed based on the numerical solution of two-dimensional Reynolds averaged Navier-Stokes equations which incorporated the Boussinesq and hydrostatic pressure assumptions.

Two governing dimensional shallow water equations, which were obtained from integration of the horizontal momentum equations and the continuity equation over depth ($h = \eta + d$, where η is the surface elevation, d is the still water depth and h is the total water depth), include the local continuity equation:

$$\frac{\partial h}{\partial t} + \frac{\partial h\bar{u}}{\partial x} + \frac{\partial h\bar{v}}{\partial y} = hS + \hat{P} - \hat{E} \tag{5.1}$$

and the two horizontal momentum equations in x and y direction, respectively:

$$\begin{aligned} &\frac{\partial h\bar{u}}{\partial t} + \frac{\partial h\bar{u}^2}{\partial x} + \frac{\partial h\overline{vu}}{\partial y} = f\bar{v}h - gh\frac{\partial \eta}{\partial x} - \frac{h}{\rho_0}\frac{\partial p_a}{\partial x} - \frac{gh^2}{2\rho_0}\frac{\partial \rho_w}{\partial x} + \frac{\tau_{sx}}{\rho_0} - \frac{\tau_{bx}}{\rho_0} \\ &- \frac{1}{\rho_0}\left(\frac{\partial s_{xx}}{\partial x} + \frac{\partial s_{xy}}{\partial y}\right) + \frac{\partial}{\partial x}\left(hT_{xx}\right) + \frac{\partial}{\partial y}\left(hT_{xy}\right) + hu_sS \end{aligned} \tag{5.2}$$

$$\begin{aligned} &\frac{\partial h\bar{v}}{\partial t} + \frac{\partial h\overline{uv}}{\partial x} + \frac{\partial h\bar{v}^2}{\partial y} = -f\bar{u}h - gh\frac{\partial \eta}{\partial y} - \frac{h}{\rho_0}\frac{\partial p_a}{\partial y} - \frac{gh^2}{2\rho_0}\frac{\partial \rho_w}{\partial y} + \frac{\tau_{sy}}{\rho_0} - \frac{\tau_{by}}{\rho_0} \\ &- \frac{1}{\rho_0}\left(\frac{\partial s_{yx}}{\partial x} + \frac{\partial s_{yy}}{\partial y}\right) + \frac{\partial}{\partial x}\left(hT_{xy}\right) + \frac{\partial}{\partial y}\left(hT_{yy}\right) + hv_sS \end{aligned} \tag{5.3}$$

where t is the time; x and y are the Cartesian horizontal coordinates; u and v are the velocity components in the x and y direction; $f = 2\Omega\sin\phi$ is the Coriolis parameter (Ω is the angular rate of revolution and ϕ is the geographic latitude); g is the gravitational acceleration; ρ_w is the density of water; s_{xx}, s_{xy}, s_{yx} and s_{yy} are components of radiation stress tensor; p_a is the atmospheric pressure; ρ_0 is the reference density of water. S is the magnitude of the discharge due to point sources and (u_s,v_s) is the velocity by which the water is discharged into the ambient water. $\hat{P}$ and $\hat{E}$ are precipitation and evaporation rates, and the overbar parameters indicate depth average values from $z = -d$ to $z = \eta$. (τ_{sx},τ_{sy}) and (τ_{bx},τ_{by}) are the x and y components of the surface wind and bottom stresses. The lateral stresses T_{ij} include viscous friction, turbulent friction and differential advection. These are estimated using an eddy viscosity formulation based on the depth average velocity gradients (DHI, 2014c):

$$T_{xx} = 2A_e\frac{\partial \bar{u}}{\partial x} \quad , \quad T_{xy} = A_e\left(\frac{\partial \bar{u}}{\partial y} + \frac{\partial \bar{v}}{\partial x}\right), \quad T_{yy} = 2A_e\frac{\partial \bar{v}}{\partial y} \tag{5.4}$$

where A_e is the horizontal eddy viscosity, and the bottom stress, $\vec{\tau}_b = \left(\tau_{bx},\tau_{by}\right)$, is calculated based on a quadratic friction law:

$$\frac{\vec{\tau}_b}{\rho_0} = c_f \vec{u}_b |\vec{u}_b| \tag{5.5}$$

in which $\vec{u}_b = (u_b, v_b)$ is the depth-averaged flow velocity, and c_f is the drag coefficient. The drag coefficient can be calculated from the Ch'ezy number, *Ch*, or the Manning number, M_n (the reciprocal value of the Manning number *n*).

$$c_f = \frac{g}{Ch^2} \quad \text{or} \quad c_f = \frac{g}{\left(M_n h^{1/6}\right)^2} \tag{5.6}$$

The flooding and drying depths of 0.05 and 0.005*m* respectively were specified in the model to avoid numerical instabilities in lower water depths, such as along the shoreline.

For dynamic stability of the HD module, the model Courant-Fridrich-Levy (*CFL*) number, which is defined as below, should be less than one (DHI, 2014c).

$$CFL_{HD} = \left(\sqrt{gh} + |u|\right)\frac{\Delta t}{\Delta x} + \left(\sqrt{gh} + |v|\right)\frac{\Delta t}{\Delta y} \tag{5.7}$$

in which Δx and Δy is determined based on the minimum edge length for each element (DHI, 2014d).

5.2.1.2 Spectral Wave module

MIKE 21 SW is a flexible mesh, spectral wind-wave model; which simulates the growth, decay and transformation of wind-generated waves and swell in offshore and coastal areas. Similar to the HD module, cell-centred finite volume method is applied for discretisation of the governing equation in geographical and spectral space. The time integration is performed using a fractional step approach, in which a multi-sequence explicit method is applied for the propagation of wave action. MIKE SW includes two different formulations. First, directional decoupled parametric formulation which is based on a parameterization of the wave action conservation equation in the frequency domain. In this method the zero and first moment of the wave action spectrum are introduced as dependent variables (Holthuijsen et al., 1989). Second, the fully spectral formulation, which is based on the wave action conservation equation as described in Komen et al. (1996) and Young (1999). The directional- frequency wave action spectrum is the dependent variable in this method (DHI, 2014f). The second formulation was applied in this study (Section 5.2.5)

This module includes the following physical phenomena: (a) Wave growth by action of wind; (b) Non-linear wave-wave interaction; (c) Dissipation due to white-capping; (d) Dissipation due to bottom friction; (e) Dissipation due to depth-induced wave breaking; (f) Refraction and shoaling due to depth variations; (g) Wave-current interaction and (h) Effect of time-varying water depth.

Wave action conservation equation is the governing equation, which will be used in either Cartesian or spherical coordinates. The balance equation for wave action in horizontal Cartesian coordinates is as follows:

$$\frac{\partial N}{\partial t}+\nabla.\left(\vec{v}N\right)=\frac{S_T}{\sigma} \tag{5.8}$$

in which N ($\vec{x},\sigma,\theta,t$) is the wave action density, which wave field is represented by, t is the time, $\vec{x}=(x,y)$ is the Cartesian coordinates, θ is the direction of wave propagation, $\vec{v}=($ $c_x,c_y,c_\sigma,c_\theta$) is the propagation velocity of a wave group in the four-dimensional phase space $\vec{x}$, σ and θ, S_T is the Source term for energy balance equation, and $\sigma = 2\pi f_r$ is the relative angular frequency (f_r is the ordinary frequency). ∇ is the four dimensional differential operator in the $\vec{x}$, σ and θ space. The four velocity components are given by:

$$\left(c_x,c_y\right)=\frac{d\vec{x}}{dt}=\vec{c}_g+\vec{U} \tag{5.9}$$

$$c_\sigma=\frac{d\sigma}{dt}=\frac{\partial\sigma}{\partial d_{sw}}\left[\frac{\partial d_{sw}}{\partial t}+\vec{U}.\nabla_{\vec{x}}\,d_{sw}\right]-c_g\vec{k}.\frac{\partial\vec{U}}{\partial s} \tag{5.10}$$

$$c_\theta=\frac{d\theta}{dt}=-\frac{1}{k}\left[\frac{\partial\sigma}{\partial d_{sw}}\frac{\partial d_{sw}}{\partial m_a}\right]+\vec{k}.\frac{\partial\vec{U}}{\partial m_a} \tag{5.11}$$

in which $\vec{c}_g=\frac{\partial\sigma}{\partial k}$ is the magnitude of the group velocity of the wave energy relative to the current, k is the magnitude of wave number vector $\vec{k}$ (with direction of θ), $\vec{U}$ is the current velocity vector, d_{sw} is the still water depth, $\nabla_{\vec{x}}$ is the two-dimensional differential operator in the (x,y) space. s is the space coordinate axis in the wave direction, and m_a is the coordinate axis perpendicular to that.

S_T, which is the energy source term, represents the sum of source functions describing a number of physical phenomena.

$$S_T = S_{in} + S_{nl} + S_{ds} + S_{bot} + S_{surf} \tag{5.12}$$

where S_{in} represents the energy generation by wind, S_{nl} is the wave energy transfer due to non-linear wave-wave interaction, S_{ds} is the dissipation of wave energy due to whitecapping, S_{bot} is the dissipation due to bottom friction and S_{surf} is the dissipation of wave energy due to depth-induced breaking (DHI, 2014f).

5.2.1.3 ST module

Sediment transport in the research area depends on both current and waves, primarily oblique wave breaking and the consequent alongshore current (as explained in chapter 4). Hence, the module that was selected for sediment transport modelling was "Combined Wave and Current". In this method, the drag coefficient is calculated as

$$c_f = \frac{1}{\left(\frac{1}{\kappa}\left(\ln\left(\frac{30h}{k_s}\right)-1\right)\right)^2} \tag{5.13}$$

where h is the local water depth, κ is the Von Kárman's constant (0.4), and k_s is suspended load calibration factor which is obtained from the HD model. In combined current and wave option, the sediment transport rates are derived by linear interpolation of the pre-generated sediment transport table, which is based on a quasi three-dimensional sediment transport model (STPQ3D). In this model, instantaneous and time-averaged hydrodynamics and sediment transport rate are calculated. Since the model calculates the bed load (q_b) and suspended load (q_s) separately, the final values given as the sediment transport rate are the total load (q_t) (DHI, 2014a).

$$q_t = q_b + q_s \tag{5.14}$$

Bed load calculation is conducted based on the bed load transport model of Engelund and Fredsøe (1976), where the bed load transport is calculated from the instantaneous Shield's parameter. The bed load in the mean current direction (q_{b1}) and normal to mean current direction (q_{b2}) are calculated as follows

$$q_{b1} = \frac{1}{T_w}\sqrt{(s_s-1)gd_{50}^3}\int_0^{T_w}\Phi_b(t)\cos(\phi_f(t))dt \tag{5.15}$$

$$q_{b2} = \frac{1}{T_w}\sqrt{(s_s-1)gd_{50}^3}\int_0^{T_w}\Phi_b(t)\sin(\phi_f(t))dt \tag{5.16}$$

where T_w is the wave period, s_s is the relative sediment density of the bed material, d_{50} is the median grain size, $\phi_f(t)$ is the direction of instantaneous flow, and $\Phi_b(t)$ is the dimensional bed load which is found by

$$\Phi_b = 5p\left(\sqrt{\theta'} - 0.7\sqrt{\theta_c}\right) \tag{5.17}$$

in which θ' is Shield's parameter, θ_c is critical Shield's parameter, and p is the probability that all the particles of a layer are moving.

For suspended sediment transport, the model calculates the vertical variation of the suspended sediment concentration from the vertical diffusion equation of Fredsøe et al. (1985) (equation (5.18)), and then calculates the suspended sediment flux from equation (5.19).

$$\frac{\partial c}{\partial t} = \frac{\partial}{\partial y}\left(\varepsilon_s \frac{\partial c}{\partial y}\right) + w\frac{\partial c}{\partial y} \tag{5.18}$$

$$q_s = \frac{1}{T_w}\int_0^{T_w}\int_{2d_g}^{D_w}(u_i c)dzdt \tag{5.19}$$

Where c is the instantaneous sediment concentration; ε_s is the turbulant diffusion coeficient for the sediment which is taken to be equal to the eddy viscosity ε; w is the settling velocity of the suspended sediment; D_w is the local water depth; d_g is the grain diameter; and u_i is the instantaneous flow velocity. In calculation of the sediment transport rate in this model, the influence of ripples, the bed slope, streaming, density currents and helical effects can be included (DHI, 2014a).

5.2.2 Model inputs

In order to develop a numerical model for the hydrodynamic and sediment transport of the study area, other than the applied forces such as tide, wave and wind, a series of other data/parameters are required. These include: bathymetry data, sediment properties such as grain size, grading and relative density, angle of repose for calculation of the bank erosion, water temperature and Critical Shields parameter.

5.2.2.1 Bathymetry

To create the bathymetry of the regional, and finally the local model, a number of data sources were used. A part of the data was provided by the City of Gold Coast (CGC) for the Gold Coast Estuarine Modelling Study (GEMS), which included two data sets from October 2007 and May

2008 (Davies, 2008). The same sets of data were used for the bathymetry of the local model, and the bathymetry of the Seaway area was updated with available surveying data from the Gold Coast Waterways Authority (GCWA) close to the time that the model was set up to run. Moreover, since none of the above mentioned data includes the bathymetry of the berm, the bathymetry of the areas close to the coastline edges was extracted and interpolated from available ETA survey line data from the CGC. The vertical datum of all of the bathymetry data provided was converted to MSL (Mean Sea Level) with respect to the relative semidiurnal tidal planes table.

5.2.2.2 Sediment properties

According to the previous studies, the median diameter of the sand grains in the area (d_{50}) is 200μm (DHL, 1970; Sennes et al., 2007; Turner et al., 2006). However, no sediment data was available for the ebb-tidal delta area; therefore, a field trip was arranged in August 2013 to gather sand samples offshore and from the ebb-tidal delta area. Eight sand samples were collected from depths of about -5.5 to -7.0 metres in the offshore area as shown in Figure 5.1.

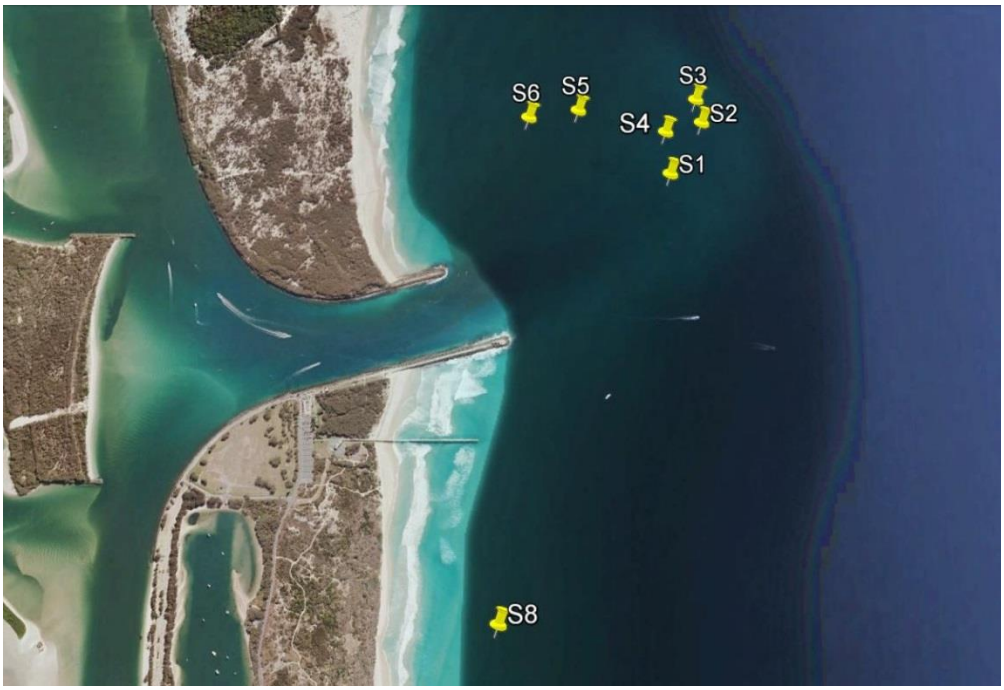

Figure 5.1. Collected sand samples locations

Since the mean diameter of sediment is known to be more than 0.075*mm*, according to AS 1289.3.6.1-2009 (Australian Standard) sieve analysis should be used to find the particle size distribution of the samples. Fine sieving, using 9 sieves as shown in Figure 5.2, was done based on AS 1289.3.6.1-2009.

Figure 5.2. Sieve analysis set up

The results of sieve analysis showed that the sediment in the ebb-tidal delta area is comprised of unimodal/bimodal (very) well-sorted, fine/medium sand. The resulted range of d_{50} (sediment median grain size) varied between 200 to 280 μm, with an average of about 250 μm. Sediment grading, defined in equation (5.20), is another parameter required in the generation of the sediment transport table in MIKE software.

$$\delta = \left(\frac{d_{84}}{d_{16}} \right)^{0.5} \tag{5.20}$$

Where, 84% of the particles in the sample are larger than d_{84}, and 16% of the particles are larger than d_{16}. Sediment grading, ranging from 1.18 to 1.40 with an average of 1.25, was calculated for the eight samples. The density of the sand samples was also calculated based on the AS 1289.3.5.1-2006 standard as shown in Figure 5.3, and the resultant sand density was 2626 kg/m^3.

Figure 5.3. The arranged set up to vaccum the sand sample in order to be used for determining sand particle density, based on AS 1289.3.5.1-2006

In order to simulate the erosion of coastlines, an angle of repose needs to be determined. This angle was set to 50 degrees from an analysis of maximum beach berm stable slope, based on ETA line survey data from CGC in several sections at different times. Based on the previous measurements by the Griffith Centre of Coastal management (GCCM), the salinity of seawater in the area is 35 ppt, and the average water temperature is about 20˚C. Therefore, according to Fofonoff and Millard (1983), the seawater density is about 1025 kg/m^3. The Critical Shields parameter (θ_c) was calculated based on the formulas proposed in Masselink et al. (2014) for well-sorted sediments, and the final value of 0.045 was denoted as θ_c for the generation of the sediment transport tables in the model.

5.2.3 Regional HD model

The regional HD model and its boundary limits were extended so that it included a reasonable area to account the tidal lags in the region when tidal levels are the only boundary conditions available (Figure 5.4). The global tidal predictions of MIKE, which are based on TOPEX/POSEIDON altimetry data and represent the major diurnal (K1, O1, P1 and Q1) and semidiurnal tidal constituents (M2, S2, N2 and K2) with a spatial resolution of 0.25 × 0.25 degrees (approximately 28×28 *km*) (DHI, 2014b), were used to extract the water levels at the boundaries of regional HD model. The details of these tidal constituents are shown in Table 5.1 from the results section of Schenewerk et al. (1999) study.

Table 5.1. Diurnal and semidiurnal tidal constitutes

Darwin Symbol	Name	Period (hours)
Semidiurnal		
M2	Principal lunar	12.42
S2	Principal solar	12.00
N2	Major lunar elliptical	12.66
K2	Luni-solar declinational	11.97
Diurnal		
O1	Principal lunar	25.82
P1	Principal solar	24.07
Q1	Major lunar elliptical	26.87
K1	Luni-solar declinational	23.93

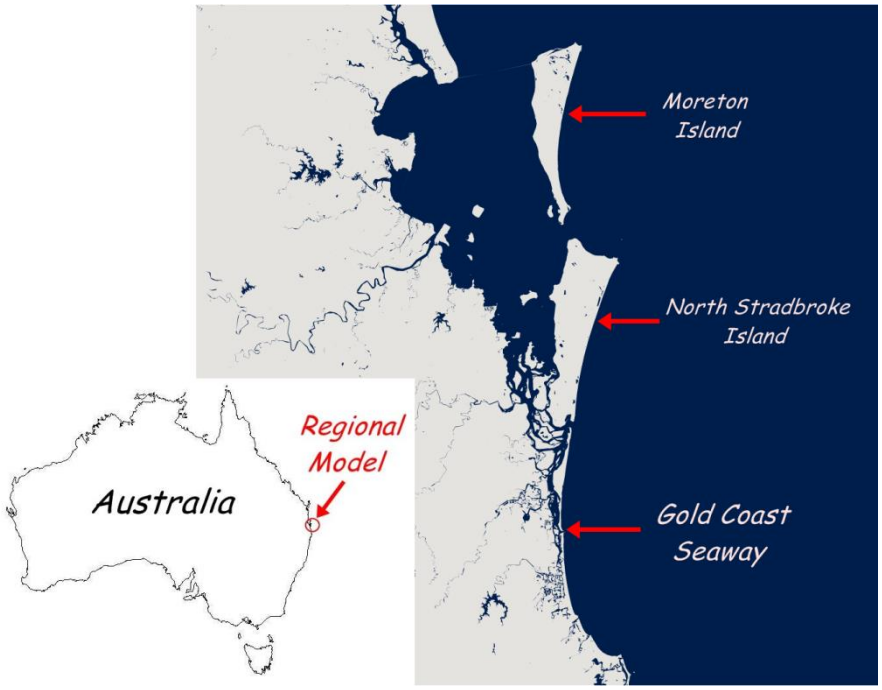

Figure 5.4. Regional HD Model domain area

Spatially varying mesh resolutions were applied throughout the domain, in which the minimum and maximum element lengths were about 30*m* and 3*km*, respectively. An outline of the regional model generated mesh properties is given in Table 5.2. The domain was subdivided

into several domains with variable mesh size resolutions to optimize the computational efficiency.

Table 5.2. Regional bathymetry mesh properties

	Regional Model Mesh
No. of Elements	226189
No. of Nodes	126317
Minimum Element Length (m)	24
Maximum Element Length (m)	3200
Minimum Element Area (m^2)	280
Maximum Element Area	4e+6

The seawater density, which is a function of the salinity and temperature, was set as barotropic mode. This mode is based on constant temperature and salinity, and the density will not be updated during the simulation (DHI, 2014d). The best calibration for the final local hydrodynamic model was achieved when most of the model area was assumed to have bed resistance equivalent to Manning's number M of 40 $m^{1/3}/s$, which is the same or within the range that were used in other studies (Jiang et al., 2011; Elias et al., 2012; Elias and Hansen, 2013). The water levels of the northern and southern rivers at the boundaries, as well as the North, South and East boundaries of the local model, as shown in Figure 5.5, were extracted from the results of the regional HD model.

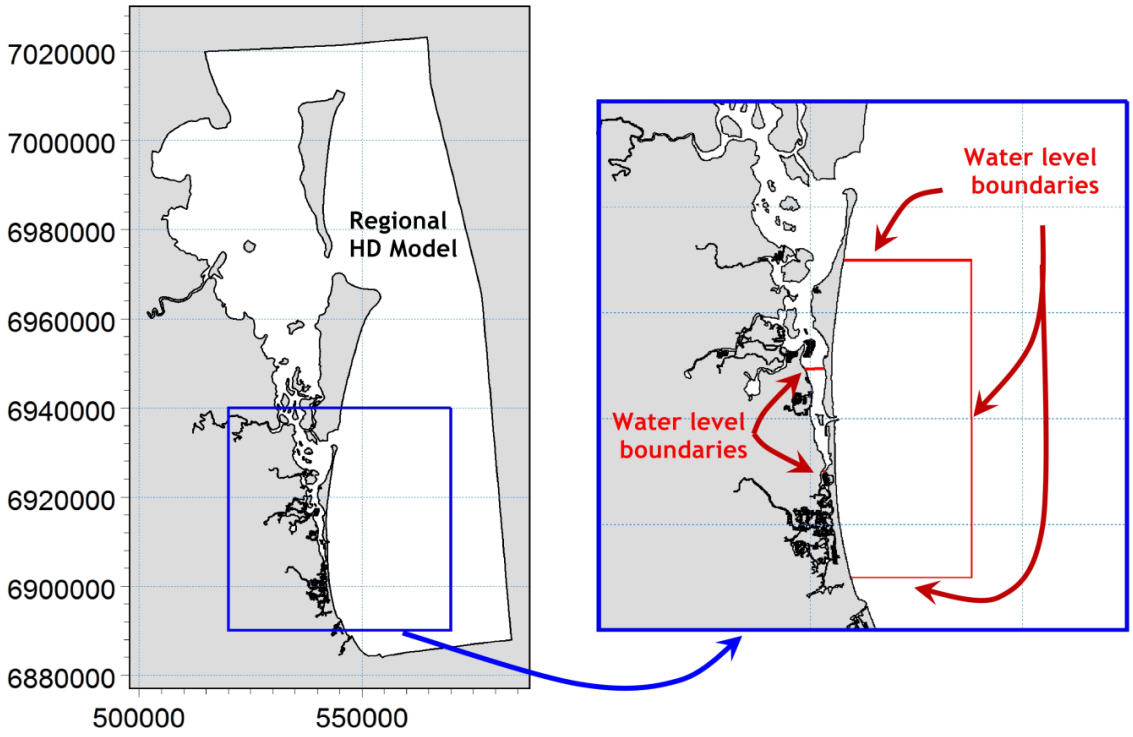

Figure 5.5. Locations of the water level boundary outputs from the Regional HD model for the local HD Model (Red lines in the right image are the boundaries of the Local HD model)

5.2.4 Regional wave model (SW)

A relatively large scale wave model, called the "Regional wave SW model", was used to simulate the wave condition in the area and provide the wave boundary conditions for the local model. Regional wave model domain covered the area from the northern extremity of North Stradbroke Island to the north and Point Danger (Tweed River Entrance) to the south, with an offshore width dependent on the location of the selected wave boundary condition (Figure 5.6). A flexible mesh was generated over the domain which has 22485 elements, with a minimum element length of approximately 50 metres near the coastline and a maximum element length of approximately 3,100 metres.

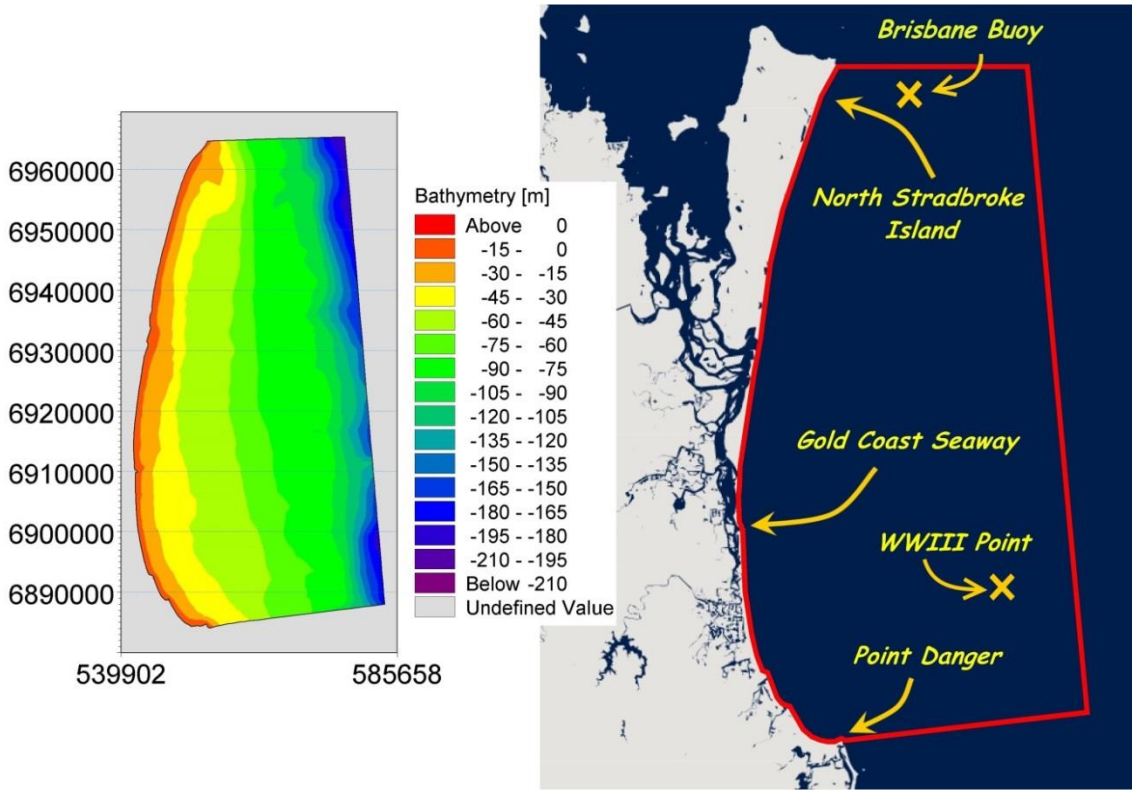

Figure 5.6. Regional Wave model domain and Bathymetry

The results provided by the regional wave model were initially used as the boundary conditions for the local model. Sensitivity analysis of the final local model results was conducted based on the selected offshore wave forcing for the regional wave model and the related extension of the regional model offshore (section 5.5.2.1). Different wave boundary conditions were applied on the boundaries of the models with variable offshore extensions of the domain. These boundary conditions included the wave parameters (Significant wave height, peak wave period, mean wave direction) from the results of large scale ocean models of European Centre for Medium-Range Weather Forecasts (ECMWF) and National Oceanographic and Atmospheric Administration (NOAA) WaveWatch III (WWIII), and also Brisbane buoy wave data measurements (Figure 5.6 and 5.9). The final local model results for all of the above mentioned wave boundary conditions and domains were acceptable. However, the best results were obtained by using Brisbane buoy measurements as the eastern boundary of the local model, and extracting the lateral boundaries of the local model from the regional wave model, in which Brisbane buoy measured data was used as the boundary condition. The mean of the measured significant wave height, peak wave period, and peak wave direction at Brisbane buoy during the ten month simulation period was 1.7m, 9s, and 120 degrees, respectively.

5.2.5 Local Model Set up

The domain of the local coupled HD-SW-ST model is shown in Figure 5.7. The mesh sizes in the GCS, as well as those of the area of the ebb-tidal delta, were reduced to an optimum value in order to have more precise simulations of hydrodynamics and the subsequent sediment transport while maintaining the numerical stability of the model. The minimum and maximum element lengths were about 15*m* and 1 *km*, respectively. Based on the minimum mesh size and approximate maximum measured velocity in the channel, and considering the maximum allowable Courant number (CFL), an initial value for time step was assumed. The optimum time step that was finally set in the model was 30 minutes, which is within an acceptable range, and the same as the one Bertin et al. (2009b) used. The same time step was also used in regional models since they provided the boundary conditions for the local model.

Current speed in the GCS channel proved to be very sensitive to variations in the bed resistance, similar to other studies such as that of Elias and Hansen (2013). Therefore, in order to determine the best current speed calibration, the bed resistance coefficient was adjusted by a trial and error approach. The software manual (DHI, 2014e) suggests using Manning numbers in the range of 20-40 $m^{1/3}/s$ with a suggested value of 32 $m^{1/3}/s$ if no other information is available. The sensitivity of the current circulation and current speed in the GCS channel for a range of constant and variable Manning numbers from 20 to 50 $m^{1/3}/s$ was examined. The results are presented in section 5.5.1.

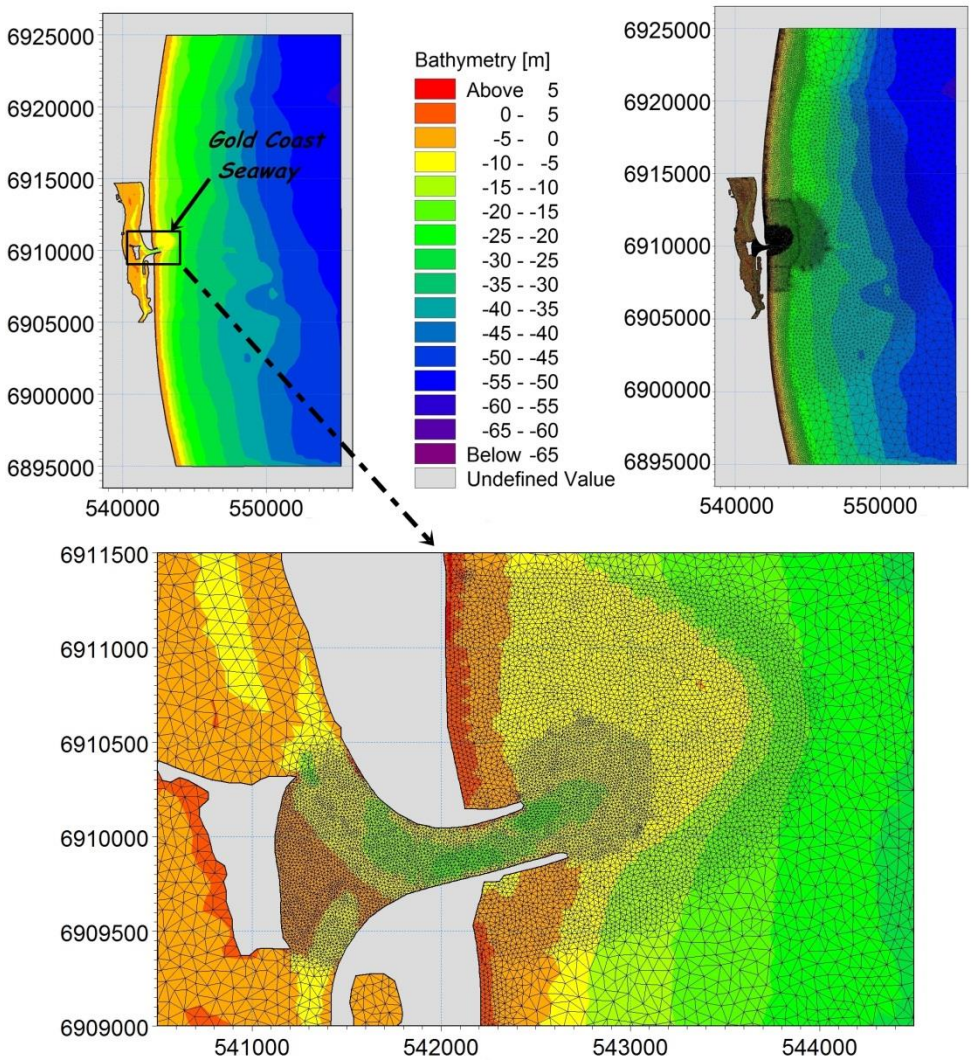

Figure 5.7. Local Model Domain and mesh distribution

Eddy viscosity in the local model hydrodynamics was assumed to be calculated from the Smagorinsky formulation with a constant Smagorinsky coefficient throughout the domain area of 0.28, which is the default value of MIKE21 model. The minimum and maximum eddy viscosity were set to default values of 1.8×10^{-6} and 1.0×10^{11}. Wind data collected by Bureau of Meteorology (BOM) at GCS station (27.9390˚ S and 153.4283˚ E) was incorporated uniformly across the model domain. Wave radiation stresses computed from the wave model were updated in HD module at each time step.

The fully spectral formulation was selected as basic equation of SW module based on the results of the sensitivity analysis which are presented in section 5.5.2.2. The wave breaking parameter γ, which corresponds to the ratio between the maximum possible wave height and the local water depth, was also used as one of the calibration factors for sediment transport and morphological changes in the area, as suggested by Bertin et al. (2009b). The rate of wave

height decay in the surfzone determines the gradient of radiation stress, and therefore controls the magnitude and the cross-shore shape of longshore currents. Thus, it is very important in reproducing the morphological changes more accurately (Bertin et al., 2009b). The sensitivity of the model results to variations of γ, and the final value of used γ, are explained in section 5.5.2.3. Water level and current variations in the SW module were updated at each time step from the HD module. Model predictions sensitivity to the bottom friction coefficient in SW module was also investigated and explained in section 5.5.2.5.

Sediment transport in the research area depends on the combined action of currents and waves. Therefore, as explained in section 5.2.1.3, the module that was used for sediment transport modelling was "Combined Wave and Current". When generating the sediment transport table, which was explained in section 5.2.1.3, the influence of ripples, bed slope and streaming were included in determining the rate of sediment transport. It should also be noted that all the open boundaries of the ST module were defined as boundaries with zero sediment flux gradient for outflow and zero bed change for inflow.

5.3 Calibration and verification Data

Current calibration and verification data were obtained from two deployments: (1) two vertically and one horizontally oriented Acoustic Doppler Current Profilers (ADCPs) inside the Seaway Channel in 2009 (Stuart et al., 2010) and (2) one ADCP deployed offshore of Narrowneck (south of the Seaway) in 2011 (Stuart and Lewis, 2011) (See Table 5.3 and Figure 5.8). For the first deployment, the vertically oriented ADCPs recorded velocity profiles every 30 minutes, from 12 May till 11 June (Seabed ADCP) and 1st May till 20th May, 2009 (Pipeline ADCP). Depth-averaged velocities were derived by averaging all the ADCP bins but neglecting the last bin data next to the water surface. This was because the top cell is influenced by the potential penetration through the surface and the noise associated with the signal moving through water and then interfacing with air. The horizontally oriented ADCP recorded data from the 25th February to 7th June, 2009 every 10 or 20 minutes. The deployments depths for Seabed, Pipeline and Horizontal ADCPs were about 8.5, 12 and 10.5 metres, respectively. These data were collected and used previously for the Smart Release project (Stuart et al., 2010). The sampling frequencies were selected to fully capture the tidal cycle. For the offshore ADCP deployment at Narrowneck, the deployment depth was 7.5*m* and it recorded current data every 10 minutes in two time intervals of 12th April till 4th May, and 9th May till 30th May, 2011. For simulation of Narrowneck ADCP data, the bathymetry file was updated for the Narrowneck area using detailed survey data from June 2011.

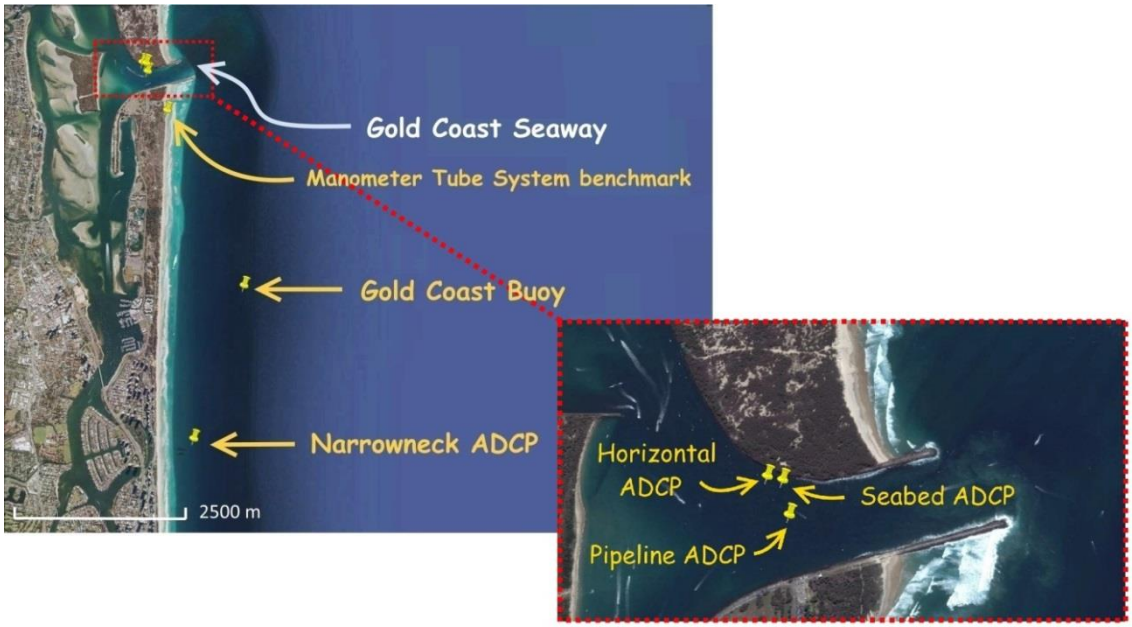

Figure 5.8. Locations of the ADCPs and Gold Coast buoy

Table 5.3. Summary of measurement stations and data used in this study

Station	Latitude, Longitude (E, S)	Waves	WL	Current	Used data
Seabed ADCP	153.4254˚ E, 27.9341˚ S		✓		12-31 May 2009
Horizontal ADCP	153.42484˚ E, 27.9340˚ S		✓		1-31 May 2009
Pipeline ADCP	153.4257˚ E, 27.9352˚ S		✓	✓	1-20 May 2009
Narrowneck ADCP	153.43535° E, 27.986˚ S	✓	✓	✓	13 April- 4 May 2011
Bunker manometers	Up to 500*m* offshore from 153.429° E, 27.941˚ S		✓		21 May 2009 (7 Manometers)
Gold Coast buoy	153.4422° E, 27.9655˚ S	✓			1-30 May 2009

Additional water level data obtained by Jafari et al. (2011) in 2009 using manometer tubes in a shore normal transect extending from the beach out to 500*m* offshore just south of the sand bypassing jetty were also used. The data used were measured on 21st May and 17th June 2009 and are described in detail by Jafari et al. (2011). In this study, Pipeline ADCP current and WL data was used for calibration, and others were applied for verification.

Offshore wave buoy (Gold Coast buoy, Figure 5.8) data for East Coast Low (ECL) in May 2009 was used for calibration of the wave model. Both offshore wave buoy and Narrowneck ADCP,

which recorded wave parameters (significant wave height, peak wave period and peak wave direction) every half an hour and every hour, respectively, were used for verification of the SW model.

For verification of the LST and, finally, the morphological evolution, the chosen simulation period was from August 2008 to June 2009, in which surveying data was available. This time interval encompassed the measured hydraulic flow data time in the GCS, and also a significant amount of morphological change occurred in response to two severe storms during this time interval (as explained in chapter 4). Therefore, this model can be applied for morphological simulation of the case study in consecutive stages of the research.

5.4 Accuracy metrics

Using accuracy metrics is very common among researchers to quantify the performance of modelling. A number of accuracy metrics used in this study are explained in section 5.4.1. Moreover, their application in other studies is illustrated in section 5.4.2.

5.4.1 Accuracy metrics definitions

Accuracy metrics used in this study are as follows:

***R* - Correlation coefficient**

A common indicator to check whether two series of measured and predicted data are related is the correlation coefficient (*R*). The correlation coefficient *R* measures the tendency of the predicted and measured (observed) values to vary together linearly. It can range from -1 to 1, with negative values indicating that the measured and predicted values tend to vary inversely. It should be noted that *R* does not show how significant the correlation is since it does not take the distribution of measured and modelled data into account. That is, even if the correlation is close to 1, the predicted and observed values may not match each other, they only tend to vary similarly. The formula for calculation of *R* is given by Sutherland et al. (2004a) as:

$$R = \frac{\left\langle \left(X_C - \langle X_C \rangle\right)\left(X_M - \langle X_M \rangle\right) \right\rangle}{\sigma_M \sigma_C} \tag{5.21}$$

With σ_M and σ_C being the measured and predicted standard deviations, and angular brackets ⟨ ⟩, denote averaging procedure.

Skill - Index of agreement (Willmott, 1981)

The Index of agreement, or Skill, represents the ratio of the mean square error and the potential error as shown in equation (5.22). The potential error in the denominator represents the largest value that the squared difference of each measured and modelled pair can attain. This accuracy metric is very sensitive to the peak conditions and insensitive to the low conditions of the variable because of the mean square error in its numerator. The range of Skill lies between zero (no correlation) and 1 (perfect fit).

$$Skill = 1 - \frac{\sum |X_C - X_M|^2}{\sum \left(|X_C - \overline{X}_M| + |X_M - \overline{X}_C| \right)^2} \tag{5.22}$$

Let X_M be a set of N observed/measured values, and X_C a set of N computed/predicted by model values. $\overline{X}$ is the average of selected modelled or measured variables. Some applications of "Skill" show that it has some disadvantages: first, relatively high values (more than 0.65) of "Skill" may be obtained even for poor model fits, which leaves a narrow range for model calibration. Second, "Skill" is not sensitive to systematic over, or under, predictions of the model. Therefore, this statistic should be used together with other statistics to judge the prediction accuracy.

RMS – Root Mean Squared Error

RMS is a frequently used measure of the size of the discrepancies between the values predicted by a model and the values actually measured (observed) from the environment that is being modelled. The individual differences are also called residuals, and the RMS aggregates them into a single measure of predictive power.

$$RMS = \sqrt{\left\langle \left(X_C - X_M \right)^2 \right\rangle} \tag{5.23}$$

MAE – Mean Absolute Error

MAE is given by (Sutherland et al., 2004b) as follows:

$$MAE = \left\langle |X_C - X_M| \right\rangle \tag{5.24}$$

the use of modulus in MAE makes it non-analytic and therefore harder to work with than RMS; however, it is less influenced by outliers than RMS (Hedges, 2001). It is applicable for both

vector and scalar quantities, and also includes both errors of magnitude and direction at the same time.

RMAE – Relative Mean Absolute Error

RMAE for parameters like wave height which are scalar:

$$RMAE = \frac{\langle |X_C - X_M| \rangle}{\langle X_M \rangle} \tag{5.25}$$

RMAE for parameters like velocity which are vector:

$$RMAE = \frac{\langle |X_C - X_M| \rangle}{\langle |X_M| \rangle} \tag{5.26}$$

ARMAE – Adjusted Relative Mean Absolute Error

ARMAE includes the errors in measurement 'ΔX_M' and represents the relative error, over and above the estimated error in measurements:

$$ARMAE = \frac{\langle (|X_C - X_M| - \Delta X_M) \rangle}{\langle |X_M| \rangle} \tag{5.27}$$

with negative values of the numerator, which means that the computed value is within the error band range of the measured value, set to zero before averaging. $\Delta H_M = 0.1m$ for wave height, and ΔV_M = 0.05m/s for current velocity (Van Rijn et al., 2003). The measurement errors are related to the physical size of the instrument, the principle that is applied in measurement and the conversion principle including the assumption of applied theories (Sutherland et al., 2004b).

Bias – average error

Bias, or the average error, is a measure of aggregate model bias, although values near zero can be misleading since negative and positive discrepancies can cancel each other. Bias shows if the model is over predicting on average (positive bias) or under predicting (negative bias).

$$Bias_X = \langle X_C - X_M \rangle \tag{5.28}$$

$$\mathrm{Re}l.Bias_X = \frac{Bias_X}{\langle X_M \rangle} \times 100 \tag{5.29}$$

SI – Scatter Index

SI is the dimensionless form of RMS.

$$SI_X = \frac{\sqrt{\left\langle (X_C - X_M)^2 \right\rangle}}{\left\langle X_M \right\rangle} \times 100 \tag{5.30}$$

BCSI – Bias-Corrected Scatter Index

$$BCSI_X = \frac{\sqrt{\left\langle (X_C - X_M - Bias_X)^2 \right\rangle}}{\left\langle X_M \right\rangle} \tag{5.31}$$

5.4.2 Accuracy metrics in previous studies

Various accuracy metrics have been applied in the literature to assess model skills, including RMS, RMS Percentage, Correlation coefficient for water elevation and current velocity. Table 5.4 shows some of the acceptable accuracy metrics which have been presented in various papers. Using accuracy metrics is very common among researchers to quantify the performance skill of the model, since applying these errors is essential to make comparisons between various models feasible.

In some studies, like those of Warner et al. (2005), Liu et al. (2009) and Elias and Hansen (2013), the index of agreement or skill that has been proposed by Willmott (1981) was applied to assess the skill of their model for prediction. One of the advantages of model skill is that it is dimensionless so a comparison over multiple parameters can be made. Some others like Elias et al. (2012) used an index of agreement or skill for flow verification. They also assessed the quality of the wave modelling by calculating relative Bias, *SI*, and BCSI for both significant wave height (H_s), and mean wave period (T_{mean})

Table 5.4. Acceptable accuracy metrics range based on literature

Reference	Water Level			Current speed		
	RMS/max Variation %	Correlation coefficient	Skill	RMS/max Variation %	Correlation coefficient	Skill
Sankaranarayanan et al. (2014)	7.8-8.9	0.96-0.97	-	8.6-10	0.91-0.93	-
Jiang et al. (2013)	3.5-9.3	0.97-0.98	-	10.1-22.2	0.63-0.9	-
Bertin et al. (2009b)	2-6.5	-	-	-	-	-
Elias et al. (2012)	-	-	-	3-12	-	0.74-0.99
Elias and Hansen (2013)	-	-	0.97-0.99	-	-	0.68-0.9

	Significant Wave Height (Hs)				Mean Period (s)		
	RMS (m)	BCSI	Rel. Bias %	SI%	BCSI	Rel. Bias%	SI %
Bertin et al. (2009b)	0.25	-	-	-	-	-	-
Elias et al. (2012)	-	0.2	-12.6	23	0.119	-3.6-1.1	12.5

Van Rijn et al. (2003) and Sutherland et al. (2004b) suggested the use of RMAE as one of the accuracy metrics for hydrodynamic simulation, as it is applicable to vectors as well as scalars and includes errors of magnitude and direction in a single statistic. ARMAE was used to reduce the effect of measurement error. A classification table was adopted which categorises the results according to the magnitude of the ARMAE for each parameter, which is presented in Table 5.5. As noted in Table 5.5 various ranges were used in these two papers to judge the quality of the modelling.

Table 5.5. Qualification of error ranges

	Wave Height; ARMAE (Van Rijn et al., 2003)	Velocity; ARMAE(Van Rijn et al., 2003)	Velocity; ARMAE (Sutherland et al., 2004b)
Excellent	< 0.05	< 0.1	<0.2
Good	0.05-0.1	0.1- 0.3	0.2-0.4
Reasonable/fair	0.1- 0.2	0.3- 0.5	0.4-0.7
Poor	0.2- 0.3	0.5- 0.7	0.7-1
Bad	> 0.3	> 0.7	>1.0

As noted above, using statistics errors for wave direction is not common among researchers since they are not applicable if directions vary around 0 and 360 degrees. Since the volume of LST can be highly sensitive to wave direction in research areas which are mostly wave dominated, like the one studied in this study, wave direction qualitative assessment should be considered through the visual inspection of the time series data. Since the wave directions were not varying around 0 and 360 degrees in this study, accuracy metrics could be also used for assessing the quality of the wave direction predictions quantitatively.

5.5 Sensitivity analysis of the coupled HD-SW-ST local model

The results of the local model's initial run for the ten month period from August 2008 to June 2009 demonstrated that a significant amount of LST and morphological evolution at the GCS area occurred during the major storm events, particularly the East Coast Low (ECL) in 19-25 May 2009 (with maximum significant wave height of 6 metres at the Gold Coast buoy). Accordingly, and also because of the computational cost of ten month simulations, sensitivity analyses to various factors were initially investigated mainly for a twelve day period, from 18th to 30th May 2009, which included the ECL in 2009. Then, the optimised parameters were then used for the ten month simulations.

In order to reach the final local model setting, several sensitivity analysis tests were carried out. Several factors were used to assess the simulation results. These included: the accuracy of HD parameter predictions at the measurements stations; wave parameter predictions at the Gold Coast buoy; the resultant LST rate; and finally, explained in the next chapter, the skill of the model prediction of the morphological changes. In the following sections a number of the sensitivity analysis settings and results are provided.

5.5.1 Sensitivity analysis of the model results to HD module settings

The initial local models, in which the HD boundary conditions were extracted from global tidal predictions of MIKE, reproduced tidal elevations with much more accuracy than the current speeds. One of the reasons for the poor initial current velocity predictions in the GCS channel was that the initial models only included a relatively short extension of the Broadwater, rather than the whole tidal prism of the GCS. This was one of the main reasons that led to the generation of the regional HD model which was used to extract more accurate water levels at the boundaries of the Broadwater in the local HD module.

Moreover, bed resistance was found to be the main calibration factor for flow simulation in the HD module. Sensitivity analyses of the water level, current speed and direction, at the location of Pipeline ADCP deployment in May 2009, to bed resistance of the domain were carried out. Several simulations using constant or variable bed resistance Manning coefficients (M) through the domain area were carried out. It should be noted that a lower Manning coefficient corresponds to a higher bed resistance and vice versa. The results show that the current speed in the channel is more underestimated when using lower Manning numbers such as 20 $m^{1/3}/s$ and 32 $m^{1/3}/s$, within the Broadwater or through the model domain. The calculated accuracy metrics statistical error for three models, using constant Manning coefficients of 32 $m^{1/3}/s$, 40 $m^{1/3}/s$ and 50 $m^{1/3}/s$ through the domain, are shown in Tables 5.6 to 5.8. As shown, the best accuracy metrics for the current speed and direction were achieved when using Manning coefficient of 40 $m^{1/3}/s$. Thus, the final bed resistance Manning coefficient applied through the model domain was 40 $m^{1/3}/s$, except along the sides of the training walls which were adjusted as 10 $m^{1/3}/s$ in order to represent the roughness associated with the submerged boulders. For the open boundaries of the model, the Manning number (M_n) of 5 $m^{1/3}/s$ was applied for numerical stability as suggested by DHI (2014e).

Table 5.6. Accuracy metrics for water level, current speed and direction predictions at the Pipeline ADCP location, for the period 1st to 20th May 2009 (ECL 2009), using Manning coefficient 32 $m^{1/3}/s$ as bed resistance.

Pipeline ADCP	Skill	Correlation coefficient (R)	RMS/max Variation %	Bias	*SI* %	ARMAE
Water level (m)	0.98	0.97	6.96	0.01	-	-
Current speed (m/s)	0.86	0.84	15.4	-0.13	35.2	0.25
Current direction (°)	0.93	0.86	13.2	-1.67	24.3	0.09

Table 5.7. Accuracy metrics for water level, current speed and direction predictions at the Pipeline ADCP location, for the period 1st to 20th May 2009 (ECL 2009), using Manning coefficient 40 $m^{1/3}/s$ as bed resistance.

Pipeline ADCP	Skill	Correlation coefficient (R)	RMS/max Variation %	Bias	*SI* %	ARMAE
Water level (m)	0.98	0.97	7.02	0.01	-	-
Current speed (m/s)	0.90	0.88	12.9	-0.10	29.7	0.20
Current direction (°)	0.95	0.90	10.9	-0.21	19.9	0.08

Table 5.8. Accuracy metrics for water level, current speed and direction predictions at the Pipeline ADCP location, for the period 1st to 20th May 2009 (ECL 2009), using Manning coefficient 50 $m^{1/3}/s$ as bed resistance.

Pipeline ADCP	Skill	Correlation coefficient (R)	RMS/max Variation %	Bias	*SI* %	ARMAE
Water level (m)	0.98	0.97	7.07	0.01	-	-
Current speed (m/s)	0.90	0.82	13.6	-0.05	31.1	0.22
Current direction (°)	0.93	0.86	13.0	0.86	23.8	0.10

5.5.2 Sensitivity analysis to SW module settings

The sensitivity of the model results were investigated to a number of parameters and settings in the SW module.

5.5.2.1 Application of different wave boundary conditions

As mentioned in section 5.2.4, different wave boundary conditions were applied on the boundaries of the regional SW model with variable offshore extensions of the domain. These boundary conditions included the results from large scale ocean models (ECMWF and WWIII) and also Brisbane buoy wave data measurements. The location of the closest data points of the ECMWF and WWIII models to the study area, as well as the Brisbane buoy, are shown in Figure 5.9.

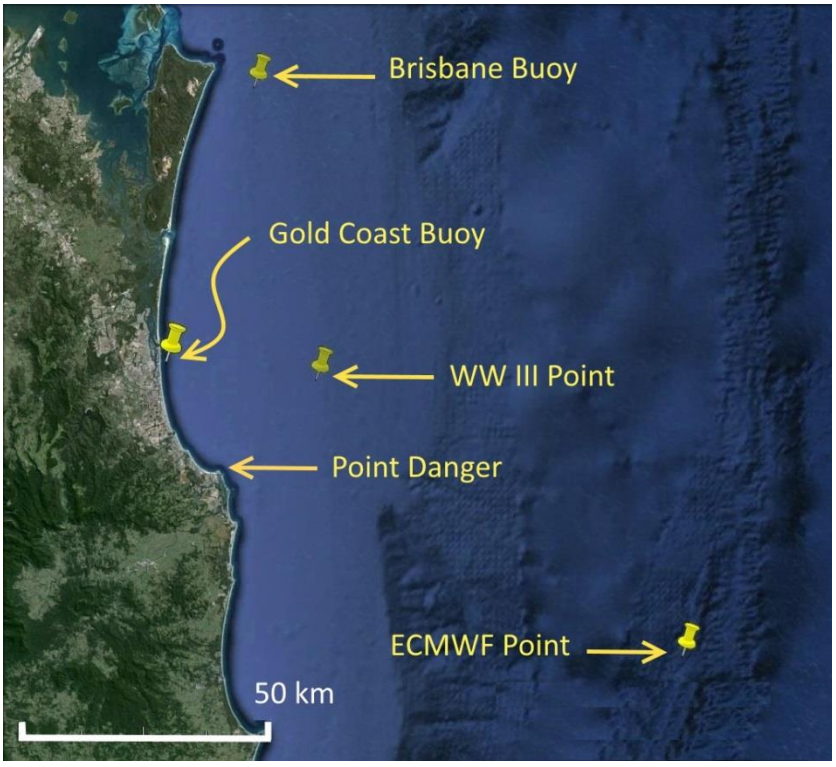

Figure 5.9. Different data points that were applied for SW model boundary condition (ECMWF, WWIII, Brisbane buoy)

The calculated accuracy metrics of the modelled wave parameters at the Gold Coast buoy during the ECL storm in May 2009, using different boundary conditions, are shown in Table 5.9 to 5.11. As shown in Table 5.9 to 5.11, overall, using all of the offshore forcings, including Brisbane buoy, ECMWF, WW3, resulted in acceptable predictions of wave parameters. However, the best results were obtained by using Brisbane buoy measurements as the eastern

boundary of the local model, and also by extracting the lateral boundaries from the regional SW wave model in which Brisbane buoy measured data was used as the boundary conditions (Table 5.11).

Table 5.9. Accuracy metrics for wave parameter predictions at the Gold Coast buoy location for the period 18th May to 27th May 2009 (ECL 2009), using ECMWF as boundary condition, fully spectral formulation and DSD 20

Wave parameter	Skill	Correlation coefficient (R)	RMS	Bias	Rel. Bias %	SI %	BCSI	ARMAE
Significant wave height (m)	0.96	0.94	0.48	-0.14	-4.32	14.7	0.14	0.08
Peak wave period (s)	0.86	0.91	1.22	-0.72	-6.53	11.0	0.09	0.08
Peak wave direction (°)	0.38	0.086	22.85	8.78	9.39	24.4	0.23	0.13

Table 5.10. Accuracy metrics for wave parameters predictions at the Gold Coast buoy location for the period 18th May to 27th May 2009 (ECL 2009), using WW3 as boundary condition, fully spectral formulation and DSD 20

Wave parameter	Skill	Correlation coefficient (R)	RMS	Bias	Rel. Bias %	SI %	BCSI	ARMAE
Significant wave height (m)	0.96	0.94	0.48	-0.15	-4.50	14.7	0.14	0.08
Peak wave period (s)	0.84	0.92	1.47	-1.23	-11.15	13.3	0.07	0.11
Peak wave direction (°)	0.26	0.09	21.98	2.94	3.14	23.5	0.23	0.10

Table 5.11. Accuracy metrics for wave parameters predictions at the Gold Coast buoy location for the period 18th May to 27th May 2009 (ECL 2009), using Brisbane buoy as boundary condition, fully spectral formulation and DSD 20

Wave parameter	Skill	Correlation coefficient (R)	RMS	Bias	Rel. Bias %	SI %	BCSI	ARMAE
Significant wave height (m)	0.98	0.97	0.38	-0.11	-3.48	11.5	0.11	0.06
Peak wave period (s)	0.95	0.91	0.86	-0.31	-2.82	7.8	0.07	0.05
Peak wave direction (°)	0.35	0.21	21.07	5.02	5.36	22.5	0.22	0.09

5.5.2.2 Different SW model formulation

As described in section 5.2.1.1, MIKE SW includes two different formulations: first, the directional decoupled parametric formulation; second, the fully spectral formulation. Running two simulations using each of these formulations illustrated that the rate of sediment transport in the region is sensitive to the selected wave formulation. Using the directionally decoupled parametric formulation in the SW module resulted in an underestimation of the LST rate. The predicted rate for the 12 day simulation, including the ECL storm in May, 2009, was about 20% less than that of the simulation utilizing the fully spectral formulation. Accuracy metrics for wave parameter predictions at the Gold Coast buoy using the directionally decoupled parametric formulation in the model are shown in Table 5.12. Comparing these with the calculated statistical errors of the model in which the fully spectral formulation was used (Table 5.11) illustrated that there is no change in the predictions of significant wave heights and negligible change in the prediction of peak wave directions. However, the peak wave periods in the model using the fully spectral formulation were found to be predicted more precisely (higher). This is one of the reasons for the more accurate predicted LST rate in the former. Therefore, the fully spectral formulation was selected as the basic equation of the SW module in the final local model.

Table 5.12. Accuracy metrics for wave parameter predictions at Gold Coast buoy location for the period 18th May to 27th May, 2009 (ECL 2009), using directionally decoupled parametric formulation

Wave parameter	Skill	Correlation coefficient (R)	RMS	Bias	Rel. Bias %	SI %	BCSI	ARMAE
Significant wave height (m)	0.98	0.97	0.38	-0.11	-3.21	11.5	0.11	0.06
Peak wave period (s)	0.92	0.91	1.06	-0.71	-6.37	9.53	0.07	0.07
Peak wave direction (°)	0.38	0.23	21.40	5.98	6.40	22.9	0.22	0.10

5.5.2.3 Wave breaking parameter (Gamma-γ)

One of the challenges in calibrating the model was the calibration of the LST rate in the area. This rate, estimated in the literature to be approximately 500,000 m^3/yr on average (Delft, 1970; Andrews and Nielsen, 2001; Patterson, 2007), was found to be underestimated in many of the simulations, including the model using the default wave breaking parameter in MIKE (γ = 0.8). In order to find the best value for γ to improve the predicted LST rate, a number of simulations using variable values of γ (from 0.6 to 0.9) were performed. It was found that the predicted LST rate increased when the γ value was increased. For instance, the results of two simulations from 18th May to 30th May, 2009 (including the ECL 2009 period), assuming two different γ values of 0.8 and 0.9, showed that the estimated LST, when using γ = 0.8, was about 30% less than that of using γ = 0.9. Therefore, the maximum LST rate was reached when using γ = 0.9 in the SW module of the coupled model. Finally, a 10 month simulation using γ = 0.9 was carried out, while all other settings remained the same as for the 12 day simulation. The resultant predicted LST rate at ETA 67 was about 410,000 m^3. If this rate had been extrapolated for 12 months, it would become about 500,000 m^3/yr, which is similar to the rates suggested in previous studies. Thus, the γ value was assumed to be 0.9 through the whole region, although previous research and measurements in the area suggest a variable γ, with a decreasing trend in the offshore direction (Jafari, 2013). This assumption is in the upper borderline of the values which have been suggested by Battjes and Stive (1985).

5.5.2.4 Degree of directional spreading of waves

Another parameter that the simulated significant wave heights and peak wave directions at the Gold buoy location, and also the resultant LST rate, were found to be sensitive to was Directional Standard Deviation (DSD) at the boundaries of the SW module. This parameter is used at the boundaries of the SW module to account for the degree of the directional spreading of waves. Several simulations using a range of values for DSD from 10 to 50 degrees were conducted, and the results were compared. As an example, the calculated accuracy metrics based on the comparison of the measured and predicted wave parameters at the Gold Coast buoy using DSD = 40 (degrees) are shown in Table 5.13.

Table 5.13. Accuracy metrics for wave parameter predictions at Gold Coast buoy location for the period 18th May to 27th May, 2009 (ECL 2009), using DSD 40

Wave parameter	Skill	Correlation coefficient (R)	RMS	Bias	Rel. Bias %	SI %	BCSI	ARMAE
Significant wave height (m)	0.96	0.97	0.51	-0.33	-9.97	15.51	0.12	0.09
Peak wave period (s)	0.95	0.91	0.87	-0.33	-3.00	7.82	0.07	0.05
Peak wave direction (°)	0.31	0.23	20.0	1.74	1.86	21.4	0.21	0.07

Comparing these with the results when using DSD = 20 (Table 5.11) illustrate that the skill of model prediction of significant wave height and peak wave direction, when using DSD = 20, is higher than that when using DSD = 40. The peak wave period predictions did not change in these two simulations, as was expected. The calculated LST rates were also compared for ten month (from August 2008 to June 2009) and 12 day (from 18th to 30th May 2009) simulations using these two DSD values. It was found that the predicted LST rate for the ten month simulation was about 30% less when using DSD = 40 compared to DSD = 20. In addition, this rate was about 65% less for the 12 day (including ECL 2009) simulation, when using DSD40 compared to DSD 20. The same comparisons were done for the other simulations using DSD values of 10, 30 and 50. The calculated accuracy metrics based on the comparison of the measured and predicted wave parameters at the Gold Coast buoy using DSD = 10 (degrees) are shown in Table 5.14. Finally, it was found that the best results for accuracy metrics and the LST rate are obtained when using DSD value of 10 degrees. Thus, a constant value of 10 degrees was finally used for the whole simulation time.

Table 5.14. Accuracy metrics for wave parameters predictions at the Gold Coast buoy location for the period 18th May to 27th May 2009 (ECL 2009), using Brisbane buoy as boundary condition, fully spectral formulation and DSD 10

Wave parameter	Skill	Correlation coefficient (R)	RMS	Bias	Rel. Bias %	SI %	BCSI	ARMAE
Significant wave height (m)	0.98	0.96	0.36	-0.03	-0.92	11.04	0.11	0.05
Peak wave period (s)	0.95	0.91	0.86	-0.31	-2.78	7.76	0.07	0.05
Peak wave direction (°)	0.40	0.22	22.0	6.93	7.41	23.52	0.22	0.11

5.5.2.5 Sensitivity to Other parameters

The sensitivity of the model results to other parameters such as "White Capping" and "Bottom friction", in SW module, was also investigated. It was found that the sensitivity of the prediction of wave parameters at the Gold Coast buoy to these parameters is negligible. On the other hand, since increasing both of these parameters will increase the dissipation rate and decrease the wave energy reaching the coastline, and hence the rate of erosion, it was found that these have an inverse correlation with the LST rate. However, this effect is relatively minor. Therefore, the bottom friction was finally specified based on the sediment mean grain size, (d_{50}) of 200 μm, through the domain. In this type of bottom friction definition, the dissipation coefficient depends on both wave hydrodynamics and sediment conditions, unlike the other methods such as using Nikuradse roughness (*kn*). In addition, the default model White Capping, which is based on the defined breaking wave dissipation source function developed by Komen et al. (1996), was used for the final local model (DHI, 2014f).

5.5.3 Sensitivity analysis to ST module settings

5.5.3.1 Application of different wave theories

In the sediment transport (ST) module, when combined current and wave actions are included, the sediment transport rate is found from linear interpolation in a pre-generated sediment transport table (see section 5.2.1.3). In developing the sediment transport table, a number of wave theories can be applied to calculate the wave motion outside the bottom boundary layer. Both classical and semi empirical non-linear wave theories are available (Table 5.15), although

it has been noted by DHI (2014a) that no wave theory exists that covers all hydrodynamic conditions perfectly.

Table 5.15. Wave theories applied in STPQ3D model and their application area

Classic theories	Application area	Semi empirical theories	Application area
Stokes theory 1st, 3rd and 5th Order (Fenton, 1985)	Deep water/ Non- breaking waves	Isobe and Horikawa (1982)	All water depths/Breaking and Non-breaking waves
Cnoidal theory 1st, 3rd and 5th Order (Fenton, 1990)	Shallow water/ Non-breaking waves	Doering and Bowen (1995)	All water depths/Breaking and Non-breaking waves
Vocoidal theory (Swart, 1982)	All water depths/Non-breaking waves		

A major portion of the LST and morphological changes in the August 2008 to June 2009 interval was found to have taken place during the ECL storm in May 2009. Therefore, the simulation of the twelve days from 18th to 30th May 2009, which included the ECL in May 2009 storm period, was performed using the various wave theories in the sediment transport calculation. Then, the resultant LST and morphological changes were compared. As shown in Figure 5.10, the results indicate that classic theories underestimate the beach erosion and the subsequent accretion on the offshore bar, as well as the leakage to the entrance mouth. In addition, the calculated LST rate using the classic theories was found to be 6 to 40% less than those using semi-empirical theories. Between the two available semi empirical theories, the LST rate which was estimated using the Isobe and Horikawa (1982) theory was about 6% less than that of using Doering and Bowen (1995). Therefore, the latter was applied for consecutive simulations.

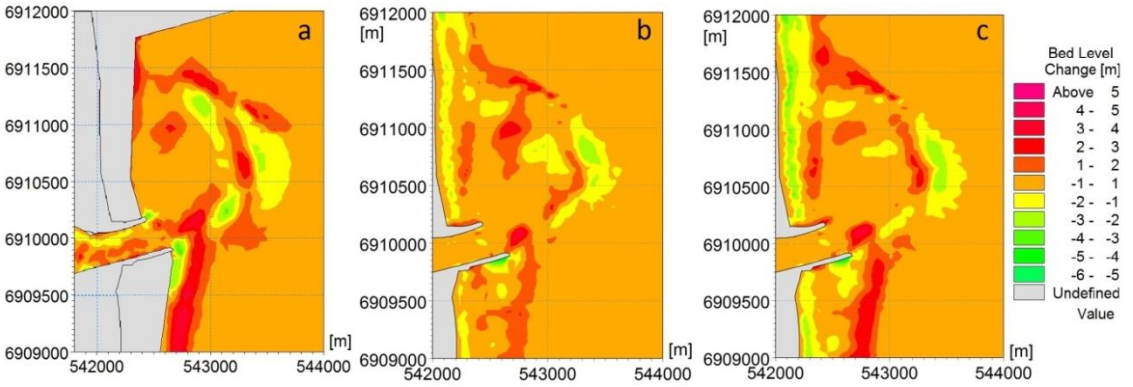

Figure 5.10. Bed level changes (a) between August 2008 and June 2009 survey data (b and c) only for the twelve day simulation from 18th to 30 May 2009, including the ECL in May 2009 storm, (b) Vocoidal classic theory (Swart, 1982) and (c) Doering and Bowen (1995) semi empirical theory was applied (+ : Accretion, -: Erosion)

5.5.3.2 Sediment median grain size

The sediment transport volume was also found to be highly sensitive to the adjusted sediment mean grain size in the area similar to previous studies (Pinto et al., 2006; Fortunato et al., 2014). The best sediment transport results were achieved by incorporating the initial assumption on sediment grain size, i.e. $d_{50}=200$ μm, which was based on previous studies of Turner et al. (2006) and Sennes et al. (2007). The sensitivity analysis shows that application of higher values for the sediment mean grain size, such as $d_{50}=250$ μm, will result in a significant reduction in the predicted LST rate compared to d_{50} of 200μm. This reduction, for the ten month simulation from August 2008 to June 2009, was found to be about 30%.

5.6 Results and discussion

The flow model was calibrated against measured Pipeline ADCP data, and the wave data was calibrated against Gold Coast buoy data for May, 2009 (Figure 5.11, 5.12, Table 5.16 to 5.18). Calibrated flow and wave models were verified against other measured ADCPs, manometers and Gold Coast buoy data. Samples of representative comparisons of the current and wave data are presented in Figures 5.11 to 5.14. These indicate that the model results have a close agreement with the measurements.

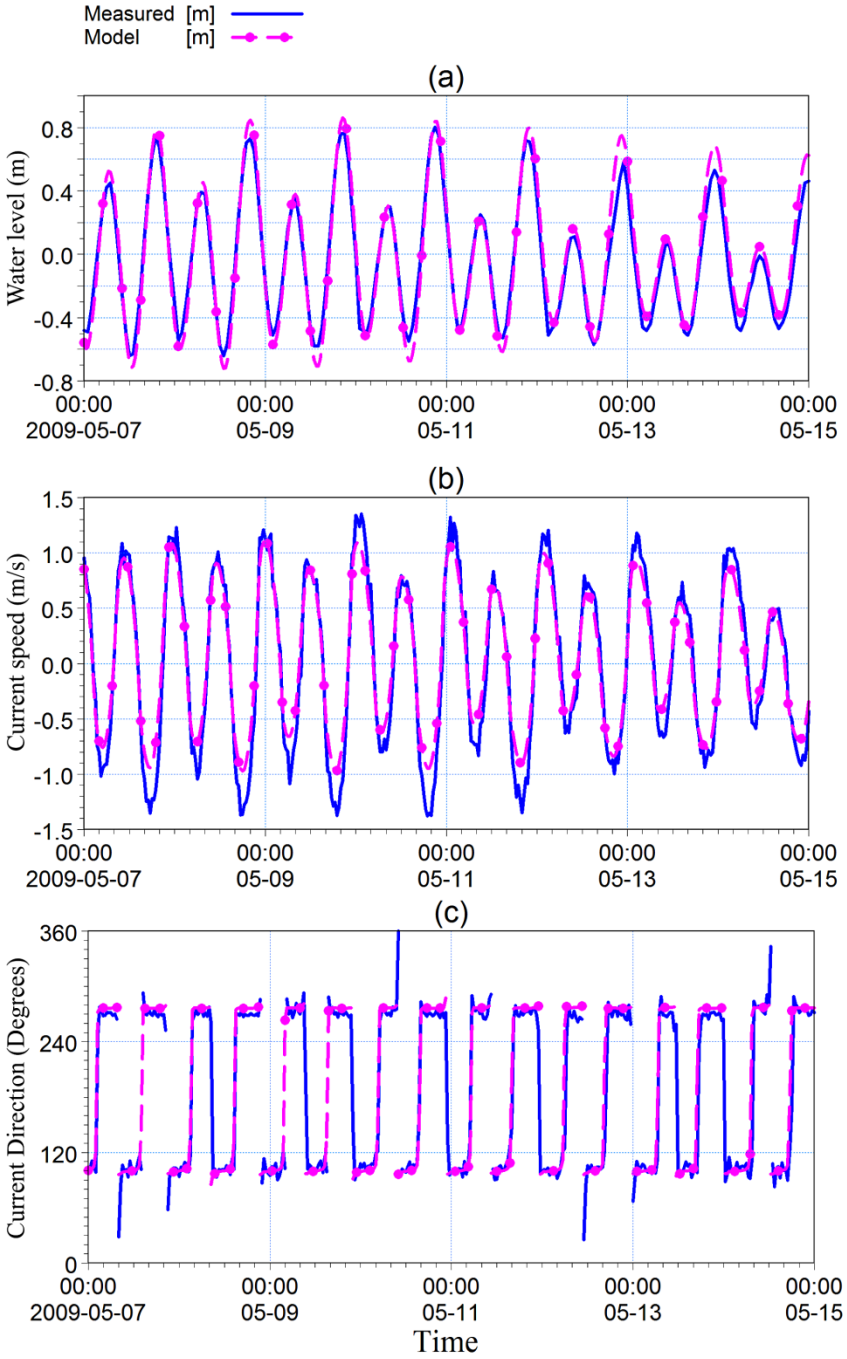

Figure 5.11. Comparison of time series plots of Pipeline ADCP and model simulated (a) water level, (b) current speed (with the sign of the inlet channel parallel velocity component *U*, ebb is positive) and (c) Current direction (clockwise from true North, going against)

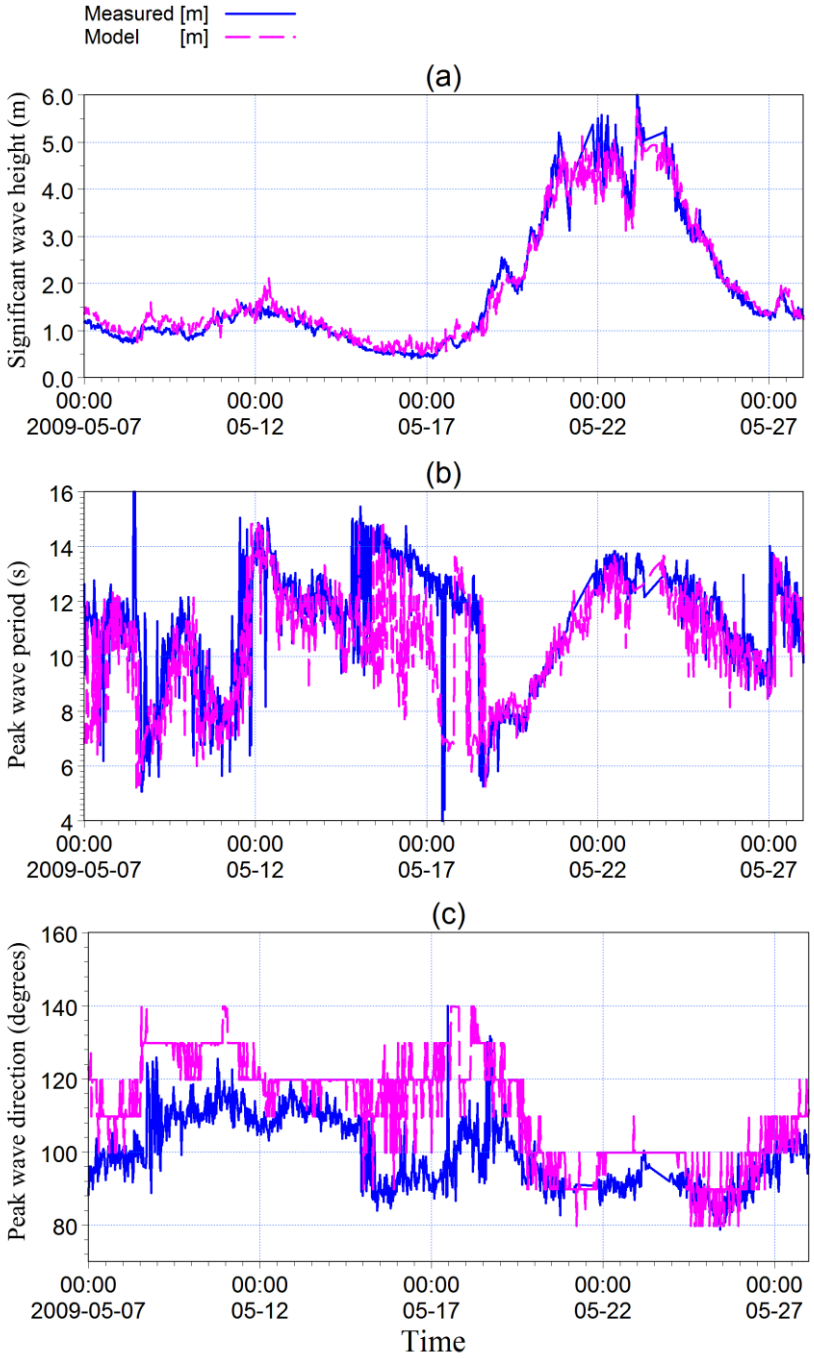

Figure 5.12. Comparison of time series plots of Gold Coast buoy measurement and model simulated wave parameters (a) significant wave height (*m*) (b) Peak wave period (*s*) (c) Peak wave direction (clockwise from true North, coming from)

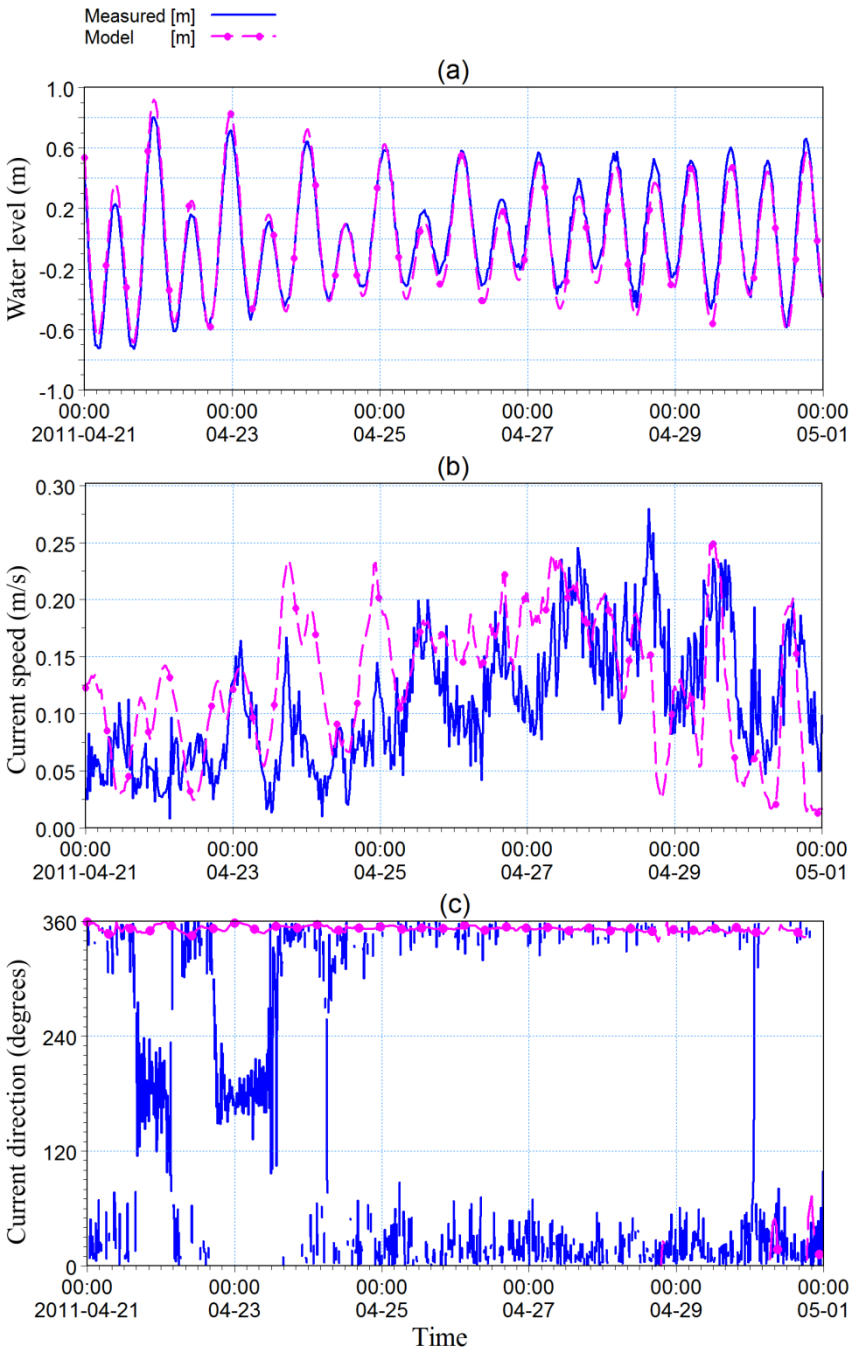

Figure 5.13. Comparison of time series plots of Narrowneck ADCP and model simulated (a) water level (*m*), (b) current speed (*m/s*) and (c) Current direction (clockwise from true North, going against)

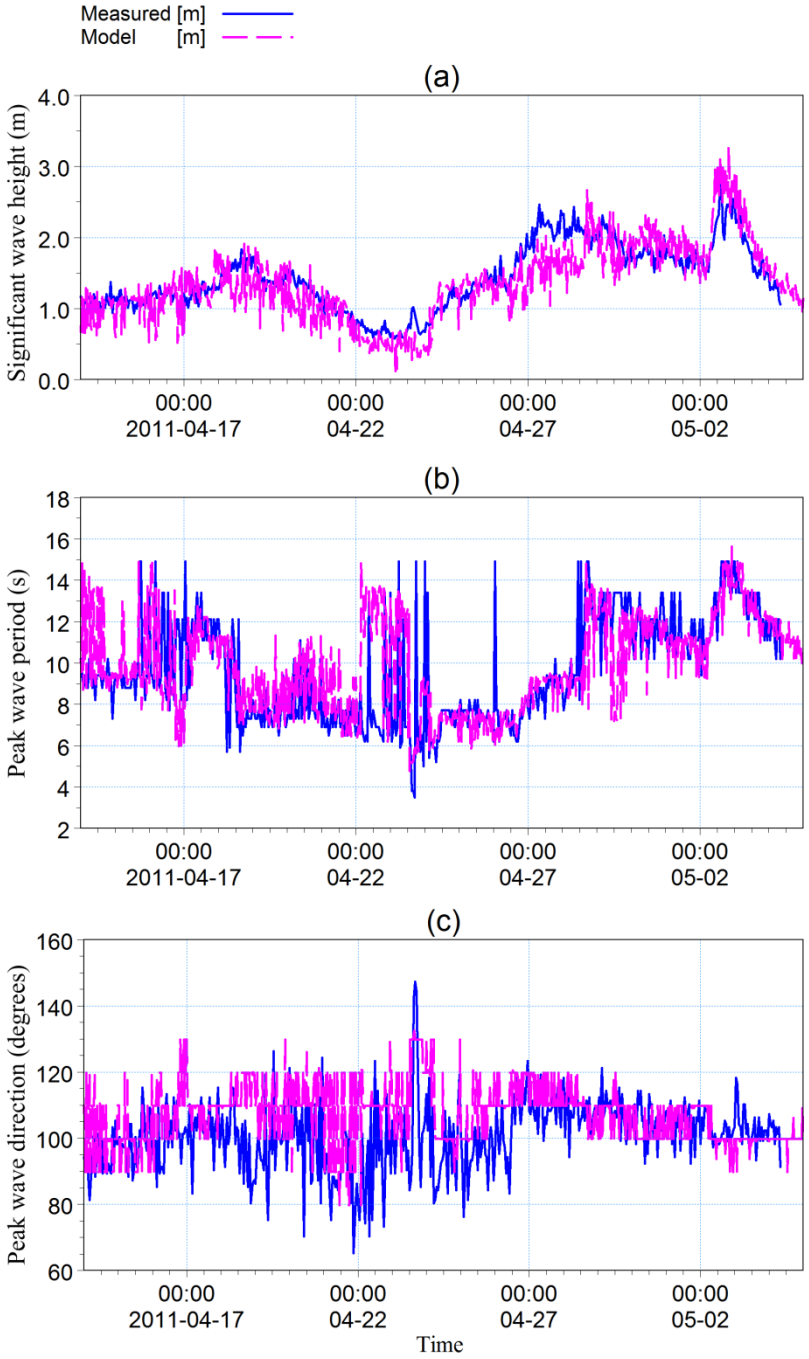

Figure 5.14. Comparison of time series plots of Narrowneck ADCP measurement and model simulated wave parameters (a) significant wave height (*m*) (b) Peak wave period (*s*) (c) Peak wave direction (clockwise from true North, coming from)

In addition to qualitative comparisons, agreement between the predicted and observed flow and wave parameters were assessed by using the accuracy metrics such as Skill, Bias, *R*, RMS, ARMAE, *SI*, BCSI, as shown in Table 5.16 to 5.21. These metrics were calculated to quantify how reliable the model predictions are and compare them with those of previous models. Overall, almost all of the metrics obtained for both flow within the Seaway and offshore Narrowneck as well as wave parameters offshore, represent a good verification of the model

compared to the ones mentioned in the literature (Van Rijn et al., 2003; Sutherland et al., 2004b; Bertin et al., 2009b; Elias et al., 2012; Jiang et al., 2013; Sankaranarayanan et al., 2014).

Table 5.16. Accuracy metrics for water level

Station	Skill	RMS/max Variation %	Correlation coefficient (R)	Bias (m)
Seabed ADCP	0.97	7.4	0.96	0.066
Horizontal ADCP	0.98	6	0.98	-0.069
Pipeline ADCP	0.98	7	0.97	0.013
Narrowneck ADCP	0.99	4.7	0.98	0.013
Bunker manometers	0.94-0.99	5.6-16.1	0.99	-0.05-0.16

Table 5.17. Accuracy metrics for current speed

Station	Skill	RMS/max Variation %	Correlation coefficient (R)	Bias (m/s)	ARMAE
Pipeline ADCP	0.90	13	0.88	-0.10	0.19
Narrowneck ADCP	0.63	16	0.38	0.01	0.45

Table 5.18. Accuracy metrics for current direction

Station	Skill	RMS/max Variation %	Correlation coefficient (R)	Bias (Degree)	ARMAE
Pipeline ADCP	0.95	11	0.9	-0.2	0.08

Table 5.19. Accuracy metrics for significant wave height

Station	Skill	Correlation coefficient (R)	RMS	Bias (m)	Rel. Bias %	SI %	BCSI	ARMAE
Narrowneck ADCP	0.9	0.82	0.31	-0.06	-4.5	22.3	0.22	0.11
Gold Coast buoy	0.99	0.98	0.27	0.056	3.3	15.5	0.15	0.07

Table 5.20. Accuracy metrics for wave direction

Station	Skill	Correlation coefficient (*R*)	RMS	Bias (°)	Rel. Bias %	SI%	BCSI	ARMAE
Narrowneck ADCP	0.58	0.22	13.2	6	5.9	13.1	0.12	0.09
Gold Coast buoy	0.62	0.36	20.5	13	13.35	21.1	0.16	0.14

Table 5.21. Accuracy metrics for peak wave period

Station	Skill	Correlation coefficient (*R*)	RMS	Bias (*s*)	Rel. Bias %	SI%	BCSI	ARMAE
Narrowneck ADCP	0.83	0.63	1.9	0.24	2.5	19.4	0.19	0.11
Gold Coast buoy	0.76	0.57	2.1	-1.07	-9.5	18.7	0.16	0.12

A closer look at the depicted current speed in Figure 5.11 shows that the model predicts the current speed well during ebb tide. However, the peak current speed during the flood tide is not perfectly captured by the model. It should be noted that according to previous studies, the hydrodynamic regime of GCS channel is ebb dominant (Sennes et al., 2007; Mirfenderesk and Tomlinson, 2008). The current model ebb flow velocity prediction has a good agreement with measurement and the calculated bias of -0.17 m/s error is mainly from underestimation of current velocity during flood. Additionally, the error of the current speed, both ebb and flood, prediction in the Seaway Channel against measurement data was calculated and is equal to RMS/maxVariation of 13% which is in the acceptable range based on other studies mentioned in section 5.4.2. Hence, it can be assumed that the negligible shortcoming in prediction of peak velocity in flood tide does not have a significant effect in the final outcome of the model. Overall, the total accuracy metrics calculated for the whole time series of Pipeline ADCP current measurement is within the excellent range based on Sutherland et al. (2004b) and good range based on Van Rijn et al. (2003). Gathering more current speed data in the region to further validate the current circulation in the domain can help to improve the flow prediction of the model.

5.7 Summary and Conclusion

In this chapter, a depth averaged coupled wave, flow and sediment transport model was developed using MIKE 21/3 Coupled Model for the GCS area. In order to improve the prediction while decreasing the simulation time, two HD and SW regional models were

developed. The Local model forcing included tidal heights and wave parameters, which were mostly extracted from the regional HD and SW models respectively, and also wind.

The local coupled model's hydrodynamics were calibrated and verified against current and wave measurements. The current velocity in the model was shown to be primarily sensitive to the choice of friction coefficient and the resultant bed resistance in the area. Several wave boundary conditions, and as a result the extent of domain, were tested to reach the best wave module predictions. The wave direction was also found to be sensitive to the choice of directional spreading index (n_s) or directional standard deviations (DSD). The spectral wave module formulation, wave breaking parameter (γ) and directional standard deviation (DSD) were the wave module parameters which were used for calibration of the rate of coastal erosion and the resultant LST. Sediment mean grain size was found to be another parameter that the resultant LST rate was severely sensitive to.

Skill assessments of the model show that the current two-dimensional hydrodynamic model of the GCS is capable of predicting the hydrodynamic behaviour within the inlet region. Therefore, the calibrated and verified current and wave model was coupled with the sediment transport module to set up a tool to study the sediment transport rate and finally the resultant morphological evolution in the consecutive stages.

6 – Numerical simulation of the longshore sediment transport and morphological changes in the vicinity of the Gold Coast Seaway

6.1 Introduction

In previous studies various approaches were applied to estimate the longshore sediment transport (LST) along the Gold Coast beaches. For instance, Patterson (2007) estimated LST using the 'Queens' method from Kamphuis (1991); Andrews and Nielsen (2001) used numerical modelling and historical analysis from 1990 to 1995; and Splinter et al. (2011) used yearly wave classes and various sediment transport formulas for the period of 1985 to 2009. In some of these studies, the net LST has been estimated to be about 500,000 – 550,000 m^3/yr to the north due to the predominant south-easterly swell wave climate (Delft, 1970; Andrews and Nielsen, 2001). However, other studies have shown that it can vary considerably between different years and along the coastline due to the location, frequency and intensity of storms with respect to the coastline (Patterson, 2007; Splinter et al., 2011). None of these studies simulated full temporal hydrodynamics and sediment transport to estimate LST in the region.

Several numerical studies have investigated the morphological changes of tidal inlets. In some of them, the resultant morphological changes were not calibrated against any subsequent surveys (Bertin et al., 2009b; Williams and Pan, 2011). In some others, the predicted morphological changes were only validated qualitatively against surveyed bathymetries (e.g. Bertin et al., 2009b; Bruneau et al., 2011; Jiang et al., 2013), and the quality of the model performances was based on the author's judgements. There are a few studies which have assessed the performance of the morphological simulation model of tidal inlets quantitatively using "Skill Scores", which are accuracy metrics. For instance, Siegle et al. (2004) calculated skill scores to validate their sediment transport simulation, which only updated the morphology at the last time step, for a 14 day period between two bathymetric surveys in November 1999. The skill scores for the result of their sediment transport model varied in different areas from 0.36 (reasonable but near poor quality) to less than zero (bad quality).

This chapter reports the application of the calibrated numerical model presented in Chapter 5 in simulating the longshore sediment transport (LST) and morphological evolution in the vicinity of the Gold Coast Seaway (GCS). A two dimensional depth averaged numerical model was developed in this study and verified against available observed flow and wave data, as discussed in Chapter 5. This model was then applied to simulate the LST in the area as well as morphological changes of the GCS ebb-tidal delta. The main purpose of this study was to develop a full temporal calibrated process-based morphological model with a reasonable skill in simulation of the morphological evolution in the research area, mainly the GCS ebb-tidal delta. The model performance is quantified using statistical "Skill Scores". This model can help to understand: the governing factors for the morphological evolution of the ebb-tidal delta; sand transport pathways and rates; and to investigate the possible sand sources for the growing ebb-tidal delta. It was also used to assess the suggested conceptual model of sediment transport in Chapter 4 for the simulated period.

6.2 Longshore sediment transport (LST)

In this study the LST rate was estimated, using the numerical simulation of hydrodynamics and sediment transport, over two one year intervals: one with relatively high wave energy and a number of storm events (August 2008 to August 2009); and one with low energy wave conditions and no major storm events (mid-July 2009 to mid-July 2010). As explained in Chapter 5, the LST rate was found to be sensitive to a number of parameters and settings, especially in the SW module. Overall, this rate was underestimated compared to those suggested in previous studies (DHL, 1970; Patterson, 2007). Therefore, the values and settings which resulted in the maximum LST rate, while not affecting the quality of the prediction of the hydrodynamics, were used. The wave breaking parameter (γ) and directional standard deviation (*DSD*) were two of these parameters, which were finally assumed to be equal to 0.9 and 10 degrees, respectively. The LST rate was also estimated by the formulas developed by USACE (1984) and Kamphuis (1991) using wave parameters' time series extracted from the model results for the August 2008 to August 2009 interval. The results were compared to the numerical model prediction and the suggested rate in the Chapter 4 conceptual model.

6.2.1 Analysis of the predicted LST rate

6.2.1.1 August 2008 to August 2009

The following methods have been used to estimate the LST in this region for the August 2008 to August 2009 interval:

- Process-based numerical model (MIKE21/3 coupled model, cf. 5)
- Kamphuis (1991) and CERC (Coastal Engineering Research Center) (USACE, 1984) equations

MIKE 21/3 coupled model results

DHL (1992) study suggested that the LST occurs up to the depth of -15*m* AHD, and no significant transport takes place across the 15*m* depth contour. The bathymetry data of the area indicates that this depth is about 750*m* offshore. Based on USACE (1984) formula, this seaward limit of the LST typically varies from 5 to 18*m* depth, depending on the wave conditions. The Cross-shore distribution of the LST extracted from the model results; shows that due to some rough weather conditions during August 2008 to August 2009, a much less significant sediment transport took place beyond 750*m* offshore (Figure 6.1). Therefore, a 1100 metre cross-shore section at the Narrowneck location (ETA67- located approximately 6 *km* south of the GCS, Figure 6.2), which is up to -20*m* depth, was considered as the active zone to determine the net LST. The results of the model indicate that this net LST value for the 12 month simulation from August 2008 to August 2009 was approximately 530,000 m^3/yr. This result is in close agreement with the 500,000 m^3/yr LST evaluated by Delft (1970), as well as the 550,000 m^3/yr mean LST potential (1985 - 2009) estimated by Splinter et al. (2011) at ETA 67, and the 550,000 m^3/yr achieved by Patterson (2007) at the Narrowneck location using the 'Queens' method of Kamphuis (1991).

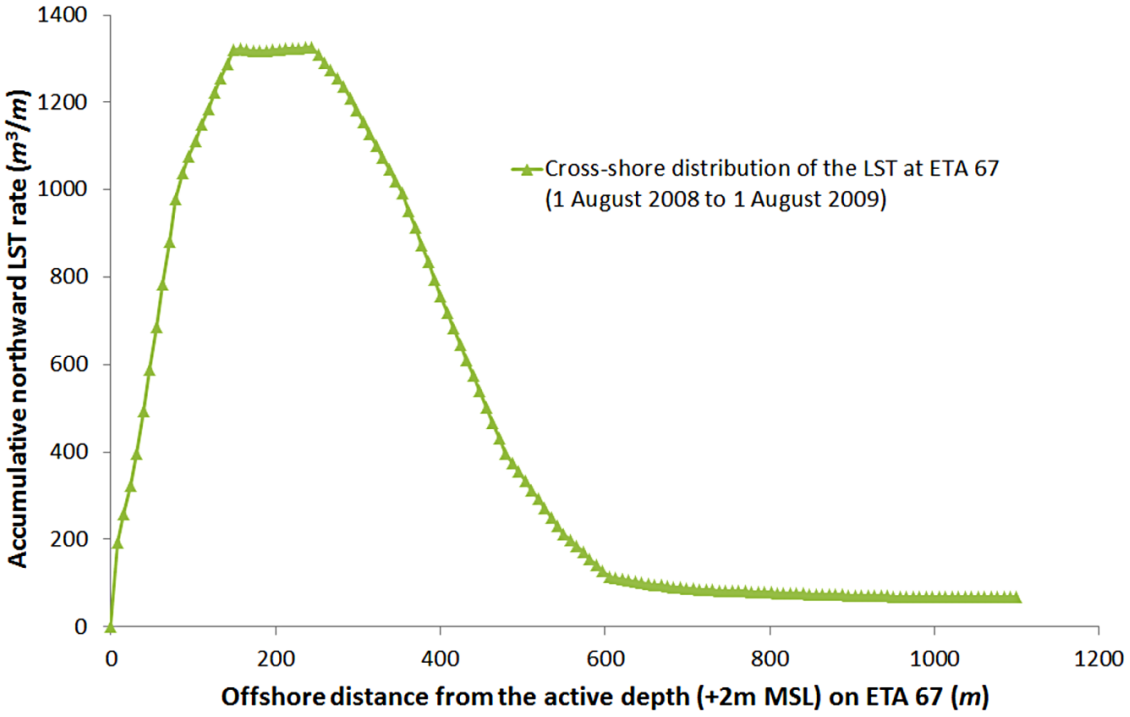

Figure 6.1. Cross-shore distribution of the accumulative LST at ETA 67 during 12 month simulation from 1 August 2008 to 1 August 2009

The accumulative LST rate was also estimated for another cross section close to the ETA 77 (Figure 6.2), where the maximum LST was recorded by the model. The resultant LST rate for the twelve month period was 610,000 m^3/yr. This is relatively close to the suggested net LST rate in 2009 at ETA 79 by Splinter et al. (2011), which was about 700,000 m^3/yr. However, based on the analysis presented in Chapter 4, the suggested LST rate for the whole year near the GCS was about 1,000,000 m^3/yr. It should be noted that the conceptual model's rate was based on the rate of the ebb-tidal delta growth, inlet channel contribution to this growth, and the measured rate of artificial bypassing. In estimation of this rate it was suggested that the major portion of the ebb-tidal growth was sourced by the LST leakage offshore from the sand bypassing system. The total artificial bypassing rate for the whole year from August 2008 to August 2009 was 599,000 m^3.

Figure 6.2. Locations of some of the GCC survey lines: ETA 67 (Narrowneck), ETA 77 and 79 (Main beach)

To investigate the reason for the model underestimation of the LST rate, compared to the suggested one for this period based on the conceptual model in 4, first, the time series of the simulated LST was analysed and also compared to the time series of the rate of artificial bypassing provided by GCWA (Figures 6.3 and 6.4). It should be noted that the provided sand bypassing rates represent only the sand volumes portion within the pumped mixture in the pipes (R. Tomlinson, personal communication, 2015). Second, using the wave parameters time series extracted from the model results in the suggested LST formulas of (USACE, 1984) and Kamphuis (1991), the LST rate was calculated and compared to the predicted one in the model.

From the comparison of the time series of the simulated LST and the artificial bypassing rates (Figures 6.3 and 6.4) a number of findings became evident. Even if it was assumed that the entire LST rate was being captured by the sand bypassing system and so there was no leakage of the LST to the ebb-tidal delta, the model underestimated the LST rate for most of the simulation period (Figure 6.3). Based on data provided by GCWA, there was no artificial sand-bypassing for more than three weeks from 18th May to 11th June, 2009 because of plant shut down due to

budget restraints. Considering this fact, the underestimation of the LST rate compared to the volumes of artificial bypassing is illustrated more significantly in Figure 6.4. Based on the analysis of the detailed daily rates of sand bypassing and the simulated LST, it was found that during the calmer weather conditions the sand bypassing rate (if it was working), was higher than the simulated LST rate in the model. This suggests that the model under predicts the LST rate during calmer wave conditions. This is based on the assumptions that the bypassing rate can be used as a measure of the LST (WBM, 2013), and the cross-shore sediment transport contribution in the bypassing rate is insignificant.

Based on the analysis presented in Chapter 4, there were three SE storms ($H_s > 3m$ at GC buoy) in the ten month period from August 2008 to June 2009 (two consecutive survey data collections). The first one, which was the least significant, was on the 4th and 5th September, 2008 with a W_{PT} (the total storm wave power, as defined in 4, equation (4.14)) of about 6×10^9 *W.s/m*. The bypassing rate during this minor storm was about 22,000 m^3 and the simulated LST rate was about 15,000 m^3. The second storm, between 30th March 2009 to 3rd April 2009, was more significant with a W_{PT} of 45×10^9 *W.s/m*, and was related to the generated waves from tropical cyclone Jasper. The rate of sand bypassing during that storm was approximately a third of the simulated LST rate (24,000 m^3 against 60,000 m^3). The higher rate of simulated LST compared to the actual bypassing during this storm suggests that the model does not underestimate the LST rate during major storm events, as it does for calmer wave conditions and minor storms. In addition, these results confirm the previous suggestion of a major leakage of the LST offshore sand bypassing system during major storm events (WBM, 2001). During the major ECL storm in May 2009 (20th to 25th) (W_{PT} of 106×10^9 *W.s/m*), which resulted in a significant LST, there was no artificial sand bypassing due to plant shut down. This means that the modelled LST in this period (about 200,000 m^3), was either trapped behind the southern training wall or leaked to the ebb-tidal delta. This will be discussed further at the end of this section.

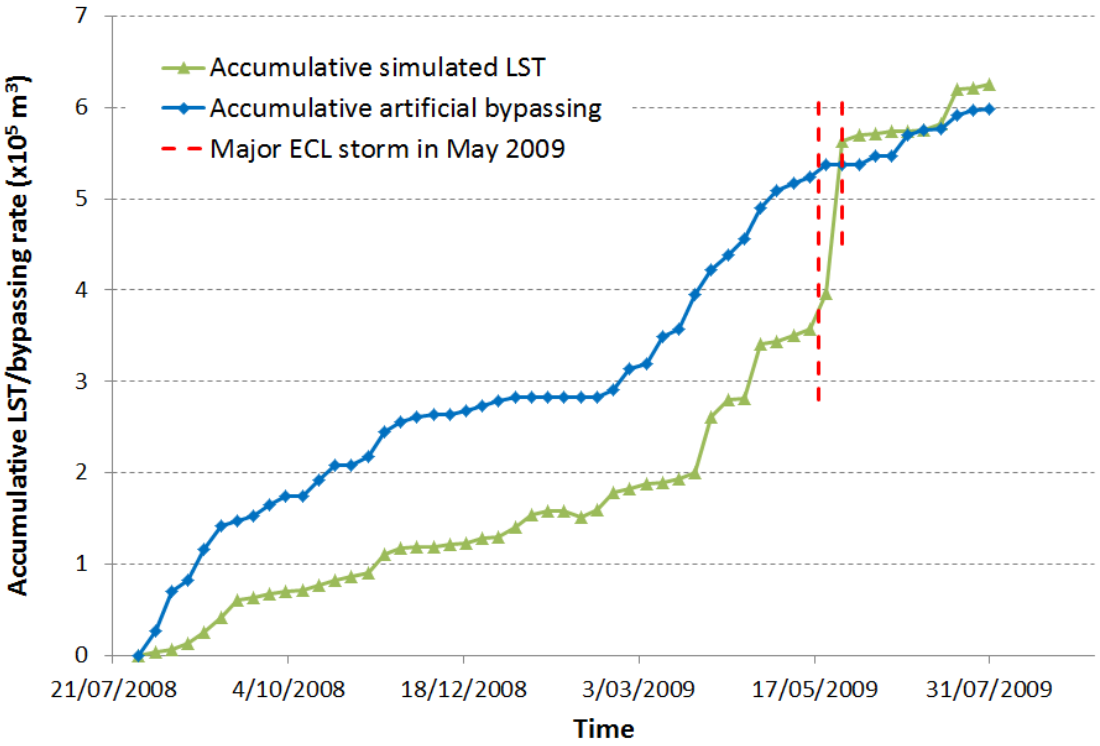

Figure 6.3. Accumumulative simulated LST rate at ETA 77 and the accumulative artificial bypassing rate from 1st August 2008 to 31 July 2009 (based on data provided), with ECL storm interval shown with dashed red lines

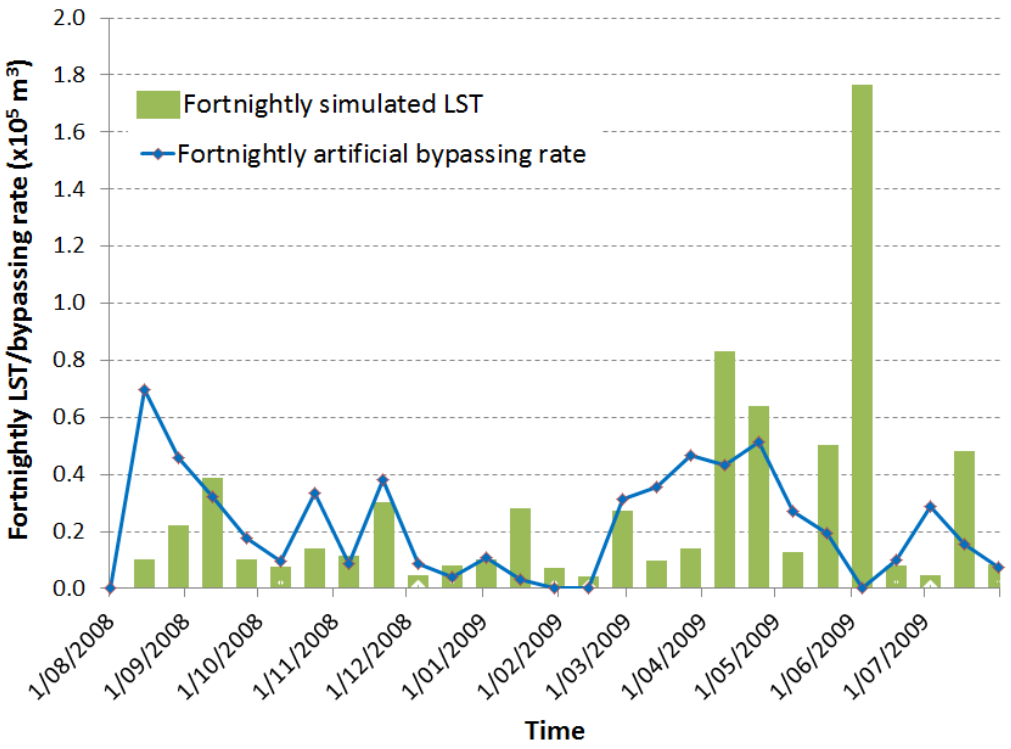

Figure 6.4. Fortnightly simulated LST rate at ETA 77 and the artificial bypassing rate

CERC and Kamphuis (1991) formulas

The LST rate was also estimated for the twelve month interval, August 2008 to August 2009, at ETA 77, by substituting the required parameter (wave and beach slope) time series extracted from the model results into the LST formulas suggested by USACE (1984) (CERC) and Kamphuis (1991) (equations (6.1) and (6.2), respectively). The CERC formula was developed by the US-Corps of Engineers and related the LST rate to the longshore wave energy flux (USACE, 1984). The Kamphuis (1991) formula for LST rate was generated based on dimensional analysis and calibration using three-dimensional, mobile-bed hydraulic beach model experiments performed with both regular and irregular waves and existing field data.

$$Q_{t,vol} = \frac{K}{16(1-p_s)(S_s-1)\sqrt{\gamma}}\sqrt{g}H_{s,br}^{2.5}\sin(2\theta_{br}) \tag{6.1}$$

$$Q_{t,vol} = \frac{2.27}{(1-p_s)(\rho_s-\rho_w)}H_{s,br}^{2}T_p^{1.5}m_b^{0.75}d_{50,s}^{-0.25}\sin^{0.6}(2\theta_{br}) \tag{6.2}$$

In which, $Q_{t,vol}$ is the LST volume (m^3/s, including pores), K is an empirical coefficient, p_s is the sediment porosity factor (≈ 0.4), S_s is sediment specific gravity, ρ_s is sediment density (≈ 2650 kg/m^3), ρ_w is the seawater density (≈ 1025 kg/m^3), γ is the wave breaker index (0.9 in the model), g is the acceleration due to gravity (9.81 m/s^2), $H_{s,br}$ is significant wave height at breaking (m), θ_{br} is wave angle at breaking (between wave crest line and coastline; or between wave propagation direction and shore normal direction), T_p is peak wave period (s), m_b is the beach slope defined as the ratio of the water depth at the breaker line and the distance from the still water beach line to the breaker line, and $d_{50,s}$ is the median sediment size in surfzone ($0.0002m$).

Application of CERC and Kamphuis (1991) formulas in previous studies

There are a number of studies which used empirical formulas to estimate the LST rates and compared them to the rates measured in lab experiments or in the field (van Rijn, 2002; Smith et al., 2003; Shanas and Kumar, 2014). The recommended value for K, in equation (6.1), by USACE (1984) is 0.39. However, they suggested that judgment is required in applying this equation and the accuracy of the resultant LST rate from this formula is about ± 50% (USACE, 1984). Therefore, the CERC equation is best used if the K coefficient is calibrated using data for a particular site (Smith et al., 2003). A variety of K values were applied in different studies to calibrate this expression for each case study (DHL, 1992; Güner et al., 2011; Shanas and Kumar, 2014) . Güner et al. (2011) obtained the LST rates at Karaburun coastal village located

near the south west coast of the Black Sea, Northwest of Istanbul, with average wave height of 0.9*m*, using CERC and Kamphuis (1991) formulas as well as LITDRIFT numerical model. They suggested that the CERC equation overestimated the net LST rates compared to the Kamphuis (1991) formula and the numerical model (LITDRIFT) by factors of 4 and 5 respectively. However, the resultant LST rate using Kamphuis (1991) formula had a close agreement with the result of the numerical model (10.8% difference) for the net LST.

Smith et al. (2003) compared the measured LST rates in a series of large scale laboratory tests and compared it with the rates obtained from CERC and Kamphuis (1991) formulas. They concluded that using the recommended *K* value (0.39) in CERC formula overestimated the LST rate by a factor of 3 to 8 depending on the breaker type (plunging or spilling respectively). However, estimation of the LST rates using Kamphuis (1991) formula was similar or up to about 25% less than the measured values. They suggested that this close agreement with the measurement, as oppose to the CERC formula, could be due to the incorporation of the wave period in Kamphuis (1991), which influences the wave steepness, and hence, the breaker type. They also concluded that if *K* value in CERC formula was calibrated for a breaker type and then applied to similar breaker types, it could provide a good estimation of the LST rate (Smith et al., 2003).

Wang et al. (1998) compared the measured LST rate under low energy conditions along the southeast coast of the United states and the Gulf coast using 29 trap experiments, and suggested that CERC prediction (using the default *K* value) overestimated the rates by a factor of 9, while Kamphuis (1991) formula overestimated it by a factor of 4. van Rijn (2002) compared the LST rates calculated from both formulas and a process-based model (CROSMOR2000) with field data sets from the USA and Netherlands which were obtained from direct sampling methods or short-term volume changes. He concluded that the results from the CERC formula during storm conditions were a factor of 2 higher, and during low energy wave conditions a factor of 5 larger than measured values of LST. In addition, the calculated LST rates based on Kamphuis (1991) formula during high energy events were a factor of 1.5 smaller, and during low wave conditions a factor of 3 larger than measured LST rates.

Wang et al. (2002) estimated the LST rates for a number of large scale laboratory experiments, and compared them with rates determined by a number of empirical LST formulas, including CERC and Kamphuis (1991). They suggested that the CERC formula overpredicted the LST rate by a factor of 6 for plunging waves, and a factor of 2.5 for spilling waves. They suggested that the Kamphuis (1991) formula predictions of the LST rates were much more consistent relative to the measured values, and it underpredicted the LST rate by 30 and 24% for spilling

and plunging cases respectively. They recommended the use of a *K* value of 0.2 instead of 0.39 in the CERC formula for a more realistic estimation of the LST rate based on the long-term record of wave parameters.

Shanas and Kumar (2014) used wave parameters obtained from the DELFT3D wave model in a number of empirical formulas, including CERC and Kamphuis (1991), to estimate the LST rate along the Kundapura coast on the central west coast of India. They compared the predicted LST rates with the measured values, and concluded that the predicted LST rate using Kamphuis (1991) formula was in close agreement with the measured values. However, the CERC formula considerably overpredicted the LST rate and needed to be calibrated for the study area. They suggested that using a correction factor of 0.38 (the equivalent to using 0.148 for *K* value) in the CERC formula improved the results, making the estimation more consistent with the measurements.

Overall, previous studies have suggested that the Kamphuis (1991) formula is a better estimator of the LST rate (Wang et al., 2002; Smith et al., 2003; Shanas and Kumar, 2014), and the CERC formula should be calibrated to match the LST rates derived from knowledge of the local sediment budget.

Application of CERC and Kamphuis (1991) formulas in the current study

The LST rate was computed using the Kamphuis (1991) formulation for the August 2008 to August 2009 interval. The wave breaker location varies with water levels and changes in the near shore profile. Therefore, measurement of the wave breaker parameters for a one year period to estimate the LST rate is not possible (Shanas and Kumar, 2014). Hence, modelled wave heights along a pre-defined survey transect (ETA 77) were used to estimate the location of breaking and extract breaking wave height, $H_{s,br}$, breaking wave angle, θ_{br}, peak wave period, T_p, and beach slope, m_b. The resultant LST was compared to that predicted by the model and the artificial bypassing rate (Figure 6.5). Assuming that Kamphuis (1991) is a good estimator of LST in this area, it is shown that the artificial bypassing rates approximately represents the LST during calm weather conditions (Figure 6.5).

The accumulative LST rate was also calculated by incorporating the extracted time series at ETA 77 into the CERC formula. Similar to previous studies, using the default *K* value of 0.39 in the CERC formula resulted in an overestimation of the net LST rate (2,230,000 m^3/yr to the north for August 2008 to August 2009). Since there was no measurement of the LST rate in that interval, assuming the artificial bypassing rate represented the LST during calm conditions (up

to the end of March 2009), K = 0.2, half of the suggested value by USACE (1984), was applied. This is similar to the K value recommended by Wang et al. (2002). The resultant accumulative LST rate using calibrated CERC formula is shown in Figure 6.5. It should be noted that DHL (1992) used a K value of 0.113 (a factor of 3.4 less) rather than the recommended value of 0.39 by USACE (1984) to reach a value of 500,000 m^3/yr for the LST rate along Letitia Spit (obtained from measured accretion rates south of the Tweed River training wall from 1962 to 1964), and therefore 530,000 m^3/yr for the Spit. As shown in Figure 6.5, using the K value suggested by DHL (1992) for the study area (0.113) results in LST of about 660,000 m^3/yr for August 2008 to August 2009. Interestingly, the resultant LST rate using K = 0.113 is very similar to the model simulated LST (Figure 6.5).

As shown in Figure 6.5 the estimated rates using the Kamphuis (1991) and CERC (1984) formulas (while using K = 0.2 in the CERC formula) were similar, with annual LST rates of 1,230,000 m^3/yr and 1,150,000 m^3/yr respectively (7% difference). These rates are relatively in good agreement with the suggested rate by the developed conceptual model for this time interval (1,000,000 m^3/yr) (13 to 19% difference). Therefore, it can be concluded that Splinter et al. (2011) underestimated the LST rate for 2009 (about 800,000 m^3/yr at ETA 79) when using the wave classification scheme instead of full temporal wave records.

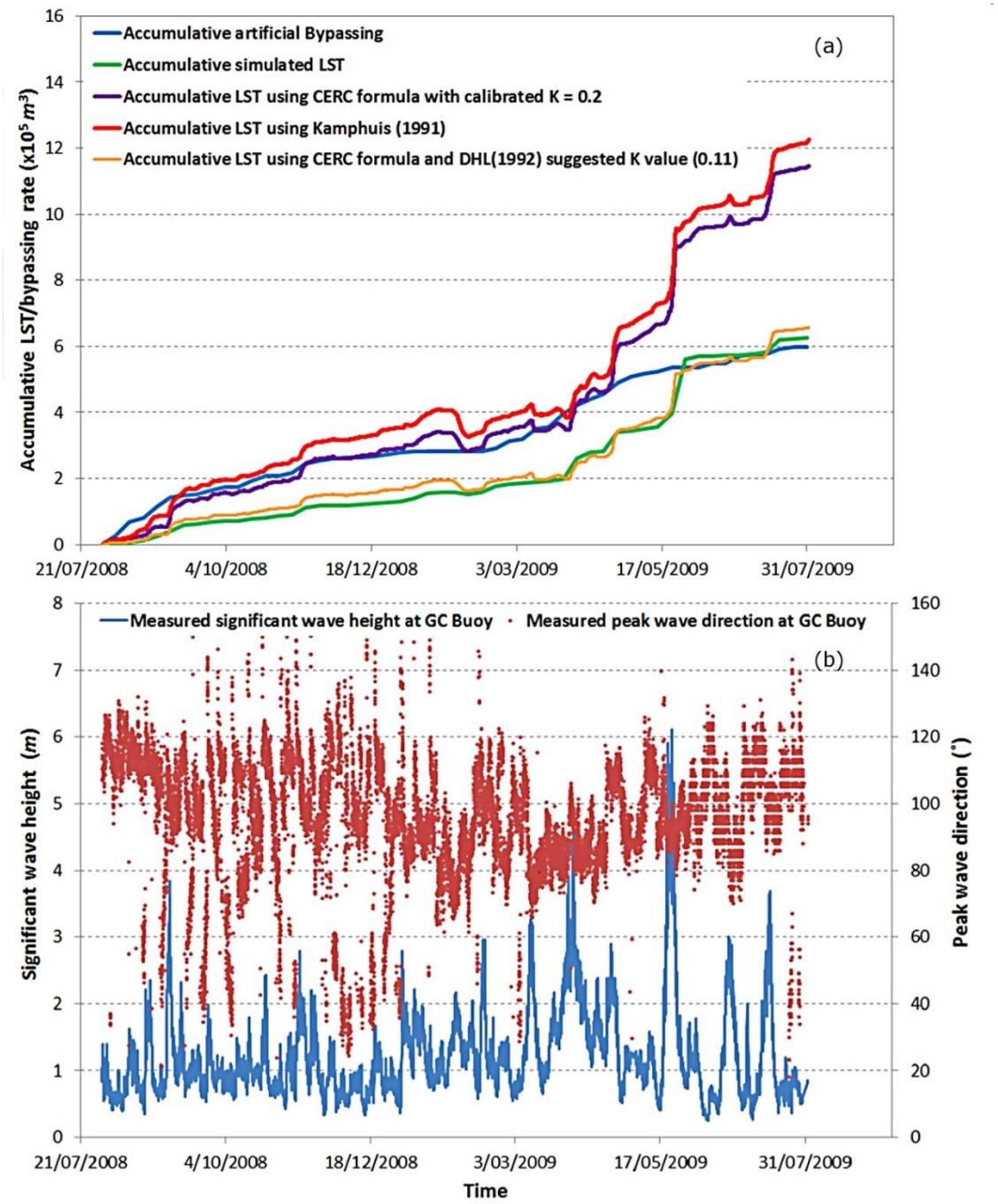

Figure 6.5. (a) Accumulative LST rates from August 2008 to August 2009, including: (1) model simulated LST, (2) and (3) Calculated LST using wave parameters extracted from the model results in Kamphuis (1991) and calibrated CERC formulas , (4) Calculated LST using wave parameters extracted from the model results in the calibrated CERC formula by DHL(1992), (5) measured artificial bypassing rate; (b) Measured H_s and PWD at the GC Buoy

6.2.1.2 Mid-July 2009 to mid-July 2010

To investigate the model underestimation of the LST rate during calmer wave conditions; another year, without any major storm ($H_s > 3m$ at GC buoy), was simulated. The selected year was from mid-July 2009 to mid-July 2010. The simulated LST rate for this period was 240,000

m^3, while the rate of sand bypassing was about 580,000 m^3, indicating that the model underestimated the rate of sediment transport by about 60%. The accumulative simulated LST and actual bypassing rate in this interval are shown in Figure 6.6, indicating the model underestimation of LST during this interval. This confirms that the model underpredicts the LST rate during calmer conditions. The possible reasons for this underestimation will be discussed in section 6.2.2.

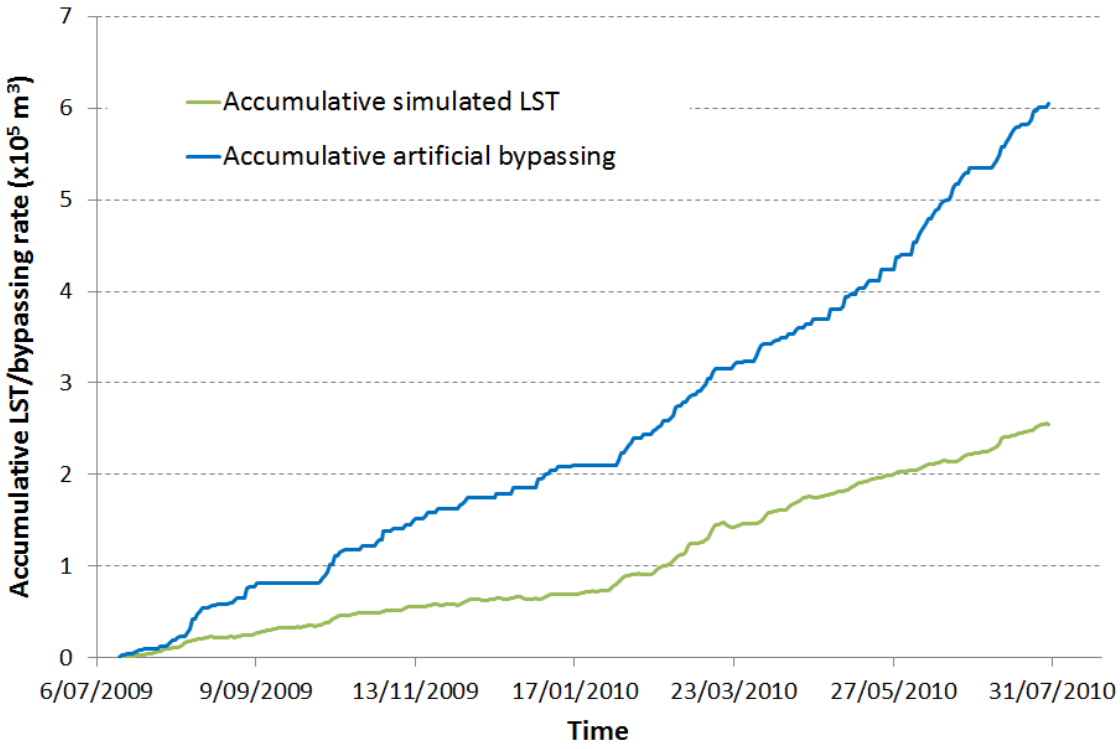

Figure 6.6. Accumumulative simulated LST rate at ETA 79 and the accumulative artificial bypassing rate (based on data provided) for mid-July 2009 to mid-July 2010.

6.2.1.3 Cross-shore distribution of the LST

The main reasons for the LST leakage offshore from the sand bypassing jetty and the southern training wall, particularly during storms events, were investigated by extracting the cross-shore distributions of the simulated LST at ETA 77 during various time intervals in the ten months simulation (August 2008 to June 2009). These are shown in Figure 6.8. As illustrated, under fair-weather condition, such as 1st August to 2nd September 2008 and 6th September 2008 to 29th March 2009, the LST rate was distributed further onshore. Even for the first minor storm event, which was from 4th to 5th September 2008, most of the LST rate occurred within the first 400 metres from the origin of ETA line 77. As shown in Figure 6.8, the LST rate distributions for the other two more significant storm events in April and May 2009 were more offshore. This was most significant for the major ECL in May 2009. Large volumes of sand moved to the

offshore bar during these events, and were transported alongshore due to the shore parallel component of breaking waves. This result agrees with the previous study of Andrews and Nielsen (2001). Comparison of two aerial images, one in November 2012, which was after a significant storm event in June 2012, and the other in November 2014 which was within a relatively calm weather condition, also confirm the existence of the traces of the offshore bar in November 2012 due to a significant storm event approximately five months earlier (Figure 6.7).

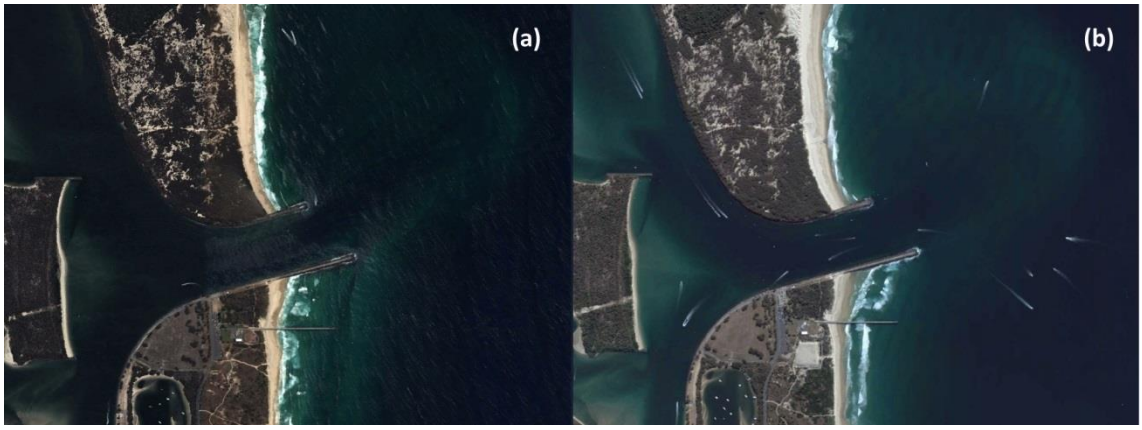

Figure 6.7. Aerial image of GCS in (a) November 2012 (b) November 2014

Therefore, the cross-shore distribution of the LST is quite sensitive to the wave conditions. This means that during higher wave energy conditions there is a much greater probability of sediment transport leakage through the sand bypassing jetty, which has a length of less than 340 metres seaward from the selected origin of ETA 77 in Figure 6.8. It should be noted that, as shown in Figure 6.8, a small portion of the LST during calmer wave conditions also occurred offshore from the sand bypassing jetty (more offshore than 340*m* from the origin). This may have caused a gradual, less significant, leakage to the ebb-tidal delta.

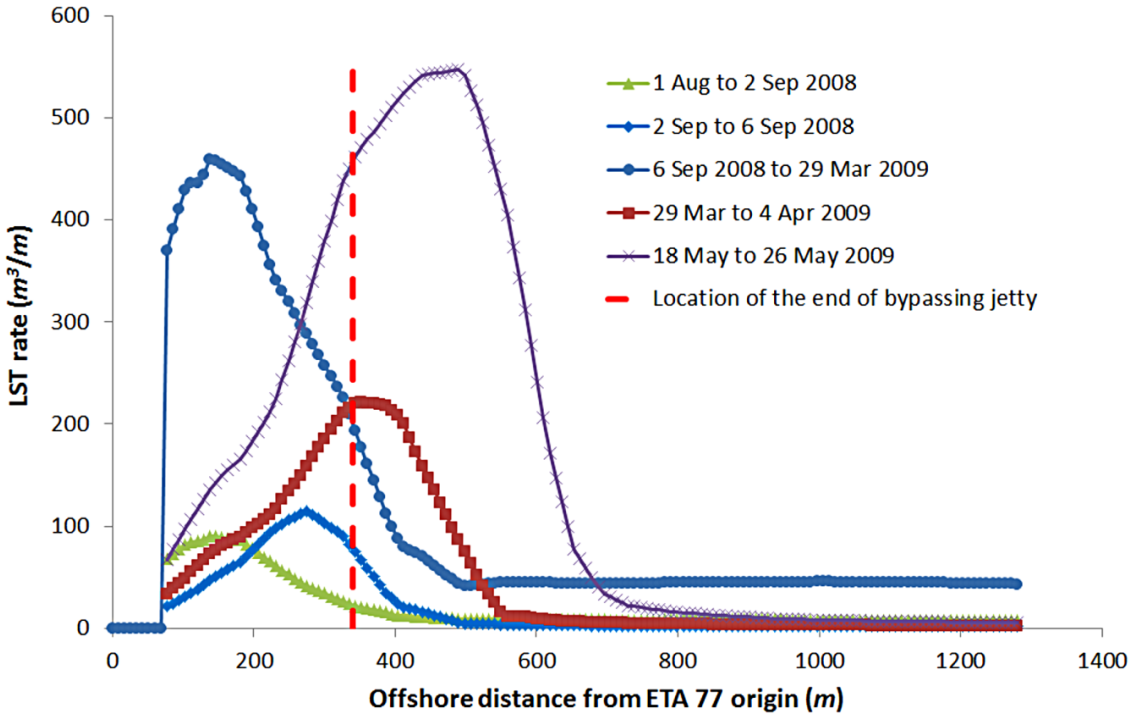

Figure 6.8. The LST rates at ETA 77 for various intervals during 10 month simulation from August 2008 to June 2009.

The more extended onshore distribution of the LST during calmer wave conditions was also confirmed by extracting the LST cross-shore distribution for mid-July 2009 to mid-July 2010 at ETA 79 (south of the bypassing jetty) as shown in Figure 6.9. As mentioned before, during this period, no storm event ($H_s > 3m$ at GC buoy) occurred. As illustrated in Figure 6.9, the cross-shore distribution of the LST in this interval was very similar to that of 6th September 2008 to 29th March 2009 in Figure 6.8, during which most of the LST rate occurred within the 400m distance from the origin of the ETA line, with the maximum being at about 150m offshore origin.

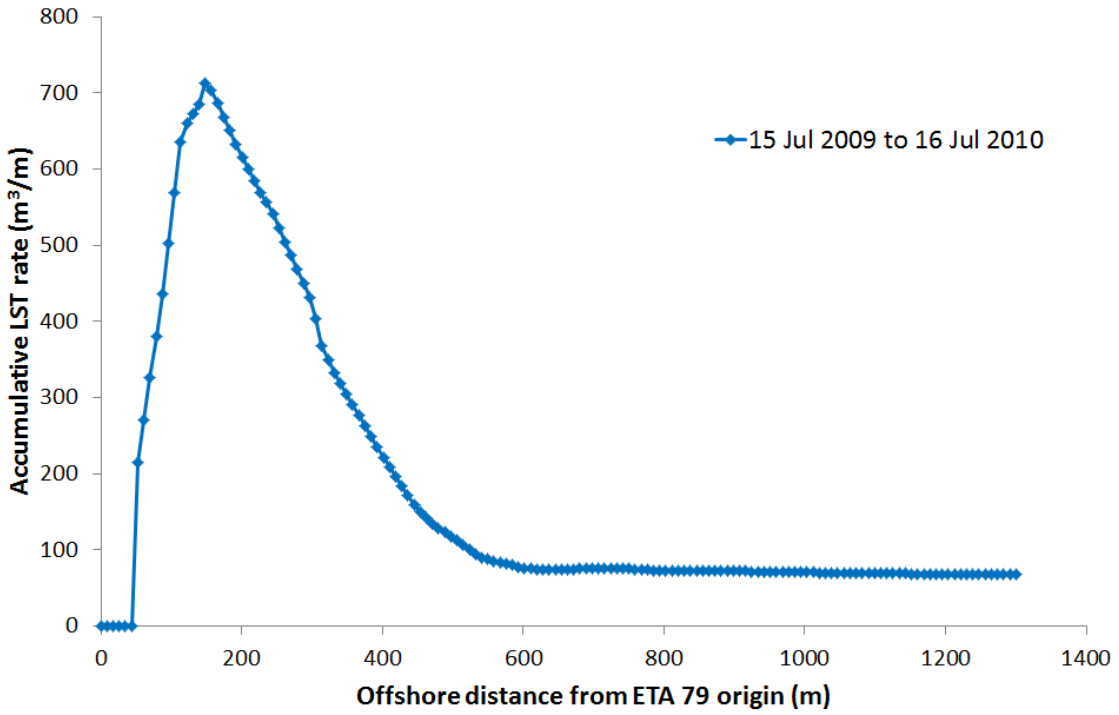

Figure 6.9. Cross-shore distribution of the accumulative LST at ETA 79 during 12 month simulation from 15 July 2009 to 15 July 2010

6.2.2 Sources of the LST underestimation

The analysis in the previous section suggests that the LST rate is underestimated during lower energy wave conditions. The sources of this underestimation have been investigated and a number of them are discussed below.

6.2.2.1 Sediment transport formula

Pinto et al. (2006) have suggested that the largest relative errors in the calculation of sediment fluxes occur in low energy conditions. As mentioned in Chapter 5, the bed load transport model of Engelund and Fredsøe (1976) is used in the MIKE 21/3 FM model when simulating combined wave and current in the sediment transport module. In addition, the vertical variation of the suspended sediment concentration is calculated according to the vertical diffusion equation of Fredsøe et al. (1985). Based on the analysis by Cheng (2002), the bed load sediment transport formulas, which are based on the bed shear excess similar to Engelund and Fredsøe (1976) formula, are not applicable for weak transport which usually occurs under conditions of $\theta' < \theta_c$ (Shield's parameter less than critical Shield's parameter). He suggests that the bed load sediment transport formulas based on θ'^{n} are preferable for lower transport rates. This is because, based on experimental observations such as the ones in Paintal (1971), there is no shear stress below which no single grain moves. Moreover, Fredsøe et al. (1985) noted that

in nature there is always a certain amount of washload present. In their study, this was assumed to be uniform over the depth and equal to the amount of suspended load just below the water surface. This was also neglected in the total load calculation of MIKE 21/3 FM. These are plausible reasons for the model's underestimation of total sediment transport under lower energy conditions considering its current formulations and may explain the model underestimation of sediment transport during lower energy wave conditions.

6.2.2.2 Availability of nearshore bathymetry data

Sediment fluxes, as determined by sediment transport formulas, are a function of physical properties such as velocity, depth and sediment grain sizes. Pinto et al. (2006) suggested that errors in the physical properties can be the dominant factor in the accuracy of the sediment flux evaluation rather than limitations of the formulas, particularly in small depths. As mentioned before, the LST during calmer wave conditions occurs more onshore, i.e. in shallower depths. Therefore, the accuracy of the bathymetry of the surfzone and swash zone can significantly affect the accuracy of the predicted LST rate. In Chapter 5 it was mentioned that the bathymetry of the berms was created based on some of the ETA line survey data available. However, there were only a few ETA lines available at the start of the simulation period, and the initial bathymetry created for the coastline and surfzone areas were not perfect.

A sensitivity analysis of the resultant LST rate to the initial bathymetry was also undertaken. The resultant LST rate for a 7.5 month period, from 1st August 2008 to 15th February 2009 (during which no storm event, $H_s > 3m$ occurred at GC buoy) were calculated for two simulations and then compared. The only difference in these two simulations was the bathymetry near the coastline where there were no measured data (ETA lines) available. In the first simulation, the generated bathymetry of the final model (using available data and interpolation) was used. In the second simulation, some additional bathymetric data near the coastline, where there were no measured data, was extrapolated based on the slope of measured bathymetry at adjacent ETA lines. The resultant LST rate for the 7.5 month period was 137,000 m^3 for the first simulation and 108,000 m^3 for the second simulation. This confirms that variations in the quantity of data (ETA lines) used to create the coastline bathymetry, could change the resultant LST rate, about 27% in this case. Therefore, availability of a precise bathymetry of these areas is critical to reach more reliable model results, which has been one of the limitations of the current research.

6.2.2.3 Sediment transport in the swash zone

Examination of the cross-shore distribution of the LST in a large scale physical model by Smith et al. (2003) illustrated that there are three distinct zones of sediment transport. These include: the incipient breaker zone; the inner surf zone; and the swash zone. A number of studies, which include large-scale lab experiments and field observations, suggested that a significant portion of the LST during lower wave energy conditions takes place in the swash zone (Swaragi and Deguchi, 1978; Bodge and Dean, 1987; Smith et al., 2003). Active sediment transport in the swash zone was also observed in several field studies (Kraus and Dean, 1987; Wang et al., 1998). In some studies, it was suggested that swash zone transport can account for up to 50-60% of the total LST rate in calmer conditions (Van Wellen et al., 2001; Elfrink and Baldock, 2002; Smith et al., 2003). Smith et al. (2003) have suggested that as incident wave height decreases the contribution of swash zone sediment transport to total LST increases.

A series of large scale laboratory tests was carried out by Wang et al. (2002) to investigate the LST during low wave energy conditions. It was found that for both plunging and spilling breaker waves, a significant portion of sediment transport occurred in the swash zone. This was about 27% of the total LST for the spilling cases, and 34% for the plunging cases. Observations during the experiments indicate a more active uprush during the plunging cases compared to spilling cases, which was suggested to be responsible for the significant sediment flux above the still-water shoreline in plunging cases. It was also found that, as shown in Figure 6.10b, the peak of the LST during the spilling breaker cases occurred in the swash zone. In addition, two sediment transport peaks were measured for the plunging breaker cases, one in the swash zone and one near to the breaker line (Wang et al., 2002) (Figure 6.10b). However, analysis of the cross-shore distribution of the LST in the model shows that the current model does not simulate the peak of LST in the swash zone, especially for plunging breaker types, where the sediment transport contribution in the swash zone is more significant (Figure 6.10a).

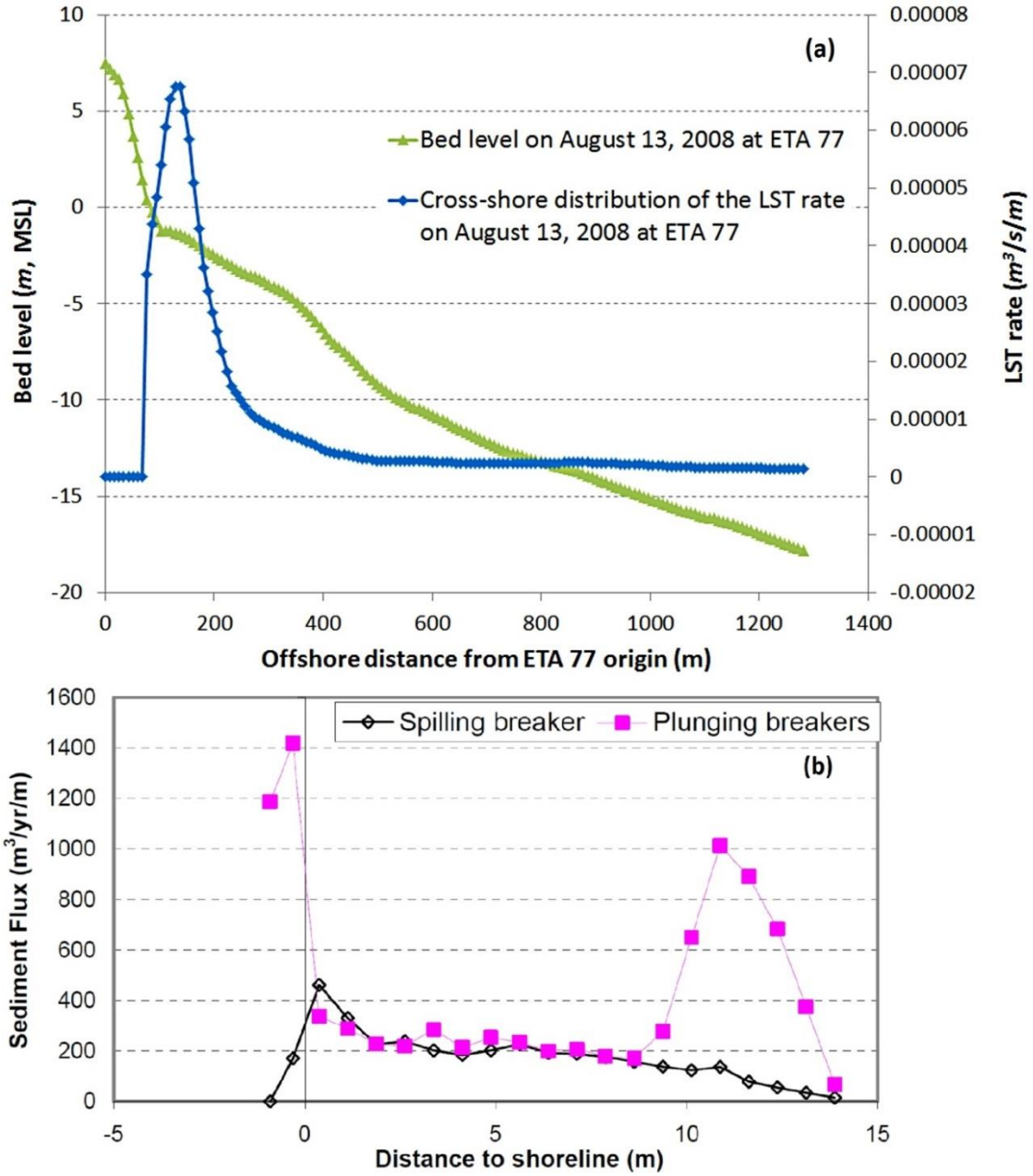

Figure 6.10. (a) Cross-shore distribution of the LST on August 13, 2008 at ETA 77 due to plunging breaker ($H_s \approx 1m$ offshore) (b) Cross-shore distribution of LST measurments by Wang et al. (2002) in a large scale sediment transport facilityduring plunging and breaker cases

Van Wellen et al. (2001) also suggested that most LST models either completely ignore, or merely include the swash zone sediment transport as part of the total LST. For example, in van Rijn (2002) process based model, CROSMOR2000, LST results during storm conditions were a factor of 1.5 larger, and during calm conditions a factor of 2 smaller than measured values. He suggests that the under prediction for low wave energy conditions might be related to the exclusion of the LST in the swash zone, which is relatively important for low wave conditions, in the model. Therefore, it is suggested that one of the main reasons for the model's significant

underestimation of the LST rate in the current study during calmer weather conditions is related to not accounting for the LST rate in the swash zone.

6.3 Morphological evolution

The selected morphological simulation time was the ten month period from August 2008 to June 2009, between two subsequent surveyed bathymetry, during which a significant amount of morphological change occurred. The simulation time of the local model for the ten month simulation was about two weeks using a 64-bit Windows machine, which had an Intel core Xeon CPU X5670, 2.93 *GHz*, and a 12*GB* RAM. For ten month simulations, the artificial sand bypassing should have been considered in the model. However, the MIKE 21 coupled model is incapable of including source and sink of sediment when the sediment transport module is set to 'wave and current'. Therefore, the initial solution was to include the sand bypassing by manually transporting the weekly recorded bypassing volumes of sand, which were provided by GCWA, from upstream to downstream of the GCS. This method needed several subsequent simulations which each required a mesh generation and the inevitable accumulative interpolation errors severely affected the resultant bed level change. Therefore, the ten month simulation prediction using this method was not used to estimate the skill of the model morphological simulation. Although the final simulated morphological changes in the model could not be used for the model skill assessment, this set of simulations had one positive outcome. It was found that due to the dominant northward longshore current in this period, the volume of sand backpassing from the bypassing system outlet downstream to the ebb-tidal delta was negligible. Therefore, it can be concluded that the growth of the ebb-tidal delta in this interval was not due to the sand backpassing from downdrift the inlet.

Since simulation of the artificial sand bypassing was not practical, the ten month simulation was carried out without considering the artificial sand bypassing. The main purposes of this simulation were to (a) check whether the model was capable of predicting the expected LST rate in the area; (b) check if the model could predict the expected natural processes in the area in the absence of artificial sand bypassing and (c) illustrate if there was any leakage of sand from the southern training wall due to the more seaward distribution of the LST, specifically during the storm events; as suggested in Chapter 4.

6.3.1 Skill metrics

The final morphological model skill can be assessed quantitatively using "Skill Scores" (Sutherland et al., 2001; Siegle et al., 2004). These are used to estimate the accuracy of prediction relative to the accuracy of a baseline prediction. Two of the most commonly used skill scores are the Brier Skill Score (BSS) and Adjusted Brier Skill Score (ABSS), which are based on Mean Square Error (MSE) as shown in equations (6.3) and (6.4) (Van Rijn et al., 2003; Sutherland et al., 2004a).

$$BSS = 1 - \frac{MSE(z_C, z_M)}{MSE(z_0, z_M)} = 1 - \frac{\sum (z_C - z_M)^2}{\sum (z_0 - z_M)^2} \tag{6.3}$$

$$ABSS = 1 - \frac{\sum \left(|z_C - z_M| - \Delta z_M\right)^2}{\sum (z_0 - z_M)^2} \tag{6.4}$$

where z_C is a set of N computed (predicted) by model bed level values, z_M is a set of N observed (measured) bed levels, z_0 is the initial bed levels (reference), Δz_M is measurement error which is set to $0.2m$ based on surveying accuracy. BSS and ABSS values range from less than zero, which represents no agreement, to 1 which represents perfect agreement (see Table 6.1). It should be noted that negative values of the term in ABSS's numerator bracket are set to zero.

Table 6.1. Proposed classification for the quality of morphological prediction based on Brier Skill Score (Van Rijn et al., 2003; Sutherland et al., 2004a)

	BSS	*ABSS*
Excellent	1.0 - 0.5	1.0 - 0.8
Good	0.5 - 0.2	0.8 - 0.6
Reasonable/fair	0.2 - 0.1	0.6 - 0.3
Poor	0.1 - 0	0.3 - 0
Bad	< 0	< 0

One of the advantages of using MSE measure of accuracy and the corresponding BSS is that they can be broken down into components which each describe a specific element of simulation quality (Bosboom et al., 2014). For instance, Murphy and Epstein (1989) broke down the MSE into correlation, conditional (amplitude) and systematic bias terms as follows:

$$MSE = \sigma_{Cw}^2 (1 - \alpha + \beta + \lambda) \tag{6.5}$$

Where

$$\alpha = \rho_{CM}^2 \tag{6.6}$$

$$\rho_{cm} = \frac{\sigma_{\mathrm{CM}}}{\sigma_{\mathrm{Cw}}\sigma_{\mathrm{Mw}}} \tag{6.7}$$

$$\beta = \left(\rho_{CM} - \frac{\sigma_{Cw}}{\sigma_{Mw}} \right)^2 \tag{6.8}$$

$$\lambda = \frac{\left(\langle \mathrm{C} \rangle - \langle M \rangle\right)^2}{\sigma_{Mw}^2} \tag{6.9}$$

Here σ_{Cw} and σ_{Mw} are the weighted standard deviations of C (computed/predicted) and M (measured/observed) values. α is the coefficient of determination defined as the proportion of the variation in the values of M that can be linearly explained (in a statistical sense) by C (or vice versa) (Taylor, 1990). β is the conditional bias, which is non-zero if the slope $\rho_{CM}\,\sigma_{Mw}/\sigma_{Cw}$ of the regression line of the measurements (M), given the predictions (C), deviates from 1 (Bosboom et al., 2014). λ is a normalized map-mean error. σ_{CM} represents the weighted covariance of M and C values. ρ_{CM} is the weighted Pearson product-moment correlation between the predictions and the measurements (Bosboom et al., 2014). Murphy and Epstein (1989) presented equation (6.10) for BSS by substituting the components of MSE from equation (6.5) in the BSS definition in equation (6.3), given that $C' = C - r$ and $M' = M - r$ (r is the reference (z_0)).

$$BSS = \frac{\alpha' - \beta' - \lambda' + \varepsilon'}{1 + \varepsilon'} \tag{6.10}$$

Livezey et al. (1995) defined α' as the phase association between C' and M', and 1- α' as the phase error. However, Gerritsen et al. (2011) explained that α' shows the degree of the similarity between the spatial patterns of accretion and erosion. This means that $\alpha' < 1$ may result from dissimilarities between the predicted location, shapes and relative magnitudes of the accretion/erosion features. It should be noted that α' does not distinguish between positive and negative correlations (Bosboom et al., 2014). Livezey et al. (1995) have also suggested that β' represents the bias or amplitude error, and λ' represents the reduction of skill due to map mean errors. Therefore, α' denotes the skill in the absence of biases. Bosboom et al. (2014) proposed that due to the nature of MSE, BSS tends to reward predictions that underestimate variability, and this leads to a higher diagnosed skill (BSS) when the model under predicts the variance of cumulative bed changes. In addition, Sutherland et al. (2004a) have noted that a non-zero β' only reflects the amplitude error (i.e. that wrong volumes of sand have been moved) when $\rho_{C'M'}$ is equal to 1. Therefore, Bosboom et al. (2014) suggested that, when neglecting systematic bias,

σ'_{Cw} / σ'_{Mw} rather than β' is a more appropriate overall indicator of the agreement between the predicted and measured amplitude of bed level changes, with σ'_{Cw} / σ'_{Mw} = 1 showing the perfect prediction of the amplitude.

6.3.2 Morphological simulation results

The initial and resultant bed levels after the ten month simulation are shown in Figure 6.11.

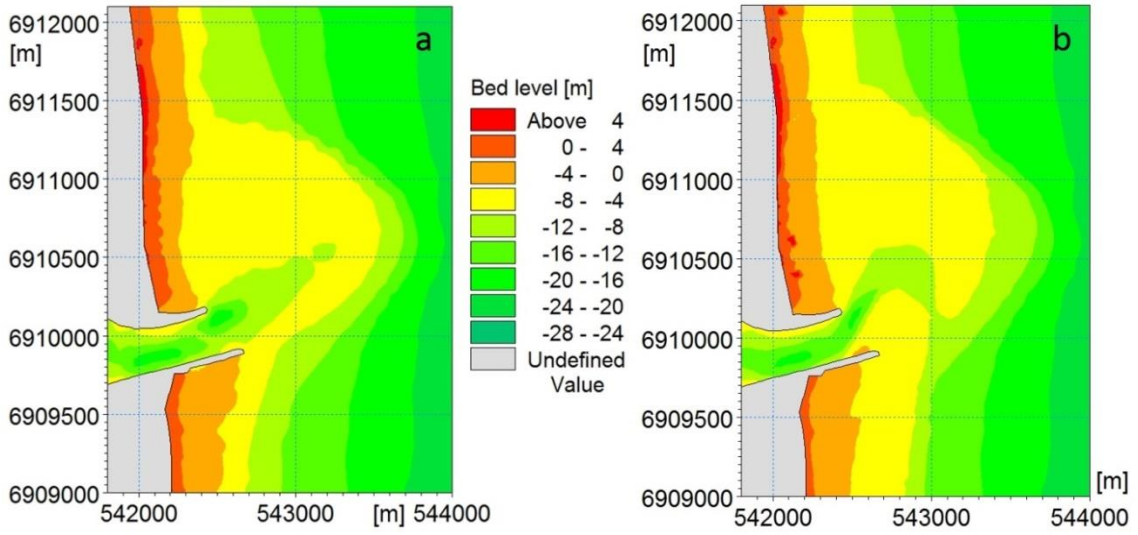

Figure 6.11. (a) Initial bathymetry in August 2008 (b) Final simulated bathymetry for ten month simulation until June 2009 without artificial sand bypassing

As mentioned before, the ten month simulation could not be used to quantitatively assess the model prediction because the artificial sand bypassing rates could not be simulated. However, it could be used to check the capability of the morphological model in simulating the expected natural processes in the GCS tidal inlet area in the absence of an artificial sand-bypassing system. Overall, the ten month simulation predicted the expected dynamics of the inlet. These include (1) the annual accumulative LST consistent with assessments of the net longshore transport rate in previous studies (DHL, 1970; Patterson, 2007; Splinter et al., 2011), as mentioned in section 6.2.1; (2) the natural sand bypassing of a portion of the LST that leaked from the southern training wall around the seaward edge of the ebb-tidal delta (Figure 6.12) as expected for tidal inlets without artificial sand bypassing (Sha, 1989; FitzGerald et al., 2000); and (3) a tendency of the offshore component of the inlet channel to northward migration, with the ebb tidal delta deflecting northward under the prevailing net LST (Figure 6.11a, b). This is consistent with the historical behaviour of the inlet prior to stabilisation, as explained in Chapter 3. Historically, the inlet was migrating northward due to the dominant northward LST. This northward movement was accompanied with the elongation of the Spit upstream. This

phenomenon of the Spit elongation and the northward movement of the offshore component of the channel are noticeable offshore from the southern jetty to the inlet entrance, when the bed level is compared before and after the ten month simulation (Figure 6.11a, b).

The ten month simulation has also revealed that during fair weather conditions the sand transported by longshore currents was partially trapped behind the GCS southern training wall (Figure 6.12). This process, and the gradual natural sand bypassing which was partially trapped in the ebb-tidal delta for the ten month period, resulted in a negative sediment budget on South Stradbroke Island. This lack of LST caused the gradual erosion of the downdrift beaches to the north of the northern training wall, as well as at the central part of the ebb-tidal delta (Figure 6.13). The excessive erosion of the central part of the ebb-tidal delta is also possibly attributed to increased flow velocities directed towards the north-east in the seaway channel caused by the sand leakage around the southern wall leading to a narrower channel.

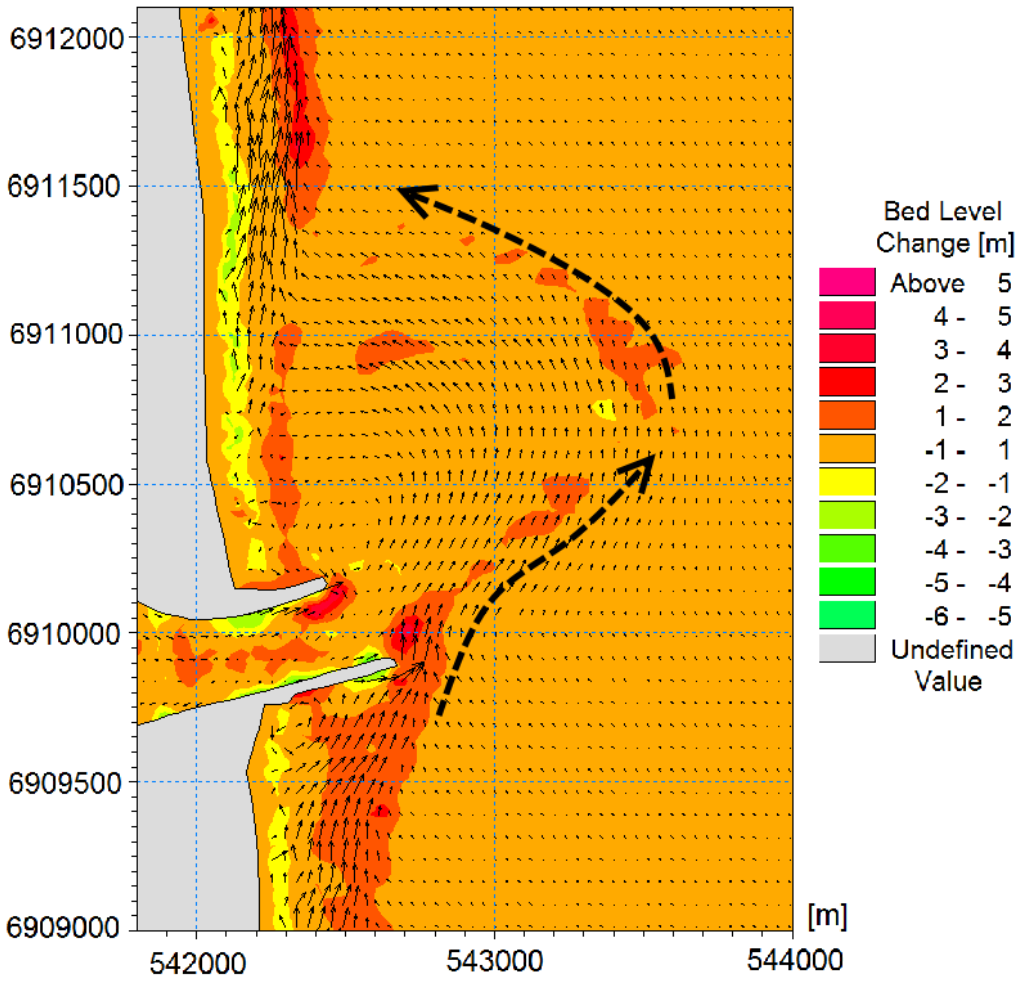

Figure 6.12. Natural bypassing on the offshore edge of the delta, sand accumulation upstream southern wall, small arrows indicate the accumulative sediment transport intensity and direction (snapshot of bed level change from August 2008 until mid November 2008)

As illustrated in Figure 6.13, the leakage of LST seaward of the southern training wall resulted in accretion near the southern wall of the entrance. In high energy conditions, such as the ECL in 2009, and owing to more offshore distribution of the LST (as shown in Figure 6.8), this leakage is relatively higher. The resultant bathymetry changes in the ten month simulation without artificial sand bypassing and from the survey data are shown in Figure 6.14 a and c. Due to accretion in the vicinity of the southern part of the inlet channel, demonstrated by the model results, a more intensive flow jet in the northern channel resulted in an overestimation of the erosion at the northern part of the entrance mouth compared to the observed morphological evolution with the artificial sand bypassing (Figure 6.14 a, c). This eroded sand was diverted to the downdrift beaches to partially compensate for the lack of LST (Figure 6.13).

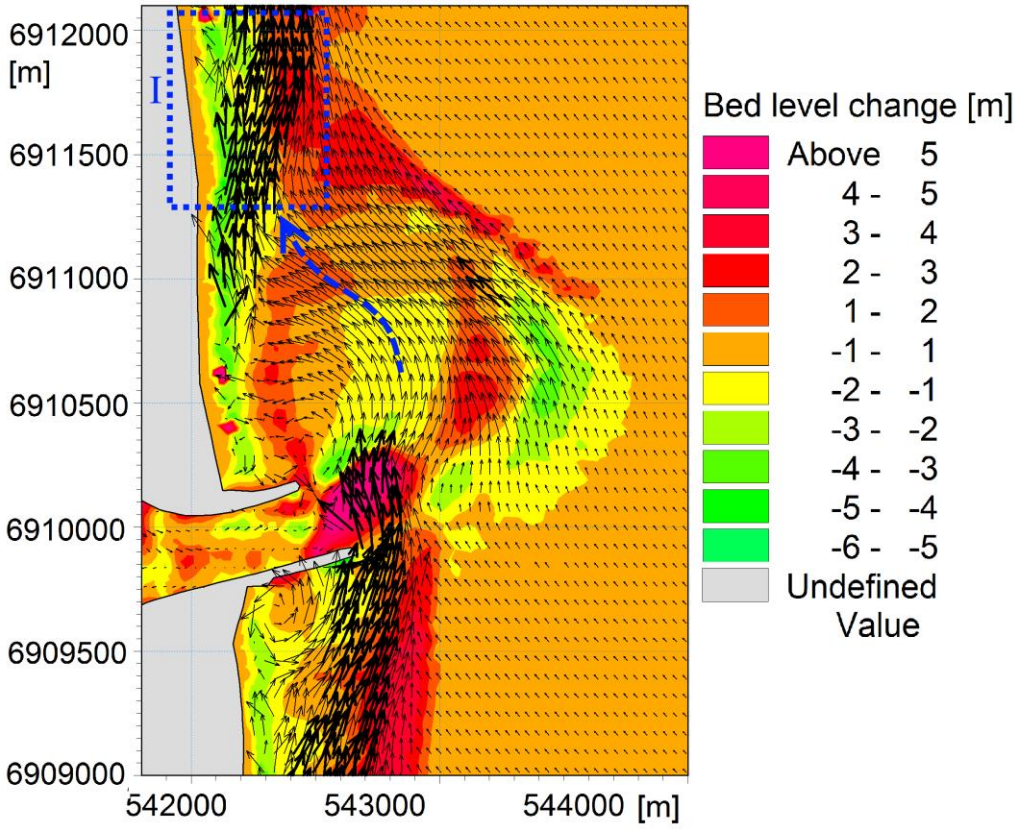

Figure 6.13. Simulated bed level change for the ten month simulation without sand bypassing. Arrows indicate the accumulative sediment fluxes during the ten months. Due to lack of LST downstream, further erosion in area I and the central part of ebb-tidal delta is noticeable.

As shown in Figure 6.14b, c, the results of the ten month simulation, without any artificial sand-bypassing, demonstrated that a significant amount of morphological evolution of the ebb-tidal delta occurred in response to the major storm events, particularly the East Coast Low (ECL) during 19-25 May, 2009 (with a maximum significant wave height of 6 metres at the Gold Coast Buoy, located about 1 *km* offshore with the water depth of about 17 metres). This is

similar to the finding for the Teign Inlet, UK (Siegle et al., 2004) where the sediment transport on the ebb-tidal delta primarily depends on the waves. It should be noted that both the ten month and the May 2009 twelve day simulations qualitatively captured most of the morphological evolution patterns in the ebb-tidal delta (Figure 6.14). However, only the ten month simulation final bed level change shows the deposition on the north- east of the delta similar to that of the survey data (Figure 6.14 a and c). Analysis of the morphological changes during the ten month simulation illustrated that this deposition was due to the interaction of tidal currents and the natural bypassing process (which was shown in Figure 6.12). This sediment was mainly sourced from the leakage of the LST offshore from the sand bypassing jetty and the southern training wall.

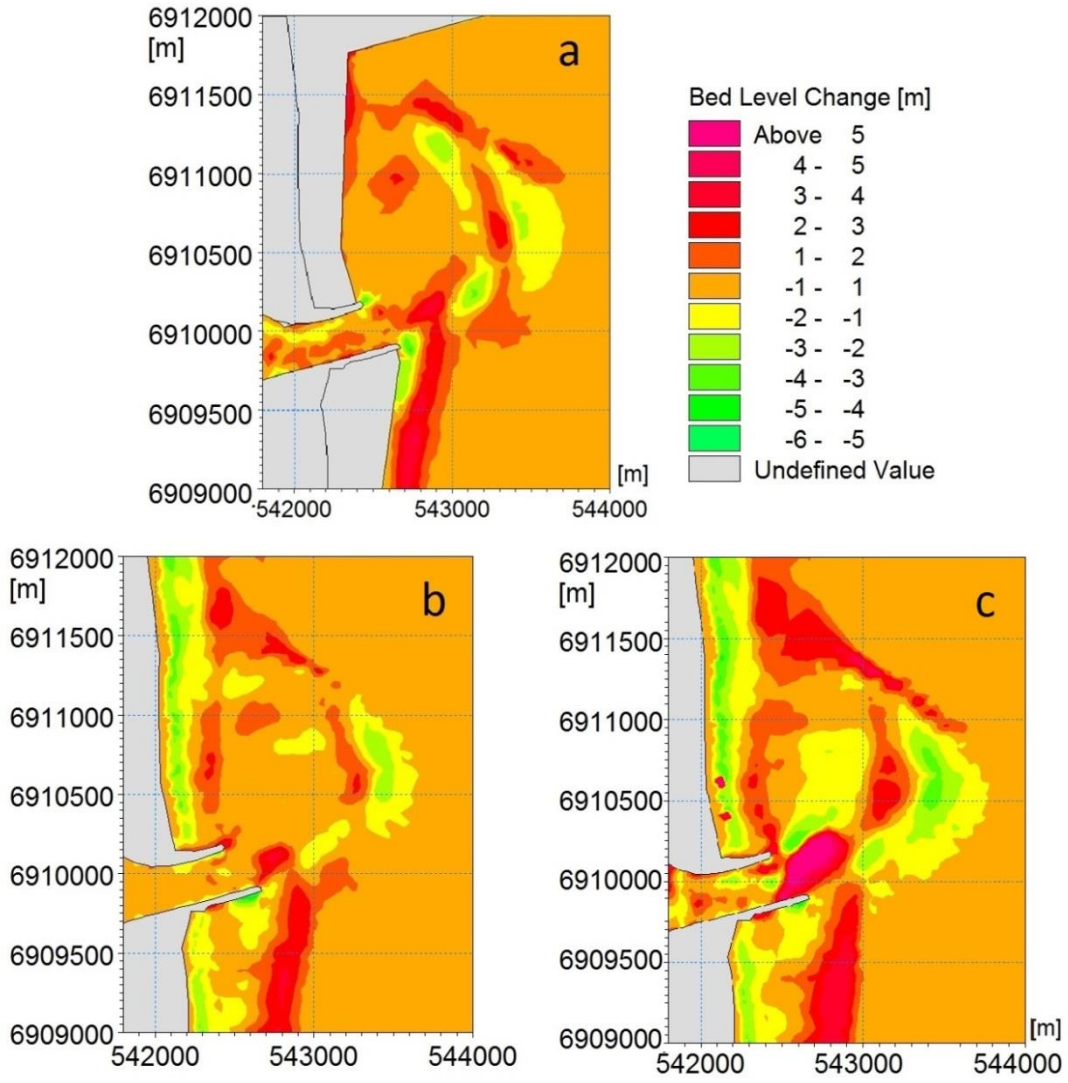

Figure 6.14. Bed level change (a) between August 2008 and June 2009 survey data (b) only for the twelve day simulation including the ECL in May 2009 storm (c) for the ten month simulation from August 2008 to June 2009 without simulation of the artificial sand bypassing (+ : Accretion, -: Erosion)

6.3.3 Morphological model performance

The morphological model prediction accuracy in the vicinity of the ebb-tidal delta was assessed using the simulated morphological evolution during the ECL in May 2009 due to three main reasons. First, the ten month simulation suggested that most of the morphological evolution occurred during this event, and based on data provided by GCWA, there was no artificial sand-bypassing during this event. Second, due to the limitation of the model, mechanical sand bypassing simulation was not practical and accurate simulation of the calmer periods where the bypassing is influential was not possible. Third, according to the more onshore cross-shore distribution of the LST in the lower wave energy period, it can be assumed that the artificial bypassing system captured most of the LST and the effect of the leakage of LST in the ebb-tidal delta morphological changes was relatively small compared to the ECL storm event. Therefore, it was decided to assess the quality of the model prediction in the vicinity of the ebb-tidal delta both qualitatively and quantitatively using the simulated morphological evolution during the twelve day simulation from 18th to 30th May 2009, which included the ECL storm in May 2009.

6.3.3.1 Qualitative validation

As suggested by Bosboom et al. (2014), visual assessment of the quality of a morphological simulation is the initial and vital step in validation of a model prediction along with using the skill score. Therefore, the measured bathymetry changes of the ten month period and the simulated bed level changes during the twelve day simulation were qualitatively compared. As shown in Figure 6.15 the pattern of morphological changes was very similar, with most of the defined erosion/deposition subdivision areas in the subtraction of the surveys (Figure 6.15a) simulated in the twelve day simulation. The only area, in which a relatively significant accretion was illustrated in the measurement but not in the twelve day simulation, was area A1 in Figure 6.15 at the north east of the ebb-tidal delta. The deposition in this area was mainly due to the gradual natural bypassing, as explained in section 6.3.2.

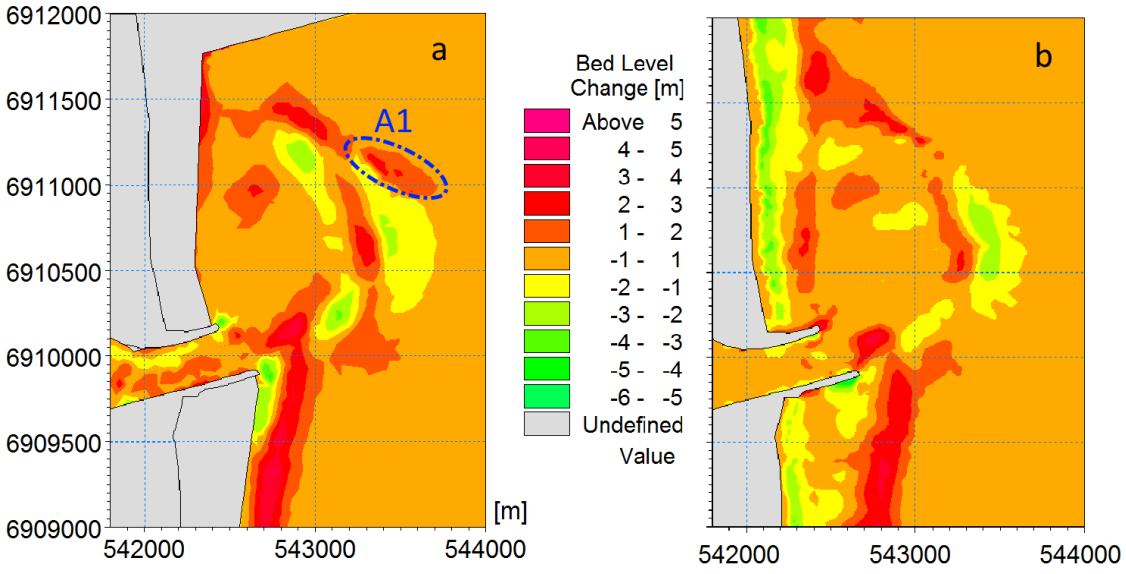

Figure 6.15. Bed level change (a) between August 2008 and June 2009 survey data (b) only for the twelve day simulation including the ECL storm in May 2009

6.3.3.2 Morphodynamic model skill

The twelve day simulation, including the ECL in May 2009, skilfully predicted the morphological evolution of the ebb-tidal delta area from August 2008 to June 2009. The overall ABSS skill for the whole area of the survey data (Area A, Figure 6.16) was 0.66 (good agreement), and the ABSS skill for the ebb-tidal delta only (Area B, Figure 6.16) was 0.6 (good agreement) (Van Rijn et al., 2003). The calculated ABSS for the delta crest erosion (Area C, Figure 6.16) was about 0.83 (excellent agreement, see Table 6.1). The morphological evolution of area C was found to be independent of wave breaking, and was associated with the interactions between the wave induced current before breaking and the bathymetry. By varying the sediment size and comparing the resulting skill scores, it was also found that slightly coarser sediment size (220 μm) in the domain, specifically in area C, could have improved the model prediction of the bed level change. The slightly coarser sand grain size in more offshore areas is consistent with the sediment grain size that has been suggested by Delft (1970).

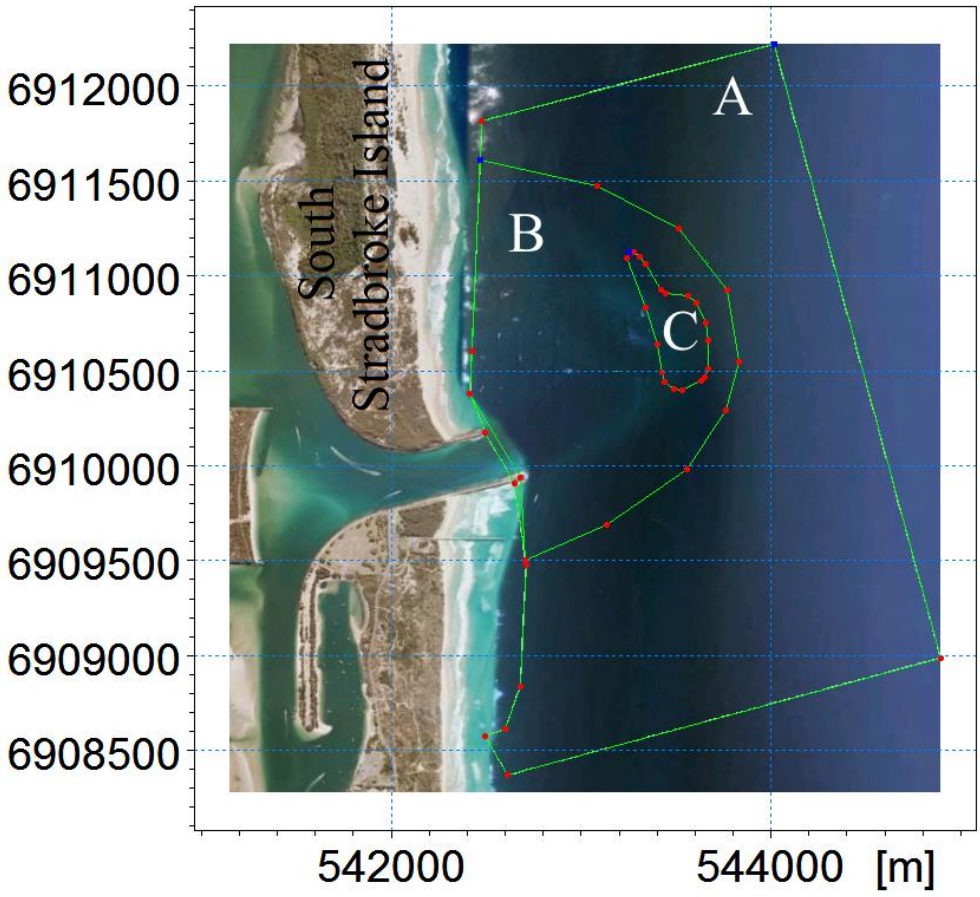

Figure 6.16. Areas of skill score calculation (A) whole survey area (B) only the ebb-tidal delta (C) only the crest of the ebb-tidal delta erosion

The BSS (skill score) as well as its α', β' and λ' components, as suggested by Murphy and Epstein (1989) and explained in section 6.3.1, were calculated for the whole survey area (area A) and the ebb-tidal delta (area B in Figure 6.16). The ratio of $\sigma'_{cw} / \sigma'_{mw}$ was also calculated as a measure of the prediction's amplitude error, as suggested by Bosboom et al. (2014). These values are shown in Table 6.2. As illustrated, β' and λ', which were suggested to be the indicators of model amplitude error and systematic error respectively, were very low. The $\sigma'_{cw} / \sigma'_{mw}$ ratio for both of these areas was relatively close to 1 (perfect agreement), which also confirmed their low amplitude error. This means that the predicted (lower than 1) BSS for these areas were mainly influenced by α', a measure of structural similarity between the measurements and the model predictions.

Table 6.2. Calculated BSS (skill score) and measures of sturctural similarity (α'), amplitude error (β'), systematic error (λ'),and amplitude similarity ($\sigma'_{cw} / \sigma'_{mw}$) for twelve day simulation

	α'	β'	λ'	$\sigma'_{cw} / \sigma'_{mw}$	BSS
Area A	0.48	0.04	0.04	0.88	0.46
Area B	0.44	0.03	0.05	0.84	0.4

6.4 Concluding points

Sediment transport and morphological evolution in the GCS area ebb-tidal delta were investigated using depth averaged numerical modelling with MIKE 21/3, which combined flow, spectral wave and sediment transport. The model was applied to simulate the annual LST in two one year intervals, as well as the morphological evolution of the area between two subsequent surveys (August 2008 and June 2009). The results of the final coupled model with the morphological update for a twelve-month simulation, from August 2008 to August 2009, showed the rate of total LST close to that of previous studies for the GCS area. However, based on the conceptual model presented in Chapter 4, the model underpredicts the LST rate. Based on the resultant LST rate for two different years, it was suggested that this underestimation was occurring more significantly during calmer wave conditions.

The ten-month simulation reproduced several morphological patterns expected for river entrances without the artificial sand bypassing system. These included the sediment accumulation upstream the southern jetty in fair wave conditions; leakage and natural bypassing of a portion of the LST around the offshore edge of the ebb-tidal delta; and excessive erosion from the central part of the delta and the downstream coastline due to the lack of LST downstream. The resultant morphological change for the ten month simulation suggested that the bulk of the morphological change at the ebb-tidal delta was driven by the ECL in May 2009. Utilising the categorization by Van Rijn et al. (2003), the overall BSS/ABSS skill scores during the ECL in May 2009, for the whole survey area and only the ebb-tidal delta were good. The BSS/ABSS skill scores, for some of the smaller sub-areas, such as the ebb-tidal delta crest, were categorized as excellent.

Considering both the twelve day and the ten month simulations, it was determined that a significant portion of the LST occurred during the major storm events. It was also inferred that the main input source of sediment to the ebb-tidal delta was from the leakage of the LST offshore from the southern training wall. Owing to an offshore shift of the LST during storms compared to that of the fair-weather wave conditions, this leakage was much more significant during higher energy conditions. The ten month simulation showed that the sand transported towards the ebb-tidal delta via this leakage then tended to naturally bypass the delta around its offshore edge. A significant portion of the naturally bypassing sand was trapped on the ebb-tidal delta area due to the current interaction of the wave and river entrance. Therefore, it was confirmed by the numerical simulation that one of the main reasons for the continuous growth of the ebb-tidal delta is the leakage of the LST offshore from the sand bypassing system and

southern training wall especially during storms. This is similar to what was suggested in Chapter 4.

7 – Scenario analysis: sediment budget response to major storms

7.1 Introduction

In previous chapters, it was shown that the morphology of the ebb-tidal delta at the mouth of the GCS has been significantly affected by the sediment transport during major storm events. Some studies, such as that of Adams et al. (2008), have suggested a connection between global climate change and coastal evolution, based on patterns of storminess. It is therefore important to develop a more detailed understanding of the sensitivity of the morphological response of the ebb-tide delta to storms of various durations and strengths. This can help future planning and management of the inlet navigability. This chapter presents the results of a series of numerical experiments that explore the sensitivity of the longshore sediment transport (LST) rate; the leakage offshore of the sand bypassing system and the southern training wall; and the ebb-tidal delta morphological changes to a wide range of storm conditions.

7.2 Numerical experiments and results

7.2.1 Initial settings

In the following scenarios, the base physical setting of the case study was considered to be the same as the one generated for the 18th May 2009 numerical simulation described in Chapter 5. The start time of the model was assumed to be 18th May 2009, similar to the 12 day simulation for ECL in May 2009, as explained in Chapter 6. Therefore, the tidal boundaries were also assumed to be the same. HD module settings, including bed resistance, eddy viscosity, flood and dry depths, were the same as the 12 day simulation (Chapter 6) with no wind forcing. The ST module settings, including sediment properties, the sediment transport table (including wave theory used to describe the near-bed velocity), angle of repose, as well as boundary conditions were the same as those of the 12 day simulation. In the SW module, the basic equation, wave breaking parameter, bottom friction, and white capping settings were the same as those used in the 12 day simulation. The various boundary conditions for the SW module are described in detail in section 7.2.2.

7.2.2 Development of Storm Event Scenarios

To develop a set of realistic storm wave scenarios to apply along the boundaries of the SW module, the wave climate and different storm events from January 2004 to the end of August 2015 were studied. Storm events were defined to be the events when $H_s > 3m$ for a period longer than a day. The main purpose of investigating the wave parameters during storm events was to select the range of plausible wave parameters for the boundary conditions of the scenarios. Since the Brisbane buoy was the main source of boundary conditions for previous real-time local models, its measurements were used to distinguish the storm intervals. Based on the defined storm event criteria, 90 storm events were selected during the studied period. In total, these events accounted for about 4% of the time between 2004 - 2015.

It was found that there were a few storms, mainly with mean wave direction (*MWD*) of more than 130˚ (measured from North), which were not observed at the Gold Coast (GC) buoy. Therefore, GC buoy data was also taken into consideration, and storm events which did not occur at the GC buoy ($H_s < 3m$) were not included in the analysis. Then, the cumulative wave power (W_{PT}) of these storms was calculated using GC buoy data as described in Chapter 4. Many of these storm events could be categorized as minor/less significant storm events where their occurrence, as mentioned in Chapter 4, did not have a significant effect on the ebb-tidal delta morphological evolution. These storm events were categorized as having W_{PT} at the GC buoy of less than 25×10^9 ($W.s/m$). Finally, the ranges of measured peak wave periods, significant wave heights, mean wave directions and durations for the major storm events ($W_{PT} > 25\times10^9$ $W.s/m$ at GC buoy) were extracted from the Brisbane buoy data. It should be noted that the calculated total wave power of these events at the Brisbane buoy was more than 35×10^9 $W.s/m$.

The details of the ten major storm events which occurred during the studied interval are shown in Table 7.1. *MWPD* in this table stands for the "mean wave power direction". This is extracted from the direction of the sum of the wave power vectors for each storm time series. The magnitude of wave power vectors for each time step has been calculated based on the linear wave theory (as explained in Chapter 4), using $70m$ as the Brisbane buoy depth. The direction of each time step vector was assumed to be equal to the corrected measured peak wave direction at that time step. As illustrated in Table 7.1, it was found that due to the wave refraction, the measured mean wave direction at the GC buoy for the SE storm events was at least ten degrees less than the measured mean wave directions at the Brisbane buoy. Therefore, for example a storm event with a *MWD* of 93˚ at the Brisbane buoy, such as that which occurred between 29 December 2007 - 4 January 2008, was a NE storm event with *MWD* of 83˚ at GC buoy.

Table 7.1. Major storm characterisctics from January 2004 to August 2015

Time	W_{PT} at GC buoy - Brisbane buoy ($\times 10^9$ *W.s/m*)	*MWD* at GC buoy (˚)	*MWD* at the Brisbane buoy (˚)	*MWPD* Brisbane buoy (˚)	Mean peak wave period at the Brisbane buoy (*s*)
3 - 6 March 2004	34 - 53	N.A.	94	84	10.1
22 - 25 March 2004	38 - 54	N.A.	87	86	11.1
2 - 6 March 2006	53 - 94	N.A.	115	115	10
21 - 24 August 2007	27 - 43	95	109	110	10
29 December 2007 - 4 January 2008	82 - 124	83	93	93	11.6
30 March - 2 April 2009	30 - 35	96	111	109	11
19 - 25 May 2009	104 - 107	91	101	102	11.6
11 - 15 June 2012	63 - 92	94	111	109	11.8
27 - 29 January 2013	44 - 47	81	74	73	10.2
20 - 22 February 2013	27 - 38	101	123	124	10.5

For the purpose of the parametric study, the H_s time series for the storm events at the Brisbane buoy were approximated using the following Gaussian distribution (Cartwright et al., 2004):

$$H_s = A\exp\left[-\left(\frac{t-T_{\max}}{T_{ch}}\right)^2\right] \tag{7.1}$$

where A is the maximum H_s (*m*), t is time (*hr*), T_{max} is the time when the maximum H_s occurs, and T_{ch} is a characteristic time scale of the storm duration (*hr*). T_{ch} indicates the degree of concavity of the H_s distribution over time. The H_s distributions recorded at the Brisbane Buoy during some of the major storm events and the related fitted Gaussian distributions are shown in Figures 7.1 and 7.2. The suggested values for A, T_m and T_{ch} to approximately fit the Gaussian distributions are also shown in these figures.

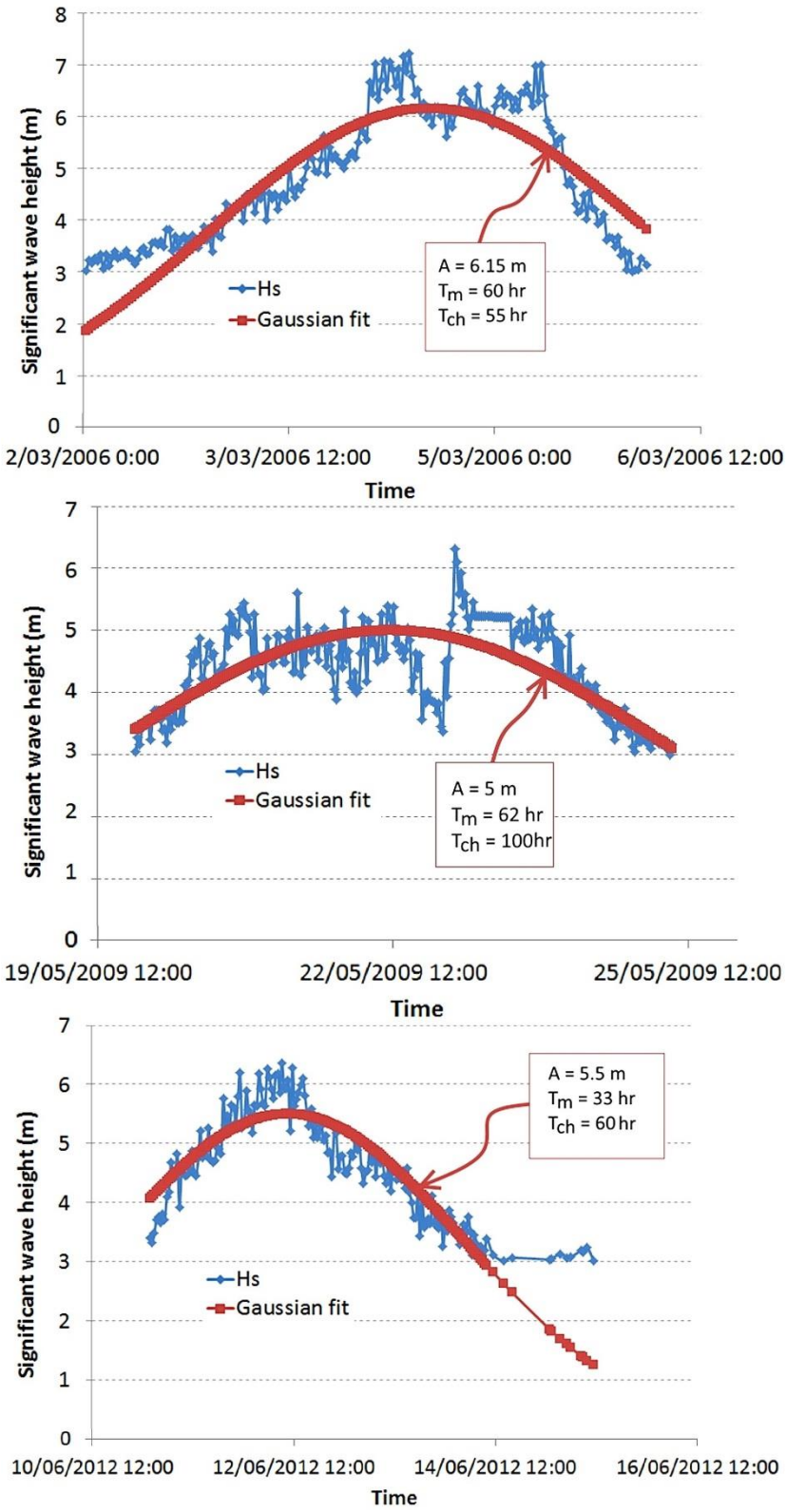

Figure 7.1. H_s distributions for three south-east storm events ($MWD > 90^{\circ}$) at the Brisbane buoy, the fitted Gaussian distributions and the related parameters

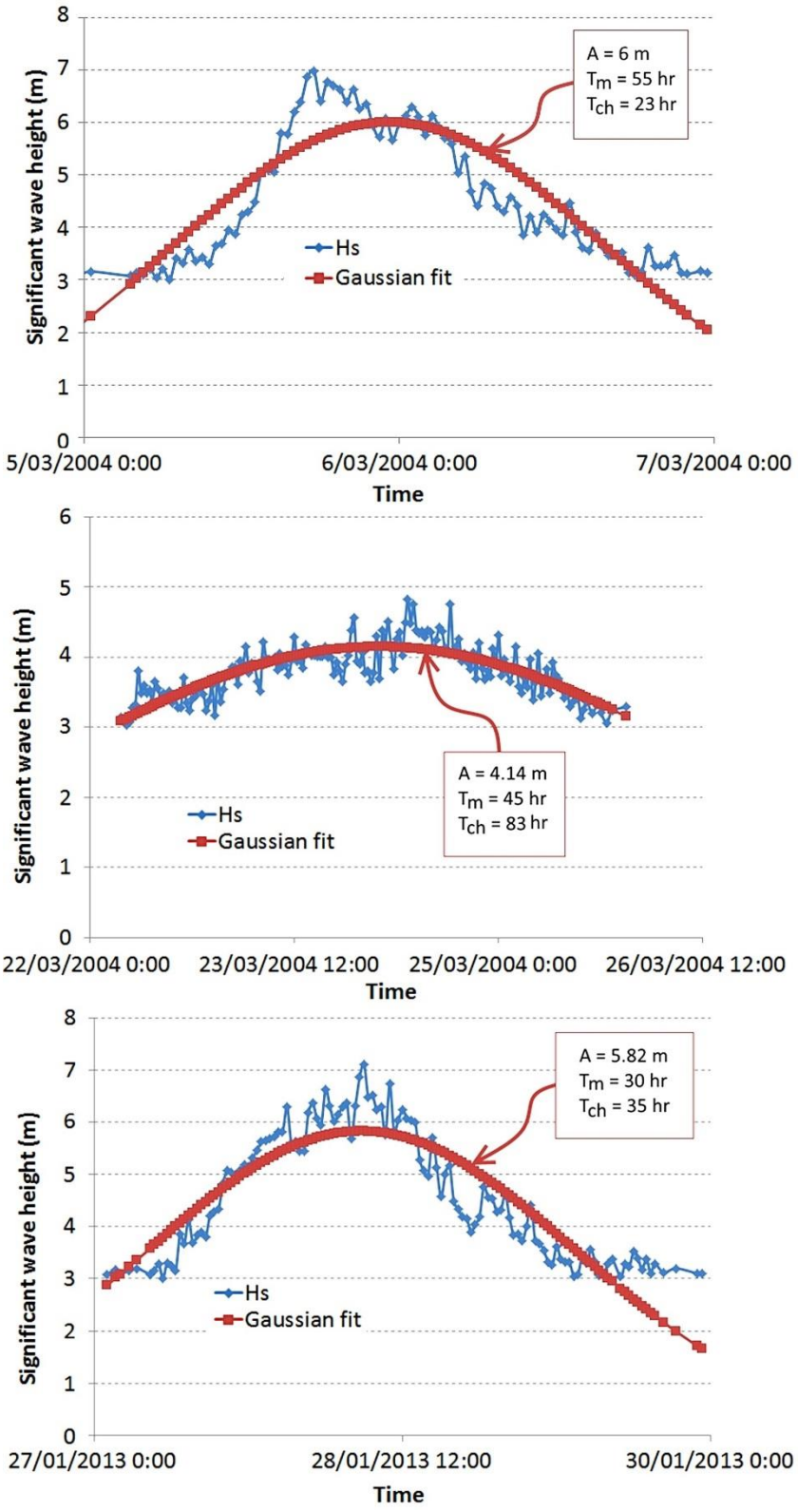

Figure 7.2. H_s distributions for three north-east storm events ($MWD < 90^{\circ}$) at the Brisbane buoy, the fitted Gaussian distributions and the related parameters

Finally, the fitted Gaussian distribution was used to generate a series of storm wave H_s distributions. A series of storm events were developed from different combinations of the

generated H_s distributions and the most probable peak wave periods and directions from NE to SE during major storm events. The ranges of the parameters that were used are shown in Table 7.2. As shown in Table 7.1, the peak wave period for the storm events ranges from 10 to 11.8*s*. van Rijn (2002) parameterisation results suggested that 10 to 20% changes of the wave period leads to an almost constant current velocity and sand transport. Therefore, only one peak wave period of 11*s* was used to reduce the required simulation time. The generated storms were applied at the open offshore boundaries of the numerical model. The duration of each simulation/storm event was dependant on the selected T_{ch}. The duration for each experiment was selected so that the initial and final H_s in the generated Gaussian significant wave height distribution corresponded to a threshold crossing of 2.5*m*.

Table 7.2. Summary of the parameters applied in the scenarios

Parameter	Assumed values
A (H_s peak) (m)	3, 4, 5, 6, 7
MWD ($^{\circ}$)	80, 90, 100, 110, 120
Peak wave period (s)	11
T_{ch} (hr)	55, 100

7.3 Results and discussion

A total of fifty simulations were conducted using various combinations of the parameters given in Table 7.1. The main purpose of this analysis was to find the threshold characteristics of the storm events that cause a significant ebb-tidal delta morphological change. In this regard, first the accumulative LST rate was found for each of the experiments at ETA 77 (Figure 7.3). Then, the accumulative sediment transport to the defined ebb-tidal delta area up to 550*m* offshore (*L1* in Figure 7.3) was calculated. In addition, the ebb-tidal delta volumetric change for each experiment was calculated for the area of the ebb-tidal delta shown in Figure 7.3 (similar to that indicated in Figure 4.2, Chapter 4). In Chapter 4, it was concluded that significant deposition occurs at the ebb-tidal delta during major SE storm events, and erosion occurs during major NE storm events. These were also investigated.

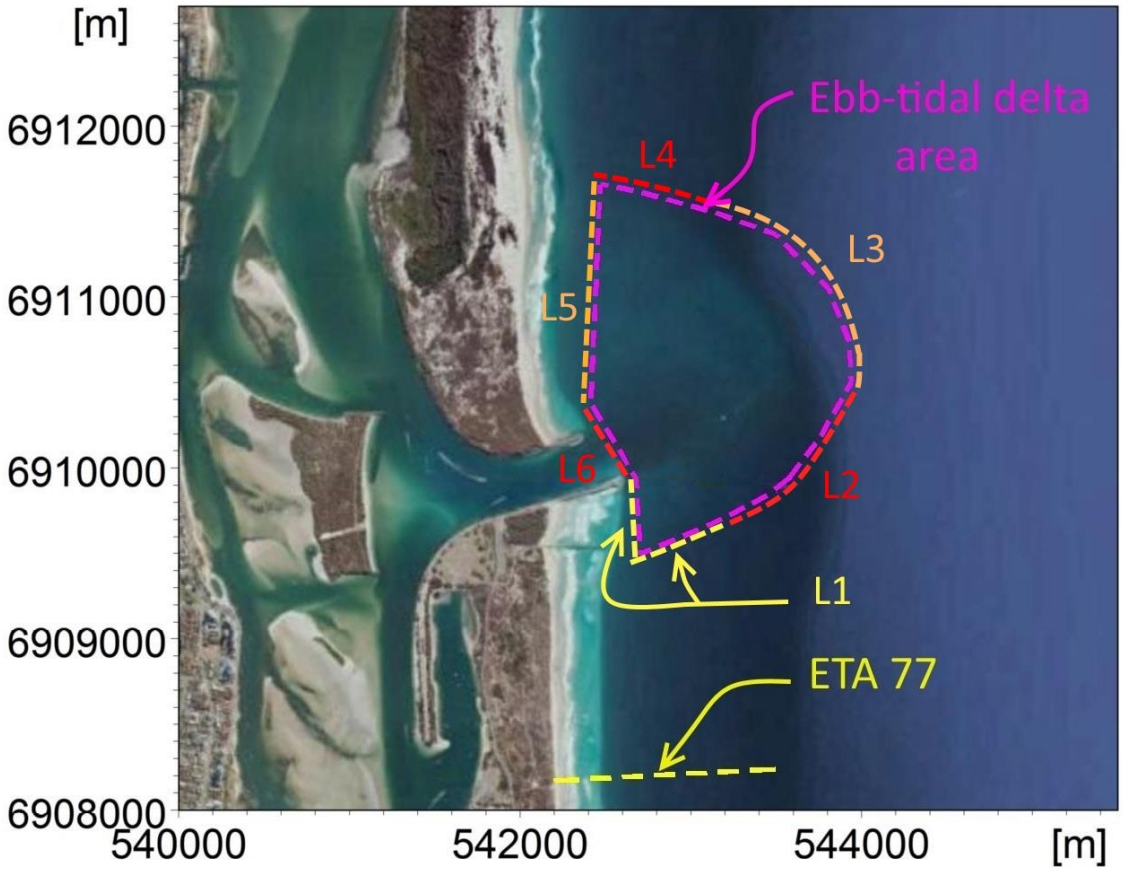

Figure 7.3. ETA 77 line, *L1* (for which leakage of LST was calculated), the defined ebb-tidal delta area, *L1* to *L6* are the subsections of the ebb-tidal delta boundary for which the sediment transport to and from the ebb-tidal delta is calculated in section 7.3.5

7.3.1 Longshore sediment transport rate south of the bypass jetty (ETA 77)

The LST rates at ETA 77 as a function of A (peak H_s at the boundaries) and MWD for two characterised durations (T_{ch}) are shown in Figures 7.4 and 7.5. As seen, the simulated LST rate with mean wave direction of 90˚ at the boundaries of the model was approximately zero. As expected, the sensitivity of the LST to changes in wave height was more pronounced than its sensitivity to the wave angle. Note that the LST curves in Figure 7.4 have an upwardly concave shape, indicating that as the H_s increases for $90^\circ < MWD < 120^\circ$, the LST increases at an increasing rate. Conversely, the LST curves in Figure 7.5 have a downwardly concave shape indicating that as the MWD increases for a given H_s, the rate of increase in the LST decreases. These patterns are in agreement with the empirical LST formulas, such as those demonstrated by CERC and Kamphuis (1991) (section 6.2.1.1, Chapter 6), where LST depends on power of 2 or 2.5 of $H_{s,br}$, as well as $\sin(2\theta_{br})$. From the trend of LST changes for different MWD, as shown in Figure 7.4, it can be concluded that the LST will increase less significantly if the storm deep water wave angle increases to more than 120˚. The resultant LST rate for $A = 3m$ was

negligible, which was partly due to the model underestimation of LST rates in lower wave energy conditions, as discussed in Chapter 6.

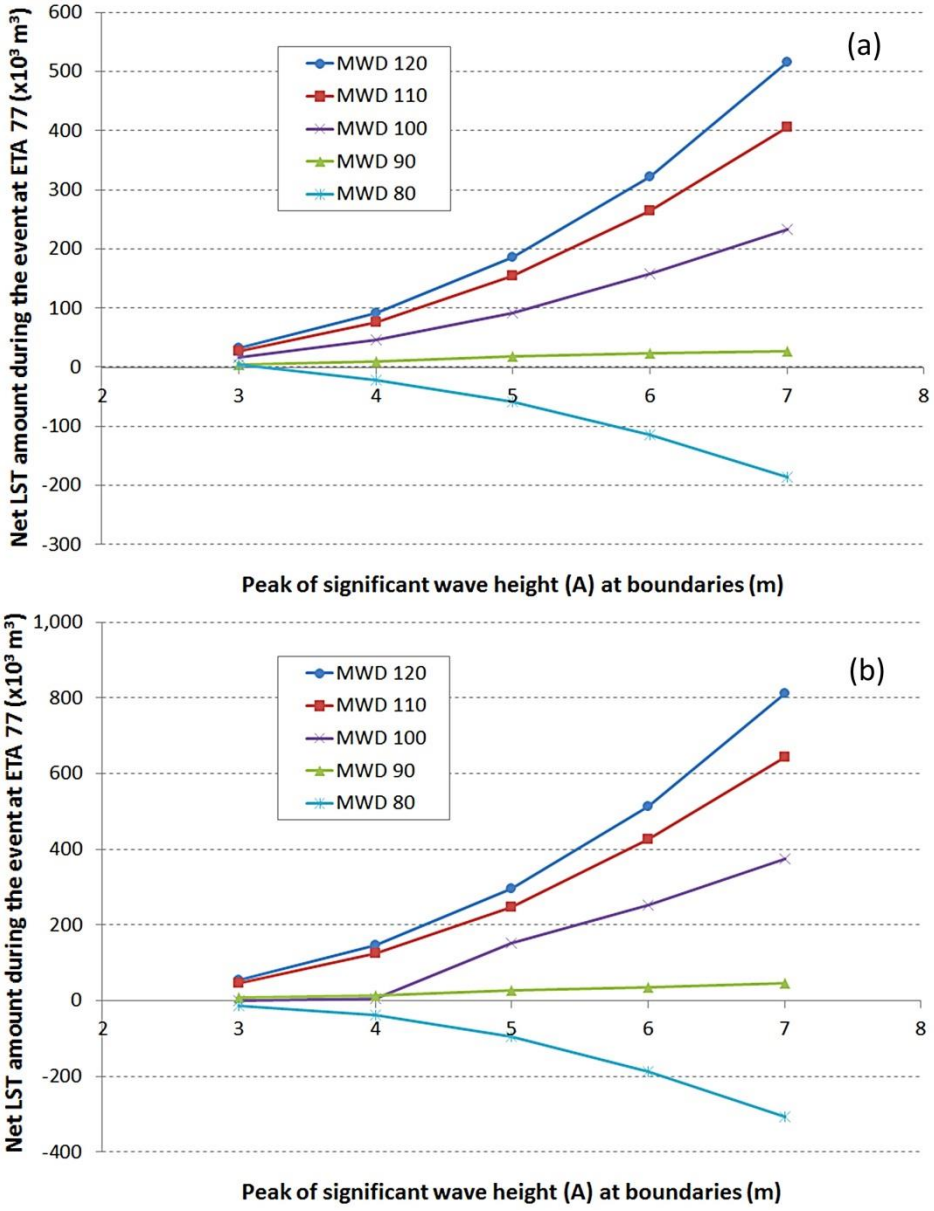

Figure 7.4. Net LST volume during the event at ETA 77 for different *A* and *MWD* values for storms (a) T_{ch} = 55*hr*, (b) T_{ch} = 100*hr*. Positive LST values mean LST to the north, and negative values mean LST to the south

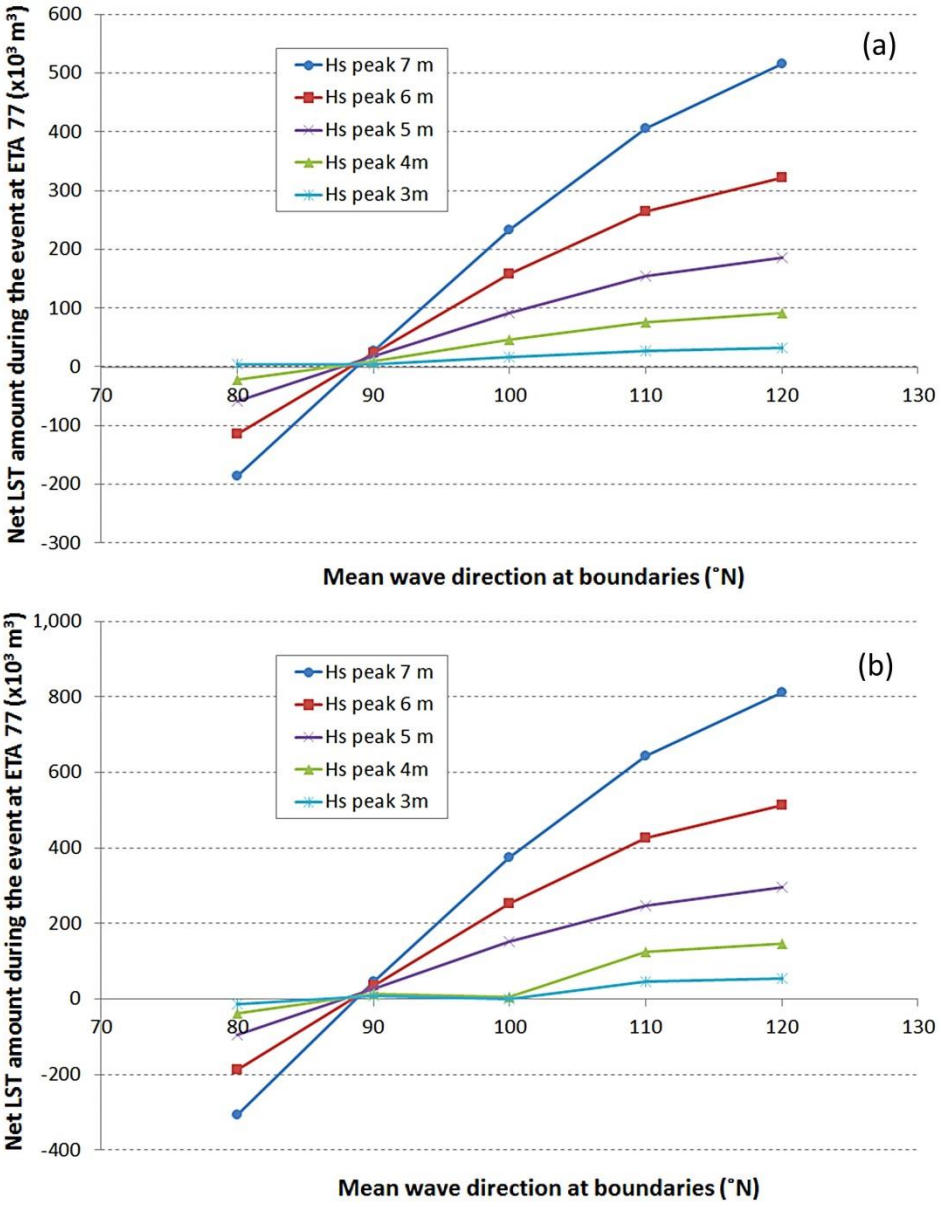

Figure 7.5. Net LST volume during the event at ETA 77 for different *A* and *MWD* values for storms (a) T_{ch} = 55*hr*, (b) T_{ch} = 100*hr*. Positive LST values mean LST to the north, and negative values mean LST to the south

7.3.2 Leakage of sediment transport to and from the ebb-tidal delta past the southern jetty

The leakage of sediment transport, to and from the ebb-tidal delta, was calculated from the offshore end of the southern jetty to 550*m* seaward on the defined boundaries of the bb-tidal delta (*L1* in Figure 7.3) and illustrated in Figures 7.6 and 7.7. As shown in Figure 7.6 for *MWD* of 80˚ and 90˚, sediment moves from the ebb-tidal delta to the south. In addition, the leakage is up to about 100,000 m^3 for storms with *MWD* of 100˚ for both characterised durations. This is while there was up to about 400,000 m^3 of LST at ETA 77 for *MWD* of 100˚, which was mostly

deposited offshore between ETA77 and the southern training wall as a result of the eddy current. This is discussed later in relation to Figure 7.8.

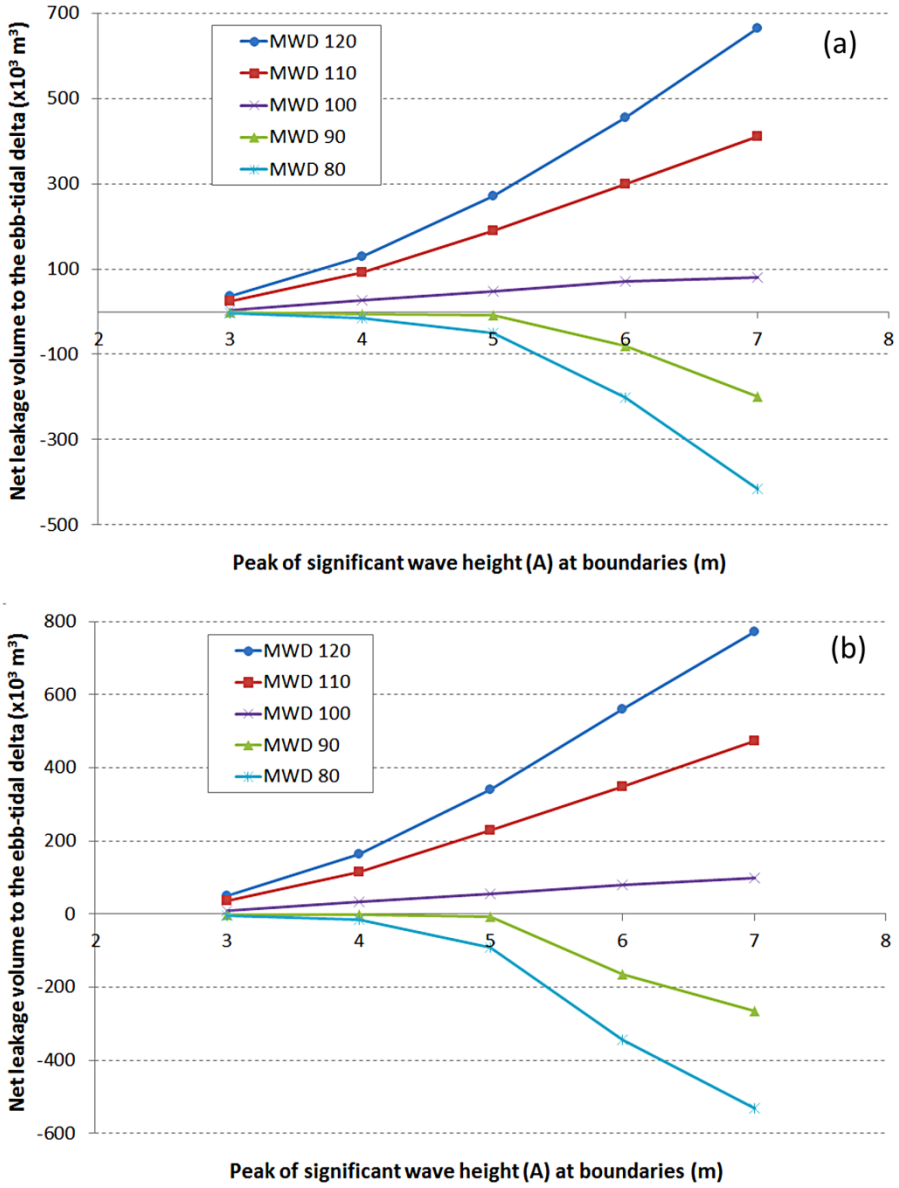

Figure 7.6. The leakage of sediment transport south of the GCS from (-) and to (+) the ebb-tidal delta for storms (a) T_{ch} = 55*hr*, (b) T_{ch} = 100*hr*.

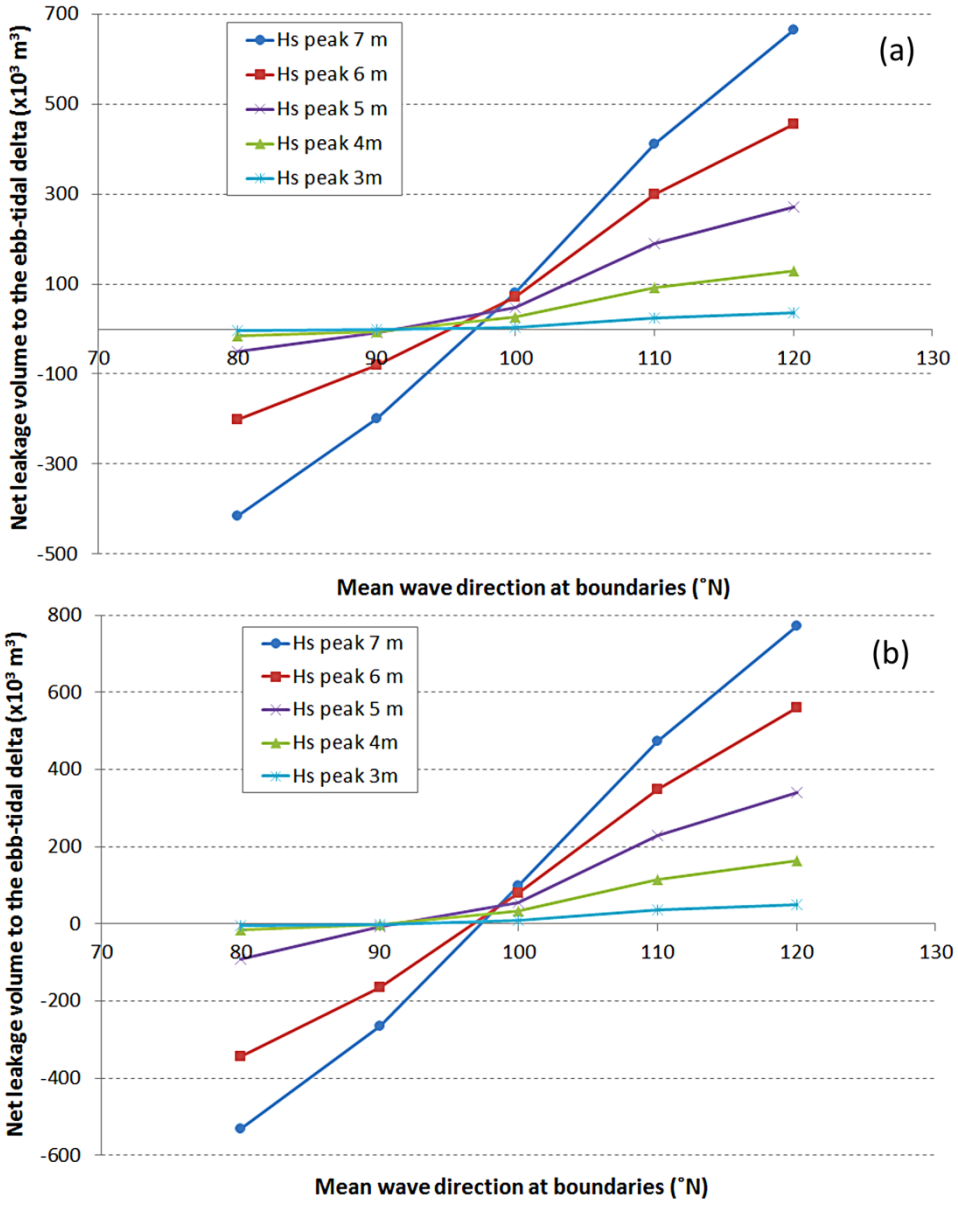

Figure 7.7. The leakage of sediment transport south of the GCS from (-) and to (+) the ebb-tidal delta for storms (a) T_{ch} = 55*hr*, (b) T_{ch} = 100*hr*.

The reason for the negligible leakage with a *MWD* of 100˚ was investigated further. The final bed level change and accumulative sediment transport for the maximum LST case with *MWD* = 100˚ (A = 7*m* and T_{ch} = 100*hr*) are shown in Figure 7.8. As illustrated, during the channel ebb current flow a significant eddy current has been generated east of the entrance mouth. This strong eddy, which was due to the interaction of wave and channel ebb current flow, prevented any leakage of LST to the ebb-tidal delta. In addition, this dominant eddy current resulted in erosion of the southern part of the ebb-tidal delta more offshore (Figure 7.8).

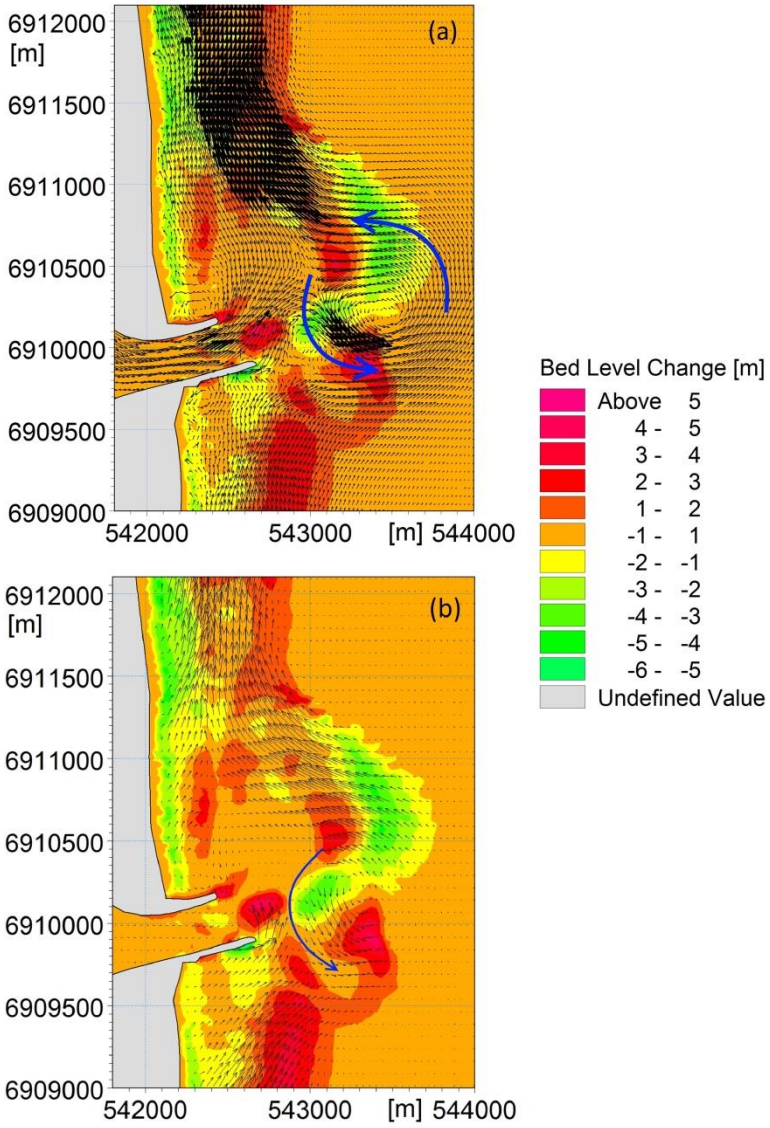

Figure 7.8. Initial and final bed level differences with $A = 7m$, $T_{ch} = 100hr$ and $MWD = 100^{\circ}$. Arrows indicate the velocity vectors at an ebb current in (a) and accumulative sediment transport directions in (b)

The predicted erosion and deposition pattern in Figure 7.8 (b) is very similar to that observed between the two surveys of August 2008 and June 2009 (Figure 7.9). During this period there was a storm event with a *MWD* close to 100˚ (102˚, cf. Table 7.1). This suggests that this erosional - depositional pattern is due to the strong eddy that occurs during storms with a *MWD* ~ 100°.

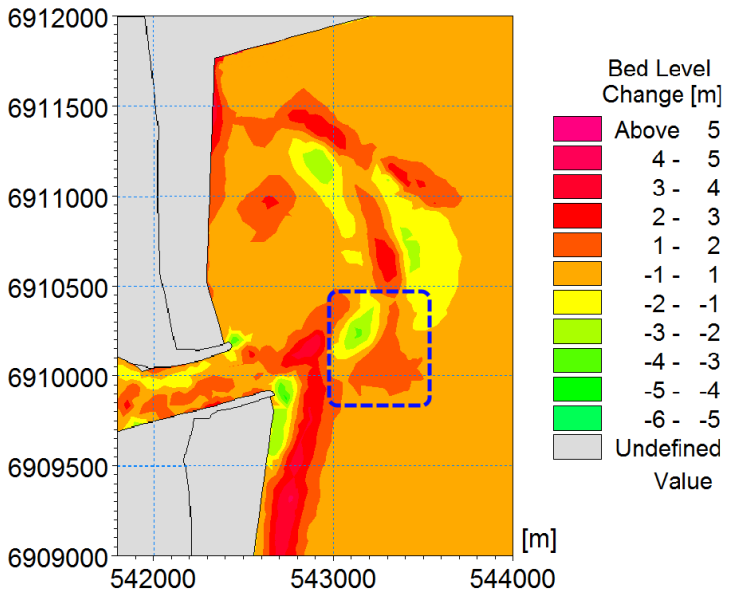

Figure 7.9. Bed level changes between August 2008 and June 2009 survey data.

7.3.3 Volumetric changes in the ebb-tide delta

The volumetric change between final and initial bed level profiles are plotted against *A* and *MWD* parameters in Figures 7.10 and 7.11. As illustrated in Figure 7.10, for less significant storm events, with $A \leq 5m$ and $MWD \leq 100^{\circ}$, the ebb-tidal delta volumetric change was insignificant. In these scenarios the simulated LST rates were less than $200\times10^3\ m^3$ and the leakage was either less than $50\times10^3\ m^3$ to the north (which was for $MWD = 100^{\circ}$, $A = 5m$), or less than $100\times10^3\ m^3$ to the south (Figures 7.4 and 7.6). Figure 7.10 also shows that the ebb-tidal delta was eroded when *MWD* was $\leq 90^{\circ}$ at the Brisbane buoy which further supports the observed erosional effect of NE storm events, as discussed in Chapter 4. The ebb-tidal delta volumetric change when $MWD = 100^{\circ}$ was negligible for $A \leq 6m$ but was erosional for higher *A* values, such as $A = 7m$, despite the fact that there was up to $400\times10^3\ m^3$ LST to the north and $100\times10^3\ m^3$ leakage to the ebb-tidal delta. Analysis of the sediment transport from the defined boundaries of the ebb-tidal delta has shown that this erosion was due to the significant amount of sediment loss from the ebb-tidal delta to downstream (North of the GCS). This will be discussed more in the conceptual model presented in section 7.3.5.

For $MWD \geq 110^{\circ}$ cases, where deposition occurred in the ebb-tidal delta, the deposition volumes in the ebb-tidal delta were either close to, or smaller, than the leakage volume. This suggests that a significant portion of the sand for the ebb-tidal delta growth during major SE storm events has been provided from the leakage. This will be discussed further in section 7.3.5. The

sediment pathways for the cases where erosion occurred in the ebb-tidal delta ($MWD \leq 100^{\circ}$) will be also discussed in section 7.3.5.

Brunn and Gerritsen (2005) suggested that inlets with an *r* value (equation (7.2), greater than 150, tend to be poor "bar bypassers" from updrift to downdrift. In contrast, inlets with an r value less than 50 tend toward closure and are good bar bypassers.

$$r = \frac{P}{M_{tot}} \tag{7.2}$$

P in equation (7.2) is the tidal prism which was equal to 60.8×10^{6} m^3 for May 2009 (as defined in Chapter 4). M_{tot} is the average annual LST brought to the inlet, which in the case of the GCS with artificial sand bypassing, is the average annual leakage of LST to the ebb-tidal delta. Based on the conceptual model presented in Chapter 4, this leakage was about 400×10^{3} m^3 from August 2008 to August 2009 (this is the maximum leakage volume suggested for the past decade). Therefore, the *r* value for GCS will be at least 150. This suggests the inlet's natural sand bypassing is poor, and most of the LST that leaks to the ebb-tidal delta area during SE storm events remains within the delta area and does not naturally bypass to downstream. This is the main reason for the ebb-tidal delta growth in the intervals which include major SE storm events, as was discussed in Chapter 4.

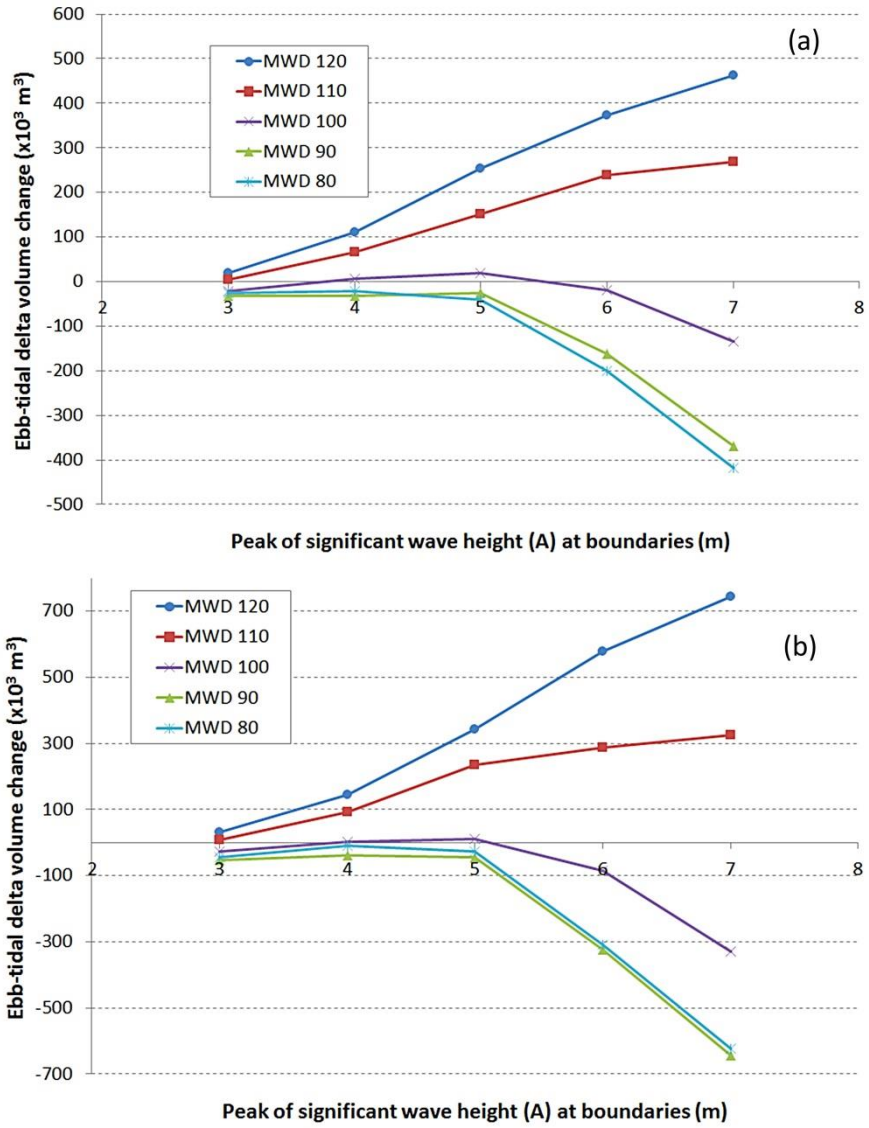

Figure 7.10. The ebb-tidal delta volume change versus storm amplitudes (A) for storms (a) T_{ch} = 55*hr*, (b) T_{ch} = 100*hr*. Positive numbers mean deposition in, and negative values mean erosion from, the ebb-tidal delta.

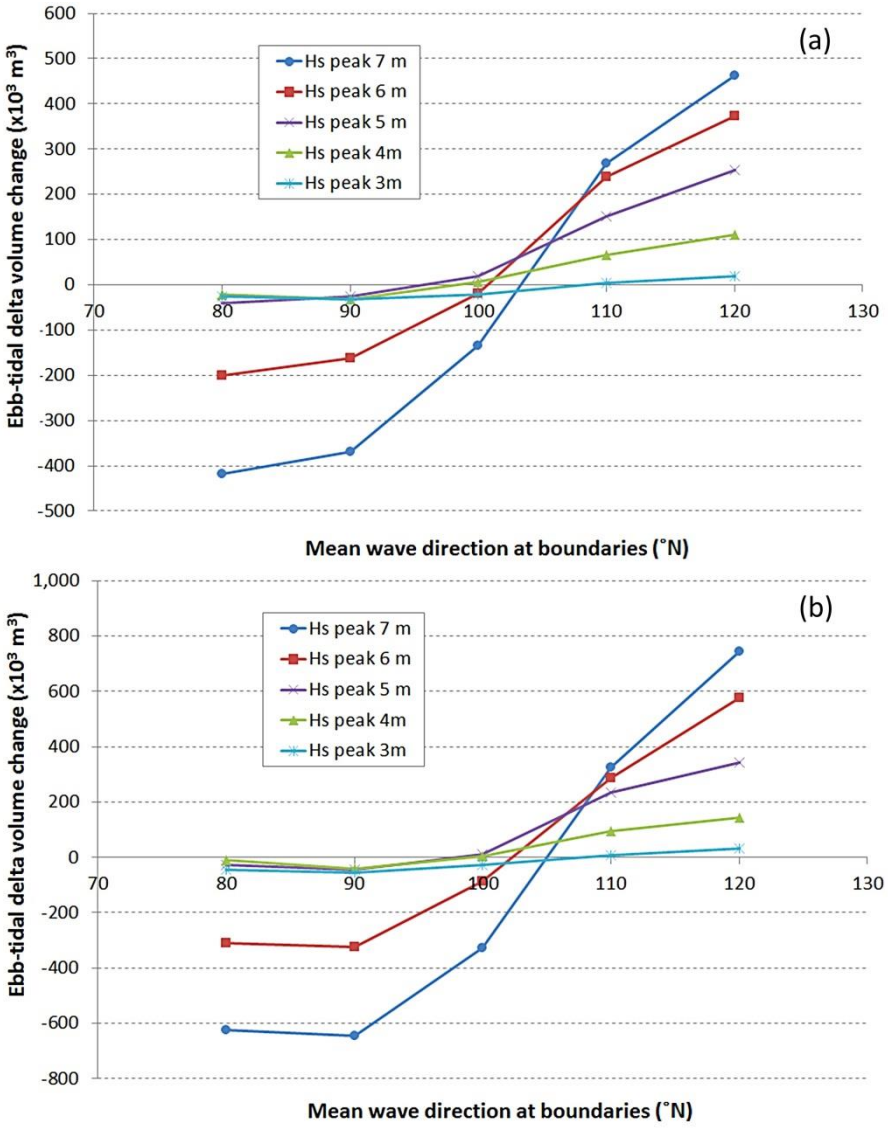

Figure 7.11. The ebb-tidal delta volume change versus storms *MWD* for storms (a) T_{ch} = 55*hr*, (b) T_{ch} = 100*hr*. Positive numbers mean deposition in, and negative values mean erosion from, the ebb-tidal delta.

7.3.4 Influence of wave power

The accumulative wave powers for $H_s > 3m$ at the boundaries were calculated for the scenarios with different characterized durations (using equation (4.14)). These were plotted against the LST at ETA 77, the leakage to/from the ebb-tidal delta through *L1*, and the ebb-tidal delta volumetric change for different *MWPD* (Figures 7.12 and 7.13). Since the direction of the storm waves was assumed to be constant during each storm, the *MWPD* would be the same as the *MWD* for these scenarios.

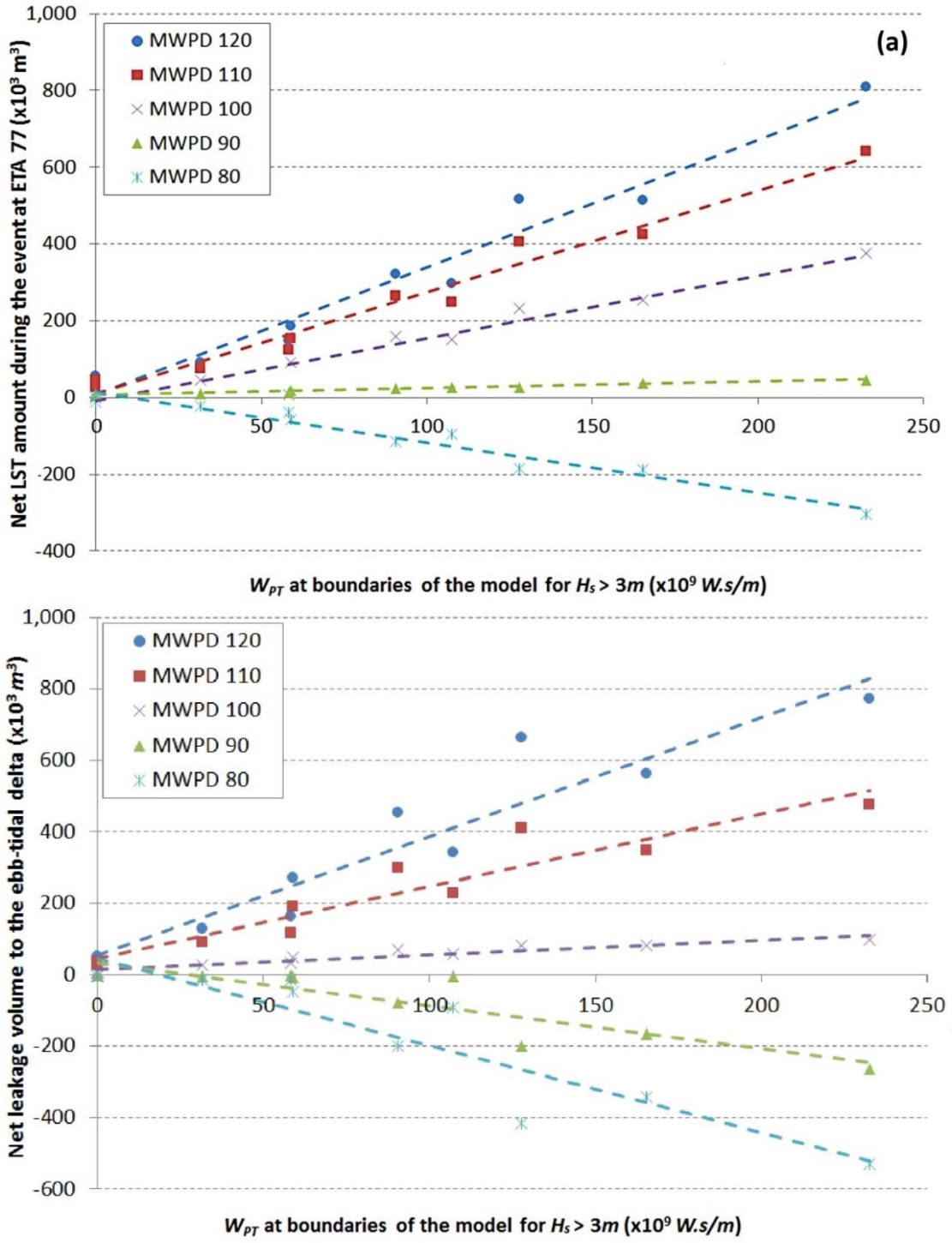

Figure 7.12. (a) Net LST volume during the event at ETA 77 and (b) The leakage of sediment transport south of the GCS through *L1*, to or from the ebb-tidal delta, against the accumulative wave power during storm events ($H_s > 3m$) at the Brisbane buoy.

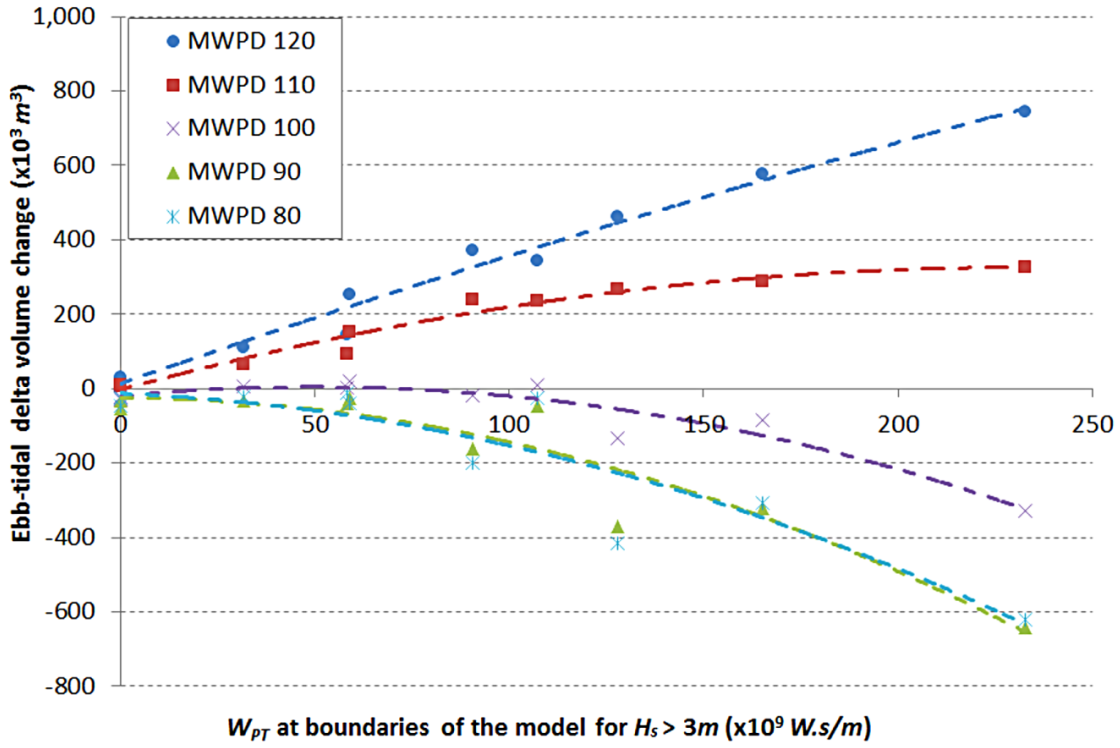

Figure 7.13. The ebb-tidal delta volumetric changes against the accumulative wave power during storm events ($H_s > 3m$) at the Brisbane buoy.

The trendlines in Figure 7.13 can be used for an approximate prediction of the ebb-tidal delta morphological evolution based on the W_{PT} of the significant storms events recorded at the Brisbane buoy. The occurrence of the storm events at the GC Buoy ($H_s > 3m$) should be also checked. This can help to obtain a rough approximation of the consequences of a major storm event on the volume of sand trapped in the ebb-tidal delta. It should be noted that in these scenarios, the bathymetry and the available sand budget, as well as the tidal level, are assumed to be constant. These are the limitations of using scenario-based graphs for prediction of the ebb-tidal delta morphological changes. These graphs could be expanded further for a wider range of storms with variable T_p, and expanded ranges for H_s and *MWD*, which was not in the scope of this study.

7.3.5 Conceptualization of the response of the ebb-tidal delta to storms

To investigate the pathway of sediment transport during different scenarios, the sand volumes passing through the ebb-tidal delta boundaries (Figure 7.3) were calculated for each scenario. The resultant conceptualized models are shown in Figure 7.14, where ΔV represents the simulated ebb-tidal delta volume change. ΔV value is positive for $MWD > 100^{\circ}$ and negative for $MWD \leq 100^{\circ}$. It is illustrated that there is no sediment loss from the eastern edge of the ebb-tidal delta (through *L2* and *L3* in Figure 7.3) during most of the storm events. An exception was an

insignificant sediment loss across the south-eastern edge (*L2*) during major storm event (*A* = 7*m*) for *MWD* = 100˚, which was explained in Figure 7.8. During all of the SE storm events (*MWD* > 90˚ at the Brisbane Buoy) there was a significant amount of leakage of northward LST to the ebb-tidal delta (0.35 to 2.9 Δ*V*). However, for the storm events with *MWD* = 100˚, the sediment loss to downstream (north and northwest, through *L4* and *L5* in Figure 7.3) was more than the sediment leakage from upstream (south, through *L1*) and resulted in total erosion of the ebb-tidal delta.

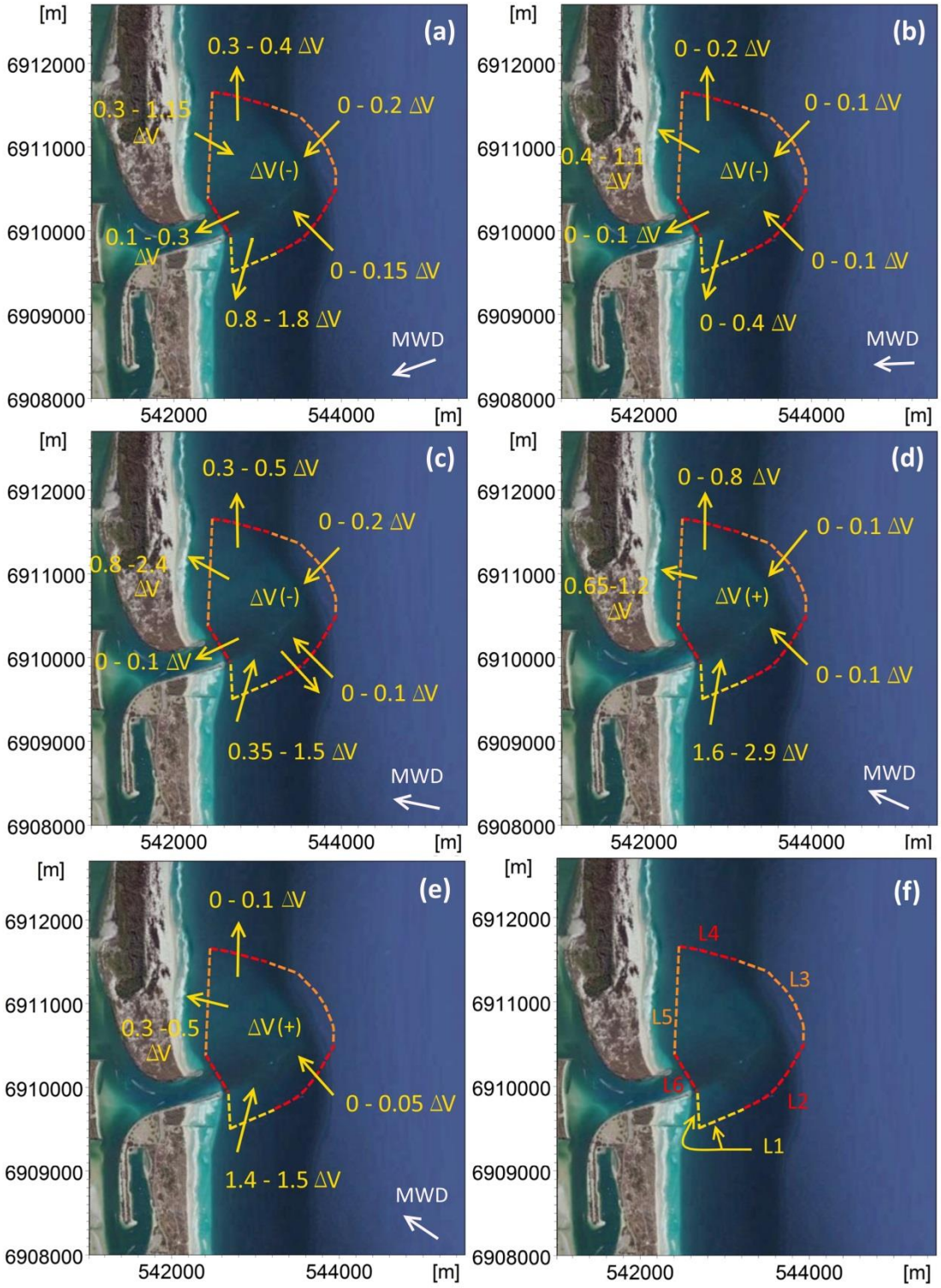

Figure 7.14. Conceptual models of sediment transport volumes based on the ebb-tidal delta volume changes during the storm events (ΔV) for (a) *MWD* = 80˚N, (b) *MWD* = 90˚N, (c) *MWD* = 100˚N, (d) *MWD* = 110˚N and (e) *MWD* = 120˚N. ΔV for a, b, c is a negative value and for d and e is a Positive value. (f) Subsections of the ebb-tidal delta boundary for which the sediment transport to and from the ebb-tidal delta is calculated.

As illustrated in Figure 7.14, during NE storm events (MWD = 80˚ at the Brisbane Buoy) there was a leakage of the resultant southerly LST to the ebb tidal delta from northwest (from *L5* in Figure 7.3). However, specifically during the more significant storm events ($A > 5m$) a substantial portion of this leakage was eroded from the ebb-tidal delta area and transported to the north. This was due to the combination of wave refraction over the ebb-tidal delta area and the produced eddies by wave and ebb/flood current interactions (Figure 7.15). Overall, due to the significant loss of sediment during these events across the south-western edge (through *L1*), the ebb-tidal delta was eroded.

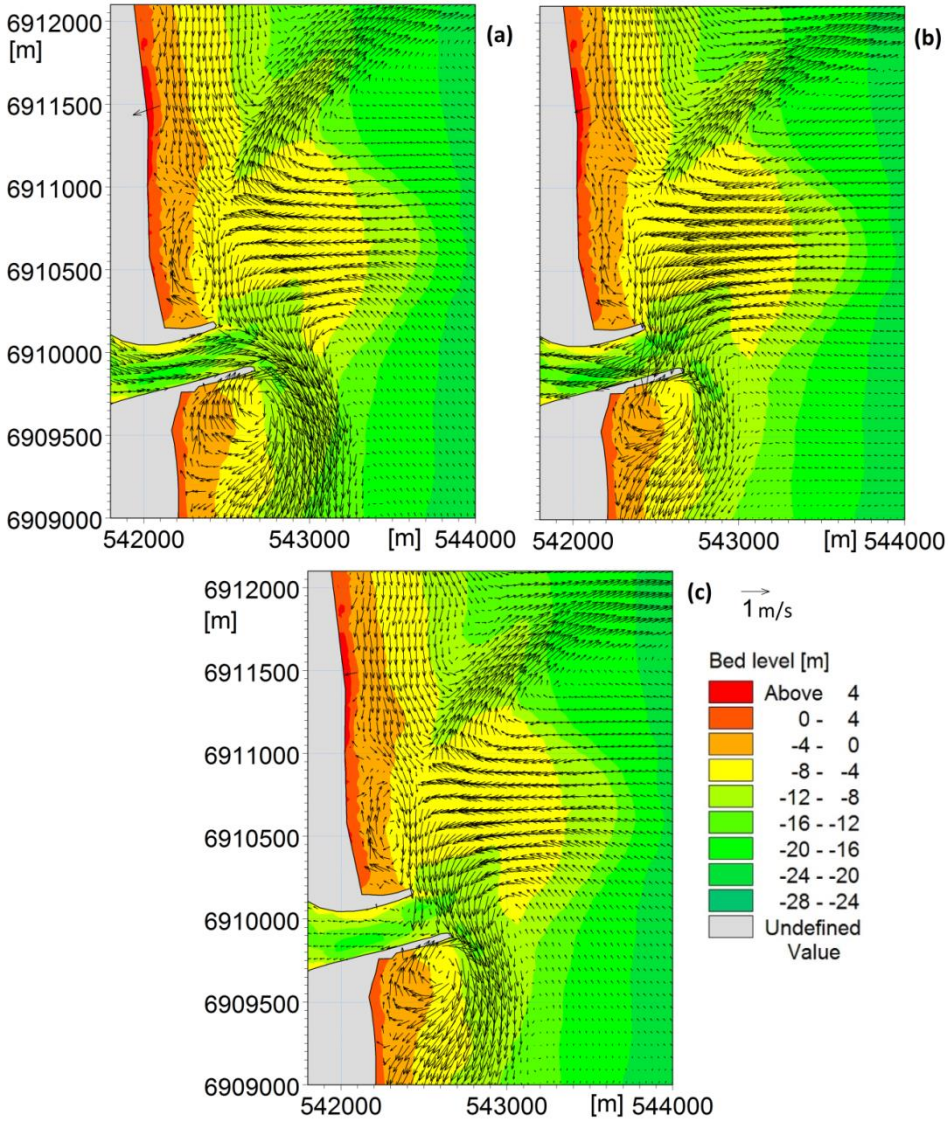

Figure 7.15. Current velocities vectors for $A = 7m$, $T_{ch} = 100hr$ and MWD = 80˚ at (a) an ebb current (b) flood current and (c) between ebb and flood

The loss of sediment from the ebb-tidal delta area for scenarios with MWD = 90˚ at the Brisbane Buoy was eroded: to the north (through *L4*); to the western boundary north of the GCS (*L5*); and

to the south (through *L1*). The erosion through *L5* to the north of the GCS was the most significant of these three.

7.4 Summary and implications

This chapter presented the results of a series of numerical experiments that have been conducted to assess the potential impacts of changes in the ocean storm wave climate on the magnitudes of the LST and the subsequent leakage to the ebb-tidal delta, as well as the resultant morphological changes. Fifty various storm events were generated, the ranges of which spanned the distributions of the major storm event wave parameters and durations in the area in the past decade. The results illustrated that the effect of changes in significant wave height on the resultant LST was more than that of the change in *MWD*. However, the rate of leakage offshore from the sand bypassing system and the ebb-tidal delta erosional or depositional pattern were extremely sensitive to deep water wave direction *(MWD)* during a storm event.

These experiments confirmed the erosional effect of NE storm events which was discussed in Chapter 4 based on survey and wave data analysis. This erosional rate was found to be significant for the storm events with $A > 5m$. The rate of erosion was found to be similar for storm events with *MWD* of 80˚ and 90˚. This was while the LST rate was negligible when *MWD* = 90˚. It was also shown that for storm events with *MWD* at the Brisbane buoy > 100˚, accretion occurred at the ebb-tidal delta. For *MWD* = 100˚, although the LST was northward, leakage to the south and erosion from the ebb-tidal delta occurred for higher energy storm events. Finally, a conceptual model of sediment transport pathways for each storm *MWD* was presented.

The predicted morphological changes in these experiments based on *WPT* could be used to predict some patterns of morphological changes of the ebb-tidal after major storm events. They can be also used for initial estimation of the LST and ebb-tidal delta volume changes based on the major storm events. To improve the predictability of these types of graphs, first, more realistic types of significant wave height distributions, instead of the Gaussian distribution, can be used. Second, more scenarios with a wider range of wave directions and peak wave periods can be simulated. Third, less significant storm events ($2 < H_s < 3m$) where *MWD* is greater than 100˚ can be included in the analysis. Forth, the variation of tidal level, which can affect the sediment transport, can be considered. These types of graphs can also be useful from a coastal management point of view, such as managing the rate of artificial bypassing during storm events. The methodology adopted here could be used for more precise planning for the future of the sand management of the GCS based on climate change models that can predict future forcing scenarios. The predicted weather conditions and resultant storm conditions from global

prediction models can be used to predict the upcoming storm power in the area. This can be used to predict the approximate resultant morphological changes in the ebb-tidal delta using the presented graphs in this chapter. This can help to manage the sediment supply, bypassing system and the future dredging required in the area.

8 – Conclusions and recommendations

8.1 Summary and Conclusions

This thesis has examined the evolution of the Gold Coast Seaway ebb-tidal delta using both historical survey data and a process based numerical model.

The analysis of survey data for the period 2004 to 2015 showed that the ebb-tidal delta has not yet reached an equilibrium condition, as also suggested by empirical formulas in previous studies. This decade long study, combined with the results of previous studies, confirms that the average rate of ebb-tidal delta growth since stabilisation did not diminish significantly, and therefore the ebb-tidal delta is not yet close to an equilibrium condition.

Analysis of the inlet channel morphological change during the past decade suggested an erosional trend of the inlet channel since stabilization of the inlet. Due to a dominant ebb current in the channel, it is suggested that the sediment from the inlet channel is eroded to the ebb-tidal delta. Assuming all of this sand is accreting in the ebb-tidal delta, and not transporting to upstream or downstream due to dominant wave condition at each interval, it can account for about 20% of the average ebb-tidal delta growth.

Other suggested sources of sand contributing to the growth of the delta were the sand leaking offshore from the sand bypassing system and southern training wall to the ebb-tidal delta during major SE storm events, and the sand coming from within the estuary. This was investigated by analysis of the ebb-tidal delta morphological changes in the survey intervals along with the sand bypassing rate, nourishments, flood events, and recorded wave data in the area. It was found that significant accretion in the ebb-tidal delta occurred during the intervals that were characterized by either major SE storm events, or flood events. Further analysis of the accumulative wave power and direction versus the ebb-tidal delta volumetric changes during the past decade showed an accretion of the ebb-tidal delta during intervals with major SE storm events, and its erosion during the intervals with major NE storm events. Therefore, the prevailing source of sand for the continuous growth of the ebb-tidal delta was suggested to be supplied from the leakage of LST during major SE storm events.

Based on the analyses of the past decade, a conceptual model of sediment transport volumes and pathways was developed for the GCS area. It was found that the annual LST rate can vary

significantly, depending on the storminess of each year, from 480,000 m^3/yr to 1,100,000 m^3/yr. This was based on the assumption that the artificial sand bypassing system is mainly capturing the LST and the cross-shore sediment transport contribution is negligible.

To investigate the GCS ebb-tidal delta morphological changes in more detail and check the findings made based on its historical measured bathymetry data analysis, a process-based depth averaged numerical model was developed using MIKE 21/3 Coupled model. The sensitivity of the model to a number of HD and SW module parameters, input source of boundary conditions and applied formulas was investigated first. Due to the nature of coupled models being extremely time consuming to run, and given the fact that sensitivity analysis required several runs, the entire model domain was broken down into two regional and one local model. The HD and SW boundary conditions of the local model were mainly extracted from regional HD and SW models, respectively. The model was initially calibrated and verified using measured current and wave data.

The developed model was then used to simulate the LST and morphological changes of the ebb-tidal delta. The model's estimated rate of LST was close to that of previous studies. However, it was found that the model underestimated the LST, mainly during calmer weather conditions. According to the model results, a significant portion of the estimated LST which occurred during storm events was mainly distributed offshore from the sand bypassing jetty and southern training wall. Therefore, as suggested previously, this sand accreted in the ebb-tidal delta and was not captured by the sand bypassing system. Thus, considering that the recorded artificial sand bypassing rate, which was also close to the estimated rate of LST in previous studies for the selected simulation period, was sourced from the LST during calmer conditions, the model underestimated the LST during calmer wave conditions. Hence, the final suggested rate of LST for the simulation period based on the simulation results, artificial sand bypassing rate, and ebb-tidal delta growth was close to that suggested by the conceptual model in this study. The simulated LST rate was also compared with empirical LST formulas. The results confirmed that the model underestimates LST during calmer weather conditions. A number of reasons for model's underestimation of the LST during calmer weather condition were explained in detail in Chapter 6, section 6.2.2.

The morphological changes between two subsequent survey data, during which time the ebb-tidal delta had a significant rate of growth (about 600,000 m^3) was simulated to check the quality of the model prediction. It was found that the bulk of the morphological change of the ebb-tidal delta occurred during the major storm event (ECL). Therefore, the skill of the model in prediction of morphological changes was estimated using the simulation of the most significant

storm event. The resultant model skill scores, (BSS/ABSS), for the whole survey area and only the ebb-tidal delta were categorised as “good”. This suggests that the model could be used for simulation of the ebb-tidal delta morphological changes due to storm events, which was shown to be the dominant cause of the ebb-tidal delta morphological changes.

The developed model was finally used to simulate the LST and morphological changes of the ebb-tidal delta in response to storms of various durations, directions, and strengths. These scenarios confirmed the erosion of the ebb-tidal delta under NE major storm events, which was discussed previously based on the historical analysis. The sediment transport pathways during storm events with various MWD were illustrated using conceptual models based on the scenarios’ results. The resultant graphs based on these scenarios (ebb-tidal delta volumetric changes versus the storm cumulative power, and LST versus the storm cumulative power) can be used for an approximate prediction of the ebb-tidal delta response due to a range of storm conditions.

8.2 Recommendations for future research

Future research needs to include the continued monitoring of the ebb-tidal delta and the adjacent shoreline behaviour using bathymetric surveys in order to further investigate the trend of the ebb-tidal delta equilibrium condition. A number of questions have been raised during the current study which can be investigated in future research.

(1) The cross-shore sediment transport contribution to the sand bypassing jetty.

One of the assumptions that has been made in this study for the proposed conceptual model of sediment transport in the area was that the artificial sand bypassing volumes are mainly supplied by the LST. Therefore, the cross-shore sediment transport contribution was assumed to be negligible. However, this needs to be investigated further and confirmed by simulation of the physics of the sand bypassing system and some measurements, if it is practical.

(2) The interaction between Jumpinpin inlet and the GCS.

As suggested in Chapter 4, the Jumpinpin inlet condition can affect the tidal prism of the GCS, and therefore, the equilibrium cross-sectional area of the inlet and the equilibrium ebb-tidal delta volume. Therefore, further study on the morphological evolution of the Jumpinpin inlet is essential in order to determine the final equilibrium condition of the GCS.

(3) Modelling the artificial sand bypassing.

As mentioned in Chapter 6, the MIKE 21/3 fm coupled model is not capable of simulation of artificial sand bypassing volumes using source and sink. Therefore, application of another program such as Delft3D is suggested.

(4) Sediment transport formulas.

One of the suggested reasons of underestimation of the LST by the model was that it neglects the sediment transport in the swash zone, which is more noticeable during calmer weather condition. Collecting field data on flow, sediment fluxes and wave transformation on the shallow swash zones, as well as implementing other numerical models which can simulate the sediment transport in these areas are suggested to obtain a better understanding of the sediment transport rates in the area.

(5) Prediction tools.

The model developed in this study can also be used to assess the impacts of relative sea level rise, channel or ebb-tidal delta dredging on the sediment transport process in the area.

(6) Investigation of the solution based on the knowledge gained.

The current study suggested that the main reason for the continuous growth of the ebb-tidal delta is the leakage of LST to the ebb-tidal delta during the major SE storm events. On the basis of the current findings, future studies can focus on exploring the potential of reducing this leakage by altering the inlet, bypassing jetty, or the training walls' configurations.

References

Adams, P.N., Inman, D.L. and Graham, N.E., (2008). *Southern California deep-water wave climate: characterization and application to coastal processes.* Journal of Coastal Research: 1022-1035.

Allen, M. and Callaghan, J., (1999). *Extreme wave conditions for the South Queensland coastal region,* Environmental Protection Agency Report.

Andrews, M. and Nielsen, C., (2001). *Numerical modelling of the Gold Coast Seaway*, Proceedings of Coasts & Ports 2001. Institution of Engineers, Australia, Gold Coast, Australia, pp. 469-474.

Battjes, J. and Stive, M., (1985). *Calibration and verification of a dissipation model for random breaking waves.* Journal of Geophysical Research: Oceans (1978–2012), 90(C5): 9159-9167.

Bayram, A., Larson, M. and Hanson, H., (2007). *A new formula for the total longshore sediment transport rate.* Coastal Engineering, 54: 700–710.

Bertin, X., Fortunato, A.B. and Oliveira, A., (2009a). *A modeling-based analysis of processes driving wave-dominated inlets.* Continental Shelf Research, 29(5): 819-834.

Bertin, X., Oliveira, A. and Fortunato, A.B., (2009b). *Simulating morphodynamics with unstructured grids: Description and validation of a modeling system for coastal applications.* Ocean Modelling, 28: 75–87.

Bhattacharya, B., Price, R.K. and Solomatine, D.P., (2007). *Machine learning approach to modeling sediment transport.* Journal of Hydraulic Engineering, 133(4): 440–450.

Bijker, E.W., (1968). *Littoral drift as a function of waves and current*, Proceeding of the 11th International Coastal Engineering Conference. ASCE, London, pp. 415-435.

Blumberg, A.F. and Georgas, N., (2008). *Quantifying uncertainty in estuarine and coastal ocean circulation modeling.* Journal of Hydraulic Engineering, 134(4): 403–415.

Bodge, K.R. and Dean, R.G., (1987). *Short-Term Impoundment of Longshore Sediment Transport*, DTIC Document.

Booij, N., Ris, R. and Holthuijsen, L.H., (1999). *A third-generation wave model for coastal regions: 1. Model description and validation.* Journal of Geophysical Research: Oceans (1978–2012), 104(C4): 7649-7666.

Boothroyd, J.C., (1985). *Tidal inlets and tidal deltas*, Coastal sedimentary environments. Springer, pp. 445-532.

Bosboom, J., Reniers, A. and Luijendijk, A., (2014). *On the perception of morphodynamic model skill.* Coastal Engineering, 94: 112-125.

Brooks, J., (1953). *Stradbroke Island erosion and broadwater silting, Southport.* Queensland Government Mining Journal, 54: 566-569.

Bruneau, N. et al., (2011). *Future evolution of a tidal inlet due to changes in wave climate, sea level and lagoon morphology (Óbidos Lagoon, Portugal).* Continental Shelf Research, 31(18): 1915-1930.

Brunn, P., (1986). *Morphological and navigational aspects of tidal inlets on littoral drift shores.* Journal of Coastal Research, 2: 123–143.

Brunn, P. and Gerritsen, F., (2005). *Tidal Inlets on Littoral Drift Shores.* Journal of Coastal Research: 305-451.

Bruun, P., (1986). *Morphological and navigational aspects of tidal inlets on littoral drift shores.* Journal of Coastal Research: 123-145.

Bruun, P., Mehta, A.J. and Johnsson, I.G., (1978). *Stability of tidal inlets*. Elsevier Scientific, Amsterdam, The Netherlands, 506 pp.

Camenen, B. and Larson, M., (2008). *A general formula for noncohesive suspended sediment transport.* Journal of Coastal Research, 24(3): 615–627.

Cartwright, N., Li, L. and Nielsen, P., (2004). *Response of the salt–freshwater interface in a coastal aquifer to a wave-induced groundwater pulse: field observations and modelling.* Advances in water resources, 27(3): 297-303.

Castelle, B. et al., (2007). *Dynamics of a wave-dominated tidal inlet and influence on adjacent beaches, Currumbin Creek, Gold Coast, Australia.* Coastal Engineering, 54: 77-90.

Cayocca, F., (2001). *Long-term morphological modeling of a tidal inlet: the Arcachon Basin, France.* Coastal Engineering, 42(2): 115-142.

CERC, (1984). *Shore Protection Manual.* Fourth edition. US Army Engineer Waterways Experiment Station, Coastal Engineering Research Center, US Government Printing Office, Washington, DC.

Chapman, D. and Smith, A., (1983). *Gold Coast Swept Prism-Limits.*

Chapman, D.E.M., (1981). *Coastal erosion and the sediment budget, with special reference to the Gold Coast, Australia.* Coastal Engineering, 4: 207-227.

Cheng, N.-S., (2002). *Exponential formula for bedload transport.* Journal of Hydraulic Engineering, 128(10): 942-946.

Connah, T.H., (1946). *Stradbroke Island erosion and Broadwater silting.* Queensland Government Mining Journal: 370-373.

Coughlan, P.M. and Robinson, D.A., (1990). *The Gold Coast Seaway, Queensland,* Shore & Beach 58(1).

D'Agata, M. and Tomlinson, R., (2004). *Investigation of Ebb Tidal Deltas using a Numerical Model at the Moveable Bed Physical Model Scale*, GCCM for Coastal Zone Estuary & Waterway Management, Gold Coast, Australia.

Davies, A.G. and Villaret, C., (2002). *Prediction of sand transport rates by waves and currents*

in the coastal zone. Continental Shelf Research, 22(18–19): 2725–2737.

Davies, J. and Moses, C.A., (1964). *A morphogenic approach to world shorelines*.

Davies, J.L. and Clayton, K.M., (1980). *Geographical variation in coastal development*, 1522168. Longman London.

Davies, S., (2008). *Gold Coast Estuarine Modeling Study (GEMS). Hydrodynamic, Sediment Transport and Operational Water Quality Models (Draft Report)*, DHI, Griffith Centre for Coastal Management & Gold Coast City Council, Gold Coast.

Davies, S., Mirfenderesk, H., Tomlinson, R. and Szylkarski, S., (2009). *Hydrodynamic, Water Quality and Sediment Transport Modeling of Estuarine and Coastal Waters on the Gold Coast Australia.* Journal of Coastal Research: 937-941.

Davis, J. and Richard, A., (1994). *Barrier island systems—a geologic overview*, Geology of Holocene barrier island systems. Springer, pp. 1-46.

Davis Jr, R.A. and Hayes, M.O., (1984). *What is a wave-dominated coast?* Marine Geology, 60(1): 313-329.

Davis, R.A. and Hayes, M.O., (1984). *What is a wave-dominated coast?* Marine Geology, 60(1): 313-329.

De Swart, H. and Zimmerman, J., (2009). *Morphodynamics of tidal inlet systems.* Annual Review of Fluid Mechanics, 41: 203-229.

De Vriend, H.J. et al., (1993). *Approaches to long-term modelling of coastal morphology: a review.* Coastal engineering, Elsevier, 21: 225–269.

Delft, (1970). *Gold Coast, Queensland Australia - Coastal erosion and related problems*, Report 257, Delft Hydraulics Laboratory, The Netherlands.

DHI, (2014a). *MIKE 21 & MIKE 3 flow model FM Sand Transport Module Scientific Documentation.*

DHI, (2014b). *MIKE 21 Toolbox User Guide*. MIKE by DHI.

DHI, (2014c). *MIKE 21, Flow Model FM Hydrodynamic Module, Release 2014, Scientific documentation.*

DHI, (2014d). *MIKE 21, Flow model FM, Hydrodynamic Module, Release 2014, User Guide.*

DHI, (2014e). *MIKE 21, Flow model FM, Hydrodynamic Module, User Guide*.

DHI, (2014f). *MIKE 21, Spectral Wave Module, Release 2014, Scientific documentation*.

DHL, (1970). *Gold Coast, Queensland Australia - Coastal erosion and related problems*, Delft Hydraulics Laboratory, The Netherlands.

DHL, (1976). *Nerang River Entrance Stabilisation, Report on Model Investigation*, Delf

hydraulic, The Netherlands.

DHL, (1992). *Southern Gold Coast littoral sand supply*, Delft Hydraulics, Gold Coast, Queensland Australia.

Dissanayake, D. and Roelvink, J., (2007). *Process-based approach on tidal inlet evolution–Part 1*. Janssen D, Hulscher (eds) River, Coastal and Estuarine Morphodynamics: RCEM.

Dissanayake, D., Roelvink, J. and Van der Wegen, M., (2008). *Effect of sea level rise on inlet morphology*, 7th International Conference on Coastal and Port Engineering in Developing Countries Dubai, United Arab Emirates.

Dissanayake, D., Roelvink, J. and Van der Wegen, M., (2009). *Modelled channel patterns in a schematized tidal inlet.* Coastal Engineering, 56(11): 1069-1083.

Doering, J. and Bowen, A., (1995). *Parametrization of orbital velocity asymmetries of shoaling and breaking waves using bispectral analysis.* Coastal Engineering, 26(1): 15-33.

Elfrink, B. and Baldock, T., (2002). *Hydrodynamics and sediment transport in the swash zone: a review and perspectives.* Coastal Engineering, 45(3): 149-167.

Elias, E.P., Gelfenbaum, G. and Van der Westhuysen, A.J., (2012). *Validation of a coupled wave-flow model in a high-energy setting: The mouth of the Columbia River*. Journal of Geophysical Research: Oceans (1978–2012), 117(C9).

Elias, E.P. and Hansen, J.E., (2013). *Understanding processes controlling sediment transports at the mouth of a highly energetic inlet system (San Francisco Bay, CA).* Marine Geology, 345: 207-220.

Engelund, F. and Fredsøe, J., (1976). *A sediment transport model for straight alluvial channels.* Nordic Hydrology, 7: 293-306.

Fenton, J., (1990). *Nonlinear wave theories.* the Sea, 9(1): 3-25.

Fenton, J.D., (1985). *A fifth-order Stokes theory for steady waves.* Journal of waterway, port, coastal, and ocean engineering, 111(2): 216-234.

Fenton, J.D. and McKee, W., (1990). *On calculating the lengths of water waves.* Coastal Engineering, 14(6): 499-513.

FitzGerald, D.M., Kraus, N.C. and Hands, E.B., (2000). *Natural mechanisms of sediment bypassing at tidal inlets*, DTIC Document.

Fitzgerald, D.M., Penland, S. and Nummedal, D., (1984). *Control of barrier island shape by inlet sediment by-passing: East Frisian Island,West Germany*. Marine Geology, 60: 355-376.

Fofonoff, N.P. and Millard, R.C., (1983). *Algorithms for computation of fundamental properties of seawater*.

Fortunato, A.B., Bertin, X. and Oliveira, A., (2009). *Space and time variability of uncertainty in*

morphodynamic simulations. Coastal Engineering, 56: 886-894.

Fortunato, A.B. et al., (2014). *Morphological evolution of an ephemeral tidal inlet from opening to closure: the Albufeira inlet, Portugal.* Continental Shelf Research, 73: 49-63.

Fortunato, A.B. and Oliveira, A., (2004). *A modeling system for tidally driven long-term morphodynamics.* Journal of Hydraulic Research, 42 (4): 426–434.

Fortunato, A.B. and Oliveira, A., (2007). *Improving the stability of a morphodynamic modeling system.* Journal of Coastal Research, SI 50: 486–490.

Fredsøe, J., Andersen, O.H. and Silberg, S., (1985). *Distribution of suspended sediment in large waves.* Journal of waterway, port, coastal, and ocean engineering, 111(6): 1041-1059.

GCCM, (2014). *Coastal Protection structures on the Gold Coast*.

Gelfenbaum, G. and Kaminsky, G.M., (2010). *Large-scale coastal change in the Columbia River littoral cell: An overview.* Marine Geology, 273(1): 1-10.

Gerritsen, H. et al., (2011). *Composite modelling of interactions between beaches and structures.* Journal of Hydraulic Research, 49(sup1): 2-14.

GHD, (2007). *Notional Seaway project EIS draft*, GCCC.

Google-Earth, (2015). In: 7.1.5.1557 (Editor).

Grunnet, N.M., Walstra, D.J.R. and Ruessink, B.G., (2004). *Process-based modelling of a shoreface nourishment.* Coastal Engineering, 51 (7): 581–607.

Güner, H.A.A., Çevik, E.Ö. and Yüksel, Y., (2011). *Determination of longshore sediment transport and modelling of shoreline change*. INTECH Open Access Publisher.

Hallermeier, R.J., (1981). *A profile zonation for seasonal sand beaches from wave climate.* Coastal engineering, 4: 253-277.

Harris, M.S. et al., (2005). *Quaternary geomorphology and modern coastal development in response to an inherent geologic framework: an example from Charleston, South Carolina.* Journal of Coastal Research: 49-64.

Hayes, M.O., (1979). *Barrier island morphology as a function of tidal and wave regime.* Barrier islands, 1: 27.

Hayes, M.O., (1980). *General morphology and sediment patterns in tidal inlets.* Sedimentary Geology, 26: 139-156.

Heath, R., (1975). *Stability of some New Zealand coastal inlets.* New Zealand journal of marine and freshwater research, 9(4): 449-457.

Hedges, T., (2001). *Regression and dimensional analysis in coastal engineering: some pitfalls.* Proceedings of the ICE-Water and Maritime Engineering, 148(4): 219-225.

Helman, P., (2010). *Broadwater history, south east Queensland*, GCCM, Gold Coast, Australia.

Heward, A.P., (1981). *A review of wave-dominated clastic shoreline deposits.* Earth-Science Reviews, 17(3): 223-276.

Hicks, D.M. and Hume, T.M., (1996). *Morphology and size of ebb tidal deltas at natural inlets on open-sea and pocket-bay coasts, North Island, New Zealand.* Journal of Coastal Research, 12: 47-63.

Holthuijsen, L., Booij, N. and Herbers, T., (1989). *A prediction model for stationary, short-crested waves in shallow water with ambient currents.* Coastal Engineering, 13(1): 23-54.

Hubbard, D.K., Oertel, G. and Nummedal, D., (1979). *The role of waves and tidal currents in the development of tidal-inlet sedimentary structures and sand body geometry: examples from North Carolina, South Carolina and Georgia.* Journal of Sedimentary Petrology, 49 (4): 1073-1092.

Hughes, S.A., (2002). *Equilibrium cross sectional area at tidal inlets.* Journal of Coastal Research: 160-174.

Hughes, S.A., (2002). *Equilibrium cross sectional area at tidal inlets.* Journal of Coastal Research, 18(1): 160-174.

ICM, (1997). *Recommendations for northern Gold Coast beach protection strategy. Prepared for Gold Coast City Council by International Coastal Management*, Gold Coast.

Isobe, M. and Horikawa, K., (1982). *Study on water particle velocities of shoaling and breaking waves.* Coastal Engineering in Japan, 25: 109-123.

Jafari, A., (2013). *Analysis and prediction of wave transformation from offshore into the surfzone under storm conditions*, Griffith University, Gold Coast, 165 pp.

Jafari, A., Cartwright, N. and Nielsen, P., (2011). *Stormy wave analysis based on recorded field data on south-east coasts of Queensland, Australia.* Journal of coastal Research, SI, 64: 527-533.

Jarrett, J.T., (1976). *Tidal prism-inlet area relationships*, DTIC Document.

Jarrett, J.T., (1976). *Tidal Prism Inlet Area Relationships*, GITI Report 3. US Army Coastal Engineering Research Center, Waterways Experiment Station, Vicksburg, Mississippi.

Jiang, A., Ranasinghe, R., Cowell, P. and Savioli, J., (2011). *Tidal asymmetry of a shallow, well-mixed estuary and the implications on net sediment transport: A numerical modelling study.* Australian Journal of Civil Engineering, 9(1): 1.

Jiang, A.W., Ranasinghe, R. and Cowell, P., (2013). *Contemporary hydrodynamics and morphological change of a microtidal estuary: a numerical modelling study.* Ocean Dynamics, 63(1): 21-41.

Kamphuis, J.W., (1991). *Alongshore sediment transport rate.* Journal of Waterway, Port,

Coastal and Ocean Engineering, 117 (6): 624-640.

Kamphuis, J.W., (2002). *Alongshore transport rate of sand*, COASTAL ENGINEERING CONFERENCE. World Scientific, pp. 2478-2490.

Kana, T., (1989). *Erosion and beach restoration at Seabrook Island, South Carolina.* Shore and Beach, 57(3): 3-18.

Kana, T., Hayter, E. and Work, P., (1999). *Mesoscale sediment transport at southeastern US tidal inlets: conceptual model applicable to mixed energy settings.* Journal of Coastal Research: 303-313.

Kieslich, J.M., (1981). *Tidal Inlet Response to Jetty Construction*, DTIC Document.

Kindler, J.E. and O'Connor, C., (1951). *Erosion of beaches in the town of South Coast*, Queensland. Co-ordinator-General's Department, Brisbane.

King, I., (1997). *RMA2 Version 64 User Manual*.

King, I., (1998). *RMA11 Version 2.6 User Manual*.

Komar, P.D., (1996). *Tidal-inlet processes and morphology related to the transport of sediments.* Journal of Coastal Research: 23-45.

Komen, G.J. et al., (1996). *Dynamics and modelling of ocean waves*. Cambridge university press, UK.

Kraus, N.C., (1998). *Inlet cross-sectional area calculated by process-based model.* Coastal Engineering Proceedings, 1(26).

Kraus, N.C. and Dean, J.L., (1987). *Longshore sediment transport rate distributions measured by trap*, Coastal Sediments. ASCE, pp. 881-896.

Latteux, B., (1995). *Techniques for long-term morphological simulation under tidal action.* Marine Geology, 126(1): 129-141.

Lesser, G., Roelvink, J.A., Van Kester, J.A.T.M. and Stelling, G.S., (2004). *Development and validation of a three-dimensional morphological model.* Coastal Engineering, 51 (8–9): 883–915.

Lesser, G.R., (2009). *An approach to medium-term coastal morphological modelling*, Delft, Netherlands.

Liu, Y. et al., (2009). *Evaluation of a coastal ocean circulation model for the Columbia River plume in summer 2004.* Journal of Geophysical Research: Oceans (1978–2012), 114(C2).

Livezey, R.E., Hoopingarner, J.D. and Huang, J., (1995). *Verification of official monthly mean 700-hPa height forecasts: an update.* Weather and forecasting, 10(3): 512-527.

Longhurst, R., (1996). *From Tallebudgera to the Tweed*, City of Gold Coast, Gold Coast.

Marciano, R., Wang, Z.B., Hibma, A., de Vriend, H.J. and Defina, A., (2005). *Modeling of channel patterns in short tidal basins.* Journal of Geophysical Research: Earth Surface (2003–2012), 110(F1).

Marino, J.N. and Mehta, A.J., (1987a). *Inlet ebb shoals related to coastal parameters*, Coastal Sediments (1987). ASCE, pp. 1608-1623.

Marino, J.N. and Mehta, A.J., (1987b). *Inlet ebb tide shoals related to coastal parameters*, Proceedings of Coastal Sediments '87. American Society of Civil Engineers, New York, pp. 1608-1622.

Masselink, G., Hughes, M. and Knight, J., (2014). *Introduction to coastal processes and geomorphology*. Routledge, New York, USA.

McCauley, E. and Tomlinson, R., (2006). *The evolution of Jumpinpin Inlet*, Griffith University, Gold Coast.

McInnes, K.L., Hubbert, G.D., Abbs, D.J. and Oliver, S.E., (2002). *A numerical modelling study of coastal flooding.* Meteorology and Atmospheric Physics, 80(1-4): 217-233.

Mirfenderesk, H. and Tomlinson, R., (2007). *Numerical modelling of tidal dynamic and water circulation at the Gold Coast Broadwater, Australia.* J Coast Res, 50: 77-281.

Mirfenderesk, H. and Tomlinson, R., (2008). *Observation and Analysis of Hydrodynamic Parameters in Tidal Inlets in a Predominantly Semidiurnal Regime.* Journal of Coastal Research, 24(5): 1229–1239.

Mirfenderesk, H. and Tomlinson, R., (2009). *Interaction between coastal development and inland estuarine waterways at the short-medium timescale.* Journal of Coastal Research, 25(4): 969-980.

Mirfenderesk, H., Tomlinson, R.B., Szylkarski, S. and Rasmussen, E.B., (2007). *Development of a three dimensional model to understand modified tidal entrance processes*, ICCE 2006.

Morris, B.D., Davidson, M.A. and Huntley, D.A., (2001). *Measurements of the response of a coastal inlet using video monitoring techniques.* Marine Geology, 175(1): 251-272.

Munday, D., (1995). *Coastal response to the Nerang River inlet stabilisation, Gold Coast, Queensland, Australia*, QUT, Brisbane, 81 pp.

Murphy, A.H. and Epstein, E.S., (1989). *Skill scores and correlation coefficients in model verification.* Monthly Weather Review, 117(3): 572-582.

Nahon, A., Bertin, X., Fortunato, A.B. and Oliveira, A., (2012). *Process-based 2DH morphodynamic modeling of tidal inlets: A comparison with empirical classifications and theories.* Marine Geology, 291: 1-11.

Nielsen, P., (2009). *Coastal and estuarine processes*.

Nienhuis, J.H. and Ashton, A.D., (2016). *Mechanics and rates of tidal inlet migration: Modeling and application to natural examples.* Journal of Geophysical Research: Earth

Surface, 121(11): 2118-2139.

O'Brien, M.P., (1931). *Estuary tidal prisms related to entrance areas.* Civil Engineering, 1(8): 738-739.

O'Brien, M.P., (1969). *Equilibrium flow areas of inlets on sandy coasts.* Journal of the Waterways and Harbors, 95: 43-52 (American Society of Civil Engineers).

Oliveira, A., Fortunato, A.B. and Rego, J.R., (2006). *Effect of morphological changes on the hydrodynamics and flushing properties of the Óbidos lagoon (Portugal).* Continental Shelf Research, 26(8): 917-942.

Paintal, A., (1971). *Concept of critical shear stress in loose boundary open channels.* Journal of Hydraulic Research, 9(1): 91-113.

Pattearson, C. and Patterson, D., (1983). *Gold Coast longshore transport.*

Patterson, D.C., (2007). *Sand Transport and Shoreline Evolution, Northern Gold Coast, Australia.* Proceedings. Journal of Coastal Research, Special Issue No. 50: pp. 147-151.

Pinto, L., Fortunato, A.B. and Freire, P., (2006). *Sensitivity analysis of non-cohesive sediment transport formulae.* Continental Shelf Research, 26(15): 1826-1839.

Polglase, R.H., (1987). *The Nerang River Entrance Sand-Bypassing System*, Proceedings of the 8th Australian Conference on Coastal Ocean Engineering, Australia, pp. 222-226.

Ranasinghe, R., Pattiaratchi, C. and Masselink, G., (1999). *A morphodynamic model to simulate the seasonal closure of tidal inlets.* Coastal Engineering, 37(1): 1-36.

Ridderinkhof, W., (2016). *Morphodynamics of ebb-tidal deltas*, Utrecht University.

Roelvink, J., (2006). *Coastal morphodynamic evolution techniques.* Coastal Engineering, 53(2): 277-287.

Salter, L., (2002). *South Stradbroke Island / Lindy Salter*. Lindy Salter, The Gap, Qld.

Sankaranarayanan, S., French-McCay, D. and Rowe, J.J., (2014). *Two-dimensional hydrodynamic modeling of circulation in Great South Bay and New York Bight.* Ocean Engineering, 88: 271-279.

Schenewerk, M.S., Dillinger, W.H., vanDam, T.M. and Francis, O., (1999). *Ocean-loading deformations derived from GPS observations (http://www.ngs.noaa.gov/GRD/GPS/Projects/OLT/Agu.99spring/olt.html#results).*

Sedigh, M., Tomlinson, R., Cartwright, N. and Etemad-Shahidi, A., (2016). *Numerical modelling of the Gold Coast Seaway area hydrodynamics and littoral drift.* Ocean Engineering, 121: 47-61.

Sennes, G., Castelle, B., Bertin, X., Mirfenderesk, H. and Tomlinson, R.B., (2007). *Modelling of the Gold Coast Seaway tidal inlet, Australia.* Proceedings. Journal of Coastal Research, Special Issue No. 50: pp. 1086-1091.

Sha, L. and Van den Berg, J., (1993). *Variation in ebb-tidal delta geometry along the coast of the Netherlands and the German Bight.* Journal of Coastal Research: 730-746.

Sha, L.P., (1989). *Variation in ebb-delta morphologies along the West and East Frisian Islands, The Netherlands and Germany.* Marine Geology, 89: 11-28.

Shanas, P. and Kumar, V.S., (2014). *Coastal processes and longshore sediment transport along Kundapura coast, central west coast of India.* Geomorphology, 214: 436-451.

Siegle, E., Huntley, D.A. and Davidson, M.A., (2004). *Physical controls on the dynamics of inlet sandbar systems.* Ocean Dynamics, 54(3-4): 360-373.

Smith, E.R., Wang, P. and Zhang, J., (2003). *Evaluation of the CERC Formula Using Large-Scale Laboratory Data*, Proceedings of Coastal Sediments 2003.

Speer, P. and Aubrey, D., (1985). *A study of non-linear tidal propagation in shallow inlet/estuarine systems Part II: Theory*. Estuarine, Coastal and Shelf Science, 21(2): 207-224.

Splinter, K.D., Davidson, M.A., Golshani, A. and Tomlinson, R., (2012). *Climate controls on longshore sediment transport.* Continental Shelf Research, 48: 146-156.

Splinter, K.D., Golshani, A., Stuart, G. and Tomlinson, R., (2011). *Spatial and temporal variability of longshore transport along Gold Coast, Australia*, Coastal Engineering Proceedings, pp. sediment. 95.

Stuart, G., Kerry, C. and Mortensen, S., (2010). *Gold Coast Seaway SmartRelease Project Model Set-up Report*, DHI Water and Environment PTY LTD, Gold Coast.

Stuart, G. and Lewis, J., (2011). *Gold Coast Shoreline Management Plan: Field Measurement & Data Collection*, Gold Coast City Council, Gold Coast.

Sutherland, J., Hall, L. and Chesher, T., (2001). *Evaluation of the coastal area model PISCES at Teignmouth (UK).* HR Wallingford Report TR125.

Sutherland, J., Peet, A. and Soulsby, R., (2004a). *Evaluating the performance of morphological models.* Coastal Engineering, 51(8): 917-939.

Sutherland, J., Walstra, D.J.R., Chesher, T.J., van Rijn, L.C. and Southgate, H.N., , (2004b). *Evaluation of coastal area modelling systems at an estuary mouth.* Coastal Engineering, 51 (8–9): 119–142.

Swaragi, T. and Deguchi, I., (1978). *Distribution of sand transport rate across a surf zone*. Coastal Engineering Proceedings, 1(16).

Swart, D.H., (1982). *The nature and analysis of random waves in shallow water*. Coastal Engineering and Hydraulics Division, National Research Institute for Oceanology, Council for Scientific and Industrial Research.

Tambroni, N. and Seminara, G., (2006). *Are inlets responsible for the morphological degradation of Venice Lagoon?* Journal of Geophysical Research: Earth Surface (2003–

2012), 111(F3).

Tanaka, H., Adityawan, M.B. and Mano, A., (2014). *Morphological changes at the Nanakita River mouth after the Great East Japan Tsunami of 2011.* Coastal Engineering, 86: 14-26.

Taylor, R., (1990). *Interpretation of the correlation coefficient: a basic review.* Journal of diagnostic medical sonography, 6(1): 35-39.

Tomlinson, R.B., (1991). *Processes of sediment transport and ebb tidal delta development at a jettied inlet,* Coastal Sediments (1991). ASCE, pp. 1404-1418.

Tung, T.T., (2011). *Morphodynamics of seasonally closed coastal inlets at the central coast of Vietnam.* PhD, Delft University of Technology.

Tung, T.T., Stive, M.J., van de Graaff, J. and Walstra, D.-J.R., (2008). *Morphological stability of tidal inlets using process-based modelling.* Coastal Engineering: 2182-2194.

Tung, T.T., Walstra, D.-J.R., van de Graaff, J. and Stive, M.J., (2009). *Morphological modeling of tidal inlet migration and closure.* Journal of Coastal Research: 1080-1084.

Turner, I.L., Aarninkhof, S.G.J. and Holman, R.A., (2006). *Coastal imaging application and research in Australia.* Journal of Coastal Research, 22(1): 37-48.

USACE, (1984). *Shore Protection Manual,* vol. 1. U.S. Army Engineer Waterways Experiment Station, Coastal Engineering Research Center, U.S. Government Printing Office, Washington, DC.

Van de Kreeke, J., (1990). *Can multiple tidal inlets be stable?* Estuarine, Coastal and Shelf Science, 30(3): 261-273.

Van de Kreeke, J., Brouwer, R., Zitman, T. and Schuttelaars, H., (2008). *The effect of a topographic high on the morphological stability of a two-inlet bay system.* Coastal Engineering, 55(4): 319-332.

Van der Vegt, M., Schuttelaars, H. and De Swart, H., (2006). *Modeling the equilibrium of tide-dominated ebb-tidal deltas.* Journal of Geophysical Research: Earth Surface (2003–2012), 111(F2).

Van der Wegen, M., Dastgheib, A. and Roelvink, J., (2010). *Morphodynamic modeling of tidal channel evolution in comparison to empirical PA relationship.* Coastal Engineering, 57(9): 827-837.

Van der Wegen, M. and Roelvink, J., (2008). *Long-term morphodynamic evolution of a tidal embayment using a two-dimensional, process-based model.* Journal of Geophysical Research: Oceans (1978–2012), 113(C3).

Van der Wegen, M., Roelvink, J., De Ronde, J. and Van der Spek, A., (2008). *Long-term morphodynamic evolution of the Western Scheldt estuary, The Netherlands, using a process-based model.* COPEDEC VII, Dubai, UAE.

Van der Wegen, M., Thanh, D.Q. and Roelvink, D., (2006). *Bank erosion and morphodynamic*

evolution of alluvial estuaries using a process based 2D model. Session Wed2_S1: Coastal Morphodynamics I.

Van Enckevort, I. et al., (2004). *Observations of nearshore crescentic sandbars*. Journal of Geophysical Research: Oceans (1978–2012), 109(C6).

Van Leeuwen, S. and De Swart, H., (2002). *Intermediate modelling of tidal inlet systems: spatial asymmetries in flow and mean sediment transport.* Continental Shelf Research, 22(11): 1795-1810.

van Leeuwen, S.M., van der Vegt, M. and de Swart, H.E., (2003). *Morphodynamics of ebb-tidal deltas: a model approach. Estuarine*. Coastal and Shelf Science, 57: 899-907.

Van Rijn, L. et al., (2003). *The predictability of cross-shore bed evolution of sandy beaches at the time scale of storms and seasons using process-based profile models.* Coastal Engineering, 47(3): 295-327.

van Rijn, L.C., (2002). *Longshore sand transport*, Coastal Engineering Conference. ASCE American Society of Civil Engineers, pp. 2439-2451.

Van Rijn, L.C., (1990). *Handbook of Sediment Transport by Currents and Waves, Report H461*. Delft Hydraulics.

Van Rijn, L.C., (2007). *Unified view of sediment transport by currents and waves. II: suspended transport.* Journal of Hydraulic Engineering, 133(6): 668–689.

Van Wellen, E., Baldock, T., Chadwick, A. and Simmonds, D., (2001). *STRAND-a model for longshore sediment transport in the swash zone*, COASTAL ENGINEERING CONFERENCE. ASCE AMERICAN SOCIETY OF CIVIL ENGINEERS, pp. 3139-3150.

Vila-Concejo, A., Ferreira, Ó., Morris, B., Matias, A. and Dias, J., (2004). *Lessons from inlet relocation: examples from Southern Portugal*. Coastal Engineering, 51(10): 967-990.

Voisey, C., (2004). *Moveable Bed Physical Modelling of Ebb Delta Growth Characteristics*, GCCM for Coastal Zone Estuary & Waterway Management, Gold Coast, Australia.

Vu, T.T.T., (2013). *Aspects of inlet geometry and dynamics.*

Walton, T.L. and Adams, W.D., (1976). *Capacity of inlet outer bars to store sand*, Proceedings of the 15th Coastal Engineering Conference. American Society of Civil Engineers, New York, pp. 1919-1937.

Wang, P., Ebersole, B.A. and Smith, E.R., (2002). *Longshore sand transport-initial results from large-scale sediment transport facility*, DTIC Document.

Wang, P., Kraus, N.C. and Davis Jr, R.A., (1998). *Total longshore sediment transport rate in the surf zone: field measurements and empirical predictions.* Journal of Coastal Research: 269-282.

Wang, Z., Louters, T. and De Vriend, H., (1995). *Morphodynamic modelling for a tidal inlet in*

the Wadden Sea. Marine Geology, 126(1): 289-300.

Warner, J.C., Geyer, W.R. and Lerczak, J.A., (2005). *Numerical modeling of an estuary: A comprehensive skill assessment.* Journal of Geophysical Research: Oceans (1978–2012), 110(C5).

WBM, (1992). *Broadwater hydraulic model investigations- Assessment of specific options*.

WBM, (2001). *Review of Gold Coast Seaway - Coastal processes*, WBM Oceanics Australia.

WBM, (2013). *Gold Coast Broadwater preliminary coastal and hydrodynamic investigations for cruise ship terminal options*, BMT WBM Pty Ltd, Gold Coast.

Wheeler, P., Peterson, J. and Gordon-Brown, L., (2010). *Flood-tide Delta Morphological Change at the Gippsland Lakes Artificial Entrance, Australia (1889–2009).* Australian Geographer, 41(2): 183-216.

Williams, B. and Pan, S., (2011). *Storm-driven morphological evolution and sediment bypassing at a dynamic tidal inlet: a simulation-based analysis.* Journal of Coastal Research(64): 1209.

Williams, J. et al., (2003). *Tidal inlet function: field evidence and numerical simulation in the INDIA project.* Journal of Coastal Research: 189-211.

Willmott, C.J., (1981). *On the validation of models.* Physical geography, 2(2): 184-194.

Witt, C. and Hill, P., (1987). *Gold Coast Seaway: An Overview of the Project's Design and Construction and It's Subsequent Performance.*

Work, P., Guan, J., Hayter, E. and Elci, S., (2001). *Mesoscale model for morphologic change at tidal inlets.* Journal of waterway, port, coastal, and ocean engineering, 127(5): 282-289.

WRL and GCCM, (1998). *Numerical Modelling of Sediment Movement and Budget at Seaway*, Water Research Laboratory in association with Griffith University for GCCC, Gold Coast, Australia.

Young, I.R., (1999). *Wind generated ocean waves*, 2. Elsevier, University of Adelaide, Australia.

Zhang, Y., Baptista, A.M. and Myers, E.P., (2004). *A cross-scale model for 3D baroclinic circulation in estuary–plume–shelf systems: I. Formulation and skill assessment.* Continental Shelf Research, 24(18): 2187-2214.

Appendix A. Analysis of the morphological evolution of the shoreline

A brief analysis of the coastal processes and adjacent shoreline evolution are presented in this section. As the frequency of ETA line surveys varied substantially over time, and as the distances between the surveyed lines were irregular, most of them could not be used to develop a reasonably precise bathymetry. Therefore, two bathymetries based on the ETA lines survey data from 1966 and 2013, which were the only times that plenty of ETA lines were surveyed, were developed. These bathymetries extend from the south of the entrance to the Burleigh Heads inlet, as shown in Figure A.1. It should be noted that the generated bathymetries are an approximation because of the interpolation between the ETA lines.

The resultant bed level change between 1966 and 2013 is shown in Figure A.2. The accumulative volume of bed level change over this interval shows a net total erosion of 4×10^6 m^3 of sand. It should be noted that the volumes of renourished sand were not incorporated, meaning that the actual volume of erosion was much higher. As shown in Figure A.2, accretion occurred offshore from Narrowneck, as this was to be expected due to the major additional nourishment of about 1.1×10^6 m^3 from Broadwater placed on beach from Surfers Paradise to Main Beach in association with Narrowneck reef in 1999 (plus normal annual nourishment of about 66,000 m^3 from building sites). Figure A.2 has also indicated that major erosion occurred for three kilometres in the northern end of the survey data. Comparison of the bathymetry of 1966 and bed level changes between 1966 and 2013 show that most of this erosion has occurred between a depth of 10 and 15 metres. Patterson (2007) suggested that this erosion was from the residual of an old ebb-tidal delta which was formed during the time that the entrance was further south. Analysis of the generated bathymetries of 1966 and 2013, as shown in Figure A.1d and e, has demonstrated that the 10 m depth contour line in 1966 from the north of Narrowneck to south of the entrance was oriented more offshore than in 2013. As illustrated in this figure, this contour line gradually became parallel to the shoreline at its current condition. It is also shown that if the shoreline was assumed to be zero (AHD) depth, the shoreline north of Narrowneck has recessed up to a maximum of 50 metres from 1966 to 2013.

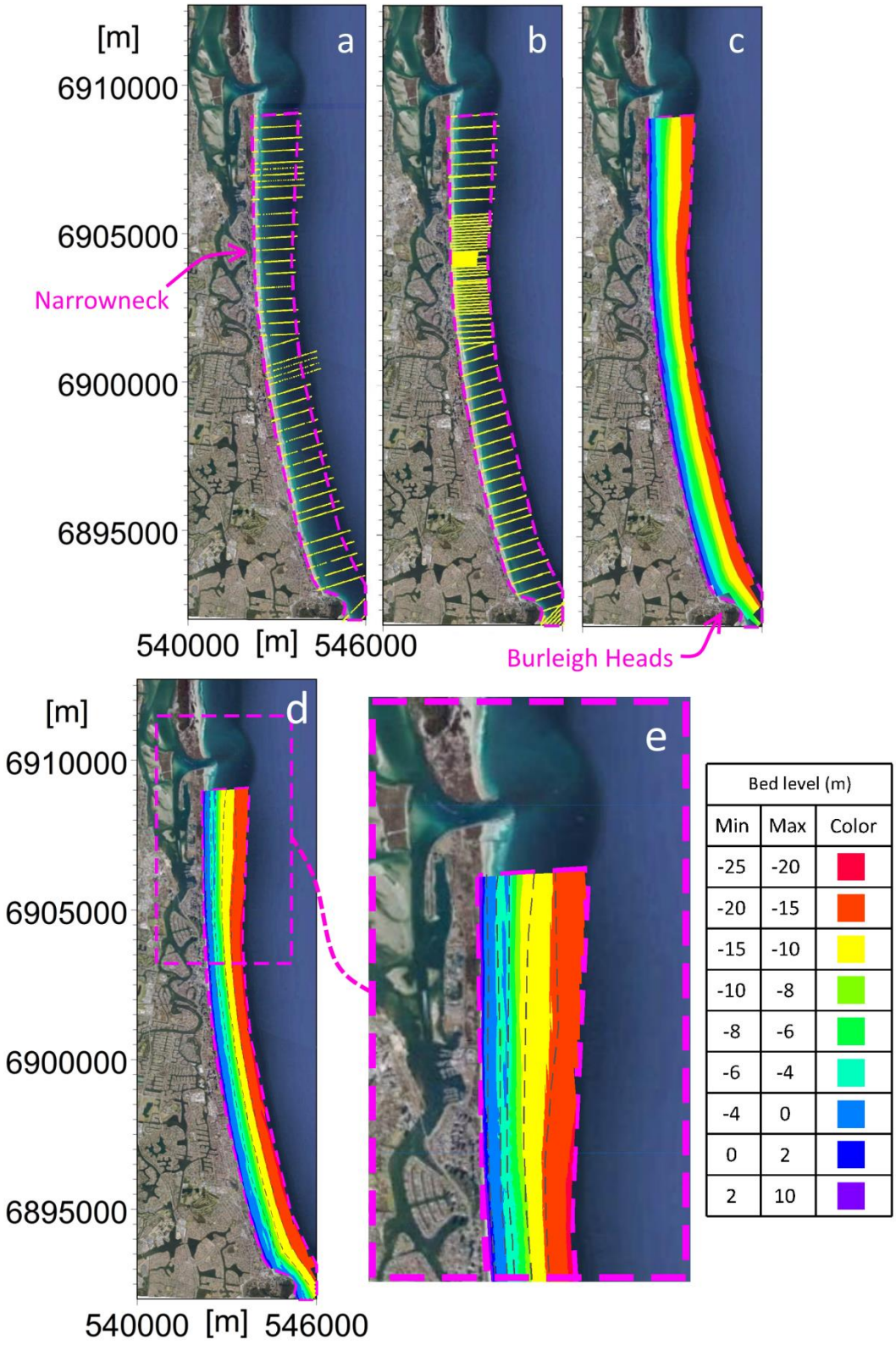

Figure A.1. (a) ETA lines survey data in 1966, (b) ETA lines survey data in 2013, (c) 1966 developed bathymetry, (d) and (e) 2013 Developed bathymetry compared to 1966 bathymetry as dashed contourlines.

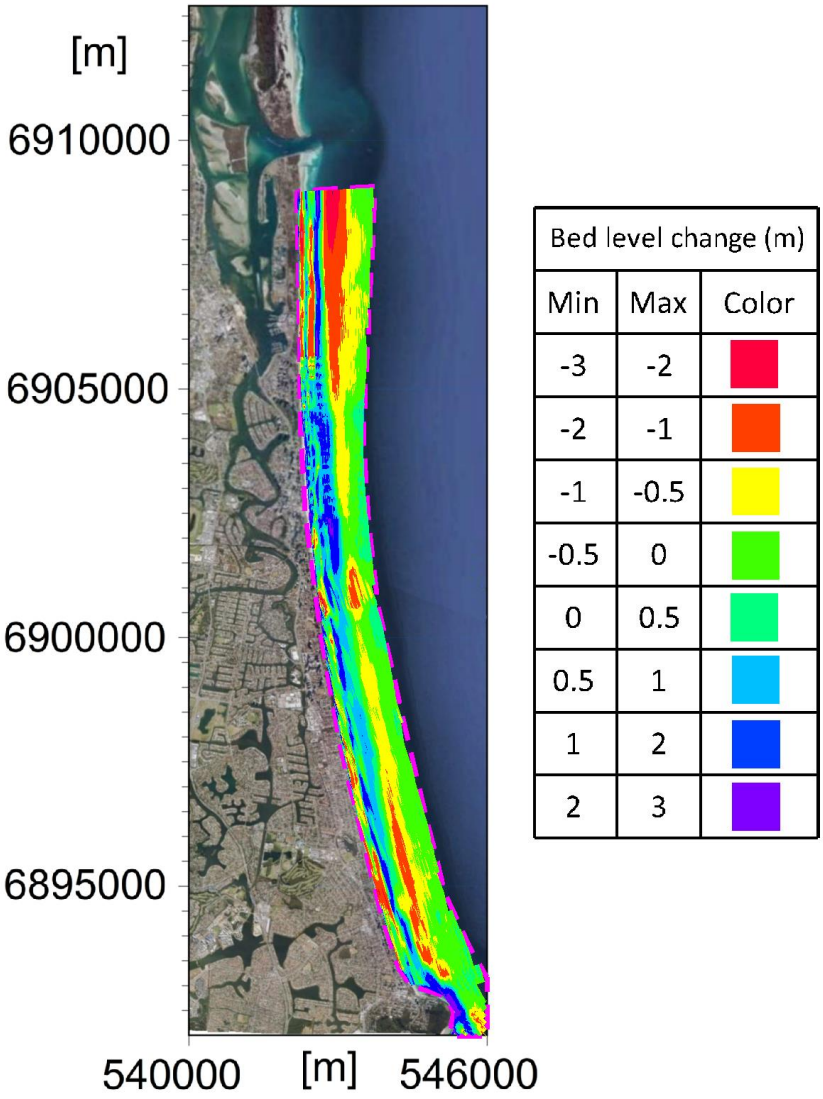

Figure A.2. Bed level changes from 1966 to 2013

Evolution of the shoreline position

The morphological evolutions of some ETA lines from Jan 1966 to Jul 2014 were also analysed. Zero AHD was defined as the shoreline location. Then, the shoreline positions for selected survey lines were investigated. The shoreline evolution for ETA 79, which is in the south of the GCS (Figure A.3), is shown in Figure A.4. As mentioned by WRL and GCCM (1998) and illustrated in Figure A.4, a significant volume of sand accumulated updrift the southern training wall between 1985 and 1986. This occurred mainly after the stabilisation of the inlet in 1985 but before the implementation of the sand bypassing system in 1986, and due to the dominant longshore sediment transport (LST). There were several fluctuations in the shoreline location during severe storms (shoreline retreat) and calm weather conditions (offshore migration).

However, the net trend of the ETA line 79 shoreline evolution since the stabilisation of the inlet was erosional while the maximum range was about 80 metres retreat.

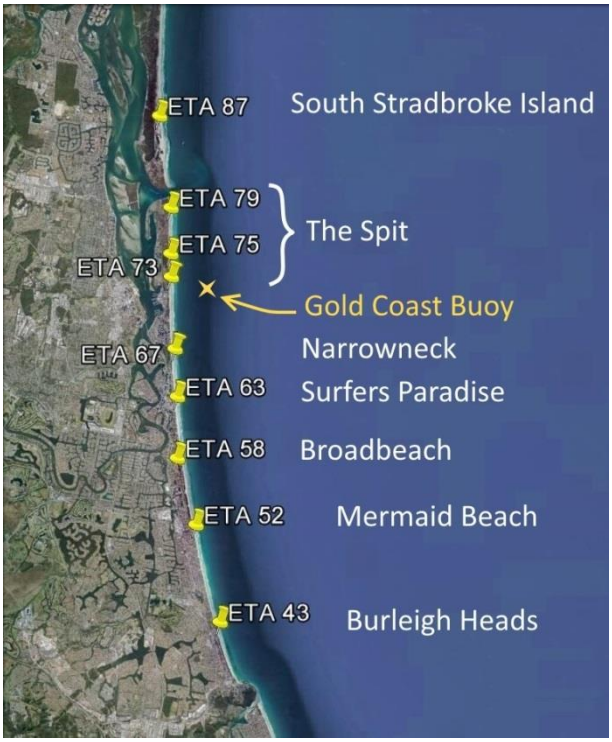

Figure A.3. Some of the ETA lines origins, the related suburbs, and the Gold Coast Buoy location

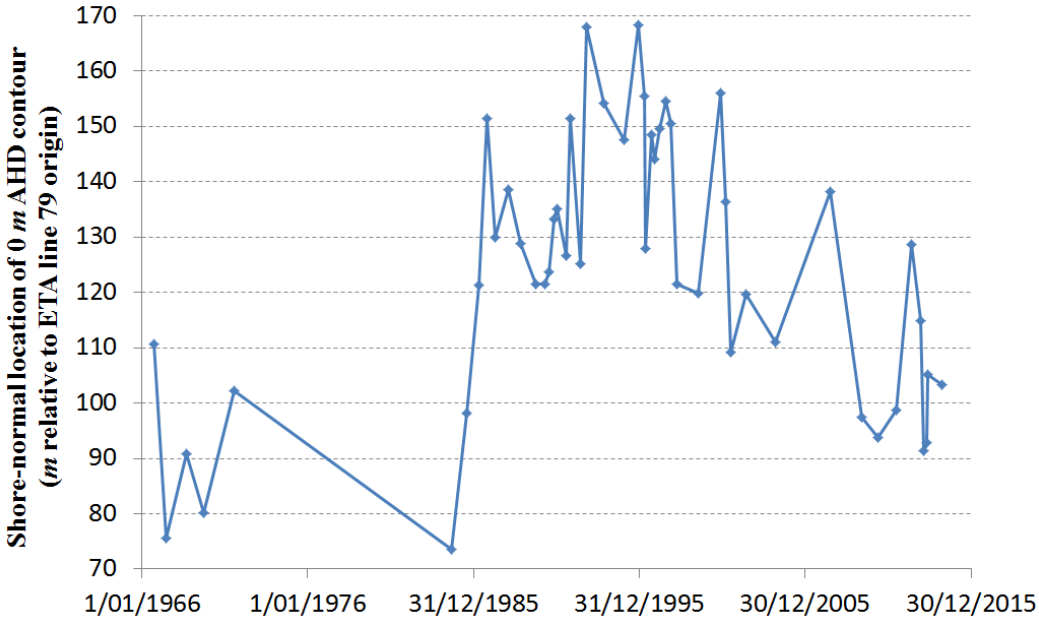

Figure A.4. Temporal variability of the shoreline (0*m* AHD) at ETA 79 (The Spit).

The trends of shoreline relocation for ETA 73 and 75 were similar, as shown in Figure A.5.

There was a net minor offshore migration of the shoreline from 1966 to 2007, while both ETA 73 and 75 showed a recessive pattern from 2007 to 2014. However, in general, the shorelines at these two ETA lines, during the period 1966 to 2014, were approximately in a dynamic equilibrium.

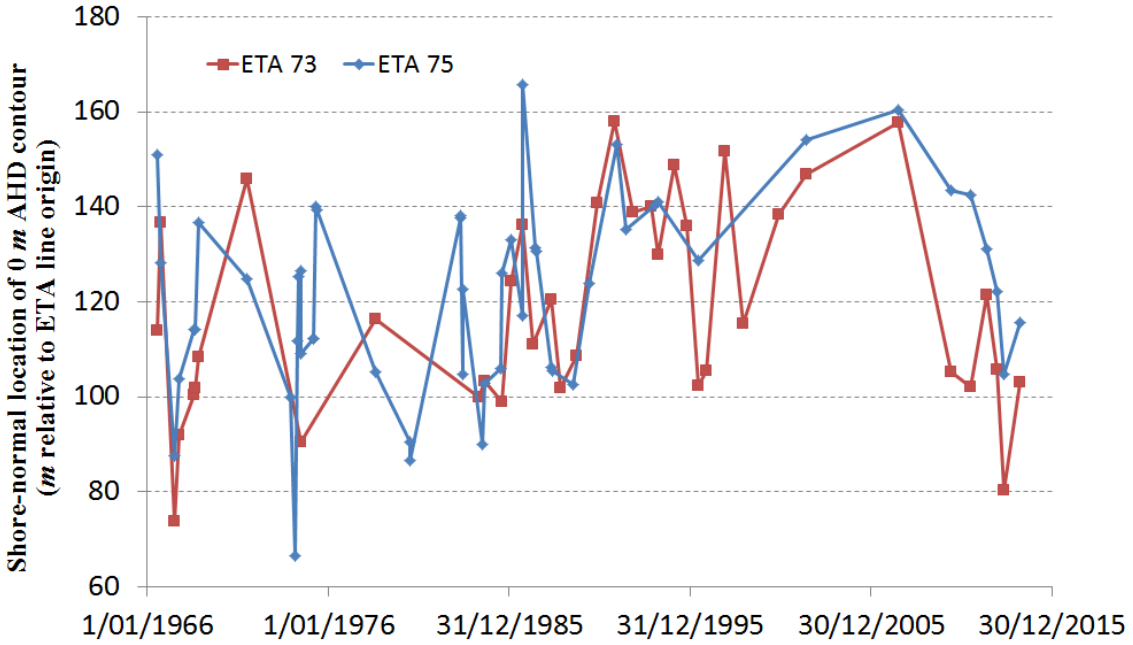

Figure A.5. Temporal variability of the shoreline (0*m* AHD) at ETA 73 and ETA 75 (The Spit).

Other ETA lines that were analysed were ETA 63 and ETA 67, which are located offshore of Surfers Paradise and Narrowneck respectively (Figure A.3). The shoreline location variations of these ETA lines are shown in Figure A.6. As illustrated, the net trend was depositional from 1966 to 2000, with the most significant accretion in 1999. This was a consequence of a major nourishment at Narrowneck in that year. Then, from 2000 to 2013, the net trend for these ETA lines was erosional.

Analysis of ETA lines 63, 67 and 79 illustrated that human interference has significantly affected the shoreline's morphological evolution at ETA line 79 (Figure A.4), due to the construction of the southern training wall; and also at ETA lines 63 and 67 (Figure A.6) due to renourishment activities.

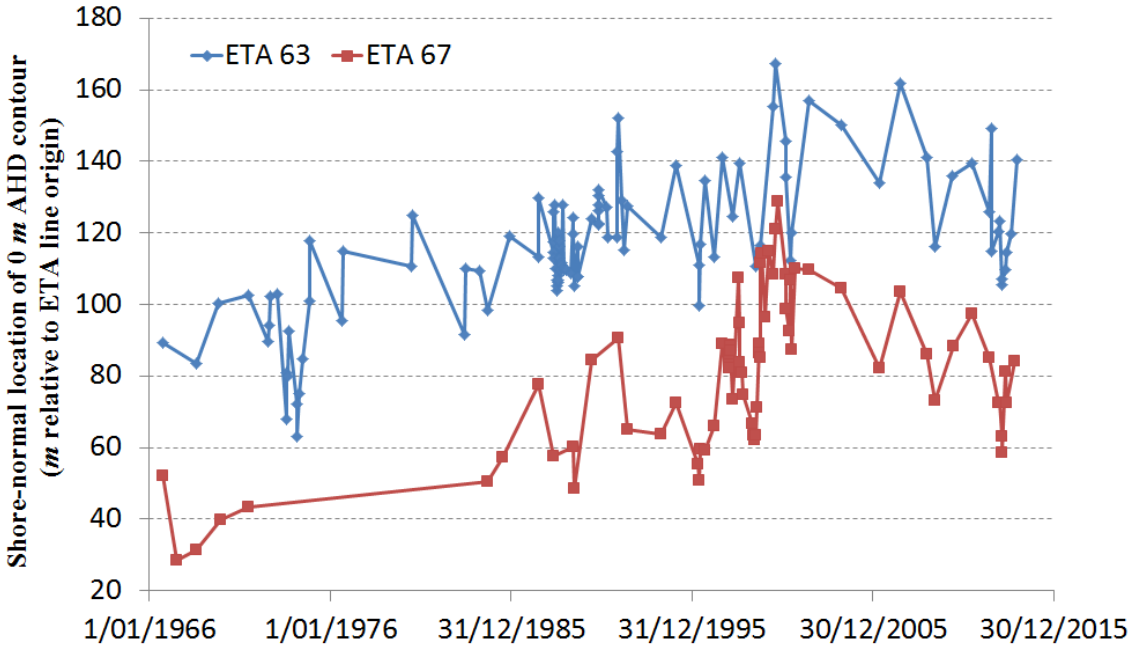

Figure A.6. Temporal variability of the shoreline (0*m* AHD) at ETA 63 (Surfers Paradise) and ETA 67 (Narrowneck).

The shoreline evolutions of ETA lines 58, 52 and 43 are shown in Figures Figure A.7, Figure A.8 and Figure A.9, respectively. As illustrated, the shoreline locations were in an approximate dynamic equilibrium, except the dominant offshore movement of ETA 58 shoreline from 1966 to 1971.

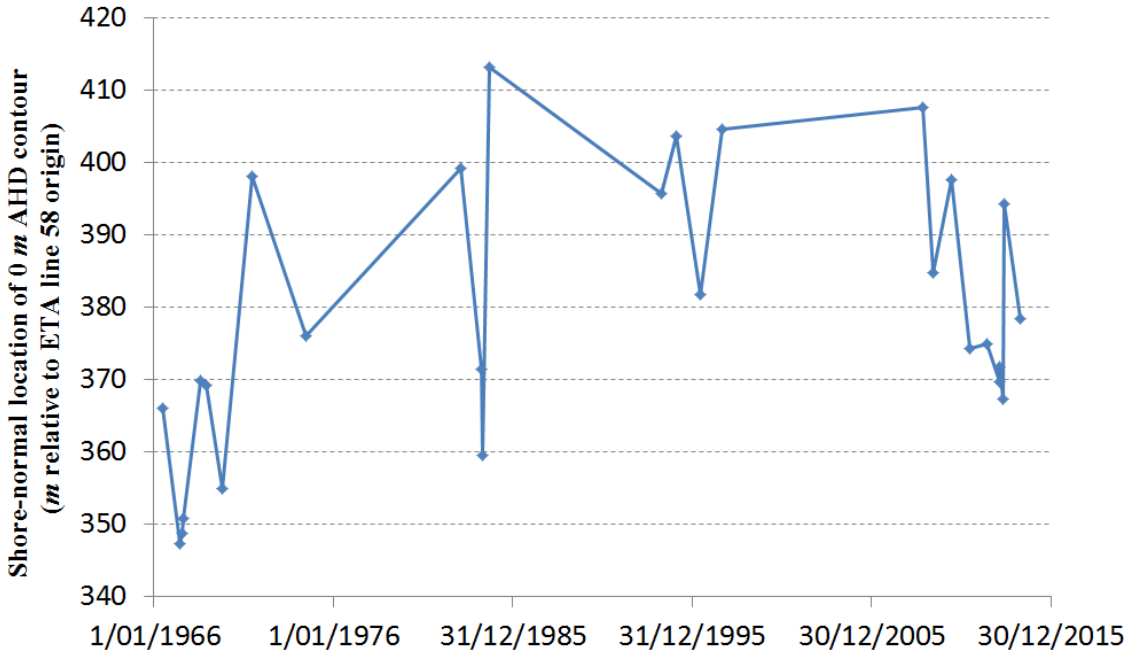

Figure A.7. Temporal variability of the shoreline (0*m* AHD) at ETA 58 (Broadbeach).

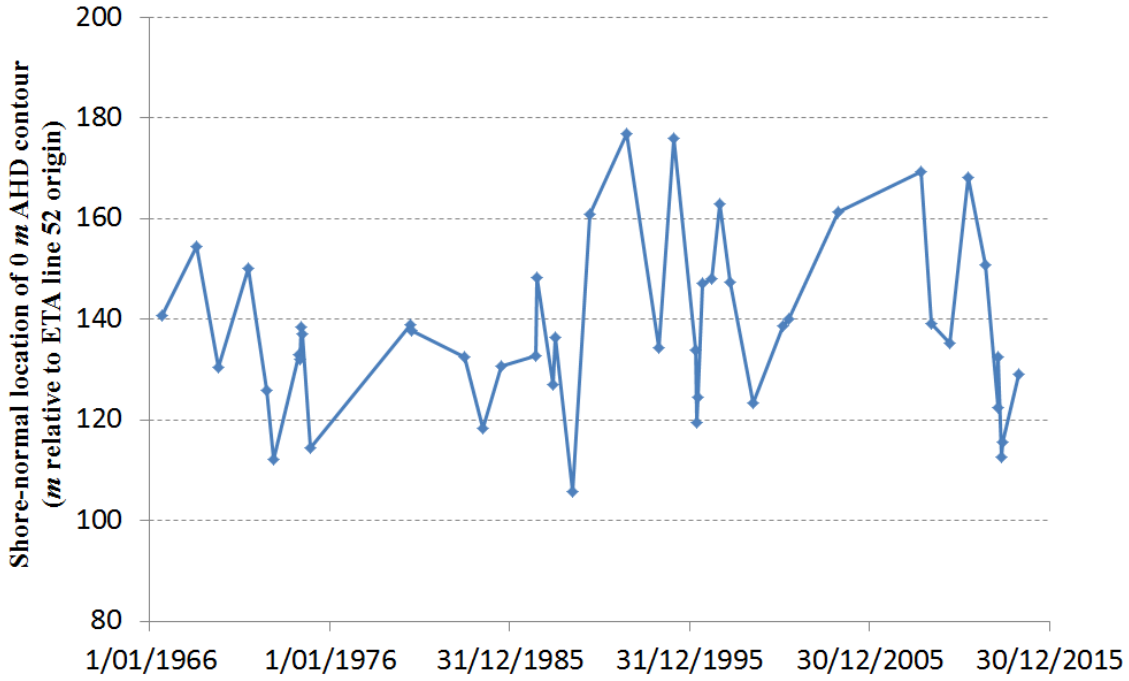

Figure A.8. Temporal variability of the shoreline (0*m* AHD) at ETA 52 (Mermaid Beach).

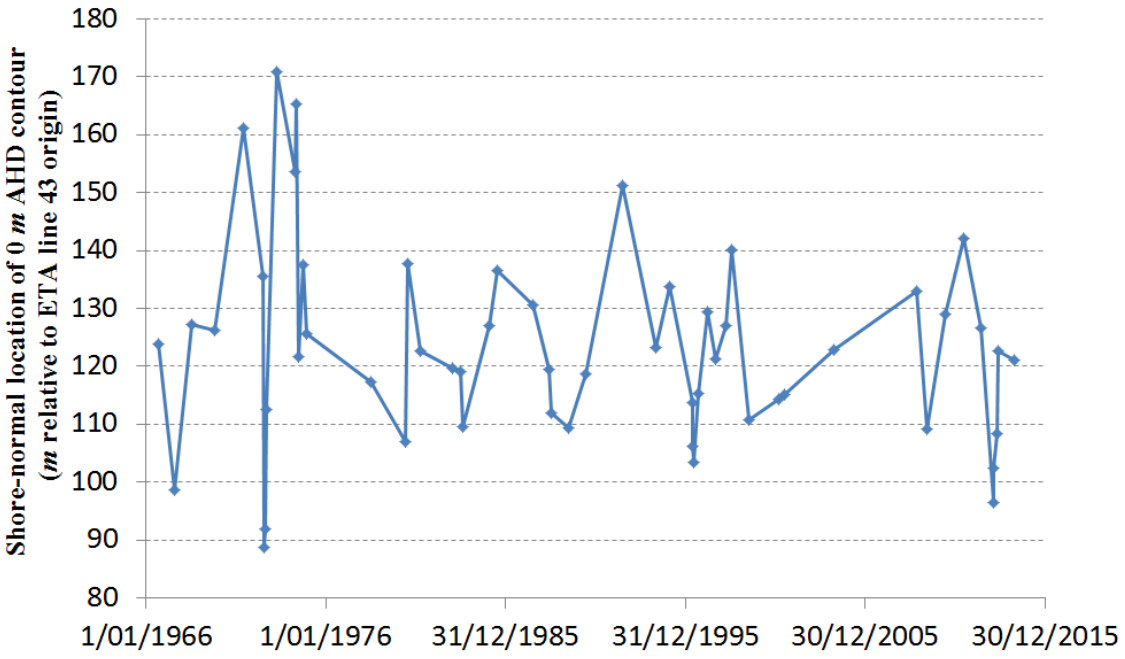

Figure A.9. Temporal variability of the shoreline (0*m* AHD) at ETA 43 (Burleigh Heads).

In regard to ETA 87 on South Stradbroke Island, north of the GCS and the northern extension of the ebb-tidal delta, there were a limited number of data sets available since the stabilisation of the inlet in 1985 and no data was available prior to the stabilisation. The shoreline evolution of this ETA line is shown in Figure A.10. As shown, there was a massive offshore movement of the shoreline from the 1985 entrance stabilisation through to 1988, and since then the

shoreline's net progress has been in a dynamic equilibrium.

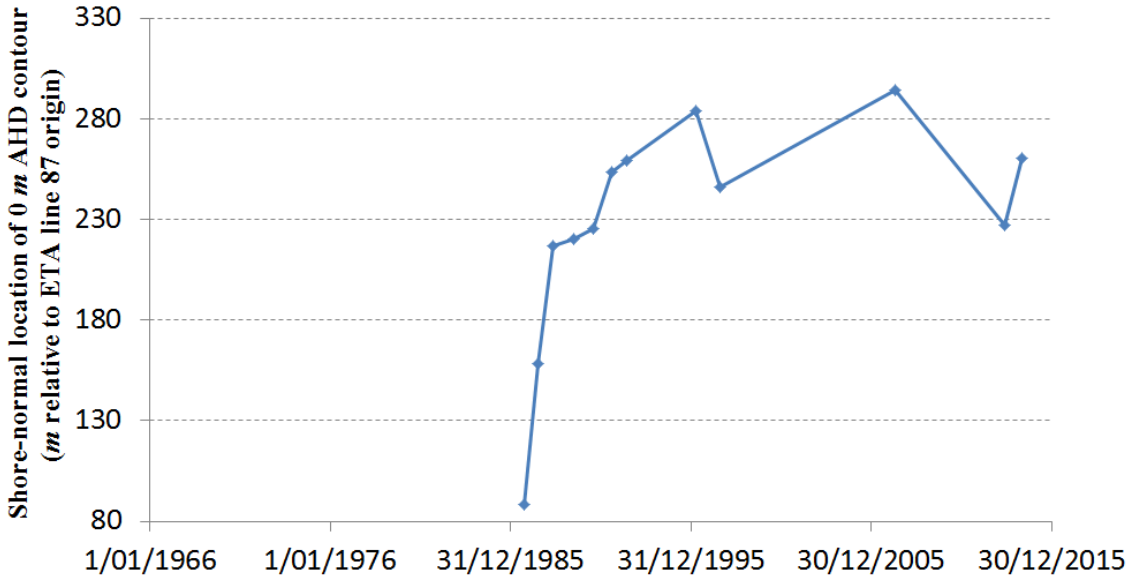

Figure A.10. Temporal variability of the shoreline (0*m* AHD) at ETA 87 (South Stradbroke Island).

To comprehensively analyse the trend of the morphological evolution of the ETA lines, detailed nourishment data, dredging, wave and LST rates are essential. However, since the main focus of this study is on the morphological evolution of the GCS ebb-tidal delta, this was not in the scope of this study. The analysis presented in this section illustrated that the GCS adjacent shorelines were mostly in a state of dynamic equilibrium. However, an increasing erosional trend was noticed since 2007 at ETA 79 which might be due to over bypassing of sediment by the sand bypassing system.